Study of minor species in the Venus night mesosphere

Daria Evdokimova

Thèse de doctorat

NNT : 2021UPASP039

Study of minor species in the Venus night mesosphere

Étude des espèces mineures dans la mésosphère nocturne de Vénus

Thèse de doctorat de l'université Paris-Saclay et Space Research Institute IKI of Russian Academy of Sciences

École doctorale n° 127 : astronomie et astrophysique d'Ile-de-France (AAIF)
Spécialité de doctorat: Astronomie et Astrophysique
Unité de recherche : Université Paris-Saclay, UVSQ, CNRS, LATMOS, 78280, Guyancourt, France
Référent : Université de Versailles Saint-Quentin-en-Yvelines

Thèse présentée et soutenue à Paris-Saclay, le 22 janvier 2021, par

Daria EVDOKIMOVA

Composition du Jury

Nathalie CARRASCO Professeur à l'Université Paris-Saclay	Présidente
Sébastien LEBONNOIS Directeur de recherche CNRS à Sorbonne Université	Rapporteur & Examinateur
Dmitrij TITOV European Space Agency (Pays-Bas)	Rapporteur & Examinateur
Alexander RODIN Directeur de laboratoire au Moscow Institute of Physics and Technology (Russie)	Examinateur
Nicholas SCHNEIDER Professeur à l'Université du Colorado (Etats-Unis)	Examinateur

Direction de la thèse

Franck MONTMESSIN Directeur de Recherche CNRS à l'Université Paris-Saclay	Directeur de thèse
Denis BELYAEV Chercheur au Space Research Institute (Russie)	Co-Directeur de thèse

CONTENTS

ACKNOWLEDGMENTS

The work on this study has become the most fascinating and instructive experience in my professional and personal life. And I would like to thank sincerely everyone who helped me to successfully complete this study and my PhD thesis.

I appreciate the wise supervision of Franck Montmessin at LATMOS. I thank you for all your advices and discussions, your support of my work and a lot of administrational assistance. Your supervision and competence made my work in LATMOS for these years being a remarkable experience. I am very grateful to my co-supervisor Denis Belyaev accompanying my work at the Space Research Institute of the Russian Academy of Sciences (IKI RAS). I thank you for proposing a subject of this study for me. Especially I appreciate that you have always been present and kind to help me with all my questions. The joint work with my supervisors allowed me to grow up my proficiency, and it was a source of every day motivation. I also would like to thank Emmanuel Marcq for sharing your experience with me and for your support with administration difficulties I have faced.

The defence of the thesis, under the joint supervision, became possible thanks to the French government BGF PhD grant 2016-2019 Vernadski, which is an honor for me. I sincerely thank the Embassy of France in Moscow. Also, I am grateful to LATMOS and to IKI RAS for providing me the chance to perform the PhD study under these terms, and for the additional financial support to complete the research.

I acknowledge the work with Anna Fedorova on the infrared spectra of Venus. I thank you for providing me a basis to perform this analysis and all your supervision and ideas during all the rough way of this research. Furthermore, I appreciate the big contribution of Oleg Korablev, the deputy director of IKI RAS, for organization of the joint supervision and of the defence. I would like to thank you as the PI of SPICAV IR spectrometer for a beautiful and informative experiment. The major part of this work was done based on the measurements of the SPICAV UV instrument, and I wish also to thank Jean Loup Bertaux, a PI of this experiment. The clues to analysis and the work with you was very important for me.

I would like to express my deep gratitude to all the members of the jury, Nathalie Carrasco, Sebastien Lebonnois, Alexander Rodin, Nicholas Schneider, Dmitry Titov, who were very kind and supportive during the organization of the defence in the complicated and stressful time of 2020-2021. I am very grateful to my two reviewers Sebastien Lebonnois and Dmitry Titov, for taking the time for careful examination of my manuscript. And I would like particularly to thank the president of my jury, Nathalie Carrasco, for full cooperation, and thank you for being a member of my thesis committee and for following steps of my work from the beginning. I am also very grateful to Franck Lefèvre for being a member of my thesis committee and for a lot of explanations concerning the Venus general circulation modeling.

In this work some results are compared with the IPSL Venus general circulation mode, which were prepared by Gabriela Gilli. I am happy to have a chance to cooperate with you and I appreciate very

much your participation in deeper analysis of the obtained experimental results. Thank you to Lucio Baggio and Loïc Verdier for cooperation during the study of data calibration efficiency.

This PhD project under the joint supervision was very supported by the directors of the École doctorale N°127: astronomie et astrophysique d'Ile-de-France (AAIF), Thierry Fouchet and Jeacques Le Bourlot, and its deputy director Alain Abergel at all the stages, and I am very grateful for this extremely valuable support. Similarly, I appreciate the assistance of the LATMOS directors: Dr. Phillip Keckhut and Pr. Francois Ravetta. I also thank the administration of the École doctorale, the Université Paris-Saclay and the Université de Versailles St Quentin en Yvelines, and the administration of the doctoral school of IKI, Angelina Shchukina and Andrey Sadovsky.

Thank you also to all my colleagues, the members of SPICAV, SPICAM and ACS teams, I have worked with in France and in Russia. It was great to have met my colleges: Loïc Rossi, Kevin Olsen, Gaetan Lacombe, Anni Määttänen, Aurélien Stcherbinine, Abdenour Irbah, Ashwin Braude, Margaux Vals, Hugo Gilardy and Jean-Yves Chaufray. Furthermore, I was happy to participate in the European research course on atmospheres, and gain a lot of the experience. And it was a great pleasure to continue working with my colleges: Alexander Trokhimovskiy, Nikolay Ignatiev, Michail Luginin, Andrey Patrakeev, Nikita Vyasovetsky, Yuri Dobrolensky, Vladimir Kotsov, Sergey Mantzevich, Alexander Lomakin, Nadezhda Rotova, Marina Patzaeva, Igor Khatuntsev and Alexandra Smirnova. I appreciate your friendship very much. I am very grateful to Sergey Khaykin for support and some Russian language in France. I would like also to thank my dear friends Olya, Alina, Slava, Kemal, Artem, Sasha, Olya and my family for continuous support, belief and guidance.

PURPOSE OF THE WORK

The structure of Venus' atmosphere and the study of its composition have remained a challenge for scientists: which processes of the planet's evolution did lead to the observed atmospheric condition crucially different from the Earth's atmosphere. Various models based on the data up to date show that an overall picture of the atmospheric composition and dynamics has not yet been obtained. Prior to the Venus Express (VEX) mission (2006-2014), a detailed study of the atmosphere and minor gas components above the clouds, where the defining processes take place, was not possible. For the first time, the VEX experiments of solar and stellar occultations studied in detail the vertical structure of the atmosphere on both planetary terminators and on the night side.

The SPICAV spectrometer could observe several trace gases using its ultraviolet (UV) channel (118-320 nm). The Venus Express mission with this instrument on board was operating for 8 years. Sensitivity of the implemented stellar occultation method establishes the observed altitude range to 85-110 km. A large amount of unique information has been accumulated for a detailed study of variations in atmospheric components. Sulphur dioxide and ozone are the two atmospheric minor species which are targets of our study in Venus mesosphere. The study of their distribution in the night mesosphere is the goal of this work. It contributes to global understanding of the main chemical processes which are the carbon dioxide and sulphur dioxide cycles in the Venus atmosphere.

Sulphur dioxide possesses ultraviolet absorption bands in 190-300 nm. The gas was extensively observed by ground-based telescopes and orbiters on the day side of the planet at the level of clouds top (~70 km) for more than 40 years on Venus. On the other hand, the SPICAV/SOIR instrument of Venus Express mission sounded the vertical distribution of SO_2 at altitudes 65-110 km on the terminator. Variations of the dioxide content occurred to be extremely high in the dayside and twilight mesosphere. So far, there was no data from SO_2 distributions at the night-time mesosphere where photochemical and temperature conditions differ from those at the day time. The first goal of our study is to obtain a mesospheric distribution of sulphur dioxide at the night side of Venus. Spatial and long-term variations are to be compared with previous dayside results.

The second scientific objective deals with the recent discovery of an ozone layer in Venus' mesosphere on the night side (Montmessin et al., 2011). Absorption of ozone in the Hartley band (~250 nm) was observed by the SPICAV UV in the stellar occultation mode at altitudes 90-100 km. Just episodic bursts of O_3 mixing ratio with a few tens ppbv were detected in 2006-2010 from 29 observation sessions. That was consistent with ozone production and destruction schemes according to reactions with oxygen and chlorine atoms in the anti-solar point at the SSAS circulation. Such a mechanism takes place in the Earth's upper stratosphere. In parallel, an abundance of ozone was recently discovered at the Venusian cloud tops near polar regions (Marcq et al., 2019) that signifies the O_3 interconnection with the atmospheric dynamics.

In the present research we have processed the whole statistics of the SPICAV UV stellar occultations in 2006-2014, that is >400 sessions. We characterize ozone distribution at altitudes 90-100 km, the region

corresponding to airmass transitions between two circulation mechanisms. This study of the ozone behaviour on the night side will improve existing atmospheric models and will provide revealing the differences between the terrestrial atmospheres.

Another process leading to ozone formation results in oxygen ($\alpha^1\Delta_g$) airglow at 1.27 μm primarily formed at about 95 km which corresponds to the altitude range of the ozone detections. Our analysis was also supplemented by the night-time observations of the O_2 emission by the infrared (IR) channel of SPICAV.

In order to accomplish the SO_2 and O_3 vertical distribution study, all processed stellar occultation spectra of SPICAV have to be cleaned and calibrated. It is important to provide the detection even at small concentrations of these gases. The importance of calibration is revealed by the analysis of the night-time SO_2 vertical distribution when considering two different calibration approaches (Belyaev, Evdokimova et al., 2017 vs. Evdokimova et al., 2020).

The thesis is organized in 6 Chapters.

Chapter 1 contains an overview of basic knowledge about Venus and its atmosphere.

Chapter 2 presents a result of sulphur dioxide and ozone observations in detail. The explanation of observed data is partially presented in several photochemical models that summarize a knowledge about chemical processes affected by the atmospheric circulation.

Chapter 3 describes the used dataset and the observation technique that was performed by SPICAV UV. The data processing algorithm is presented in detail including a test of the experiment sensitivity and improvements that were used.

Chapter 4 is devoted to the obtained results of SO_2 content and its analysis.

Chapter 5 is devoted to the obtained results of O_3 content and its analysis.

Chapter 6 considers the O_2 ($\alpha^1\Delta_g$) airglow at 1.27 μm as an additional source of the information about the Venus night mesosphere. The nadir observations by SPICAV IR are used to retrieve a nigh-side distribution of the emission intensity.

CHAPTER 1. Venus and its atmosphere

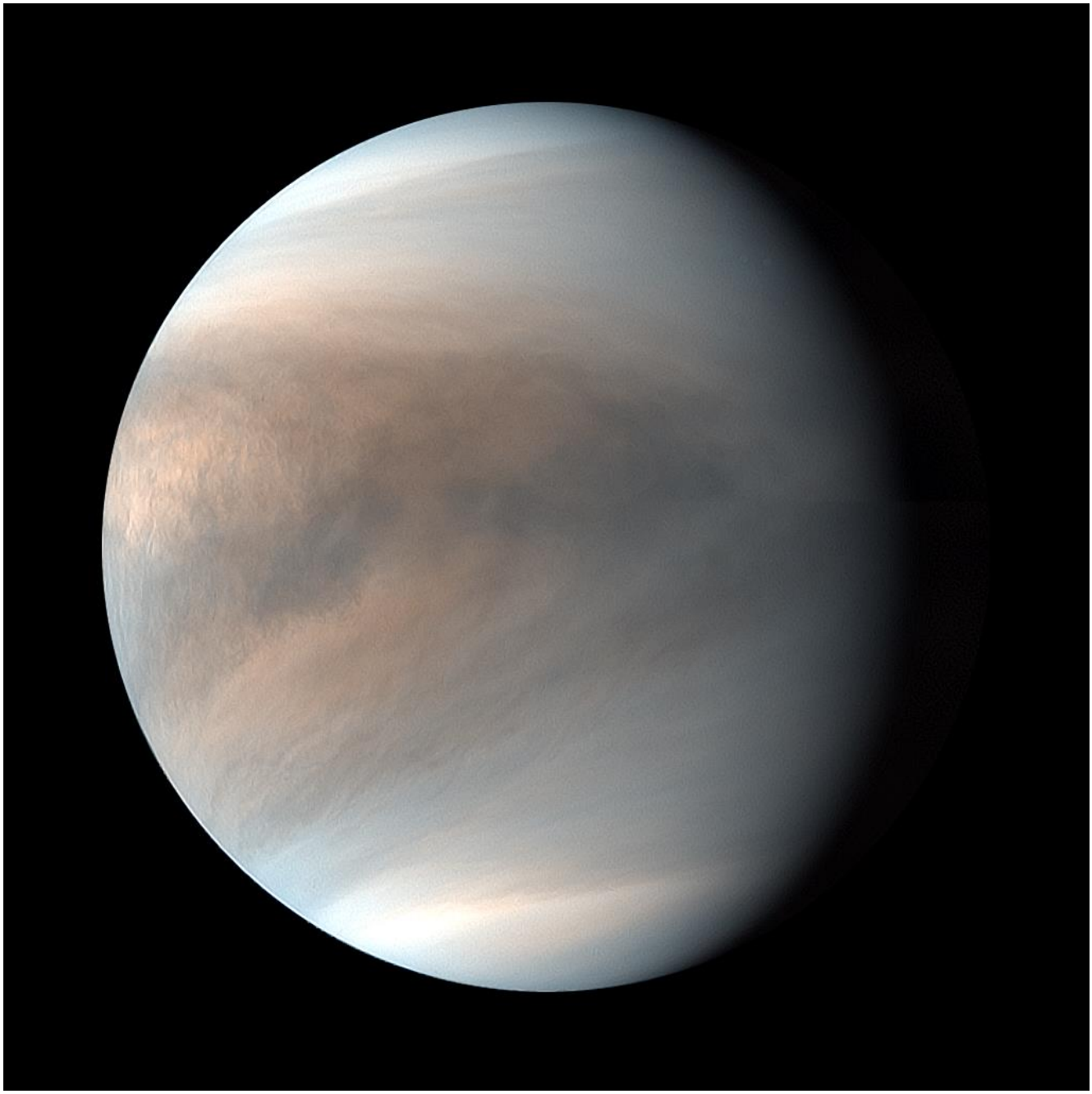

Figure 1.1. False colour image of Venus clouds by the Ultraviolet Imager (UVI) on board the Akatsuki spacecraft on the 30th of March 2018. Images at 283 nm and 365 nm were superimposed. Blue colour corresponds to the 283-nm absorption by SO_2, red colour corresponds to unknown UV absorber (365 nm). © Japan Aerospace Exploration Agency (JAXA) https://akatsuki.isas.jaxa.jp/en/gallery/data/001167.html

1.1. The Earth's evil twin

Since ancient times the second planet from the Sun and the closest to the Earth, Venus, has been the object of close attention. Out of the terrestrial planets, this planet is the most similar to the Earth in size and mass. So it is often called the «sister» planet or even the «twin» of the Earth: its radius is 6052 km and its mass is 4.87×10^{24} kg, that is 95% and 82% respectively of the Earth's. In other respects, the differences between the two planets can be significant (Colin, 1983). Moving in an almost circular orbit around the Sun, with an eccentricity of 0.00677 and at an average distance of 0.723 astronomical units (108 million km), Venus approaches the Earth at a minimum distance of 38 million kilometers. For comparison, the minimum distance to Mars, the fourth planet of the terrestrial group, is one and a half times greater. Thus, the planet makes a complete revolution around the Sun in 224.7 Earth days.

Venus is one of the two planets in the solar system with retrograde rotation. Venus' rotation axis inclination angle is 177°, thus, it is nearly perpendicular to the ecliptic plane. Such an axis tilt and orbital parameters exclude a presence of seasons on the planet. In addition, Venus rotates very slowly. The period of the planet's revolution around its own axis is approximately 243 Earth days. However, due to the retrograde rotation, a solar day on the planet lasts about 116.75 Earth days, and a complete revolution around the Sun amounts to only 1.92 Venus days. This slow rotation has allowed the gravimetric surface of Venus to maintain a spherical shape, mitigating polar compression.

Our knowledge on Venus before the beginning of the space exploration era was rather scarce. In 1610, using the first telescope, Galileo Galilei was the first who observed a change of the visible diameter of Venus and its phase that became a proof of the planetary movement around a single centre, i.e. the Sun (Chruikshank, 1983). The historical discovery was made by M.V. Lomonosov on June 6, 1761 during the planet's transit over the solar disk. He noticed a halo of light emerging around the Venus disk when observed at the Sun limb. The scientist correctly explained the pattern as light scattered by an atmosphere enshrouding the planet. In his work M.V. Lomonosov concluded: «The planet Venus is surrounded by a noble air atmosphere, such (if only not more), which is poured around our globe.» (Lomonosov, 1761, the citation is translated to English by the author). It took more than three centuries to obtain more detailed information about the structure of the atmosphere.

For an astronomical observer using the visible range of the spectrum, Venus appears as a slightly yellowish bright disk without pronounced features. This is due to an opaque cloud layer having no "holes" and hiding the surface for remote observations. At the dawn of the Venus exploration era this peculiarity of the planet was a cause of diverging hypotheses about the conditions below the clouds, at the surface and a possible presence of life. The high albedo of the clouds, which reflect about 80% of the solar radiation, provides an amount of energy received by Venus from the Sun, comparable to that of the Earth. Until the 1960s, this led some scientists to assume the planet's climate to be similar to the temperate climate of the Earth (Cruikshank, 1983). One can simply estimate the effective temperature for Venus, which is 231 K (-45° C). However, the first radio astronomical observations (Mayer et al., 1958) showed that the conditions near the surface are much more severe and not comparable to those on Earth. The planet's surface reaches 750 K (477º C). The reason for such a hot surface is the significant greenhouse effect produced by the dense CO_2 atmosphere.

A detailed study of Venus would not have been possible without the contribution made by spacecraft reaching the lower atmosphere and surface. One of the important examples is that the pressure at the surface reaching 90 bar was measured only when the Soviet station of Venera 7 released the first landing on the 15th of December 1970. The space exploration of the planet started in 1962.

1.2. A new view of Venus

The era of active spacecraft exploration of Venus coincided with increased research interest in climate change on Earth. New knowledge about the Venusian atmosphere has made this planet an example of a world where the uncontrolled greenhouse effect has heated the airmass below clouds and the surface up to enormous temperatures (Sagan, 1960; Rasool and De Berg, 1970). The discovery of this phenomenon has become a catalyst for the study of such processes on Earth. Venus gives an example of the extreme greenhouse effect in a dry carbon dioxide atmosphere. Since the two planets are similar by size and mass the researchers need to understand which processes may become responsible for triggering an uncontrollable greenhouse effect on Earth. Not only the impact of carbon dioxide is to be considered. The Venus clouds, reflecting 76% of the sunlight, should protect against the surface overheating. However, at wavelengths shorter than 2.5 μm, concentrated sulphuric acid, which dominates the composition of aerosol particles on Venus (Sill, 1972; Young, 1973), also absorbs radiation contributing to some extent to the greenhouse effect. That is why, researchers of the Earth's atmosphere have paid more attention to the chemistry of sulphur compounds. The possible impact of sulphate aerosols, both volcanic and anthropogenic, on changes in the Earth's global temperature was also reassessed (Hansen et al., 1978).

Our neighbour, being an object of scientific observation of new physical and chemical processes, has demonstrated the importance of controlling them also on Earth (Prinn, 1982). The stability of the relative carbon dioxide content (96.5%) on Venus raised the issue of a large influence of minor gaseous components on chemical processes in the atmosphere. Carbon dioxide is actively photodissociated, but it less effectively restored from the produced CO and O_2. Thus, this should reduce its amount. The first CO_2-atmosphere models of Mars and Venus showed the importance of catalytic cycles (Cruikshank, 1983; Krasnopolsky, 2011). In these reaction chains minor gas components are catalysts, and they contribute to CO_2 restoration without changing themselves. At the same time, the effect of such processes on the Earth's stratospheric ozone was studied. The observations showed a smaller amount of O_3 than a model considering only photolysis for its destruction provided (the Chapman mechanism from Chapman, 1930). Both natural sources (products of water photolysis) and anthropogenic impacts (combustion products from rocket fuel in the stratosphere) were considered. Halogens were already found in the Venus atmosphere at that time (Mueller, 1968). Works of Prinn (1971) and McElroy et al. (1973) showed the importance of chlorine compounds, namely the detected hydrogen chloride, as catalysts. The chains of chemical reactions in the photochemical model of the Venusian atmosphere also included oxygen compounds, which partly showed the effect of chlorine-containing substances on the breakdown of the ozone molecule. Later on studies of catalytic chemistry of anthropogenic emissions, especially volatile chlorine compounds (Wofsy and McElroy, 1974; Stolarski and Cicerone, 1974;

Molina and Rowland, 1974), demonstrated their effect on the ozone loss in the Earth's atmosphere (Farman et al., 1985).

With the development of exoplanet science, the existence of life on Earth started to be considered in the context of searching for habitable worlds near other stars. A «habitable zone» criterion for the planetary system was formulated by Kopparapu et al. (2013). This criterion defines the location of the planet in respect to a parent star so that conditions on its surface allow the presence of liquid water. This is the only robust criterion for the possible origin of life so far. The habitable zone also limits the runaway greenhouse effect during the planet's evolution, which brings the atmosphere to a state similar to that it is on Venus now. In the context of the habitable zone near the Sun, Venus is on its inner boundary (the orbit of Venus is 0.723 AU, while the inner boundary of the inhabited zone is 0.75 AU). However, based on current atmospheric composition knowledge, modelling also shows that conditions on Venus in its past did not rule out the possibility of an ocean on its surface (Way et al., 2020). If this hypothesis is confirmed in future studies, the limits of search for life shall be extended beyond the inner boundary of the habitable zone, into the «Venus zone», where many more planets are currently found than in the canonical habitable zone.

1.3. History of observations

1.3.1. Venus space missions

In total, 27 spacecrafts were launched and successfully performed science experiments either around Venus, or inside the atmosphere or on the surface: 19 from the Soviet Union, 6 from the United States of America, one European Venus Express orbiter in 2005, and one Japanese Akatsuki station in 2010.

The first period of active exploration of Venus was led by space programs of the USSR and the USA. At least one mission in every «astronomical window» was launched in the period from 1965 to 1985. The USSR led the series of «Venera» and «Vega» stations which successfully landed on Venus 10 times. On the U.S. side, several spacecraft (Mariner 2, the first interplanetary probe, Pioneer Venus and Magellan) were sent to the planet from the sixties to the nineties. One descent probe also reached the surface as a part of the Pioneer Venus 2 mission. Table 1.1 shows the timescale of successful missions to Venus.

The first spacecraft, which successfully reached the orbit of Venus, was the American Mariner 2 mission launched in 1962. Its measurements confirmed the slow retrograde rotation of the planet, high surface temperatures and a dense cloud cover. In addition, the calculation of the spacecraft trajectory made it possible to estimate the mass of the planet, which was not yet precisely known. In 1967, Venera 4 was the first probe which made *in situ* measurements in the atmosphere of a planet other than Earth during its descent to the surface down to 26 km. This made it possible to confirm that CO_2 was the main component of the atmosphere and that the estimated surface pressure (~100 bar) exceeded the values expected at that time (Avduevskij et al., 1968). This pressure estimate was later confirmed by radiometric soundings from the Mariner 5 probe. The Venera 5 and 6 stations also attempted to land on the planet surface, but none of them were successful due to the extreme temperatures and pressures encountered during the descent.

Table 1.1. A timeline of successful missions to Venus. The survey of 60-90s is done based on Moroz et al. (2002), Limaye (2015), Drossart and Montmessin (2015), Fukuhara et al. (2017), Horinouchi et al. (2017)

Year	Space mission	Country	Results
1962	Mariner 2 (Flyby)	USA	The first spacecraft that reached Venus.
1967	Venera 4 (Lander)	USSR	The first in situ measurements on another planet down to 26 km. Temperature measurements, structure of outer layers, CO_2 estimated at 90-95% of the composition.
1967	Mariner 5 (Flyby)	USA	Temperature measurements, structure of outer layers, CO_2 content was 85-99%.
1969	Venera 5 & 6 (Landers)	USSR	Measurements of temperature, pressure, wind speed, CO_2 content was 93-97%, N_2 - 2-5% O_2 - <4% in the range of 25-55 km. The two probes worked down to 18 km.
1970 1972	Venera 7 & 8 (Landers)	USSR	First soft landing on the surface of another planet. The temperature was found to be ~748K and the pressure ~90 bar.
1974	Mariner 10 (Flyby)	USA	Images of clouds in the IR and UV. First high-resolution UV images.
1975	Venera 9 & 10 (Orbiters, landers)	USSR	First surface panoramas. Studies of the structure and composition of the atmosphere and the cloud layer. The lower cloud boundary was found to be at 49 km, while the cloud was found to consist of 3 layers: 49-52 km, 52-57 km, 57-70 km. From the orbit, images of the cloud layer, the temperature distribution over the upper boundary of the clouds, the spectra of the planet's night glow, multiple radio soundings of the atmosphere and ionosphere were obtained.
1978	Pioneer Venus 1 (Orbiter) & 2 (4 atmo-spheric probes)	USA	Operated in orbit from 1978 to 1992. Continuous sounding of the middle and upper atmosphere. The composition of aerosol particles of clouds contains sulphuric acid. The landing modules obtained an abnormally high content of inert gases in the atmosphere, and studied the dynamics of the lower atmosphere.
1978	Venera 11 & 12 (Flyby, landers)	USSR	The mass spectrometer detected trace amounts of water vapour, chlorine, sulphur and their compounds. The location of the cloud lower boundary at 48-49 km.
1982	Venera 13 & 14 (Flyby, landers)	USSR	The first coloured panoramas of the surface. Some small gas components detected - sulphur and chlorine compounds. An abnormally small amount of water in the atmosphere.
1983-1985	Venera 15 & 16 (Orbiters)	USSR	A radar map of 30% of the surface corresponding to the Northern Hemisphere. IR observations of the atmosphere: reconstructing the temperature profile, calculating thermal winds in the mesosphere, determining the content of H_2O and SO_2 at the cloud top and studying the parameters of the clouds.
1985	VeGa 1 & 2 (Flyby, atmo-spheric probes, landers)	USSR	Balloons: study of winds, particle sizes and their composition in the cloud layer at an altitude of 53-54 km. The wind speed reached 66 and 69 m/s. Landers: multiple results on the atmosphere, including SO_2 profile below clouds. The surface composition analysis by the Vega 2 lander.
1990-1994	Magellan (Orbiter)	USA	First full-scale radar mapping of Venus from the orbit. Gravity map of 98% of the surface.
1989	Galileo (Flyby)	USA	First images and spectra of Venus night radiation in the near-IR range - thermal radiation of the lower atmosphere and surface.
1997	Cassini -Huygens (Flyby)	USA, Europe	Images and spectra of Venus night radiation in the near infrared range.
2005	Messenger (Flyby)	USA	During the flyby around Venus, the upper atmosphere of Venus was observed in the near-IR, visible, UV and X-ray ranges. Joint observations with the Venus Express mission.
2006-2015	Venus Express (Orbiter)	Europe, Russia	First observations of a double vortex at the planet's South Pole. Detection of OH in the atmosphere of Venus (VIRTIS). Detection of ozone in the mesosphere of Venus. HDO/H_2O ratio in the upper atmosphere is 240 ± 25 times higher than on Earth, and ~1.5 higher than in the lower atmosphere. Discovery of a warm layer in the night mesosphere at an altitude of 100 km.
Since 2015	Akatsuki (Orbiter)	Japan	Study of the structure of the atmosphere. The image of a global gravity wave in the cloud layer in the region of the Aphrodite-Terra mountain range in the IR range. The equatorial jet of Venus in the cloud layer.

The first soft landing was made in 1970 by Venera 7 on the night side of the planet. During its 23 minutes of operations on the surface, temperature and pressure were measured, as well as the composition of the crust using gamma spectrometry. A pressure of 90±15 bar and a temperature of 748±20 K (475±20°C) were obtained at the surface. Venera 8 confirmed the possibility of taking photos at the surface: illumination on Venus surface near the evening terminator turned out to be equal to the Earth twilight. Venera 9 and 10 landers performed the first imaging of the surface. During the descent, nephelometers studied the composition and structure of the atmosphere and of the cloud layer (see Table 1.1). Venus was then reached by the 2 Pioneer Venus (PV) missions led by NASA. PV 1 was orbiting the planet from 1978 to 1992 and sounding the atmosphere remotely. The concept of PV 2 contained 4 descent probes: one large and three small modules (the North Probe, the Day Probe and the Night Probe). The Day Probe successfully landed and transmitted data from the Venus surface for ~60 minutes (Colin, 1979). The important observations of the cloud layer structure were done during descent (Knollenberg and Hunten, 1980). Further development of the Venera program allowed obtaining unique phenomena of atmospheric lightning. The electrical activity was registered by the GROZA experiments on board the Venera 11 and Venera 12 missions (Ksanfomaliti et al., 1979). The composition of cloud aerosols was supplemented by such components as chlorine and phosphorus, although it was not possible to identify compounds. Moreover, Venera 13 and 14 conveyed the only colour surface panoramas. The Venera 15 and 16 orbiters mapped 30% of the surface in the Northern Hemisphere.

The era of the Soviet study of Venus ended with the Vega mission, which combined explorations of Venus and Halley's comet. The part dedicated to Venus contained two aerostat balloons placed into the clouds. They were tracked by the ground based NASA's Deep Space Network, and the data of their motion provided the wind velocities at an altitude of 53-54 km (Kremnev et al., 1987). Convective and turbulent activities in the cloud layer and the aerosol composition were characterized in detail. The both probes also detected lightning discharges on the night side. Vega 2 for the first time landed in a high mountain region, where the Venusian rock was found to be a close analogue of terrestrial volcanic material (Surkov et al., 1986). It is the only spacecraft measured the high-resolution temperature profile down to the surface and found the anomalius behaviour below 7 km (Crisp and Titov, 1987).

NASA's Magellan mission accomplished a topographic mapping of the surface in detail (spatial resolution ~100 m) in the early 1990s (Saunders et al., 1992; Bindschadler, 1995). Magellan payload included a synthetic aperture radar and an instrument for studying the gravitational field of Venus. In September 1990, Magellan began its scientific mission, which lasted for 4 years. Radar showed more than 1660 volcanic landforms. This number included 274 intermediate volcanoes 20-100 km in diameter and 56 large volcanoes greater than 100 km in diameter (Saunders et al., 1992). It was found that 85% of the planet's surface is covered by lava flows. The surface of Venus has different tectonic features with a variety of scales (Solomon et al., 1992). The absence of erosion has saved them in well-defined structures. As a result, 98% of the planet's surface was mapped (Figure 1.2), and moreover, stereo maps of the surface were also obtained. In addition, it was concluded that the surface of Venus is geologically young (<500 million years) because only a few impacts craters were found at the surface (Bullock et al., 1993).

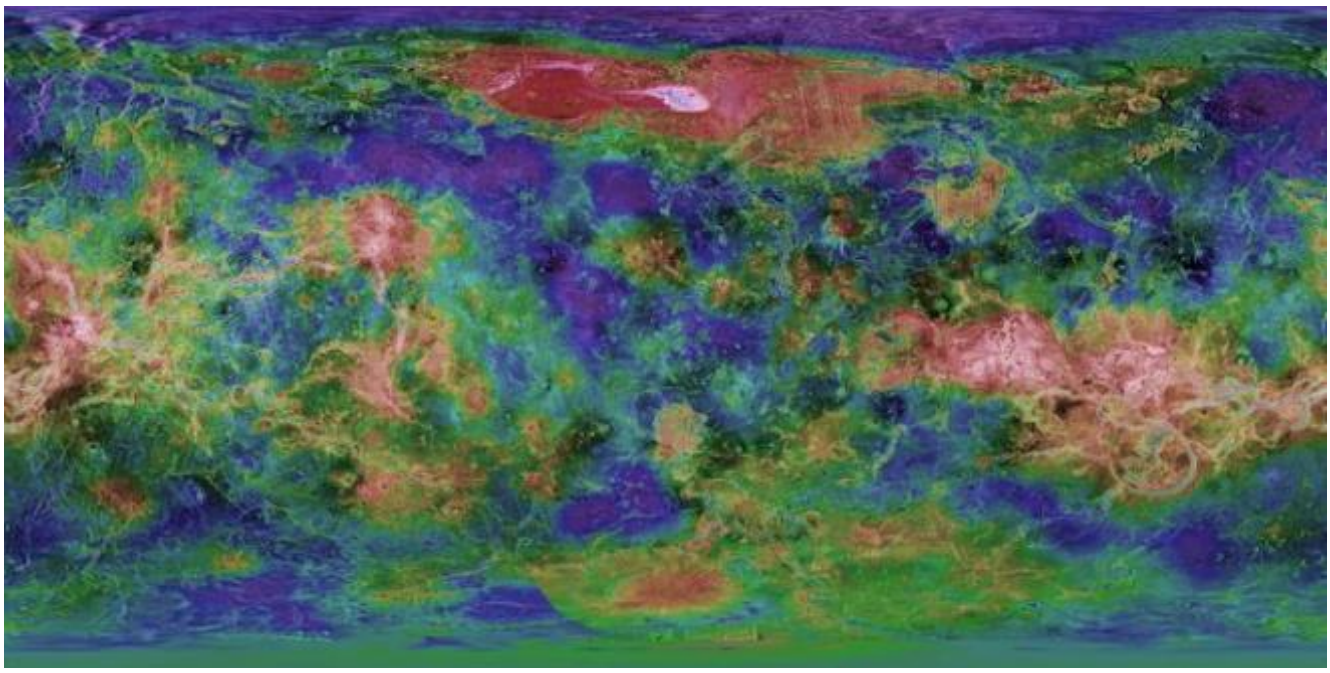

Figure 1.2. The topographic map of Venus produced by the Magellan mission.

In 1989 Galileo on its way to Jupiter was able to measure spectra of Venus transparency windows. After the Magellan mission and the Galileo flyby, there was a pause in the Venus space exploration apart from several flybys by spacecraft accomplishing a gravitational manoeuvre around Venus.

The new era of space exploration of Venus began with the launch of the European Space Agency's (ESA) Venus Express (VEX) mission (Svedhem et al., 2007). For ESA it was the first spacecraft to explore Venus. Venus Express is the heir of Mars Express (MEX) and Rosetta (Chicarro et al., 2004; Glassmeier et al., 2007). The probe was successfully launched on November 9, 2005 by a Soyuz-Fregat rocket from Baikonur, Kazakhstan. The spacecraft reached Venus on April 11, 2006, and the scientific mission started on May 6, 2006. The spacecraft's orbit was highly elliptical and quasi polar. One of the VEX goals was to investigate in detail the South Pole of the planet, which had not been explored before by other missions because of their orbit properties. The pericenter of the VEX orbit was located at a latitude of 80°N and an altitude of 250 km. The period of this orbit was 24 Earth hours.

In 2010, the Akatsuki scientific mission of the Japan Aerospace Exploration Agency (JAXA) was supposed to be inserted in orbit around Venus (Nakamura et al., 2011). However, the spacecraft entered the target orbit after the second attempt, five years later namely on December 9, 2015 (Nakamura et al., 2014). Ultraviolet camera (UVI), long-wave infrared camera (LIR), 1-μm (IR1) and 2-μm (IR2) cameras as well as lightning and atmospheric glow detectors are installed on board and keep operating at the time this manuscript is being written. After one year the IR1 and IR2 cameras stopped operations in nominal mode. Akatsuki observation in the IR identified dynamical processes occurring in lower clouds. The influence of topography was found with the presence of a gravity wave (Fukuhara et al., 2017) in the cloud layer near the Aphrodite-Terra mountain (Figure 1.3).

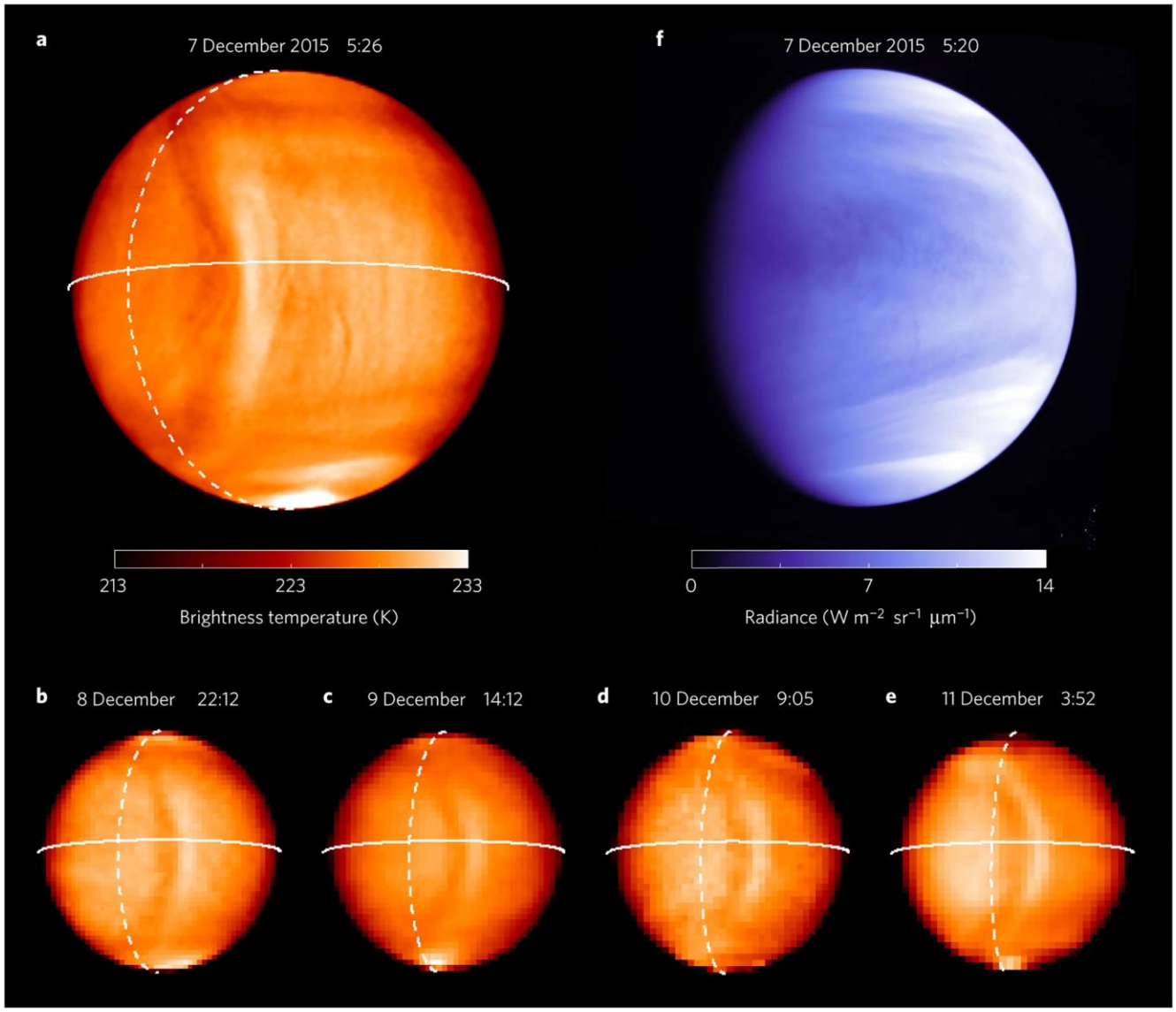

Figure 1.3. A-E. Brightness temperatures of the entire disk of Venus measured by the LIR camera on board the Akatsuki spacecraft from 7 December to 11 December 2015. Solid and dashed lines correspond to the equator and evening terminator correspondingly. The colour bar is valid only for panel A. The temperature ranges for pictures in panels B-E are adjusted so that the mean temperatures in a circle with a radius of 0.1 R_{Venus} at the disk centre are constant, where R_{Venus} is the Venus radius. F. The UV image of cloud tops obtained by UVI at a wavelength of 283 nm (Fukuhara et al., 2017).

1.3.2. Venus Express

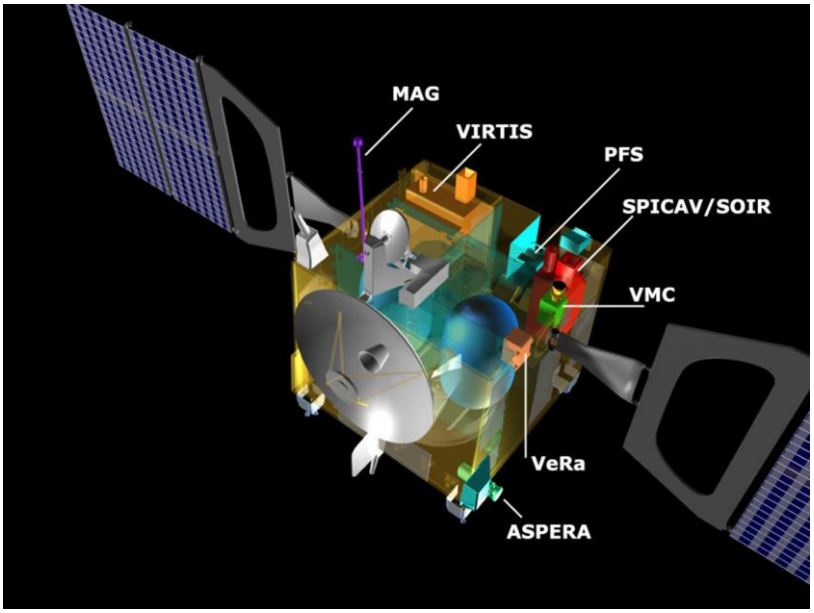

Figure 1.4. A scheme of Venus Express orbiter and its instruments.

VEX had 7 instruments on board. The Magnetometer MAG and ASPERA-4 were two instruments dedicated to study the ionosphere. MAG was designed to characterize the direction and force of magnetic fields around the instrument (Zhang et al., 2006). The Analyzer of Space Plasmas and Energetic Atoms (ASPERA-4) was designed to measure ionized and neutral particles surrounding the probe (Barabash et al., 2007). MAG and ASPERA-4 enabled to explore interactions between the Venus ionosphere, the solar wind and the resulting induced magnetic field. Also, the two instruments were used to find lightning in the atmosphere of Venus.

The wide-angle Venus Monitoring Camera (VMC) consisted of 4 channels in the visible, ultraviolet and two near infrared spectral filters (Markiewicz et al., 2007). The visible (~550 nm) and the UV (~365 nm) bands were used to visualize and monitor the cloud top that absorbs in the UV. The clouds' motion and the wind speed distribution were tracked thanks to the contrast UV images of VMC (Khatuntsev et al., 2013). Two IR bands of 0.965 and 1.0 μm were aimed to map the brightness coming from the layers close to the surface and search for possible volcanic activity. The IR data provided candidates of a volcanic eruption event (Smrekar et al., 2010; Shalygin et al., 2015).

The Planetary Fourier Spectrometer (PFS), inherited from the MEX payload, was designed to probe the atmosphere in nadir in the range of 0.9-45 μm at a spectral resolution of 2 cm^{-1} by two channels (Formisano, 2006). Its main tasks were to study the composition of cloud layer particles and minor gaseous components of the atmosphere, as well as the spatial temperature field below 100 km. Unfortunately, the Venusian PFS collected no data because of a mechanical defect in the scan mirror (Drossart and Montmessin, 2015). The unfulfilled science tasks were partially resolved by the VIRTIS spectrometer.

The Venus Radio Science (VeRa) performed radio occultation experiments (Häusler et al., 2006). The instrument transmitted radio waves from the spacecraft to the Earth's antenna through the Venus

atmosphere or after a reflection from the Venus surface. The purpose of this experiment was to analyse the ionosphere, atmosphere and surface of Venus. It allowed retrieving vertical profiles of atmospheric temperature and density from 40 to 100 km (Tellmann et al, 2009).

The Visible and Infrared Thermal Imaging Spectrometer (VIRTIS), which was previously designed for Rosetta mission, consisted of three spectrometric channels (Drossart et al., 2007). VIRTIS-M in the IR and visible operated in the 1.02-5.13 μm and 0.28-1.10 μm spectral ranges respectively, while VIRTIS-H covered the 1.84-5.00 μm range. These two IR channels included several Venus transparency windows to study the composition of the lower atmosphere. Emission of hydroxyl at 1.40-1.49 and 2.6-3.14 μm was discovered (Piccioni et al., 2008).

The SPectroscopy for Investigation of Characteristics of the Atmosphere of Venus (SPICAV) has been successfully operating for 8 years (Bertaux et al., 2007b; Vandaele et al., 2008; Korablev et al., 2012). It consisted of the UV (118-320 nm) and the IR (0.65-1.7 μm) channels. SOIR (SOIR - Solar Occultation in InfraRed) is an independent high-resolution spectrometer in 2.3-4.2 μm, which was part of the SPICAV/SOIR assembly (Vandaele et al., 2008).

1.3.3. Future missions

The discoveries by the missions of the last 15 years, however, still leave unresolved questions concerning present volcanism and geological activity on the surface, the lower atmosphere structure, the unknown UV absorber in the clouds, the water evolution on the planet, etc. The answers require continued study of Venus both from the Earth and by new exploratory missions to Venus, including modern atmospheric and landing modules. Therefore, the world space agencies assume launches of new missions with a wide range of scientific tasks.

The first in the list is the orbital mission to Venus from the Indian Space Research Organization (ISRO), whose launch was initially scheduled for 2023 (Shaji, 2019) and recently postponed to 2025. The planned mission named Shukrayaan-1 (translated as “Venus craft”) will be devoted to remote sensing of the surface, the atmosphere and the ionosphere. The payload includes VIRAL and IVOLGA spectrometers provided by Roscosmos. The VIRAL IR spectrometer is being developed at the Space Research Institute with the participation of LATMOS. The IVOLGA heterodyne laser spectrometer for the near-IR range is being developed at the Moscow Institute of Physics and Technology.

A post-2025 launch is planned for a new Roscosmos mission in collaboration with NASA. Venera-D or «Venus the Long-lived» will contain a lander based on previous Vega missions with a capability to improve results of previous descent and landing probes. The lander will include one or more long-lived small station LLISSE (Long-Lived In-Situ Solar System Explorer) that is assumed to operate on the surface of Venus for about 60 days (Zasova et al., 2014). It is also planned to implement a module, flying in the clouds, with an ability to manoeuvre vertically and to explore different layers. There will be an orbiter, for data relay, with science objectives similar to those of VEX and with a Fourier spectrometer on board, in order to compensate the PFS loss in 2006. The planned launch date for Venera-D is 2029 or 2031.

One of the candidates for ESA is the new EnVision mission (Widemann et al., 2020), which is being prepared in collaboration with NASA. In case of positive selection in 2021 the launch will be in 2032. The objectives of this orbital mission are mapping the surface with a very high spatial resolution (1-30 m), studying its properties in the IR spectrum and studying the atmosphere.

There are six NASA missions as well that are in a designing stage, none of which has yet been selected for launch: VERITAS, DAVINCI, VISE, SAGE, VCM, VITaL. VERITAS (Venus Emissivity, Radio Science, InSAR, Topography, and Spectroscopy) would aim to high-resolution surface study (Smrekar et al., 2016). The combination of IR spectroscopy in transparency windows, radar mapping and gravity field measurements is planned to improve the knowledge about the Venus inner structure and ongoing geological activity. DAVINCI (Deep Atmosphere Venus Investigation of Noble gases, Chemistry, and Imaging) is a proposed atmospheric probe to Venus (Glaze et al., 2016). Venus In Situ Explorer (VISE) and The Surface and Atmosphere Geochemical Explorer (SAGE) concepts propose to land close to a volcano (Squyres, 2011; Esposito, 2011). The Venus Climate Mission (VCM) is a more complex program including an orbiter, a balloon, a mini-probe, and two dropsonde observational platforms (Grinspoon et al., 2010). Similar to VCM is the Venus Intrepid Tessera Lander (VITaL) concept, which is considered for landing on one of the oldest parts of the Venus surface: mountainous tessera regions (Gilmore et al., 2010).

1.4. The surface of Venus

Venus clouds hide its surface. Remote investigation of its composition is almost impossible. Landers studied the surface which appeared to be similar to the terrestrial basalt rocks (Surkov, 1983) that are associated with volcanic activity. Radar measurements made by Magellan revealed that the Venus surface is rather flat, and is mainly shaped by lava plains, produced by more than 1660 volcanoes on Venus (Saunders et al., 1992). The small number of craters implies that the Venus surface is geologically young (<500 million years, according to Bullock et al., 1993).

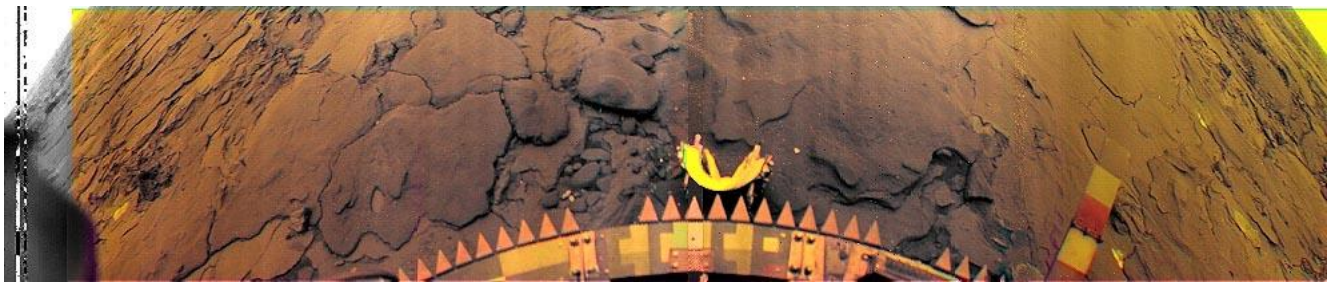

Figure 1.5. Coloured panorama by Venera 14 at 13.055°S, 310.19° (Phoebe Regio).

The question of active volcanism on Venus is still open. Observations of surface emissivity in the infrared is compatible with an opinion of ongoing volcanic processes. The Venus Express mission revealed four candidates named «hotspots» associated with increased surface emissivity possibly caused by fresh lava flows (Smrekar et al., 2010; Shalygin et al., 2015). This activity was detected near the highest volcano of Venus, Maat Mons, which is located in the Alta rift region. Radar shows light solidified lava flows around the volcano itself, overlapping darker plains with wrinkled ridges.

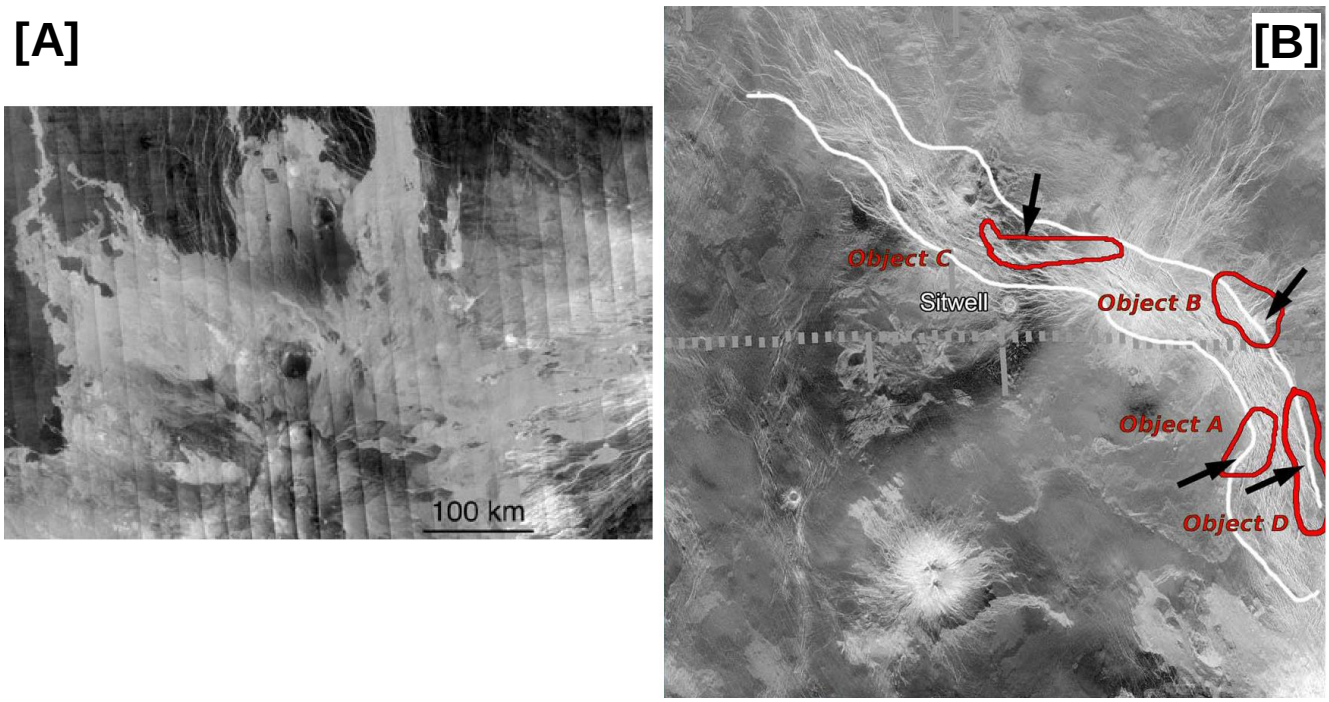

Figure 1.6. (A) The northern part of Maat Mons (2°N, 195°E), the highest volcano of Venus (Basilevsky and Head, 2003). (B) Magellan's radar map of Northern Atla Regio. Objects A-D are the areas where the candidates for recent volcanic activity were detected. Black arrows show locations where lava flows and rifts are interacting. Radar-dark parabola is the crater Sitwell (Shalygin et al., 2015).

1.5. The atmosphere of Venus

1.5.1. Composition

The first spectrometric observations (Adams and Dunham, 1932) established that Venus' atmosphere consists of 96.5% carbon dioxide (CO_2). The second most abundant gas, nitrogen (N_2), constitutes ~3.5% (Von Zahn et al., 1983). Other gases have been measured in much smaller quantities. Trace species are sulphur dioxide (SO_2), water vapour (H_2O), carbon monoxide (CO), hydrogen chloride (HCl), etc.

Venus is a very dry planet. The water vapour content under the clouds is 30 ppmv (de Bergh et al., 2006), 1-2 ppmv above the clouds (Fedorova et al., 2008). Water is also contained in clouds' droplets (Esposito, 1983). This loss of water by Venus is explained by the fact that its molecule dissociates into oxygen and hydrogen. In the absence of a magnetic field on Venus the loss of light hydrogen molecules by the atmosphere is effective. This mechanism is confirmed by the abnormally high HDO/H_2O ratio. On Earth, the standard isotopic HDO to H_2O ratio is equal to 3.1153×10^{-4} (Hagemann et al., 1970). In the lower atmosphere of Venus, the HDO/H_2O ratio is ~150 times higher than on Earth (Donahue and Russell, 1997). And above the clouds it was measured on average 240±25 terrestrial values, and it is ~1.5 times higher than in the lower atmosphere (Fedorova et al., 2008). Isotopic ratio for hydrogen halides DF/HF = 420±200 and DCl/HCl = 190±50 observed at ~74 km is also high (Krasnopolsky et al., 2013). This is an evidence of an active escape of hydrogen from the atmosphere (Donahue et al., 1997; Gérard et al., 2017).

The loss of water, even if it existed in the liquid state on the planet's surface in the past (Way et al., 2020), is related to the greenhouse effect. CO_2 and H_2O are mainly responsible for the greenhouse effect that warms up the surface and the atmosphere. These gases effectively absorb infrared (IR) radiation from the warm surface, making it difficult for heat to escape into space. The tiny amount of water vapour contributes less significantly, which is the opposite in the Earth atmosphere. However, the H_2O absorption regulates the transmission of several IR transparency windows of the Venus atmosphere (Section 1.5.4). On Venus, the cloud aerosol particles (Section 1.5.3) are very reflective making the spherical albedo of Venus equal to 0.76. However, ~3% of solar radiation reaching the surface maintains the enormous greenhouse effect increasing the temperature of the atmosphere by about 200 K. On Earth, the greenhouse influence is about 35 K. The cloud layer additionally to filtering of solar radiation contributes to atmospheric heating on Venus. The aerosols are opaque in most of the IR spectrum of the thermal radiation from the planet's surface.

While the difference in CO_2 abundances in the atmospheres of the Earth and Venus is large, the global inventory of CO_2 on both planets is comparable. On the Earth, most of CO_2 is trapped as carbonates at the floor of oceans. If this trapped CO_2 would be released in the Earth's atmosphere, it would end up in creating a 100 bar-thick atmosphere of CO_2, that is very close to the Venus atmosphere.

1.5.2. Structure of the atmosphere

Like on Earth, several compartments can be distinguished in the atmosphere of Venus: the troposphere, the mesosphere, the thermosphere and the exosphere. Yet, there is no evidence for a stratosphere on Venus, reflecting the absence of an absorbing layer like the terrestrial ozone, which causes a temperature inversion. It is seen in Figure 1.7 showing the temperature profiles on both day and night sides of the planet.

The troposphere, covering altitudes up to 65 km, contains 99% of the entire mass of the atmosphere. The upper part of the troposphere is characterized by active convection. Then the temperature decreases uniformly with increasing altitude, and the atmosphere becomes neutral. The temperature gradient dT/dz was measured to -7.7 K/km (Seiff, 1983) and it is close to the adiabatic lapse rate equal to -g/Cp. The airmass is delivered from the near-surface to the clouds deck while sustaining adiabatic relaxation. Such a behaviour can be traced upon descent in very deep atmospheric layers down to an altitude of ~7 km, where the planetary boundary layer (PBL) begins. The vertical gradient measured by VeGa 2 represents the high instability here (Linkin et al., 1986; Linkin et al., 1987). Possibly, CO_2 and N_2 can be fractionated in the deep atmosphere as their properties correspond to super fluid liquids under high temperature and pressure conditions. Then, the N_2 abundance should decrease to zero near the surface and this change of molecular mass would stabilize the lapse rate (Lebonnois and Shubert, 2017). In the vertical structure, there is a layer around ~50 km characterized by the terrestrial normal conditions, which is 1 bar and 293 K. Another peculiarity of the troposphere, there is no significant temperature difference between day and night since the high-density greenhouse CO_2 provides constant thermal balance under the thick clouds. Here thermochemistry contributes significantly to chemical processes. With an increase in temperature and a decrease in the amount of sunlight, thermochemistry becomes the dominant process into the deep atmosphere. Vertical transport delivers constituents to the upper

atmosphere. For instance, water vapour and sulphur compounds pass through the cloud layer extending from the upper troposphere to the lower mesosphere.

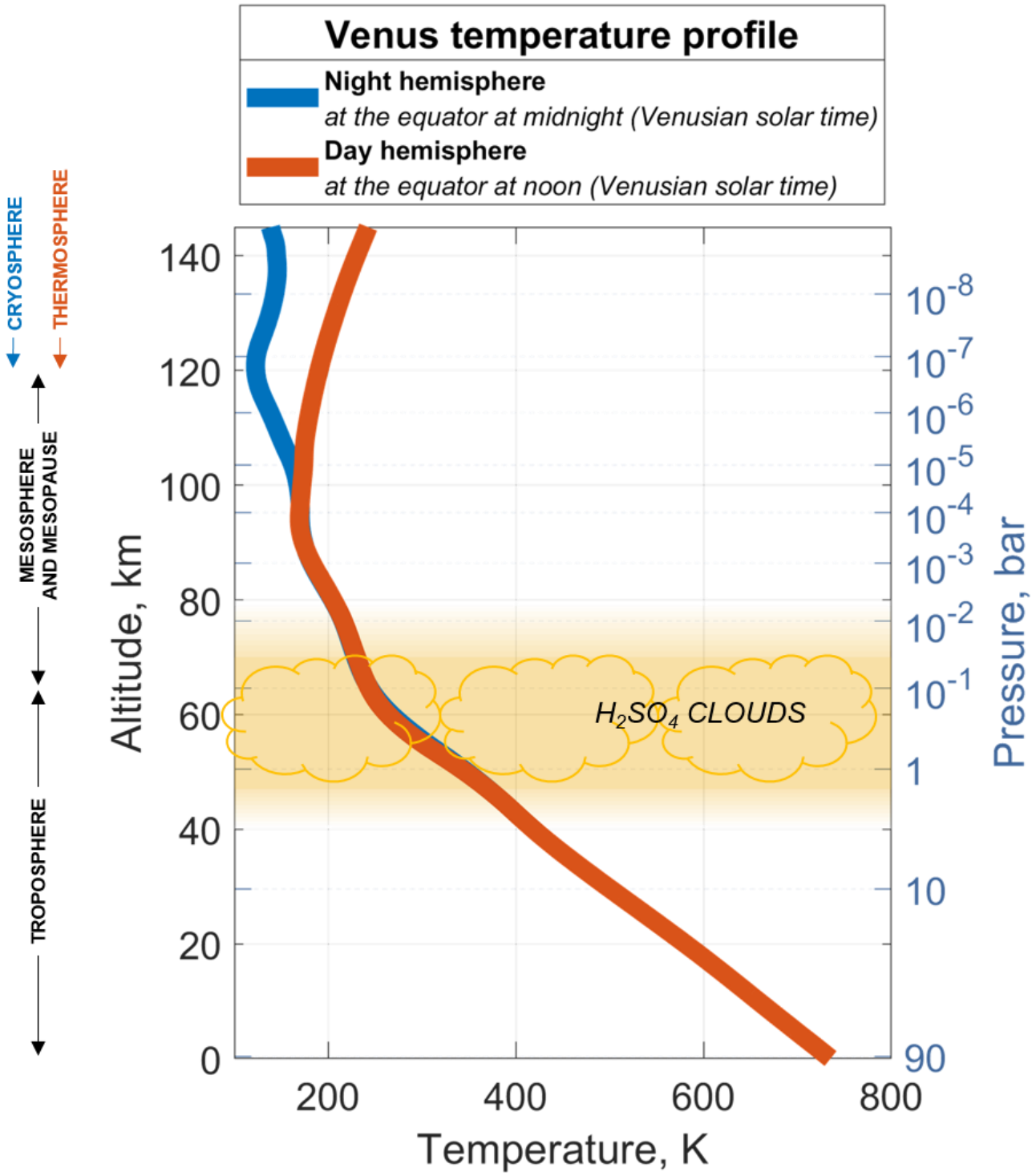

Figure 1.7. Temperature profile in the atmosphere of Venus as a function of altitude and pressure at noon and midnight at the equator, according to the VIRA climate database (Zasova et al., 2006; Seiff et al., 1985).

Over the clouds, chemistry driven by solar radiation prevails over thermochemistry. The altitude interval from 65 to 120 km corresponds to the mesosphere, where the temperature gradient approaches zero. The mesospheric temperature drops from 250 K (upper edge of the clouds) down to 170 K. The altitude

interval between 90 and 120 km, where the temperature of the day side reaches a minimum hosts the mesopause. On the night side, altitudes above ~100 km are occupied by the cryosphere with a further slight temperature decrease. A warm layer by 20-40 K was detected here around 100 km from Venus Express observations (Bertaux et al., 2007a). It is likely produced by the adiabatic heating within a downwelling motion or, possibly, by the presence of aerosols (Bertaux et al., 2007a; Picciali et al., 2015).

The thermosphere is located above 120 km up to 200 km (Limayer et al., 2018). On the day side, temperatures are 270-400 K. On the night side, the atmosphere is very cold, which has led scientists to call it "cryosphere". There, temperatures reach 100 K which is the minimum temperature encountered on Venus. In that range the homosphere becomes the heterosphere, since the homopause on Venus was measured at 120-132 km (Mahieux et al., 2015). So the CO_2 is the dominant gas of the Venus thermosphere up to ~140 km and ~155 km on the night and day sides respectively (Niemann et al. 1980; Kasprzak et al. 1997). But at higher altitudes abundances of lighter compounds increase (Niemann et al. 1980; Seiff and Kirk, 1982).

Above 120 km, the number of particles ionized by the UV radiation, the solar wind and cosmic rays, increases. The maximum density of the ionosphere on the daytime side is located at an altitude of 140 km. Venus does not have a magnetic field, so the particles of the solar wind interact directly with the atmosphere, changing the characteristics of the ionosphere depending on the activity of the Sun. The ionosphere determines the parameters of the induced magnetic field of Venus, which turns the solar wind particles around the planet.

1.5.3. The cloud layer

The first data on the composition of aerosol particles in the cloud layer were obtained on the basis of measurements of the brightness temperature and polarimetry (Sill, 1972; Young, 1973; Hansen et al., 1974; Pollack et al., 1974). These measurements forced the community to discard the hypothesis of water-dominated clouds. Knowledge about the depth and the structure of the clouds was derived from descent probes. It is still the most valuable dataset for describing the vertical layering of Venusian clouds.

The vertical thickness of the cloud layer was measured to be more than 20 km, with particles detected in the altitude range from 47 to 70-75 km. Three modes of aerosol particles are forming the cloud layer. Each mode is characterized by a specific modal radius: <0.4 μm for the mode 1, 1.05 and 1.25 μm for modes 2 and 2' correspondingly, 3-4 μm for mode 3 (Esposito et al., 1983). The modes populate three cloud layers, upper and lower hazes differently: the largest mode (mode 3) prevails in the lower and middle cloud layers and the lower haze, which forms the bulk of the clouds. Mode 1 and 2 are contained in the upper layer (50-70 km) and in the upper haze (>70 km). The lower haze was detected down to 30 km. The upper haze reaches an altitude of ~110 km.

The main component of aerosol particles in the Venusian cloud layer is an aqueous solution of sulphuric acid (75-90%). Sulphuric acid is mainly produced from SO_2 and H_2O under solar light in the upper cloud layer, considered as a photochemical "factory" (Titov et al., 2017).

$$SO_2 + O \rightarrow SO_3$$

$$SO_3 + H_2O \rightarrow H_2SO_4$$

SO_2 and H_2O are transported upward from the lower atmosphere to supply the production of sulphuric acid. H_2SO_4 formation is followed by condensation. While the aerosol particles descend lower in the cloud deck forming larger particles until they evaporate. Below clouds H_2SO_4 is decomposed in thermodynamic equilibrium reactions back to SO_2 and H_2O to restart the cycle (Mills et al., 2007).

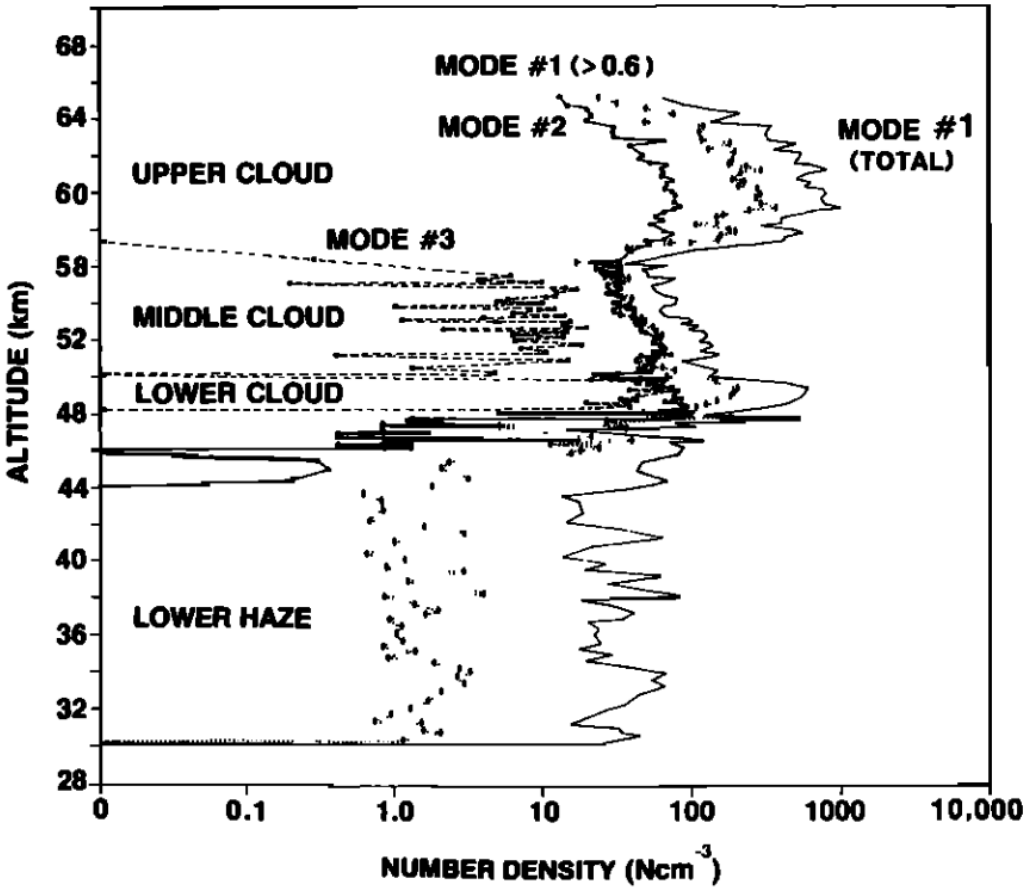

Figure 1.8. Modal partitioning of number density by the cloud particle size spectrometer on board the Pioneer Venus Sounder probe (Knollenberg and Hunten, 1980).

The largest particles form the bulk of the clouds. However, it is controversial whether it is a separate mode or a tale of the mode 1 and 2 distribution. Mode 3 detailed composition is still a mystery. It is also controversial if these particles are crystallized or liquid and if the mode 3 includes some other species additionally to H_2SO_4 (Knollenberg and Hunten 1980). Descend probes of Venera 13, 14 and Vega 1, 2 detected the presence of sulphur, chlorine, phosphorus and iron (Petryanov et al., 1981; Andreichikov, 1987) without specification of the substance.

Some uncertainty remains in the composition of the lightest aerosol particles. Remote observations in the UV range have shown that the clouds contain an unknown absorber effective at λ>320 nm. It is associated with additional substances whose composition is not fully known. Many candidates have been proposed: sulphur (S_8, S_3, S_4, OSSO or S_2O) and chlorine ($FeCl_3$ or SCl_2) species, organic compounds, mineral dusts or even bacteria (Mills et al., 2007; Zhang et al., 2012; Marcq et al., 2017; Carlson et al., 2016; Frandsen et al. 2016; Krasnopolsky, 2017; Krasnopolsky, 2018; Limaye et al., 2018).

Numerous new results were collected by three instruments on board Venus Express mission: VMC, VIRTIS and SPICAV. The upper boundary of the cloud layer was found to decrease from 72±1 km at low and middle latitudes to 61-67 km in polar regions (Ignatiev et al., 2009; Cottini et al., 2015; Fedorova et al., 2016). SPICAV IR data showed that the upper haze reaches an altitude of ~110 km and also has a latitudinal trend similar as that of the cloud top (Luginin et al., 2016).

1.5.4. Transparency windows

The thermal emission emitted by the hot lower atmosphere and the surface is not totally shielded by the cloud layer and the gases. Between the strong absorption bands of CO_2 there are several intervals where clouds do not absorb and only scatter photons mostly in the forward direction. In these «transparency windows» the IR thermal radiation escapes to outer space. This phenomenon was discovered by David A. Allen and John W. Crawford (Allen and Crawford, 1984) at 1.74 and 2.35 μm. This discovery provided a new tool to study atmospheric properties from the cloud layer down to the surface (Marcq et al., 2008; Arney et al., 2014; Bézard et al., 2011; Fedorova et al., 2015). Thermal radiation of the lower atmosphere and the surface of Venus can only be observed on the night side of the planet since on the dayside the solar radiation is overwhelming in this spectral range.

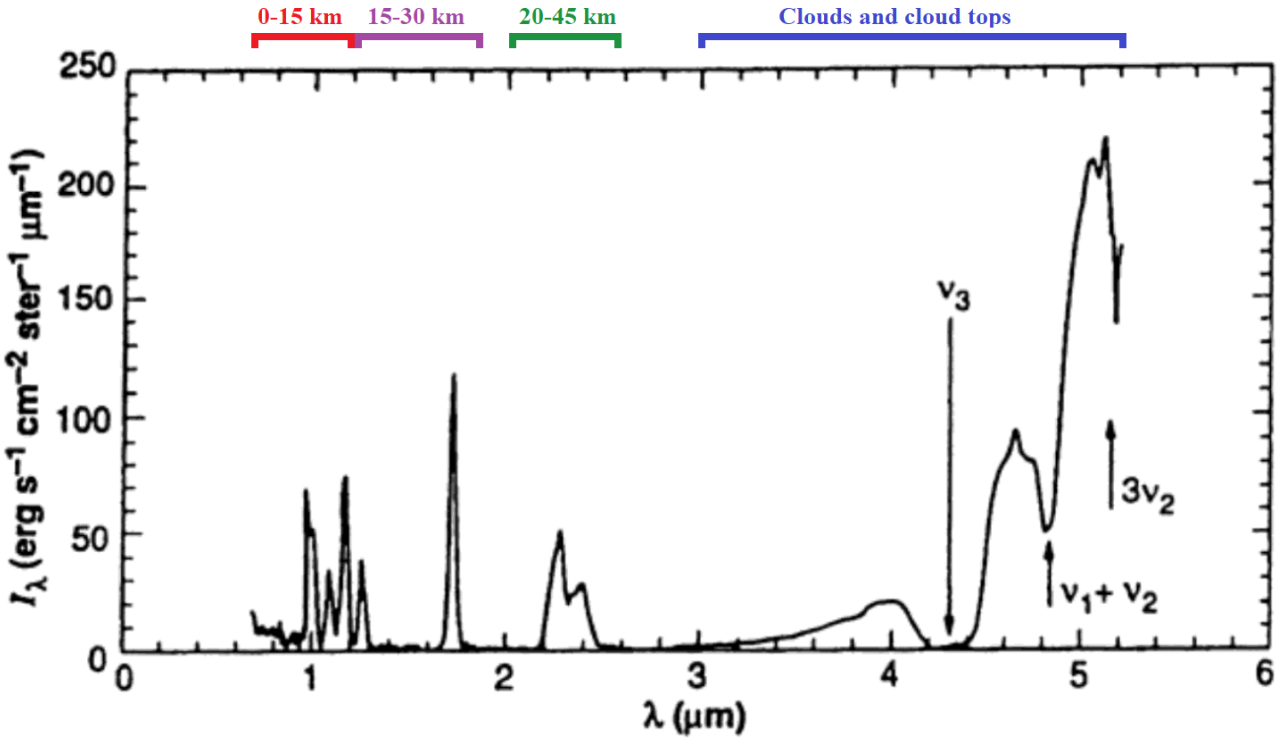

Figure 1.9. Venus night-side spectrum measured by Galileo mission (Taylor et al., 1997).

Subsequently all transparency windows in the near infrared from 0.85 to 2.5 μm were inventoried (Crisp et al., 1991). The windows in 0.85-1.0 μm correspond to the surface radiation and allow studying its thermal properties and geological processes. For example, the possible volcanic activity of Venus (Smrekar et al., 2010; Shalygin et al., 2015). Radiation of 1.1- and 1.18-μm intervals originates from the first-scale heights, i.e. 0-15 km. The other two transparency windows at 1.28 and 1.31 μm are sensitive to the 15-30 km altitude range (Taylor et al., 1997). At 1.51 and 1.55 μm there are two additional

transparency windows. They are characterized by significantly weaker intensity formed at 20-35 km, the difference between their intensity and one of the following 1.74-window is 2 orders in magnitude (Wilson et al., 2009). The 1.74 and 2.35 μm windows correspond to emission formation at 20-30 km and 20-45 km respectively (Taylor et al., 1997).

The transparency windows are located in a range where there are no strong absorption lines for carbon dioxide, which dominates the atmosphere of Venus. Absorption by carbon dioxide is determined only by far-wings of its strong absorption lines. However, the study is also sensitive to trace gases in the lower atmosphere. The absorption bands of water overlap the transparency windows of 1.1, 1.18, 1.74, and 2.35 μm. HCl coincides with the absorption band of water vapour at the maximum of the 1.74-μm transparency window. The transparency window at 2.35 μm is the most sensitive to minor gaseous constituents of the lower atmosphere where the CO, OSC, and SO_2 bands are also present.

The main parameter controlling the thermal brightness is the concentration of aerosol in the observed atmospheric column: mainly the scattering by the largest particles of the cloud layer which are found in the lower and middle clouds. Moreover, the intensities in the transparency windows of 1.28 and 1.31 μm, which are insensitive to changes in surface properties and to absorption by trace gas components, are modulated only by variations in the clouds.

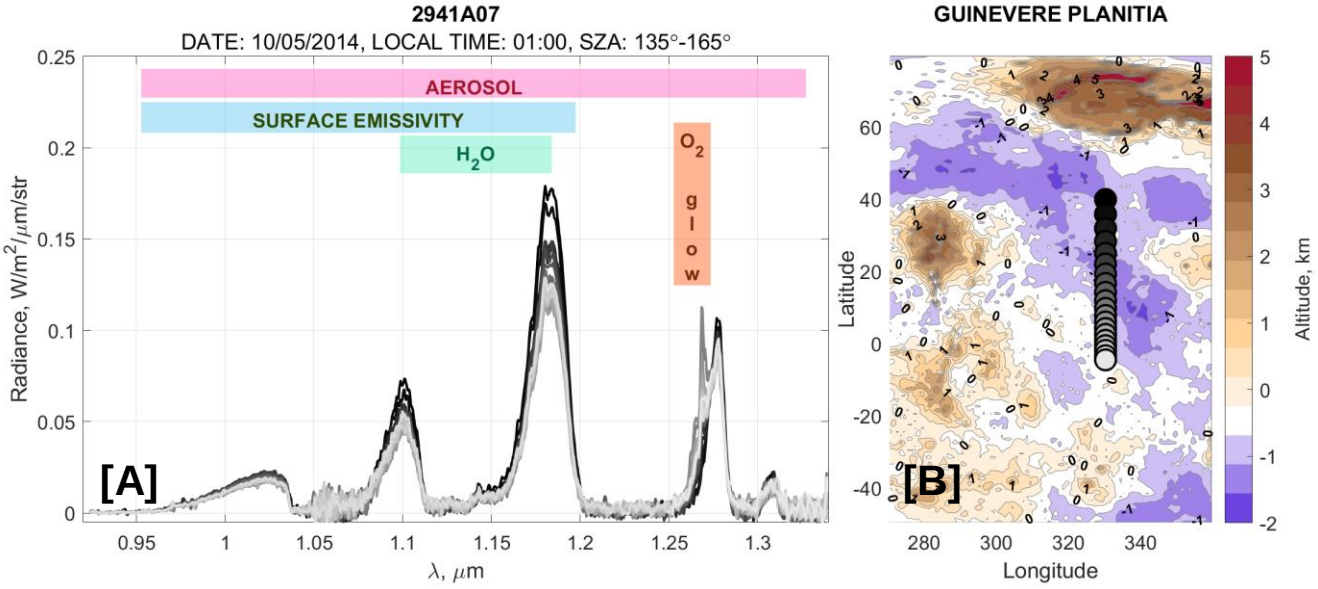

Figure 1.10. (A) Spectra measured in five transparency windows during one observation #2941A07 by SPICAV IR spectrometer on board Venus Express spacecraft. Coloured rectangles show factors that modulate the thermal emission in different spectral ranges: aerosol scaterring, surface emissivity and water vapour absorption. The orange rectangle highlights the spectral range of the mesospheric O_2 ($a^1\Delta_g$) airglow at 1.27 μm. (B) The geographical locations corresponding to measured spectra.

The first space measurement of the full night IR spectra of Venus was done during Galileo flyby in 1989 (Figure 1.9). The IR emission has been monitored by ground-based high-resolution spectrometers and during the Venus Express mission. It has been shown that it can change significantly at small scales reflecting so far unknown variability in the lower cloud layers (Figure 1.10), surface emissivity and minor species content. The 1.28-μm window is contaminated by the mesospheric oxygen emission at 1.27 μm that needs to be separated to enable the study of the thermal emission spectrum in that range.

1.5.5. Mesosphere and atmospheric dynamics

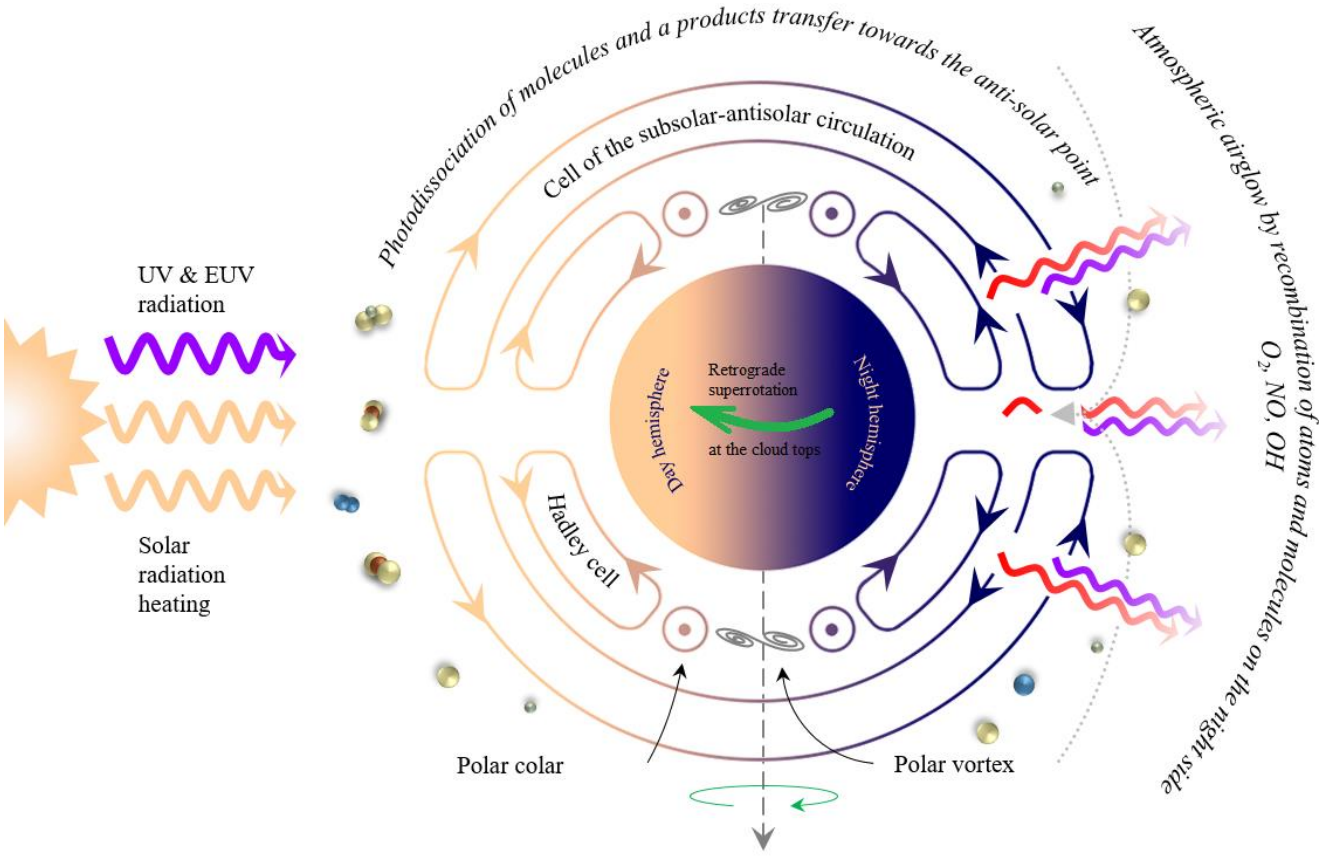

Figure 1.11. Diagram of the main mechanisms of matter transfer in the Venus mesosphere above the cloud layer.

The mesosphere is a very active region where two regimes of atmospheric circulation dominate in two different altitude ranges. A powerful zonal motion dominates in the upper cloud, but at an altitude of ~100 km atmospheric components are subject to a different global circulation regime, characterized by a global motion going from the subsolar point to the antisolar one (Sub-Solar Anti-Solar or SSAS circulation). A retrograde superrotation of the cloud top was obtained by tracking the cloud features exhibited large contrast in the UV. A speed of 110 m/s was then measured. The period of rotation of Venus is 243 terrestrial solar days while the clouds need only 4 days for a full rotation around the planet. There are only two solid surface bodies having this type of global atmospheric circulation: Venus and Titan, the largest satellite of Saturn in the Solar System. Mainly this effect is related (Imamura et al., 2020) to an angular momentum transfer from the slow rotating body to the atmosphere according to the mechanism discussed by Gierasch (1975). This superrotation has its maximum at the cloud tops, however, it was measured down to the surface with a decreasing speed with altitude (Rossow et al., 1980; Counselman et al., 1980; Lellouch et al., 1997)

The cloud top winds have been particularly well studied by the tracking of large-scale features characterised by lower albedo in UV. In the first era of Venus exploration the UV contrasts monitoring was done by Mariner 10 (Limaye and Suomi, 1981), Pioneer Venus (Rossow et al., 1980) and Galileo

(Peralta et al., 2007) missions. The cameras on board Venus Express (Khatuntsev et al., 2013; Patsaeva et al., 2015; Bertaux et al., 2016) and Akatsuki (Horinouchi et al., 2018) orbiters resumed this study. The dynamics of the deeper cloud layer was derived from the VeGa balloons (Blamont et al., 1993) and from the continuous monitoring of Akatsuki IR cameras (Horinouchi et al., 2017).

Venus rotates very slowly and the planet's atmosphere is in cyclostrophic balance. So the zonal winds are directed along the equator due to a balance between the equatorward component of centrifugal force and the meridional pressure gradient (Leovy, 1973). The cyclostrophic winds can be modelled based on the temperature field measurements. The temperature in the Venus atmosphere (40-200 km) was measured from orbiters (Taylor et al., 1983; Zasova et al., 2007; Limaye et al., 2017). However, the process of such acceleration of the atmosphere is still a subject to study, as is the observed dependence of wind speed on altitude.

The zonal super rotation in the upper layer of the clouds is supplemented by a meridional transfer of matter to the poles in Hadley cells of each hemisphere. This meridional transport is carried out at a much slower speed than the zonal one. The speed is lower than 10 m/s. It is assumed that the meridional circulation is effective on Venus in transferring warm air masses to the poles and colder air masses towards the equator (Limaye, 1985). Observations (Limaye, 2007; Peralta et al., 2007; Khatuntsev et al., 2017) show that the Hadley cell exists between the equator and latitude about 65º. It is the region where the top of the cloud going deeper affecting the radiative balance, a cold collar is observed (Garate-Lopez and Lebonnois, 2018). The polar collar is a cold air belt around the polar vortex. Its temperature inside the collar is about 30 degrees colder than outside at the same altitude (Piccioni et al., 2007) that may be caused by an adiabatic cooling of upwelling air.

The superposition of zonal rotation and meridional advection leads to the formation of a giant vortex at each of the poles, where air is rotating downwards with a period of 2.8 terrestrial days. The northern polar vortex was studied by Pioneer Venus and the southern one by means of VMC and VIRTIS instruments on board Venus Express (Piccioni et al., 2007). The vortices are similar in nature to a tropical cyclone on Earth (Limaye et al., 2009) and have a complex structure. On average, it is the dipole (Schofield and Diner, 1983) but the shape can be an ellipsoid to a tripodal structure (Sánchez-Lavega et al., 2017). However, a full description of the vortex dynamics is still to be established by global circulation models.

The wind speeds of zonal rotation decrease from 70 km to ~85 km (Piccialli et al. 2012), but their variation increase (Sánchez-Lavega et al., 2017). At the altitudes nearing the mesosphere boundary (110 km) the SSAS circulation dominates. SSAS transfers air masses from the subsolar to the anti-solar point, as a result of the significant contrast between day and night temperatures in the thermosphere and the cryosphere. Its speed reaches 100-300 m/s (Sánchez-Lavega et al., 2017). The details of atmospheric motion in the transition from the range between zonal superrotation in the lower layers of the mesosphere have not been established yet.

The SSAS circulation transfers different atoms and ions to the night side produced by photolysis in the dayside. Several airglows are the products of this dynamic process as a result of the downwelling atoms motions of airmasses leading to excited state molecular recombination in the night-time mesosphere.

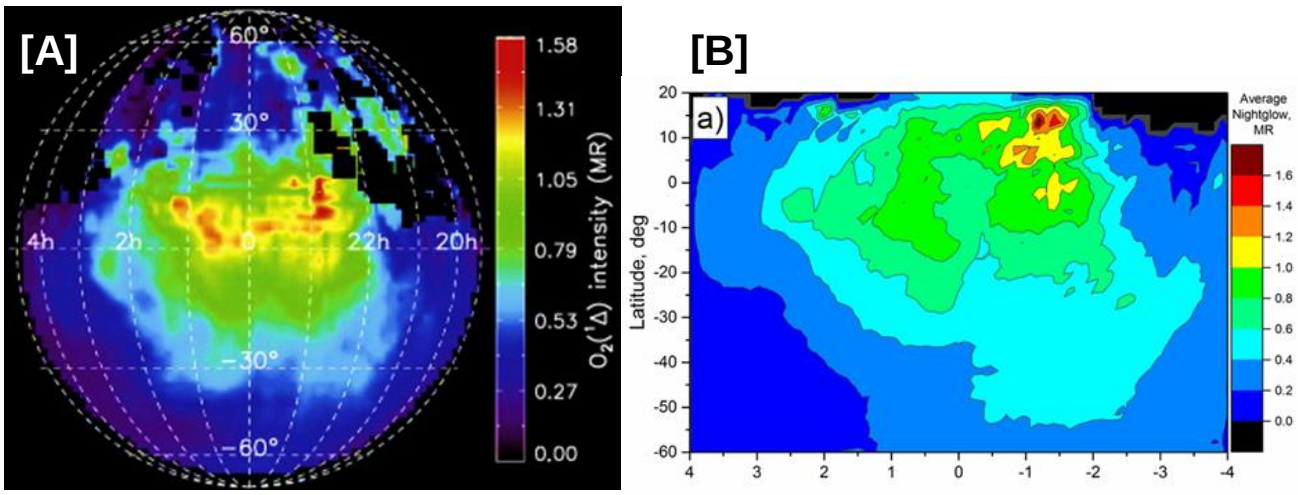

Figure 1.12. O_2 ($a^1\Delta_g$) airglow intensity distribution in the night hemisphere obtained by VIRTIS-M nadir measurements reported in works of (A) Soret et al. (2012) and (B) Shakun et al. (2010).

The most eloquent illustration of this process is the oxygen atoms advected to the night mesosphere where they recombine to form excited O_2 ($a^1\Delta_g$) molecules. The corresponding infrared airglow at 1.27 μm (Connes et al., 1979) is the result of the radiative relaxation of these molecules to the ground state through a three-body process involving CO_2 molecules (see in more detailes in Section 6.1). Oxygen atoms supplying this process are produced by CO_2 and CO photodissociation on the day side. Its maximum brightness is observed at 96±2 km and the general spatial distribution demonstrates a significant increase in intensity towards the antisolar point (Gérard et al., 2012). An interaction between oxygen atoms and molecules leads to a formation of ozone. The O_3 reaction with hydrogen (Bertaux et al., 2007a) results in the OH emission by the Meinel process (Bates and Nicolet, 1950) at 1.48 μm. The hydroxyl airglow was also obtained at the altitude of about 96 km. This emission also tends to increase in brightness towards the antisolar point. However, the intensity of OH glow is lower than one of O_2 ($a^1\Delta_g$). The statistical distribution of these emissions demonstrates a domination of the SSAS circulation in the 90-100 km range.

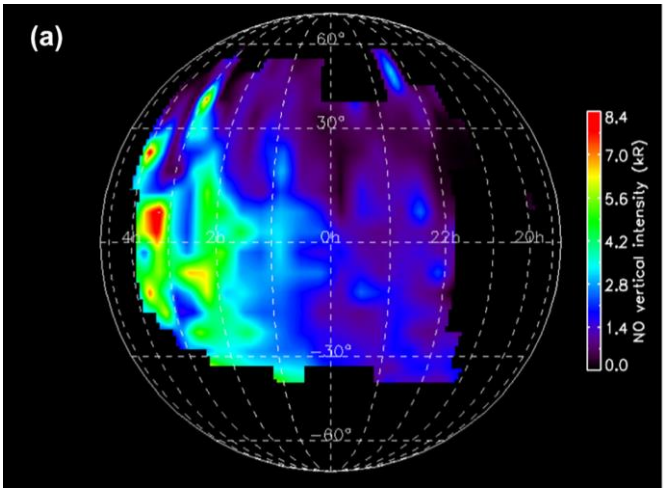

Figure 1.13. Global intensity of nitric oxide airglow measured during nadir observations by the SPICAV UV spectrometer on board Venus Express mission. The pixel size for averaging the data is 5° of latitude and 20 minutes of local time (Stiepen et al., 2013).

The nitrogen atoms brought by SSAS transfer are recombining with oxygen on the night side, and the nitrogen emission in δ- and γ- bands is resulted. Its maximum intensity corresponds to the higher altitudes of ~115 km and it completely differs from the one observed at ~95 km. Its spatial distribution surprisingly displayed a significant shift towards the morning terminator (03:00-04:00). It results from a joint influence of gravity wave propagation, thermal tides and large scale planetary waves (Gilli et al., 2020) that are partially explained by the recent results of the Venus Global Climat Model (VGCM) developed at the Institute Pierre-Simon Laplace (IPSL), further noted IPSL Venus GCM (see in more detailes in Section 2.3).

1.6. The SPICAV instrument

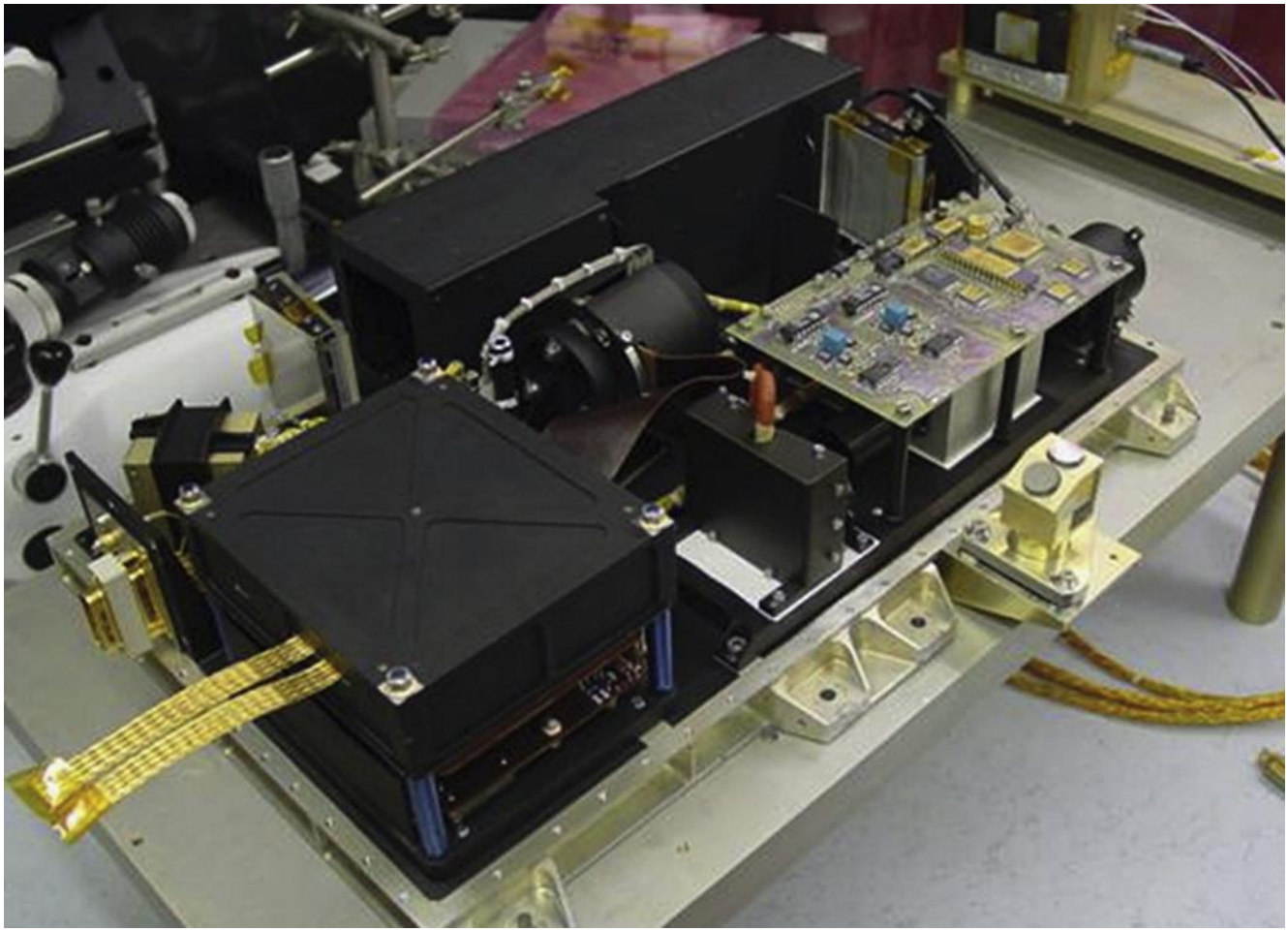

Figure 1.14. Image of the SPICAV instrument without a cover (Korablev et al., 2012) without the SOIR spectrometer.

The SPICAV/SOIR instrument was a set of three spectrometers (Bertaux et al., 2007a; Vandaele et al., 2008; Korablev et al., 2012) that was designed by Laboratoire Atmosphères, Milieux, Observations spatiales (LATMOS, France) in collaboration with the Space Research Institute of the Russian Academy of Sciences (IKI, Russia), and the Royal Belgian Institute for Space Aeronomy (BIRA-IASB, Belgium). All of them operated around Venus during the 8 years of the Venus Express mission, from April 2006 to December 2014, however, the full scientific phase of observations began on May 14, 2006.

The SPICAV part consisted of the UV (118-320 nm) and the IR (0.65-1.7 μm) channels that could observe the atmosphere in different modes (Bertaux et al., 2007a). For the first time, three instruments

performed solar occultations of the upper atmosphere of Venus, and the SOIR spectrometer was particularly dedicated to this mode of observations. This technique of observations enabled one to study in detail the vertical distribution of CO_2, SO_2, H_2O and other trace gases and the cloud haze on the Venus terminator (Fedorova et al., 2008; Mahieux et al., 2015; Chamberlain et al., 2020; Luginin et al., 2018).

The technique of stellar occultation was also accomplished for the first time around Venus. It provided information about the vertical distribution of CO_2, SO_2 and O_3 gases in the night mesosphere. SPICAV UV also measured the night airglow of nitrogen monoxide (NO) and the Lyman-alpha emission at 121.6 nm. The Ly-α emission monitoring gives access to the distribution of atmospheric neutral hydrogen in the exosphere. The distribution of CO_2, SO_2, and O_3 gases in the night-time mesosphere was studied using the stellar occultation regime, also for the first time realized from the orbit of Venus during the mission (Bertaux et al., 2007a).

Daytime nadir observations in the IR and UV ranges were used to study gases at the upper boundary of the cloud layer. Absorption of SO_2, O_3 were able to be detected in UV (Marcq et al., 2013; Marcq et al., 2019). The IR range was used to track water vapour abundance and to study the altimetry of clouds (Fedorova et al., 2016). The SPICAV IR measured the polarization of reflected solar radiation to study the properties of cloud aerosol particles (Rossi et al., 2015).

At the night side the nadir and limb observations allowed to study IR and UV emissions originated from different atmospheric sources. The UV channel observed the night-time atmospheric emission of nitrogen monoxide (NO) (Stiepen et al., 2013; Royer et al., 2016). The scattered Lyman-alpha emission was used to restore the distribution of atmospheric neutral hydrogen in the exosphere (Chaufray et al., 2015). SPICAV IR tracked the oxygen emission at 1.27 μm originating at ~96 km.

SPICAV IR was the only channel of the SPICAV/SOIR set that was able to sound below the clouds. Thermal emission spectra of the hot lower atmosphere and the surface of Venus were measured in nadir around transparency windows of 1.0, 1.1, 1.18, 1.28, and 1.31 μm (Bézard et al., 2011; Fedorova et al., 2015).

1.6.1. Ultraviolet channel of the SPICAV spectrometer

The UV channel of the spectrometer (SPICAV UV) was the only instrument in capacity to observe stars and perform stellar occultations. It is a spectro-imager, which works in the 118-320 nm spectral range. The measurements were taken with two main geometries: nadir and limb observing modes. The latter mode is the one employed for stellar occultations. The instrument was commanded by its main electronic unit, which interacted with the main control unit of the spacecraft.

The optical scheme of the UV channel of SPICAV is shown in Figure 1.15. The device consisted of a telescope focusing the incoming radiation to the input of the spectrometer. A flat mirror was used to orient the line of sight (LOS) of the channel. The instrument also allowed the use of a slit, narrowing the SPICAV field of view. Decomposition of the incident light into a spectrum was achieved by a concave holographic grating. The spectrum was recorded by a Thomson TH7863 TE CCD, cooled at 270 K with a Peltier, having a size of 288×408 pixels. Only the 288×384-pixel area corresponded to the actual field of view of the spectrometer, while 8 and 15 pixel rows at respectively the left and right edges of the

CCD had a technological purpose, being covered for dark current monitoring. Spectra were decomposed into 384 spectral pixels (henceforth spectels). The rows of the detector (288 pixels) display the spatial distribution of the observed scene. An «image» appears on the CCD with the vertical axis representing the spatial dimension (288 pixels) of the field of view while the 384-pixel wide horizontal axis represents the spectral dimension. The maximum resolution of the spectrum reached 1.5 nm, which corresponds to approximately 3 pixels, each being ~0.54 nm wide. Spectra of a point source, like stars, can achieve this resolution regardless of the use of the spectrometer slit. For spatially extended sources however, achieving the native spectral resolution requires to put the steerable slit in place. This slit has two parts. A wide one (~0.2º) located in the upper portion, while the remainder consists of the narrow part (~0.02º). The latter was designed to fulfil the Shannon sampling criterion in the imaging plane, providing the optimal optical configuration for achieving the native spectral resolution of the SPICAV spectrometer. During stellar occultations, the slit was either retracted or the star was placed into the wide part of the slit. Both options permitted to alleviate the constraints on pointing as even tiny variations of the star position resulted in large spurious fluctuations of the signal when the slit was in place and the star located in the narrow portion.

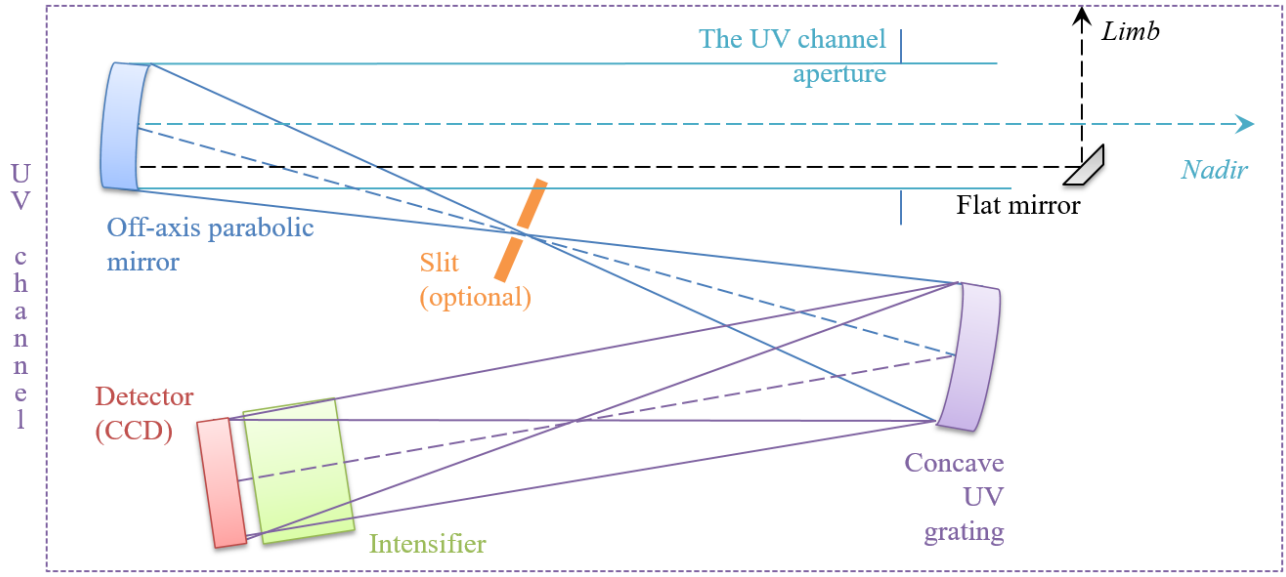

Figure 1.15. Scheme of the UV channel of the SPICAV spectrometer.

The full field of view (FOV) of the spectrometer was 2º×3.16º, which is equivalent to an instantaneous FOV (IFOV) for each pixel of 25×25 arcsec^2. The instrument could cope with a large dynamics of sources' brightnesses thanks to an image amplifier powered by a DC/DC converter delivering voltages from 500 to 900 V depending on telecommands. The voltage was set by the digital gain level (HT) changing 0 to 255. Each incoming photon generates an electric output on the CCD recorded converted into digital units (ADU - analog to digital units). At HT = 20 (gain level for daytime observations), each photo-event is equivalent to ~1.5 ADU, and at HT = 200 - about 40 ADU. When observing weak stars, an HT gain >100 was used. The main characteristics of the spectrometer are summarized in Table 1.2.

The spectrometer is characterized by its point spread function (PSF), which is best represented by a Voigt profile with a Gaussian core characterized by a standard deviation of ~3 pixels and wide weak

wings. The PSF of the device therefore distributes the incoming light of a point monochromatic source within a ~20-pixel diameter disk (Figure 1.16A).

Table 1.2. Main characteristics of the SPICAV UV spectrometer.

Characteristics	**Value**
Spectral range	118-320 nm
Number of spectral points	384
Resolution (Δλ)	~1.5 nm
Resolving power (λ/Δλ)	~150
Atmospheric absorption altitude range	85-145 km
Weight of the spectrometer	4.7 kg
Field of view(FOV)	2º×3.16º (without slit) 0.2º×0.98º (wide part of the slit) 0.02º×1.9º (narrow part of the slit)
Instantaneous field of view (IFOV) per pixel	25”×25”

To optimize telemetry, only a fraction of the full image obtained by the CCD was transmitted. In the stellar occultation mode, it concerned the portion of the CCD where the star was focused. The selected part of the signal was binned along the spatial axis into five contiguous bands (bins) consisting of *n* detector lines. Starlight concentrated in the third, i.e. central, bin. The rest of the bins contained the wings of the PSF, that is a small part of the stellar signal, as well as some background signal (scattered light, atmospheric radiation at the planet’s limb, etc.). The number *n* of spectra (CCD rows) per bin in the stellar occultation mode could be selected among 4, 8, 16 or 32. Then each group of lines was summed up into one spectrum, and the resulting set of 5 spectra was transferred to the Earth (Figure 1.16B). An example of a signal distribution over a CCD from a point source, i.e. stars, in the absence of background illumination, is shown in Figure 1.16A.

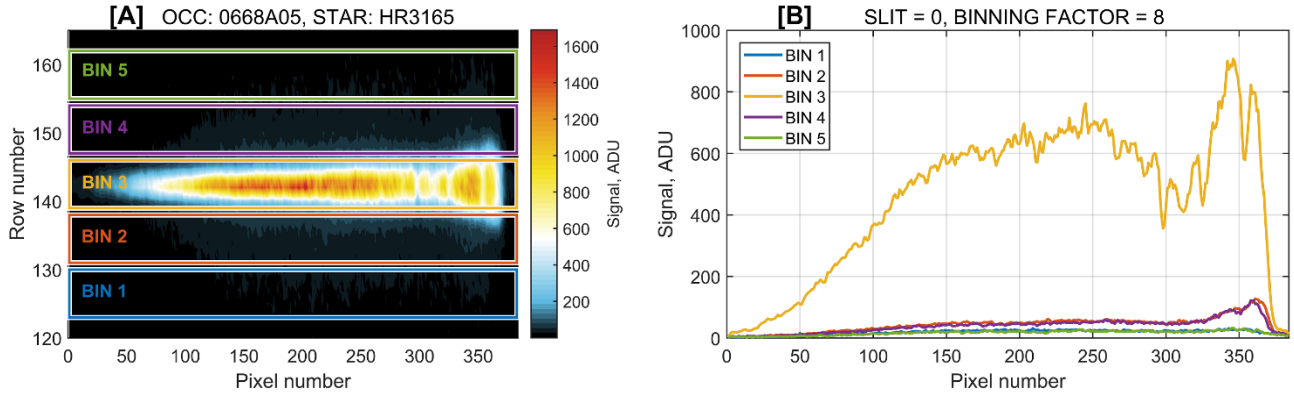

Figure 1.16. (A) A measured image represents the spreading of starlight among several CCD rows at the occultation #0668A05. (B) An example of 5 spectra transferred to the Earth after onboard summing within different bins where the colors of lines correspond to bin areas highlighted in Panel A.

1.6.2. Infrared channel of the SPICAV spectrometer

The infrared channel of the SPICAV spectrometer (Korablev et al., 2012) is based on the IR channel of the SPICAM spectrometer created for the Mars Express space mission. The instrument was developed and prepared for flight at IKI RAS, then integrated to the SPICAV module and calibrated in Service d'aéronomie du CNRS (now LATMOS/IPSL). The main element of this instrument is an acousto-optic tunable filter (AOTF) which is a narrow-band variable filter based on the Bragg's diffraction of light on an ultrasonic acoustic wave excited in a birefringent crystal. Piezoelectric transducers are attached to the TeO_2 crystal, and they generate radio frequency acoustic waves in the range of 80-250 MHz. Depending on the frequency of the signal, you can adjust the filter to a required wavelength.

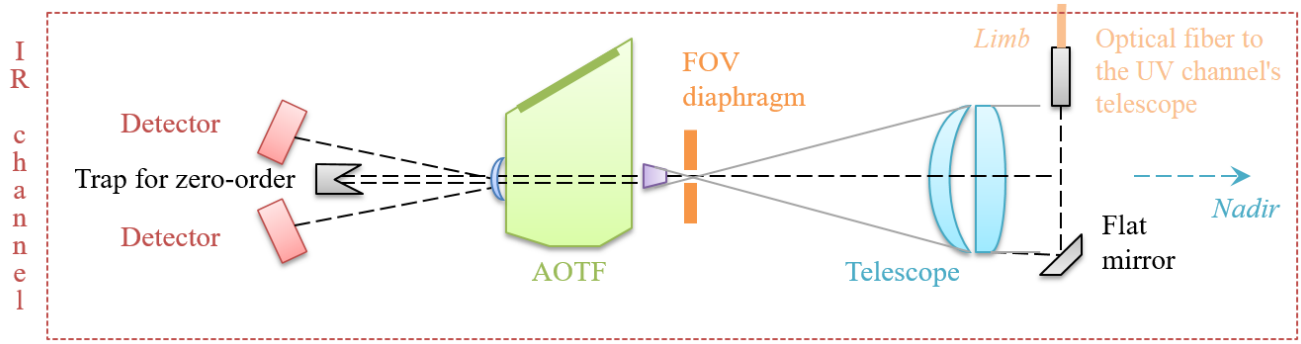

Figure 1.17. Optical scheme of the IR channel of SPICAV.

Table 1.3. Main characteristics of the long-wavelength channel of the SPICAV IR spectrometer.

Feature (longwave channel)	**Value**
Spectral range	1.05 – 1.7 μm
Resolution (Δυ)	5.2 cm^{-1}
Resolving power (υ/Δυ)	~1400
Number of spectral points	664 (optimized night side observations)
Covered transparency windows	1.10 μm 1.18 μm 1.28 μm 1.30 μm 1.51 μm 1.55 μm
Mass	0.7 kg
Field of view	2º (circular)

The optical layout of the spectrometer is shown in Figure 1.17. For observations in the nadir, the incoming radiation is collected by a telescope which has the circular field of 2º. The FOV is equivalent to a step of 9 km along the planet's surface if an observation is held at the pericenter of the orbit. When observing solar occultations, solar radiation is collected by the telescope of the UV channel, and transmitted using a fiber-optic wire to the input of the SPICAV IR channel. In this case, the field of view is 4' in diameter. Telescope is focusing the beam to the diaphragm plane, 1.1 mm in size, after which a

collimator is installed. After the AOTF filter, another lens system is installed that separates the beams of diffracted rays with orthogonal polarization and separates the “zero” order. The separated beams fall on two identical photodiode detectors consisting of Si and InGaAs layers. The silicon photodiode provided recording of short-wavelength radiation (0.65-1.05 μm), and the InGaAs detector - long-wavelength (1.05-1.7 μm). The photodetectors can be cooled using two built-in Peltier elements. In this study only the dataset obtained in the long-wave range is considered. The particular capacities of the instrument at these wavelengths are summarized in Table 1.3.

When observing the night side, IR radiation at each wavelength was integrated for 44.8 or 89.6 ms. Some measurements in nadir, due to the long integration times of the signal, were carried out only for the long-wavelength range. The recorded signal is the sum of the dark current and the photo-signal proportional to the radiation intensity. For calibration, the dark current was measured separately at the beginning and end of each signal integration.

CHAPTER 2. Sulphur dioxide and ozone in the atmosphere of Venus

2.1. Overview of sulphur dioxide research

Sulphur compounds play a key role in the chemistry of the atmosphere of Venus. They are formed as a result of volcanic activity on the planet and participate in the formation of clouds consisting of concentrated H_2SO_4 acid droplets. Moreover, the unknown UV absorber in the upper part of the cloud is also associated with sulphur compounds, inexplicably reducing the albedo of Venus in the UV range (Frandsen et al., 2016; Krasnopolskiy, 2018). Sulphur dioxide is the third most abundant gas making up 0.015% of Venus's atmosphere. Thus, any major changes in SO_2 content occurring in the upper atmosphere can be indicators of photochemical processes and dynamics on Venus. The sulphur dioxide is destroyed by chlorine and hydroxyl radicals as well as by an effective photodissociation on the day side. The catalytic processes are noticeable on the night side, where fluxes of atoms and molecules are brought by the global SSAS circulation at altitudes of about ~100 km.

2.1.1. Temporal and spatial distributions of sulphur dioxide

The entire history of observations of sulphur dioxide on Venus showed significant variations in its amount at the cloud top (~70 km) presented in Figure 2.1. SO_2 gas was first detected in the cloud tops by a ground-based ultraviolet telescope with a content of 0.02-0.5 ppm (Barker, 1979). The SO_2 abundance was mainly measured at the altitude corresponding to the cloud top level on the day side, that is about 70 km. Several instruments aboard the first spacecraft to Venus showed a global decrease of the SO_2 volume mixing ratio of (VMR) in the upper atmosphere in the 80s and 90s (Figure 2.1). During this period some local peaks of the gas abundance were obtained. This result mainly came from ten years of monitoring by the ultraviolet spectrometer (UVS) on board the Pioneer Venus Orbiter (PVO). The reduction of the amount was steep at the beginning, and then it was followed by a gradual decline in the SO_2 mixing ratio. It was confirmed by several other instruments working in the UV. The International Ultraviolet Explorer (IUE) observed Venus in 1979 (Conway et al., 1979) and 1987-1988 (Na et al., 1990; Na et al., 1993), when the corresponding mixing ratios changed from 380±70 ppbv to 50±20 ppbv. Lower abundance of sulphur dioxide was also obtained based on observations by the Venera-15 Fourier spectrometer in the IR range (Moroz et al., 1990; Zasova et al., 1993). Its data originally corresponded to 60-62 km but the value was scaled to an altitude of 70 km in order to compare with the UV observations (Zasova et al., 1993). Rocket observations in 1988 and 1991 measured SO_2 equal to 80±40 ppbv and 120±60 ppb respectively (McClintock et al., 1994). The further observations by IUE and ground based facilities (Barker et al., 1992; Esposito et al., 1997) showed the local maximum of the SO_2 content in 1991-1992. In 1995, the Hubble Space Telescope (HST) completed the first era of continuous SO_2 exploration on Venus and gave a value of 20±10 ppbv (Na et al. 1995), which was 2-5 times less than previous measurements.

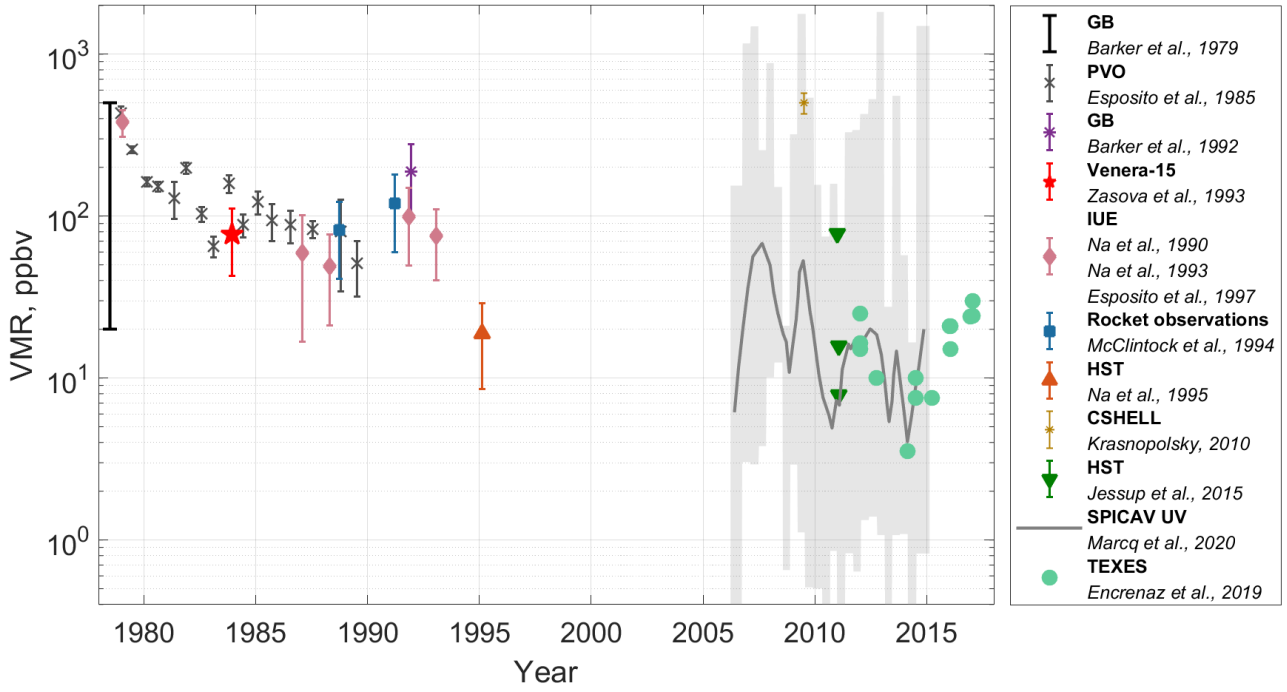

Figure 2.1. The timeline of sulphur dioxide observations at the cloud tops on the day side of Venus. The references are given in the legend. The SPICAV UV observations are presented with the corresponding variability of obtained values within 4-month intervals. The full range of obtained values is represented by the grey area which is accompanied by a median curve (grey solid line).

This behaviour was puzzling. The sulphur compounds are rather associated with geological activity. So, the main hypothesis to explain the observed SO_2 change has considered a link with possible episodic volcanic eruptions on Venus. It was assumed that one event would inject sulphur compounds into the atmosphere, and the vertical transfer would distribute them over clouds. Then SO_2 depleted and a monotonic trend of its VMR was observed (Esposito, 1984).

For spatial variations sulphur dioxide was studied in the IR range (7 μm, 8 μm and 19 μm) using a Fourier spectrometer on board the Soviet spacecraft Venera-15. The study of latitudinal distribution revealed an increase in gas content from the equatorial zone and middle latitudes to the poles of the planet. At a pressure level of 150 mbar (corresponding to ~ 62 km), the amount of SO_2 at low latitudes was 0.3-0.5 ppm, and 1-2 ppm in the polar regions. The same picture was observed at the level of the cloud top (40 mbar, ~ 69 km).

SO_2 monitoring on Venus was resumed in 2006, when the Venus Express spacecraft began its orbital mission (Titov et al., 2006) with a set of three SPICAV/SOIR spectrometers on board. UV and IR instruments covered SO_2 absorption bands at 190-300 nm (for SPICAV UV) and about 4 μm (for SOIR). In this period there were several ground-based observations by instruments in various spectral intervals: STIS/HST (Space Telescope Imaging Spectrograph/Hubble Space Telescope), IRTF/TEXES (Infrared Telescope Facility/Texas Echelon-Cross-Echelle Spectrograph), JCMT (James Clerk Maxwell Telescope), ALMA (Atacama Large Millimeter/Submillimeter Array) and the CSHELL (Cryogenic Echelle) spectrograph. STIS measures in the same spectral range as SPICAV UV while CSHELL operates at 4.04 μm. These instruments observed the cloud top level. SPICAV UV in nadir mode and STIS were able to perform measurements only on the day side of Venus. Solar occultations by SOIR

and SPICAV UV had limited local time and latitude coverage corresponding to the Venus terminator mainly in the northern polar area. Stellar occultations by SPICAV UV were designated for the night-time observations. Other listed instruments probe both the day and night sides. TEXES measures the thermal IR radiation from Venus at 7 μm and 19 μm. The wavelength of 7 μm corresponds to emission forming at 60-80 km while the signal at 19 μm originates from altitudes several kilometres lower. JCMT and ALMA performed microwave observations of the SO_2 abundance in the upper mesosphere.

SPICAV/SOIR observed Venus in nadir mode and (for the first time) in solar and stellar occultation modes. In the nadir mode the UV spectrometer monitored the atmospheric composition at cloud tops. The occultation modes allowed to obtain the detailed vertical profiles of aerosols and several atmospheric gases including SO_2 in an altitude range from 65 to 140 km depending on spectral range and an absorbing particle. Nadir UV observations by SPICAV supplemented the long-term trend of SO_2 VMR (Marcq et al., 2013; Marcq et al., 2020). These long-term variations were not clearly confirmed by solar and stellar occultations over 70 km (Belyaev, Evdokimova et al., 2017). However, fluctuations in the observed values remained significant; the annual dependence of VMR showed individual sporadic maxima.

The continuous monitoring in the present era of Venus observations showed a high variability of SO_2 abundance in short term. Observations made by SPICAV UV in nadir and simultaneous full-disk observations from the Earth clarified some patterns of SO_2 variability. The SO_2 variations are more significant at low latitudes in comparison with polar regions (Encrenaz et al., 2019). The same conclusion is done by SPICAV UV monitoring (Marcq et al., 2020). According to those data, the latitudinal behaviour depends on an average SO_2 VMR. A decrease towards poles was observed in periods of large SO_2 abundance. But the latitude trend was inverse in SO_2 minima (Marcq et al., 2013).

At the cloud tops the sulphur dioxide mixing ratio increases on average from midday towards the morning and evening terminators (Marcq et al., 2020). The TEXES particularly observes «SO_2 plumes» which are areas on the Venusian disk with high SO_2 VMR values. These plumes had a lifetime shorter than 24 hours. It also signifies that SO_2 geographical pattern cannot remain in long time periods. The probability of such plumes corresponds well to the SPICAV SO_2 local time distribution, and the maximum probability is in 0:00-6:00 time interval (Encrenaz et al. 2019).

The stellar occultations measured the night-time abundance of sulphur dioxide being 3-4 times higher than it was observed at the terminator at the altitude of ~ 95 km (Belyaev, Evdokimova et al., 2017). The increase of SO_2 abundance at night also presented in the sub-millimeter (sub-mm) observations by JCMT at 85-100 km (Sandor et al., 2010). Individual sessions of measurements by ALMA showed more puzzling behaviour. The maximum in the morning near equator and the SO_2 absence at night were mainly associated with short-term variability and a low signal to noise ratio (Encrenaz et al., 2015).

2.1.2. Vertical profile of SO_2 obtained by SPICAV/SOIR instrument on board Venus Express and ground based facilities in the mesosphere

Since the first observations at the cloud tops, SO_2 variations were significant in space and time. The present knowledge about vertical distribution of sulphur dioxide is combined by various experiments for

the entire period of Venus exploration (Figure 2.2). Altitudes from the surface to the mesosphere were probed by different instruments mounted on landers and orbiters as well as on ground-based telescopes. The most detailed profiles below 65 km are results from *in situ* observations performed by ISAV ultraviolet spectrometers on board two Vega descent probes (Bertaux et al., 1996). Only these measurements provided SO_2 altitude distribution with a good vertical resolution.

Before ISAV experiments the SO_2 content of 185±43 ppbv (Oyama et al., 1979, 1980) was measured only by a gas chromotograph on the PV large probe indeep atmosphere. However, the ISAV-1 and -2 showed 5 times lower values (Bertaux et al., 1996). Below 40 km, the SO_2 VMR profile decrease steadily with decreasing altitude down to the surface meaning that the SO_2 is transformed to another sulphur-bearing molecules. That behaviour is complicated to interpret from the theoretical point of view to the thermal chemistry in the deep atmosphere (Esposito et al., 1997).

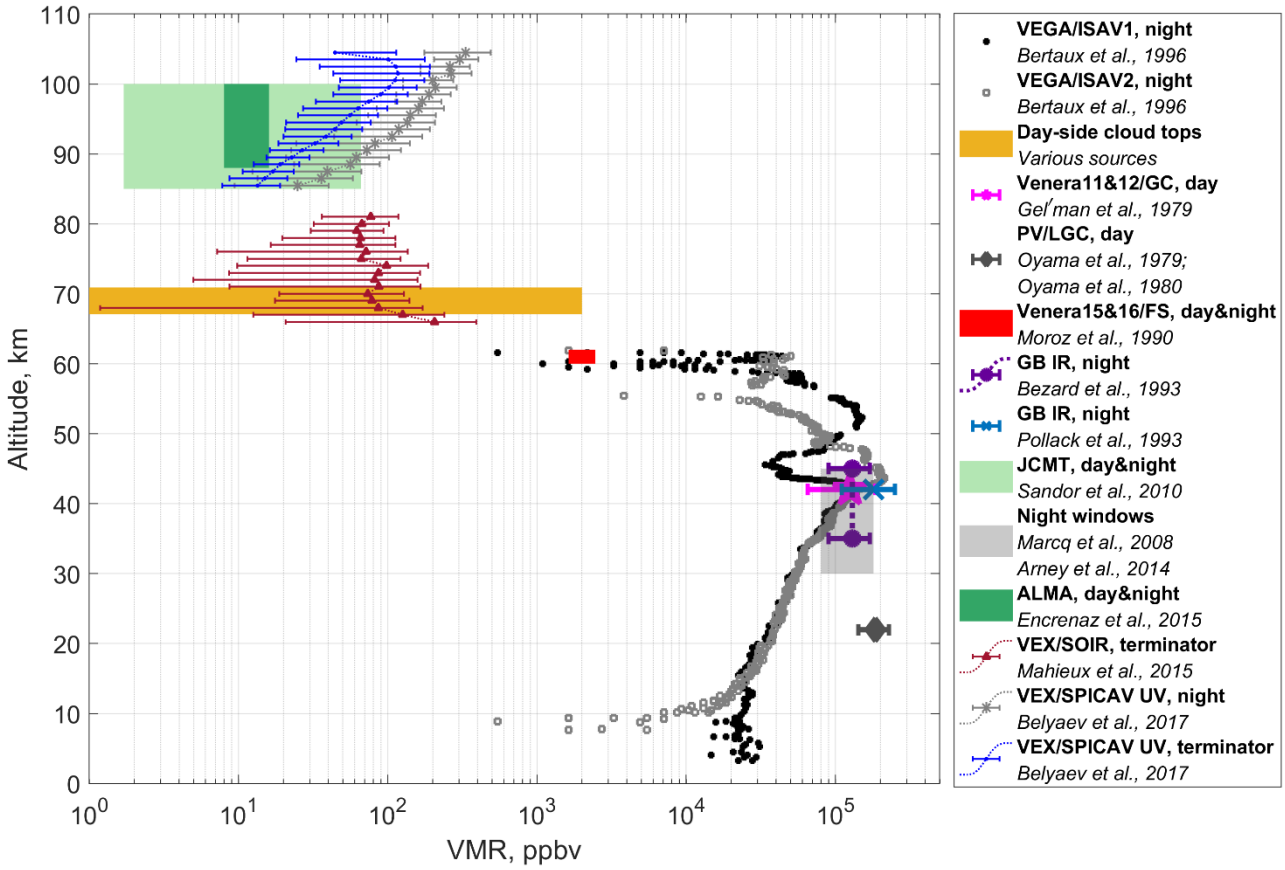

Figure 2.2. The vertical distribution of SO_2 VMR obtained by different instruments through the entire era of Venus exploration. The references are presented in the legend.

The ISAV measurements were confirmed by other observations that sounded higher altitude layers. The Fourier spectrometers on board Venera 15&16 were sensitive to a range of 60-62 km and observed VMR about 2000 ppbv (Moroz et al., 1990). *In-situ* Venera 11&12 observations by gas chromatography provided values about 100 ppm at the lower cloud border that coincided with Vega's profiles (Gel'man et al., 1979). The IR thermal emission at 2.3 μm is a way to a remote sensing of the atmosphere at 30-45 km. Such observations were done by ground based instruments (Bézard et al., 1993; Pollack et al., 1993; Arney et al., 2014) and by VIRTIS-M (Marcq et al., 2008). The most recent IR data showed 156±42 ppm in the Northern Hemisphere and 135±36 ppm in the southern hemisphere. In general, no

significant variations of the SO_2 content below the clouds were revealed. It is in correspondence with expecting stability of the lower atmosphere.

The gas abundance was studied over the clouds in much more detail by the SPICAV/SOIR instrument during the period of the Venus Express mission. SO_2 absorption was measured in the first UV and IR observations of solar and stellar occultations (Figure 2.2). The altitude distribution retrieved from those occultations demonstrates an inversion layer of the SO_2 content around 85-100 km. On average, an increase of the SO_2 VMR with altitude from 8-20 ppbv at 85-90 km to 50-180 ppbv at 100 km was observed (Belyaev et al., 2012; Belyaev, Evdokimova et al., 2017). This distribution was supplemented by the SOIR data with a decrease of the SO_2 abundance from 100-300 pbbv at 65 km to 50-100 ppbv at 80 km possessing large uncertainty values (Mahieux et al., 2015). The previous results of the stellar occultation data revealed the SO_2 VMR rising with altitude from 10-30 ppbv at 85-95 km to 100-300 ppbv at 100-105 km (Belyaev, Evdokimova et al., 2017). However, this increase is re-investigated further in this work in the framework of the detailed calibration study.

All in all, one can see significant short-term changes in the amount of sulphur dioxide in the mesosphere that are interpreted by different models. Discussions of the models that could be compared with our occultation data are presented in Section 2.3 of this Chapter and in Chapter 4. The comprehensive overview of SO_2 content variations with time, altitude and latitude retrieved from experiments and analysed by models is presented in papers of Vandaele et al. (2017a, 2017b).

2.2. Ozone in the atmosphere of Venus.

Ozone on Venus excites a great interest for researchers due to its active participation in basic atmospheric chemical processes, as well as its bio-protective function in the terrestrial atmosphere. On the Earth the large amount of the UV radiation is absorbed by the abundant O_3 layer in the stratosphere where the vertical temperature profile is inverted. Here the Hartley band of ozone absorption at 240-300 nm is saturated, and the atmospheric transmission in this range is close to zero. On Venus, where the total O_3 content is expected to be $>10^3$ times less than on the Earth, the Hartley band is applicable for the spectral investigation. Before this first detection, the ozone presence was estimated by different photochemical models (Yung and DeMore, 1999; Krasnopolsky, 2010a; Mills, 2007). However, so far, except for the molecular O_2 airglows another oxygen species was not quantified experimentally on Venus. It constrained estimation of the ozone concentration in the atmosphere. The upper limit for the oxygen abundance was estimated to <2 ppmv that signified extremely low amounts of the Venusian ozone (Mills, 1998).

The discovery of ozone on Venus concluded a presence of this gas on three terrestrial planets: Earth, Mars and Venus. Due to the Earth, with the O_3 protection of the biosphere, and Mars, with an evidence of oxygen-rich airmasses, ozone is considered in a search of possible life. It is known that such a protection from the strong UV radiation requires a significant abundance of O_3. The observed values in the Earth atmosphere are around 300 DU (Dobson Units), where 1 DU corresponds to a column concentration of 2.69×10^{16} molecules per cm^2. Mars and Venus have a tiny amount of ozone compared to the terrestrial quantity. The Martian ozone compiles <1 DU (Lefèvre et al., 2004; Lebonnois et al.,

2006; Montmessin and Lefèvre, 2013; Määttänen et al., 2013), while the Venusian one is observed to be less than 0.5 DU (Montmessin et al., 2011; Marcq et al., 2019).

2.2.1. Discovery of ozone in the atmosphere

Ozone on Venus was discovered by Montmessin et al. (2011) in SPICAV UV stellar occultation spectra. It was confidently detected in 29 night-side sessions in the beginning of the mission at altitudes ~100 km with number densities of 10^7-10^8 cm^{-3} (Figure 2.3). Those concentrations appeared as an episodic peak of ozone content that demonstrated some sporadic presence of the gas in the mesosphere. After the discovery the occultation processing of the whole dataset, which counts >400 sessions, was necessary in order to characterize the O_3 mesospheric distribution in detail. Venusian ozone is characterized by a vertically confined and horizontally variable layer residing at a mean altitude of 100 km.

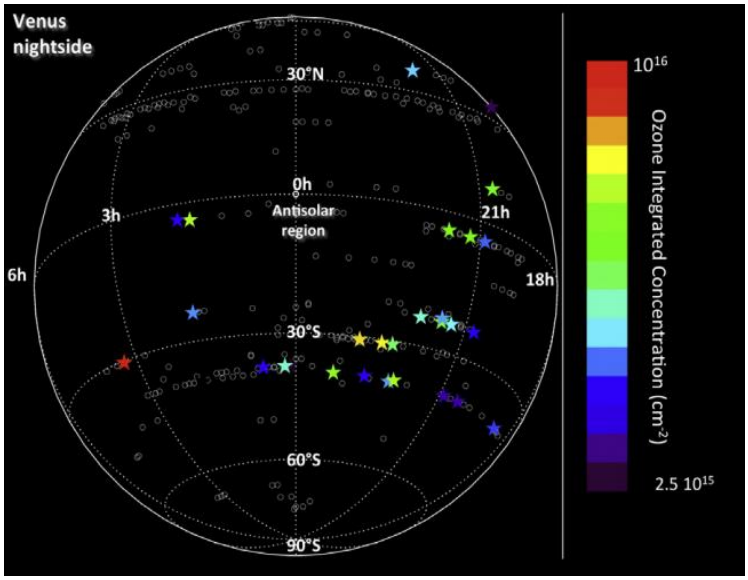

Figure 2.3. The spatial distribution of the first reported detection of ozone in the mesosphere of Venus (Montmessin et al., 2011).

2.2.2. Ozone at the top of the clouds

More recently, an analysis of SPICAV UV nadir dayside observations established an abundance of O_3 around 10-20 ppbv at the cloud top (~70 km) at latitudes over 50° in the both hemispheres (Figure 2.4, Marcq et al., 2019). Those values correspond to the column ozone amount above the clouds of about 0.1-0.5 DU (Marcq et al., 2019) that is ~10 times less abundant than on Mars (Perrier et al., 2006), and ~10^3 times less than on the Earth.

The IPSL Venus GCM (Lebonnois et al., 2010) was able to predict the ozone formation spatially distributed at the cloud tops in correspondence with the SPICAV observations (Figure 2.4). It is linked to a circulation in Hadley cells which contributes to oxygen accumulation in the polar regions. Since the polar ozone layers are a consequence of dynamic processes, a 1D model was not able to reproduce this effect. The GCM indicates that the O_3 layer formation is similar to a mechanism that was established for the Martian upper atmosphere (Montmessin and Lefèvre, 2013). But in the case of Venusian ozone, no obvious seasonal effect and/or temporal trend was noted.

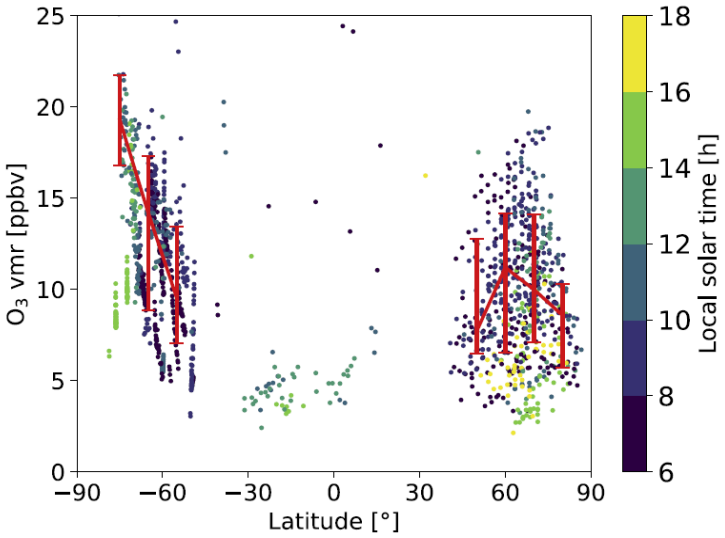

Figure 2.4. The latitudinal dependence of the first detection of cloud-top ozone layers at the polar regions (Marcq et al., 2019).

2.3. Photochemistry: a review of atmospheric models for SO_2 and O_3

A study of the mesosphere holds the key of fundamental components of the main chemical cycles determining the current atmospheric content. The major position is occupied by carbon dioxide and sulphur dioxide cycles. The carbon dioxide is dominant on Venus that intensifies a role of the CO_2 cycle in the mesosphere. The great issue of theoretical comprehension is the stability of the CO_2 mixing ratio being equal to 0.965 (von Zahn et al., 1983). Main processes of the cycle are a photolysis of CO_2 on the day side, a production of O_2, and a recombination of CO and O_2 with a formation of CO_2. The mixing ratio of CO has been observed at 20-30 ppmv at 36 km (Pollack et al 1993). A theoretical estimation shows that photolysis should produce this amount of the gas in a short period, 50 ppmv demand about 200 years (McElroy et al., 1973). The large volume of CO_2 and correspondingly low abundance of CO also coincide with the very small upper limit of oxygen in its ground state. The ground-state oxygen amount was obtained to be lower than 2 ppm above 60 km from observations of the mid-latitudinal region of Venus (Mills, 1999). This limit indicates that the production of CO_2 is approximately balanced by its loss via photolysis. However, the existence of oxygen emission at 1.27 μm observed on Venus argues the fast formation of O_2 in the ground state (Connes et al., 1979; Crisp et al., 1996). The reproduction of CO_2 from CO and O_2 is a slower process (Nair et al., 1994; Mills, 1998). Thus, the stability of CO_2 requires another process different from a simple oxidation. There might be a net of catalytic reactions (Yung and DeMore, 1982), however, it is not evidently resolved which process is the general one.

The sulphur cycle drives the cloud formation of a thick sulphuric acid droplets layer enshrouding Venus globally. A central position in the net of reactions is occupied by the sulphur dioxide. SO_2 is the third most abundant gas in the Venusian CO_2-atmosphere (<150 ppm) after the dominant carbon dioxide at 96.5% and nitrogen (3.5%). Its oxidation is a primary process leading to a formation of the H_2SO_4 acid. The latter further condenses at the cool cloud tops region and descends until its evaporation and dissipation becomes prevailed. The resulting SO_2 and H_2O are transferred upward supplying the

mesospheric SO_2 content. Sulphur acid synthesis is a prevailing process independent of the local time, and it results in a sharp decrease of SO_2 in the upper cloud layer (Figure 2.2).

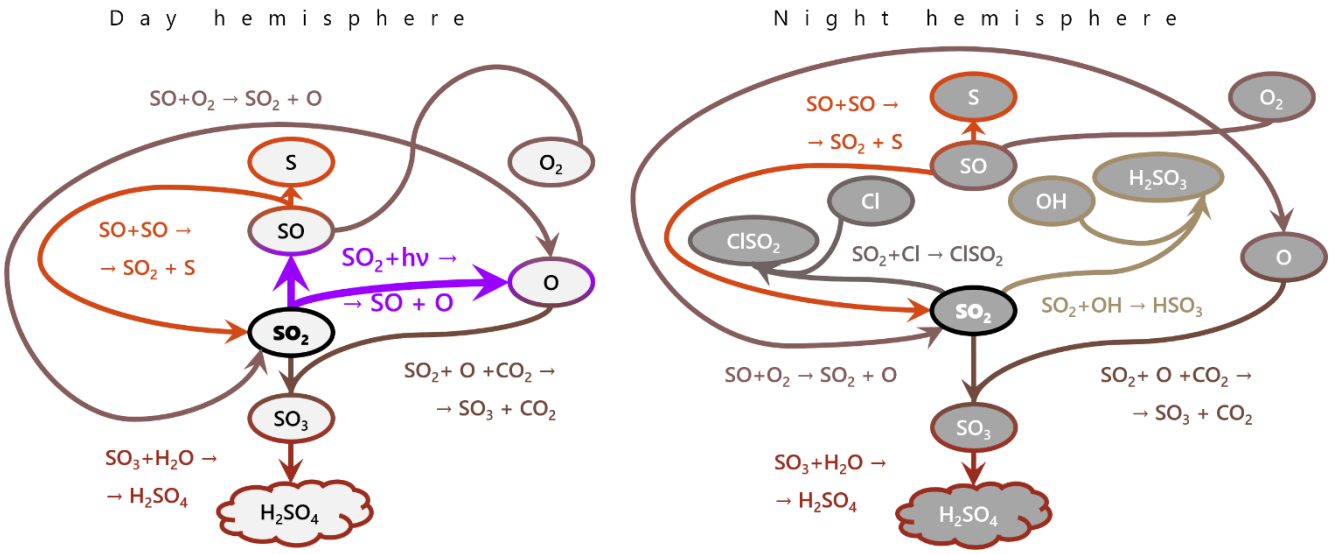

Figure 2.5. The main reactions of the sulphur chemical cycle in the day and night parts of the mesosphere.

Another sink of SO_2 is its photolysis occurring in the daytime atmosphere. Sulphur monoxide and pure sulphur are formed and their oxidation is maintaining the cycle. At night a significant role of reactions with Cl radicals and hydroxyl takes place while they are involved in the SSAS circulation. However, those components destroy the SO_2 molecule less efficiently than the photodissociation process that leads to an increase of SO_2 in the night mesosphere.

Figure 2.5 presents an overview of the most prominent processes with SO_2 in the mesosphere of Venus. However, such a simplified scheme does not resolve the following questions that rise up:

(1) A dramatic decrease of SO_2 through the cloud layer that could not be explained only by the oxidation.

(2) An inversion of SO_2 volume mixing ratio at 80-100 km that was observed in occultation experiments by SPICAV on board Venus Express,

(3) The sub-mm observations have revealed correlations between SO and SO_2 contents that argue the hypothesis of a closed cycle between the SO_2 depletion and the SO oxidation, so it indicates that another species also impacts the sulphur bulk in the mesosphere.

A simulation of photochemical processes shows which reactions are decisive in the atmosphere and which gaseous species are establishing equilibrium in the atmospheric chemical cycles. There are two general approaches used to model the vertical distribution of species in the Venus atmosphere. The first one is a 1-D model neglecting a horizontal transport in the atmosphere. It is a reasonable approach to characterize the average vertical distribution of atmospheric species. A more complex 3-D model, i.e. general circulation model, is able to quantify in detail occurring spatial and temporal variations. So far the required accuracy has not been achieved to explain by models the observed ozone and sulphur dioxide distributions.

Table 2.1. An overview of discussed photochemical models of Venus' atmosphere.

	Model	Type	Diurnal cycle	Altitude range, km	Ref.	SO_2	O_3
DAY	Caltech/JPL Photoche-mical Model (KINETICS)	1-D	Global average	58-110	Yung, DeMore (1982)	A: a decrease from ~4 ppbv at 80 km to ~2 ppbv at 90 km B: a decrease from ~10 ppbv at 80 km to ~6 ppbv at 90 km C: a decrease from ~10 ppbv at 80 km to ~8 ppbv at 90 km	A: ~25 ppbv at 100-105 km decreasing to ~ 2.5 ppbv at 80 km B: 20 ppbv at 95-100 km decreasing to ~6 ppbv at 80 km C: 12 ppbv at 100-105km decreasing to ~0.08 ppbv at 80 km
		1-D	Global average	58–112	Mills, Allen (2007)	~40-50 ppbv at 80-100 km (Vandaele aet al., 2017)	
		1-D	Diurnal average at 45° latitude	58–112	Zhang et al. (2010)	Min. ~6 ppbv at 75 km A: a decrease <2 ppbv at 100 km B: max. at 100 km of 90 ppbv C: max. at 100 km of 1.5 ppmv	
		1-D	Diurnal average at 70° latitude	58–112	Zhang et al., (2012)	Min. at 80 km of 30 ppbv Max. at 97 km of 300 ppbv	Max. 20 ppbv at 100 km A decrease to 0.2 ppbv at 80 km
	Krasnopolsky Mesosphere model	1-D	Global average	47–112	Krasnopolsky (2012)	~25 ppbv at 85 km ~30 ppbv at 95 km	10 ppbv at 90-95 km forming an ozone layer
	IPSL Venus GCM	3-D		0–96	Stolzenbach et al. (2014)	Nearly constant at around 8 ppbv at 80-100km (Vandaele et al., 2017a)	Ozone polar layers and an increase over 80 km (Marcq et al., 2019)
	IPSL Venus GCM	3-D		0-150	Gilli et al. (2017)	Nearly constant at around 200 ppbv at 80-100 km (Gilli, in priv. commun.)	Maximum VMR at 100 km: ~8 ppbv (Gilli, in priv. commun.)
NIGHT	Krasnopolsky Mesosphere model	1-D	Night mesosphere	80–130	Krasnopolsky (2013)	100 ppbv at 80-106 km	A thin layer with a maximum at 95 km of 20-40 ppbv depending on the assumed Cl ions flux.

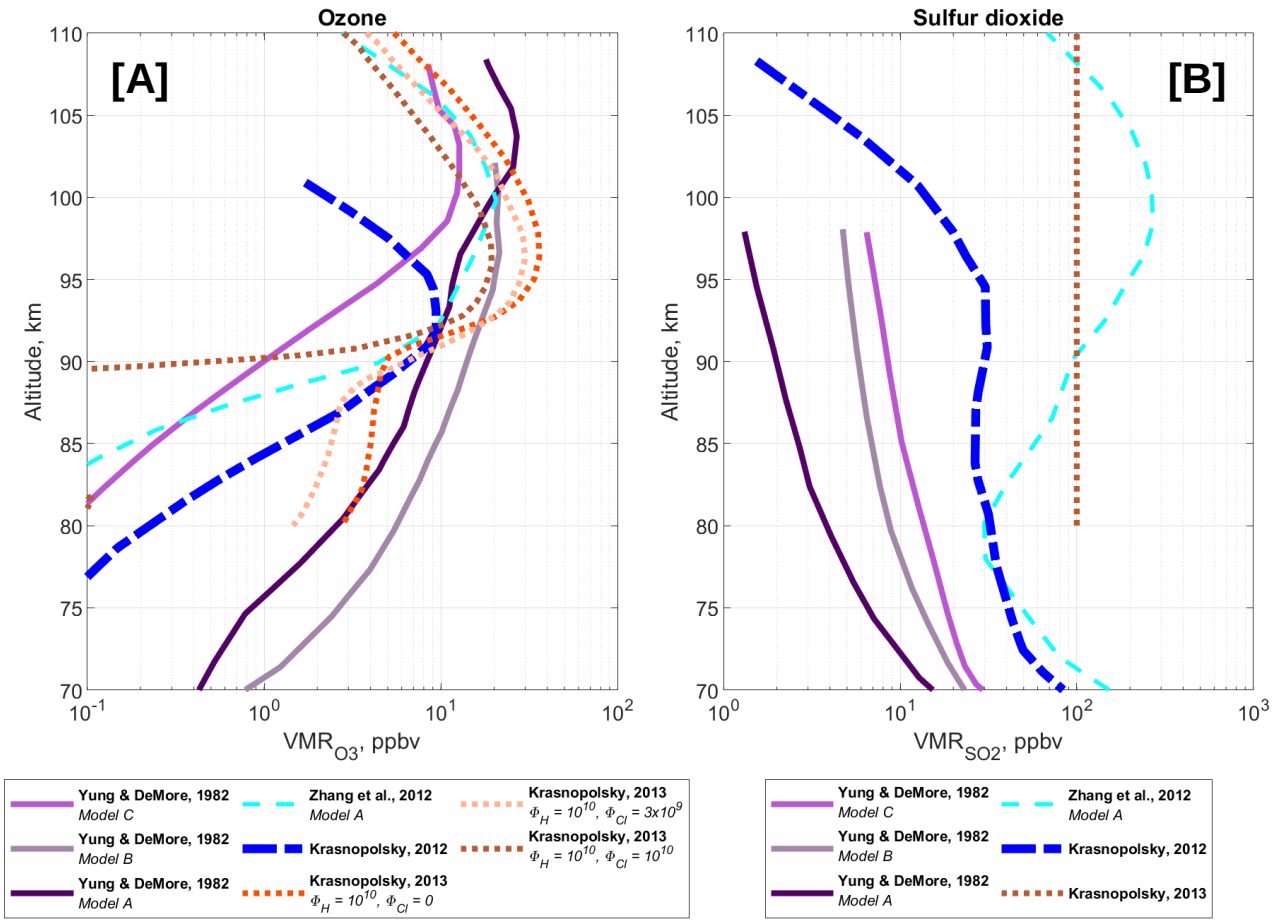

Figure 2.6. Synthetic ozone (A) and sulphur dioxide (B) vertical distributions in the mesosphere of Venus.

The Caltech/JPL Photochemical Model (KINETICS) was a base of several atmospheric models considering gaseous abundances without any diurnal changes. The solar conditions differ in different models, however, there are no simulations of the nightside atmosphere.

The first model that is considered is a work by Yung and DeMore (1982). The model estimates an influence of three possible catalytic cycles influencing a first CO_2 restoration in the atmosphere. The OH_x, NO_x and ClO_x cycles are considered in models A, B and C respectively. The model A considered a high flux of H_2. The model B of the nitrogen influence just slightly decreases the oxygen compounds abundance. The chlorine cycle was preferred by the results of the model C, and model A and B demanded correspondingly rather high values of hydrogen and nitric oxide. Thus, model C concluded the lowest O_2 and corresponding O_3 abundances. It is a reasonable approach since the ClO was recently detected in the Venus night mesosphere confirming an abundant chlorine budget (Sandor et al., 2018). However, a lack of resulting sulphur dioxide abundance also results from the calculations.

The space exploration gave a number of data about the sulphur dioxide decrease through the cloud layer. The simple oxidation is insufficient to explain accurately the SO_2 VMR reduction in 3-orders of magnitude from 40 km to 70 km (Vandaele et al., 2017a). Most of the models are focused on a description of its mesospheric distribution, i.e. the SO_2 gradient over ~65 km (Vandaele et al., 2017a).

The comprehensive sulphur chemistry (Krasnopolsky, 2012; Mills and Allen, 2007; Zhang et al., 2012) includes metastable sulphur and chlorine species, OSSO, S_2O, $ClSO_2$ and others, that extend the effective lifetime of SO_2 against oxidation to SO_3 at an altitude of about 70 km. It increases the vertical transport of SO_2 compared to simplified models of sulphur chemistry (Zhang et al., 2010). These models provide small vertical gradients for SO_2 at an altitude within 75-90 km. All observational studies qualitatively conclude that the inversion layer of SO_2 VMR exists. The most significant inversion layer was modeled by Zhang et al. (2012) considering H_2SO_4 and S_8 bulk above 90 km. In particular, it was simulated in a high-latitude region which SPICAV/SOIR solar occultations were observed. The ozone layer was also obtained by this model with a present maximum at 95-105 km of 20 ppbv.

Other models, such as Krasnopolsky (2012), Mills and Allen (2007) and Stolzenbach et al. (2014), show almost constant SO_2 VMR between 80 and 95 km (Figure 2.6) that is in the range of SPICAV observations.

The particular interest of our study is aimed at the only one 1-D chemical model of the night side, which assumes the night airglows and the detected ozone layer (Krasnopolsky, 2010a; Krasnopolsky, 2013). It describes how the layer thickness is determined by the chlorine radicals flux to the night side. The nightside O_3 abundances appeared to be higher than simulated ones for a diurnal average. However, a presence of high values of the Cl flux is still questionable.

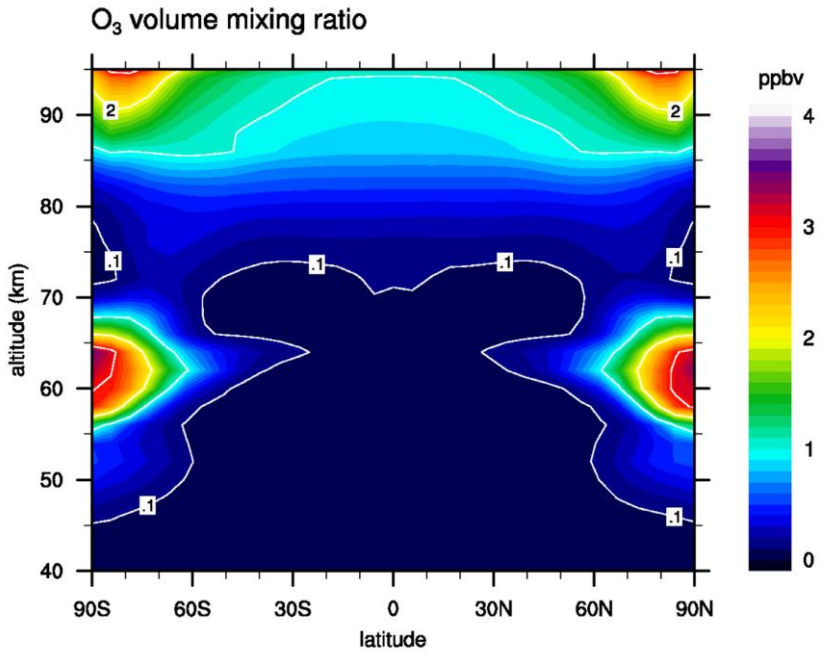

Figure 2.7. Diurnal average of O_3 volume mixing ratio depending on latitude and altitude (Marcq et al., 2019) synthesised by the IPSL Venus general circulation model, which was developed for 0-96 km (Stolzenbach et al., 2014).

The IPSL Venus general circulation (Lebonnois et al., 2010) and photochemical (Stolzenbach et al., 2014) models are adopted for Venus from the Earth's (Hourdin et al., 2006) and Martian (Forget et al., 1999) analogues. Consideration of joint dynamics and photochemistry by carbon dioxide, oxygen, hydrogen, chlorine and sulphur compounds proved the influence of the global circulation to minor

species. In this model, the minimum VMR profile decreases from 75 to 80 km when moving to the poles, so in the middle and high latitudes a strong inversion of the VMR profile is evident, but at the equator the profile is almost constant between 75 and 80 km. The model shows that this behaviour has a dynamic effect when SO_2 or its source transports to the Pole and then down to the lower mesosphere due to the Hadley circulation. Thus, the IPSL Venus model shows that the dynamics can play an important role in the mentioned inversion, as it was observed in the Martian atmosphere (Montmessin and Lefèvre, 2013). Moreover, the model successfully predicts the Hadley circulation influence as well to O_2 and O_3 latitudinal distributions. The O_2 molecule was not observed directly, while the ozone polar layers were obtained recently by SPICAV UV nadir observations at 68-70 km (Figure 2.4 and 2.7; Marcq et al., 2019)

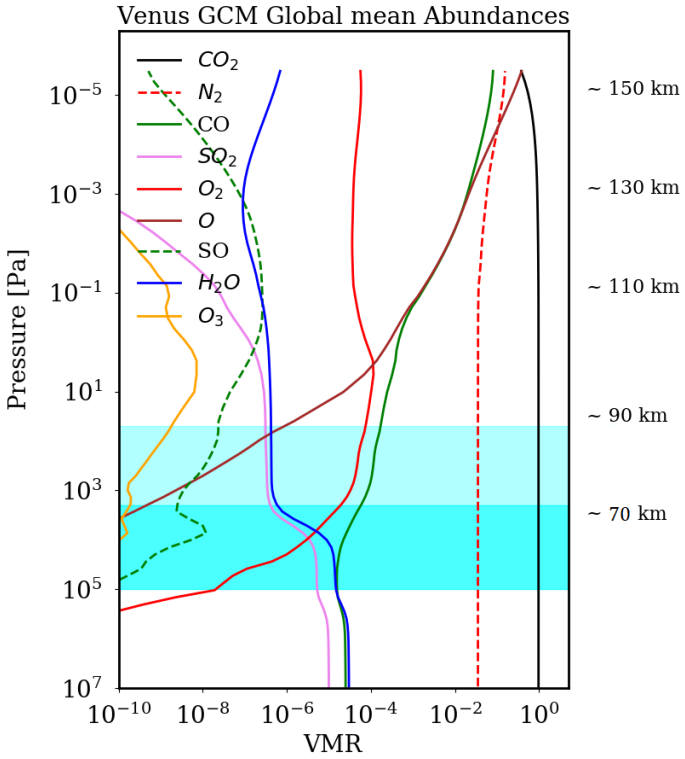

Figure 2.8. Global mean vertical distribution of minor species (G. Gilli in priv. communication) extended to the thermosphere as obtained by the IPSL Venus general circulation model, which was developed for 0-150 km (Gilli et al., 2017).

The dynamics of Venus is very complicated. There are still some uncertainties in the description of transient dynamic phenomena such as gravity waves propagation and breaking. The upper boundary of 96 km limits the theoretical investigation of the active upper mesosphere. That is why, the IPSL Venus GCM was extended up to 150 km to consider important radiative and chemical processes above 100 km, as well as non-local thermodynamic equilibrium (LTE) conditions over 110 km on Venus (Gilli et al., 2017). The model is under development to provide the best correspondence between theory and observations of temperature fields, and contents of CO and O, since these species are tracers of the circulation in the lower thermosphere. There are some uncertainties remaining for the non-LTE parameterisation that may influence the result. However, this model provides the only theoretical representation of joint dynamic and photochemistry influence on the atmosphere over 90 km. The global

VMR profile of O_3 shows a thick ozone layer with a maximum at 100 km. The average SO_2 VMR does not depend on latitude in 70-100 km and decreases higher in the lower thermosphere (Figure 2.8). These results are important since SPICAV UV particularly sounded altitudes of 85-110 km.

The review of the described models highlights that ozone together with chlorine-bearing species can expose a substantial fraction of reactions presiding to the main chemical cycles. The absence of direct measurements of the O_2 abundance in a fundamental state has left the appraisal of Venus's atmosphere oxidizing capacity with major unknown. It is nevertheless possible to estimate this capacity indirectly by probing species related to the presence of oxygen. During the night, O_3 formation via the O_2 + O reaction is balanced by its loss through the following main reaction presented on Figure. 2.9. From the first night ozone detections it was concluded that the observed ozone concentrations are consistent with values expected for a chlorine-catalysed destruction scheme (Montmessin et al., 2011).

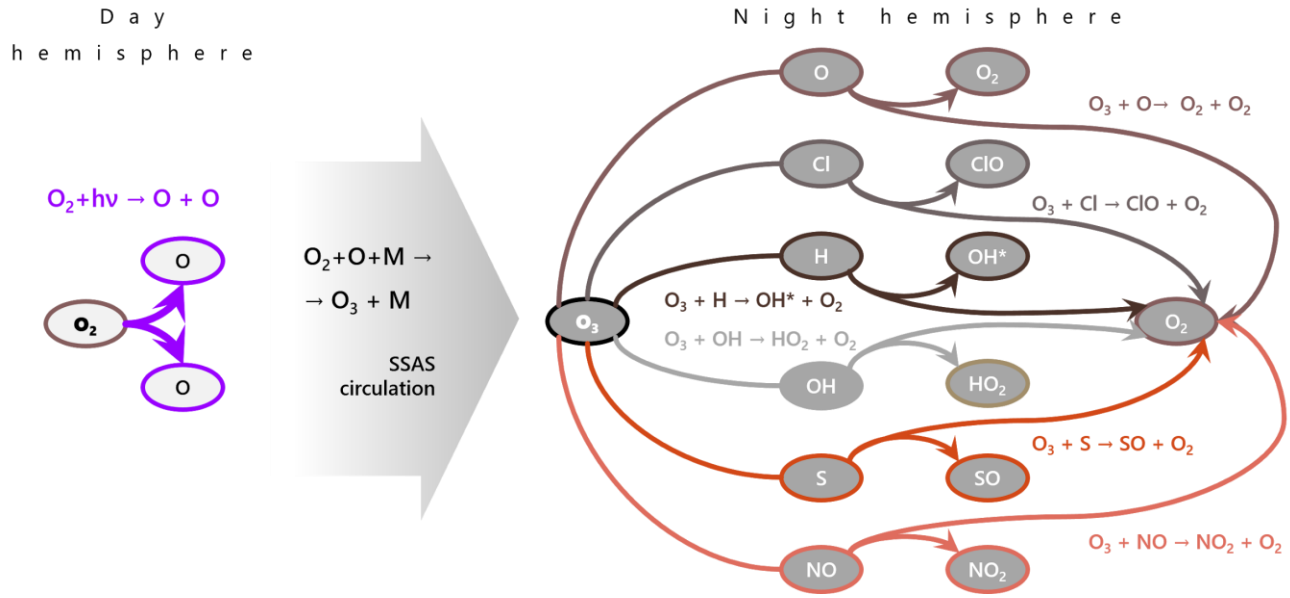

Figure 2.9. The main reactions of the ozone chemical cycle including its source and formation (left) and the main sinks (right).

CHAPTER 3. Data processing of stellar occultation spectra

3.1. The stellar occultation technique: retrieving the atmospheric composition from transmittance spectra

Stellar occultation occurs when a star is tracked through the atmosphere of a planet while a spacecraft is moving along its orbit. On board the spacecraft, an instrument is collecting a sequence of spectra of the stellar light partially absorbed by the atmospheric species while the star is rising or setting behind the planet (Figure 3.1A). It is an efficient way to study the vertical distribution of atmospheric absorbers such as gas molecules or aerosol particles. Venus has a very dense atmosphere and very opaque clouds. This makes the method of stellar occultation usable only for studying the atmosphere above them. Occultations can probe up to an altitude where absorption features in the spectrum are overwhelmed by signal noise (Figure 3.2). The line of sight (LOS) of the instrument gradually crosses layers of the atmosphere, sensing atmospheric gases with a varying density. Absorption by the upper haze particles is what eventually limits the depth of sounding. As a result, the UV stellar occultation technique is only effective in the upper mesosphere and the lower thermosphere. SPICAV starts to be sensitive above 83-85 km (pressure ~1 mbar) up to 145 km (pressure ~10-6 mbar) (Bertaux et al., 2007a) and allows one to study the vertical structure of the planet's night-time atmosphere. On the dayside the scattered solar light does not allow one to observe weaker sources like stars. It should be noted that at the considered altitudes, atmospheric refraction can be neglected due to the low gas concentrations.

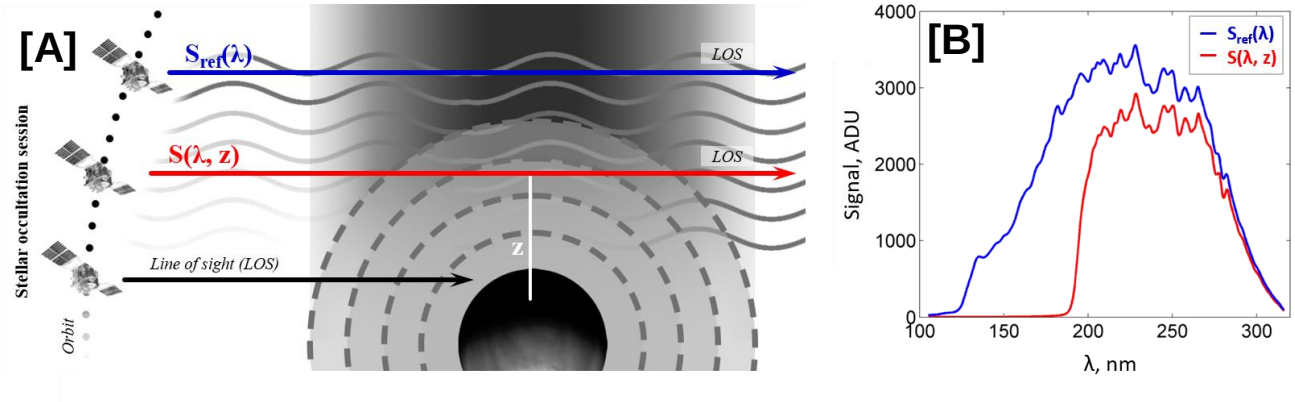

Figure 3.1. (A) A sketch of the stellar occultation technique. The arrows show the LOS of the spectrometer pointing to the star. The occultation session begins above the planet's atmosphere (blue arrow), then the star is tracked through the atmosphere (red arrow), and the session ends when the stellar light is completely absorbed by the atmosphere (black arrow). (B) Two spectra of a star obtained by SPICAV in one occultation session. The blue curve corresponds to the reference spectrum of the star measured above the atmosphere ($S_{ref}(\lambda)$), the red one - the stellar spectrum of the star's radiation attenuated by atmospheric absorption and scattering ($S(\lambda, z)$).

In space, the occultation method was originally used to scan ozone in the Earth's atmosphere on board satellites OAO-2 (The second Orbiting Astronomical Observatory) (Hays et al., 1972) and Copernicus (OAO-3) (Atreya et al., 1976). In the 90-170 nm range, UV spectrometers on Voyager-1 and Voyager-2 conducted studies of the vertical distribution of hydrogen and methane in the atmosphere of Jupiter and then Saturn, Uranus, and their satellites (Broadfoot et al., 1977). Then, a predecessor of the Venusian

spectrometer SPICAV, SPICAM, has successfully observed stellar occultations in the UV from orbit around Mars for more than ten years (Montmessin et al., 2017). On Venus, the stellar occultation method was first implemented by SPICAV on board Venus Express.

Theoretically, the attenuation of light due to atmospheric absorption at an altitude height (z) of the target point is described by the Beer-Lambert law. The altitude of the target point is the minimum distance between the LOS and the planet's surface.

$$T(\lambda, z) = \frac{S(\lambda, z)}{S_{ref}(\lambda)} = \mathrm{e}^{-\tau(\lambda, z)} \tag{2.1}$$

Where λ is the wavelength in nm, z is the altitude of the target point, $\tau(\lambda, z)$ is the optical depth, $S(\lambda, z)$ is the spectrum of starlight partially absorbed and scattered by atmospheric gases and aerosols, $S_{ref}(\lambda)$ is a «clear» or «reference» spectrum of the star meaning the one undistorted by absorption (Figure 3.1B), $T(\lambda, z)$ – transmission spectrum of the atmosphere.

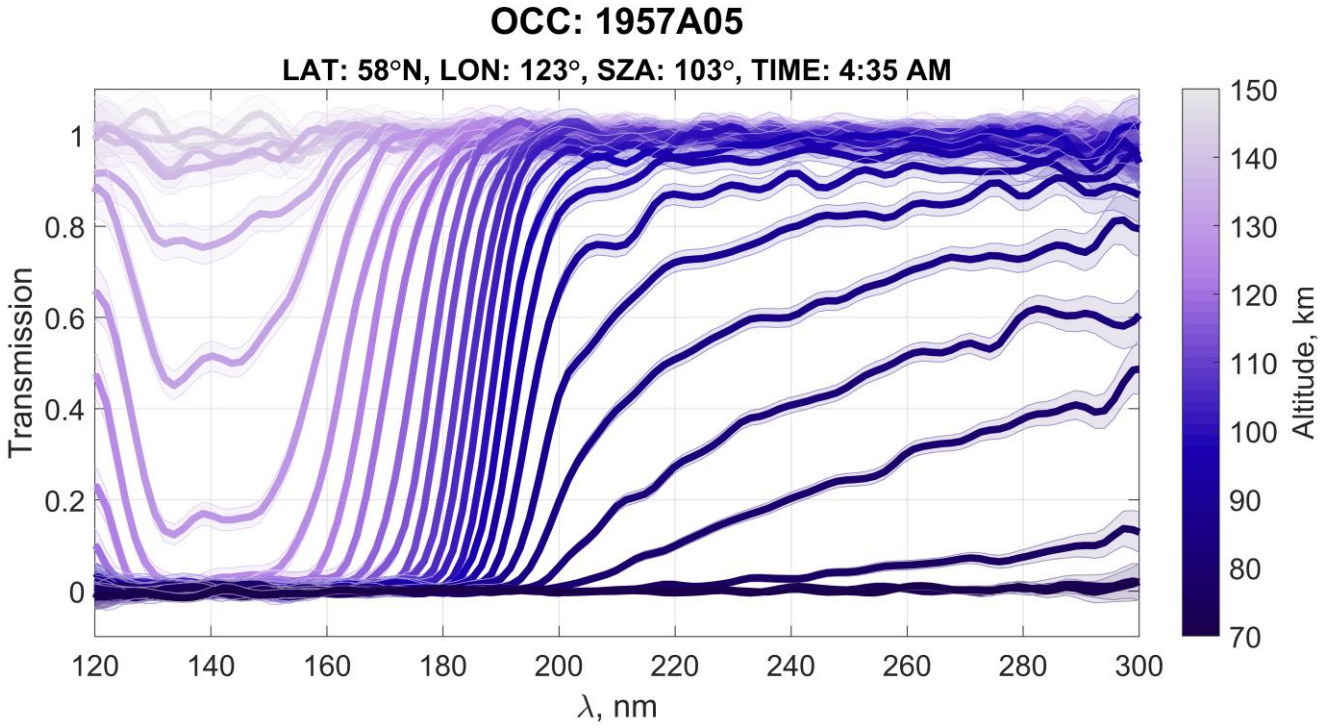

Figure 3.2. Altitude dependence of the atmospheric transmission in the stellar occultation session #1957A05 performed on August 30, 2011. Spectra are smoothed by a moving average encompassing 11 spectral points (~16 nm) and are presented with measurement error bars.

Equation 2.1 indicates that atmospheric transmission $T(\lambda, z)$ is determined by the LOS optical depth, which includes both the absorption and scattering occurring in the atmosphere. These processes are determined by the integral of the amount of gas and aerosol attenuation along the LOS. For this reason, the optical depth only has two components related to gas molecules and aerosols:

$$\tau(\lambda, z) = \tau_{gas}(\lambda, z) + \tau_{Rayleigh}(\lambda, z) + \tau_{aer}(\lambda, z) \tag{2.2}$$

where $\tau_{gas}(\lambda, z)$ is the optical depth for the gas component, the Rayleigh scattering is taken into account by $\tau_{Rayleigh}(\lambda, z)$, $\tau_{aer}(\lambda, z)$ is the optical depth for the aerosol component.

The optical depth of gases is a superimposition of the absorption by each gas. In the UV range, the absorption cross-sections of various types of molecules are weakly dependent on temperature and pressure, which makes it possible to express the optical depth of gas absorption in terms of the integral amount of gases along the LOS, such that:

$$\tau_{gas}(\lambda, z) = \sum_{G} \sigma_G(\lambda) N_G(z) \tag{2.3}$$

where σ_G is the gas absorption cross-section G (cm^2), and N_G is a slant concentration of the same gas (cm^{-2}).

The optical depth of Rayleigh scattering is equal to the scattering cross-section ($\sigma_{Rayleigh}$) multiplied by the average slant concentration of the atmosphere at height z (N_{atm}). On Venus, carbon dioxide constitutes 96.5% of atmospheric gases, so in the case of Rayleigh scattering the optical depth is:

$$\tau_{Rayleigh}(\lambda, z) = \sigma_{Rayleigh}(\lambda) N_{atm}(z) = \sigma_{Rayleigh}(\lambda) N_{CO2}(z) \tag{2.4}$$

Aerosol absorption becomes significant at altitudes below 100 km. In the 150-300 nm range, the absorption by aerosols slowly decreases with increasing wavelength, and it can be described by an empirical power-law dependence, which was approximated by the so-called «α-model»:

$$\tau_{aer}(\lambda, z) = \tau_{ref} \left(\frac{\lambda_{ref}}{\lambda} \right)^{\alpha} \tag{2.5}$$

where the exponent α is the Ångström coefficient, which is empirically related to the size of the H_2SO_4 aerosol particles for scattering approximated by the Mie theory (Montmessin et al., 2006; Wilquet et al., 2009; Belyaev, Evdokimova et al., 2017), λ is the wavelength in nm, and λ_{ref} = 235 nm is the wavelength chosen at the minimum of gas absorption (see Section 3.2.1 and Figure 3.3), against which the aerosol absorption is calculated. When studying the absorption by aerosol particles of the Martian atmosphere, an equivalence was shown between this α-model in the range of 150-300 nm and the Mie theory (Montmessin et al., 2006; Määttänen et al., 2013).

3.2. Calibrations and stray light correction in the raw data.

3.2.1. Studied trace gases

The spectral range of SPICAV (118-320 nm) covers absorption bands of several types of molecules contained in the Venusian atmosphere. At wavelengths shorter than 200 nm, absorption by carbon dioxide (CO_2) dominates. Longward of 200 nm, there are absorption bands of several minor species: sulphur dioxide (SO_2) and monoxide (SO), and ozone (O_3). SO_2 absorbs between 180 and 220 nm and between 250 and 290 nm. The SO band coincides with the 180-220 nm absorption band of SO_2. O_3 absorbs between 220 and 280 nm, corresponding to the Hartley band. As it is indicated previously, Rayleigh scattering is also accounted for as an additional component of the CO_2 cross-sections. A compilation of all the cross-sections considered in the SPICAV UV range are shown in Figure 3.3.

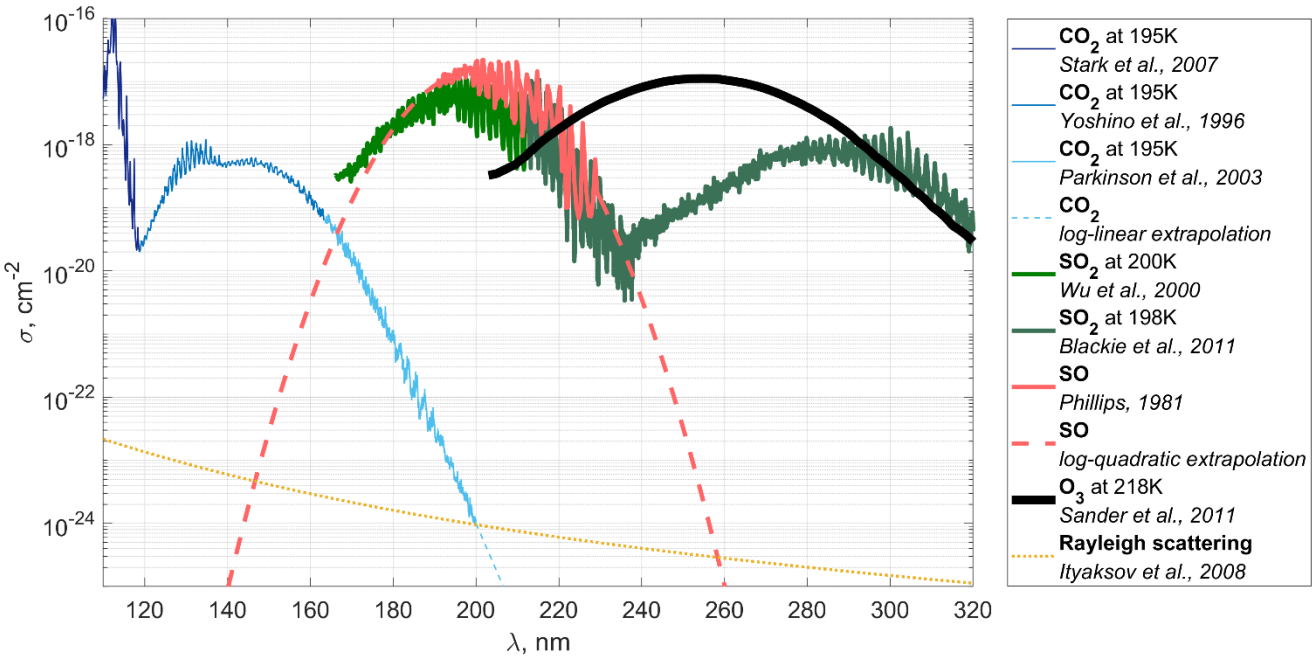

Figure 3.3. Review of the main gas absorption bands in the SPICAV UV spectral range. CO_2 cross-sections: Stark et al., 2007 (dark blue solid line), Yoshino et al., 1996 (blue solid line), Parkinson et al., 2003 (light blue solid line). The light blue dashed line shows the linear-logarithmic extrapolation of the CO_2 absorption cross-sections. SO_2: Blackie et al., 2011 (green solid line), Wu et al., 2000 (dark green solid line). SO: Marcq et al., 2020 (pink solid line). The pink dashed line shows the SO absorption cross-sections extrapolated by the parabolic-logarithmic law. O_3: Sander et al., 2011 (black solid line). Rayleigh scattering (yellow small dotted line) is based on Ityaksov et al., 2008.

Table 3.1. Absorption bands of various molecules observed by SPICAV UV.

Registered gases	**Absorption band**	**Typical altitudes of detection**
CO_2	118-200 pm	85-145 km
SO_2	180-220 nm 250-290 nm	85-105 km
SO	180-220 nm	85-105 km
O_3	220-280 nm	85-110 km

Environmental conditions in the upper mesosphere on the night side are characterized by temperatures of 120-200 K and pressures of 10^{-4} to 1 mbar. Absorption cross-sections data for the molecules in SPICAV spectral range is limited to temperatures above 195 K. Thus temperature variations in the upper mesosphere are not considered in our analysis.

The influence of Rayleigh scattering in a CO_2 atmosphere cannot be neglected on Venus in the SPICAV UV range. Its effect was computed based on Ityaksov et al. (2008). A value of the scattering cross-section is small in comparison with maxima of gaseous absorption cross-sections, and it is negligible while the CO_2 absorption band is not saturated. Below 110 km the atmospheric density becomes significant enough to observe the CO_2 absorption at wavelengths longer than 190 nm (Figure 3.2). In

this spectral range the Raleigh scattering and CO_2 cross-sections are comparable, so the scattering mainly contributes to the atmospheric transmission below 110 km.

SO_2 absorption cross-sections are combined from Wu et al. (2000) and from the high-resolution measurements of Blackie et al. (2011). There is a lack of databases for SO. For this reason, we use data from Marcq et al. (2020), which used the data of Phillips (1981) in the range of 190–230 nm. These values were extrapolated to the rest of the range by a parabolic dependence on a logarithmic scale (Marcq et al., 2019):

$$\log_{10}(\sigma[cm^{-2}]) = -\left(\frac{\lambda - 200.132\ nm}{20.961}\right)^2 - 16.780 \quad (2.6)$$

Unlike Marcq et al. (2020) we extrapolate the cross-sections in this way for the entire SPICAV range, without fixing the constant value in the long-wave part of the range.

Ozone absorption is based on Sander et al. (2011), where the cross-sections for O_3 in the 196–343 nm band were obtained at a temperature of 218 K.

3.2.2. UV Signal considerations with SPICAV

Venus Express orbited around Venus from 2006 to December 2014. During a stellar occultation the SPICAV FOV is pointed to the star. The vertical step in one observation session varies from 1 to 8 km, depending on viewing geometry. A typical occultation lasts 30 minutes, during which a reference stellar spectrum is collected based on the average of the stellar spectra collected above 200 km. Observations cover all latitudes of the night side from 18:00 to 06:00.

Typical SPICAV data, like the one used in this work, is a sequence of observations where each acquisition consists of five individual UV spectra (corresponding to the five bins mentioned earlier. A raw (so-called Level 0) spectrum is a 408-spectel vector on values in ADU, where only 384 spectels contain an actual signal. Level 1 data are obtained after removing pixel dark current, also known as DC, whose pattern across the detector was estimated from dedicated technological observations (see next paragraphs). Level 1 also includes a correction for readout systematic, and cosmic ray outbreaks that contaminate nearby pixels. Also, to minimize bias in weak signals, pixel readout includes a fixed offset that is accounted for as well as other instrument artefacts.

The CCD of the SPICAV UV channel is characterized by an average DC of about 10-20 ADU per second while pixel dynamics is limited to 4095 ADU (12-bit conversion). DC increases with temperature at a rate specific to each pixel. However, this non-uniformity pattern of the DC is stable and has been monitored throughout the mission. Special observation sessions carried out at HT = 0, preventing any photo-event to reach the CCD, allowed one to collect only the dark signal (sum of DC and offset). Then, a DC non-uniformity (DCNU) model for the entire detector could be inferred by fitting the recorded dark signal with a linear law, such as:

$$DCNU_{ij} = S_{dark\,i} \cdot a_{ij} + b_{ij} \quad (2.7)$$

Where $DCNU_{ij}$ is the sum of dark and offset signals in a pixel of coordinates i (row) and j (column), $S_{dark\,i}$ is the signal collected by the masked pixels at the edge on the same row of the detector, and (a,b) are the linear coefficients established for each pixel during the technological observation at HT=0.

A weak (~6 ADU) readout systematic with a 14-pixel period affects the spectra, especially for very low signals. The line-by-line readout of the SPICAV CCD generates a correlated variation in the phase of the periodic readout pattern. Several techniques have been developed to correct for this readout systematic by the engineering team that are based on identifying the phase and amplitude of this spurious periodic signal that can be then removed from spectra and permit a better exploitation of low-signal spectra.

Also, the recorded signal was sometimes distorted by cosmic rays hitting the detectors, creating temporarily «warm» pixels easily discernible from the rest of the detector as they usually constitute an isolated event affecting only the adjacent pixels. It is to be noted that with the branding strategy used to cope with the telemetry constraints, such an event is smoothed out by the line binning, yet remains an identifiable feature that is easy to spot and correct.

The influence of the spectrometer PSF and the detector flat field on the spectra was not corrected in the Level 1 data used to create transmittance. Flat field has no impact in the context of spectra created by the ratio of two signals, like the transmittance. The PSF consideration was sequentially handled in the forward model used to fit the collected transmittances.

With regard to the ancillary information, Level 0 data carry a set of geometrical parameters at the tangential point, which is defined as the point along the LOS closest to the surface, computed at the centre of each bin of the detector, that is for 5 different points along the slit. This information is dependent on how well we know the pointing of the instrument A great advantage of stellar occultation is that the observation geometry can be accurately determined without knowing the exact pointing of the main axis of the instrument. Indeed, one has to only consider the optical path between the target star, whose celestial coordinates are known with outstanding precision, and the body of the spacecraft whose position around Venus is given by the Venus Express ephemerides which is likewise extremely well constrained. This is this information that we retain for our retrievals and in particular to produce altitude-dependent concentrations of gases and aerosols.

3.2.3. Estimation of errors in atmospheric transmission spectra.

The SPICAV UV channel detector is characterized by linear charge coupling, therefore, for the signal-to-noise ratio (SNR), this is the formula

$$SNR = \frac{S}{\sigma} = \frac{S^{SPICAV} G}{\sqrt{(S^{SPICAV} G + (S^{DC} + S^{OFF})/g + \sigma_{SE}^2)}} \qquad (2.8)$$

where S^{SPICAV} is the number of ADU corresponding to the detected UV radiation, S^{DC} and S^{OFF} are the signals from the dark current and the offset current, and $\sigma_{S^E}^2$ is the variation for electronic noise. By

multiplying the signal by the gain *G* of the detector which is set by the digital equivalent of HT, the number of photons entering the detector is calculated. To estimate the error of the dark current, the signal is multiplied by *g*, since dark current electrons are subject to Poisson statistics. The *g* coefficient was determined from a set of purely stellar observations.

The standard measured signal corresponds on average to a level of 2000 ADU signal. DC is on average 20/400 ADU when the Peltier cooler is on/off, and the amplitude of readout systematic was estimated around 6 ADU. The gain *g* changes from 0.3 to 12 ADU/photo-event. The estimation of the average signal-to-noise ratio (SNR) gives a value of 50. According to this formula, each pixel can be assigned a corresponding 1-σ uncertainty, which includes all the known sources of noise affecting the measurement.

3.2.4. Sources of an additional emission registered by the UV channel of SPICAV

The SPICAV spectral range is sensitive not only to the stellar radiation. Its range of 118-320 nm allows observing several types of UV radiation coming from various sources such as atmospheric nitric oxide (S^{NO}) emission, the Lyman-α hydrogen line at 121.6 nm ($S^{Ly\text{-}\alpha}$), and the scattered light from the Sun (S^{SUN}). Thus, the measured signal (S^{SPICAV}) is the addition of several signals, where all the aforementioned emissions are considered as «stray» light (S^{STRL}) since contaminating the signal of interest, that of the star (Equation 2.9).

$$S^{SPICAV} = S^{STAR} + (S^{NO} + S^{Ly-\alpha} + S^{SUN}) = S^{STAR} + (S^{STRL}) \quad (2.9)$$

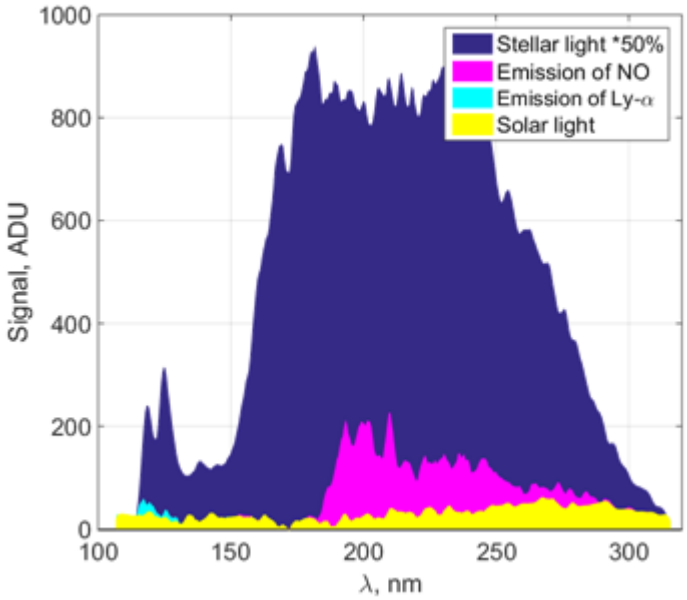

Figure 3.4. Several components of the signal obtained in the occultation session #2721A05: (1) the spectrum of a star (purple) with atmospheric absorption lines at 98 km whose intensity is divided by two to better visualize the signal from other weaker UV radiation source, (2) the NO (pink), (3) Lyman-α (cyan), (4) the Sun scattered light (yellow). The NO emission obtained in 90-110 km, the Lyman-α and solar spectra are averaged over 200 km. More detailes of the the Lyman-α and solar signal extraction can be found in Annex 5, for more detailes of the nitric oxide emission extraction see Section 3.2.9.

This «stray» light component depends on the observation geometry and on the FOV size determined by the presence or absence of the slit. While the spectrum of a star, which is a point source, does not change

due to the presence of a slit, the spectral resolution and shape of the spectrum of extended sources emission is convolved by the angular aperture and is therefore slit-width dependent. Also, the light of the star is almost completely collected in the central bin and in the corresponding spectrum, and the PSF scatters just a few percent of it into the other 4 bins. In the absence of the slit, which is the most recurrent configuration of the stellar occultation mode, the radiation of extended sources is integrated over the entire field of view of the spectrometer, and can be thus a major contamination for the target star.

3.2.4.1. Lyman-α emission

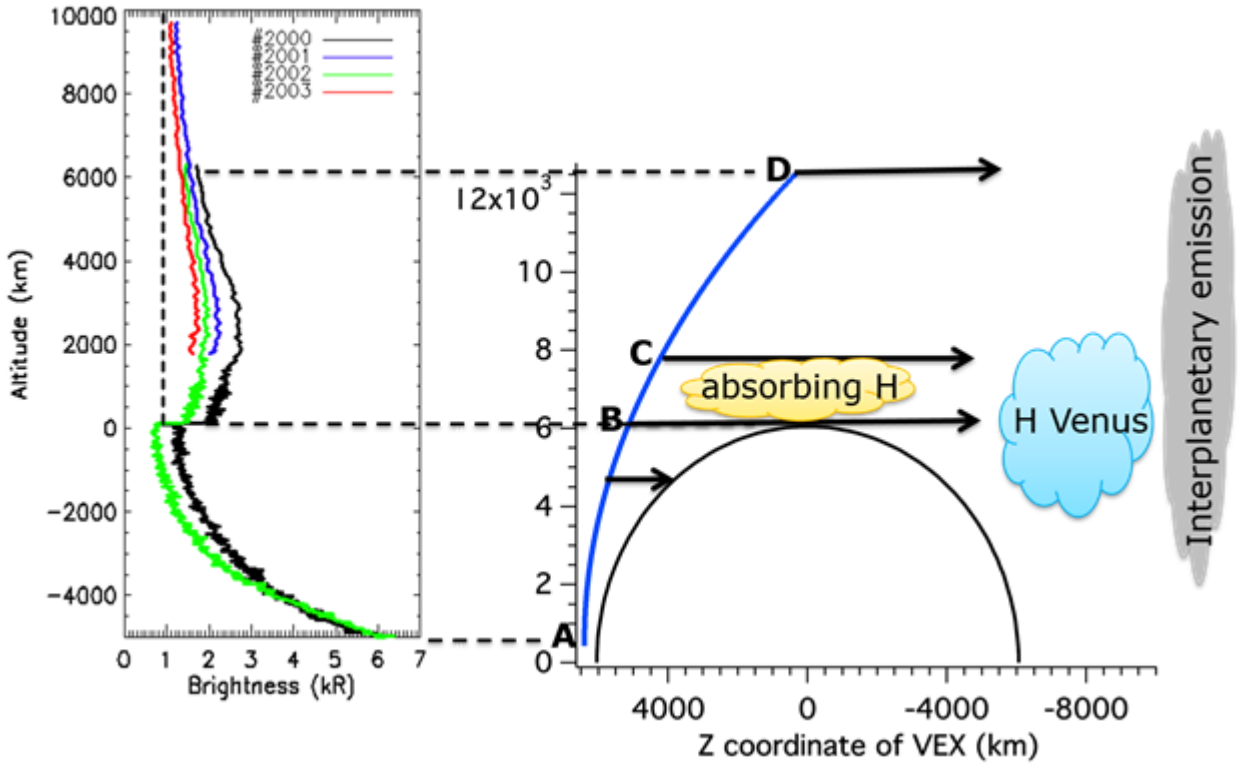

Figure 3.5. Observations of the night hydrogen corona on Venus from the limb scans by the UV channel of the SPICAV Venus Express spectrometer for observations #2000, #2001, #2002, #2003. The result is taken from the work of J.-Y. Chaufray et al. (2015).

Lyman-α emission is the result of the resonant scattering of sunlight by hydrogen atoms present in the planet's exosphere and interplanetary space. The emission serves as a source of information about the hydrogen content in the exosphere of planets and about its temperature. The first Venusian Lyman-α emission was studied during a flyby of the Venera-4 and Mariner-5 spacecraft (Barth et al., 1967; Kurt et al., 1968). SPICAV UV observations showed that the intensity of the Lyman-α line changes with decreasing altitude and increasing atmospheric density (Chaufray et al., 2015), as well as depending on the geometry of observations. The registered glow is a superposition of radiation scattered by atoms of interplanetary and Venusian hydrogen. Also, when moving into deeper atmosphere layers (below 2000 km), the altitude dependence of emission begins to show absorption by cold H atoms, which reduces the intensity of Lyman-α (Figure 3.5).

In general, Lyman-α is a weak emission that only matters when observing faint stars, for which high signal amplification (HT equal or greater than 100) is employed.

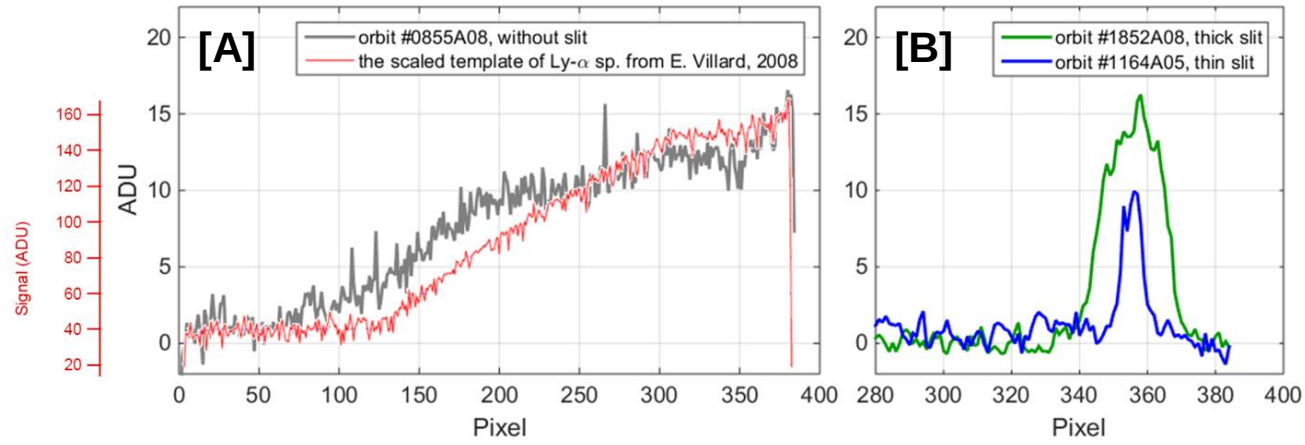

Figure 3.6. Spectra of Lyman-α emission on the night side of Venus for various observation conditions: (A) without a slit (grey solid line), (B) using the wide part of the slit (green solid line) and with its narrow part (pink solid line). The spectrum in red (A) is the scaled Lyman-α spectrum measured at the orbit in a dedicated technological observation (Villard, 2008).

The spectrum of the Lyman-α line has a trapezoidal shape, whose spectral width depends on the width of the slit. It can illuminate a large portion of the spectral range when the slit is absent. Figure 3.6 shows examples of Lyman-α spectra for observations without slit, as well as observations using its wide and narrow parts. Figure 3.6 shows that the Lyman-α line is better distinguished when observing with the slit, being otherwise a feature-less inflation of the continuum over ~200 pixels.

3.2.4.2. Airglow of nitric oxide

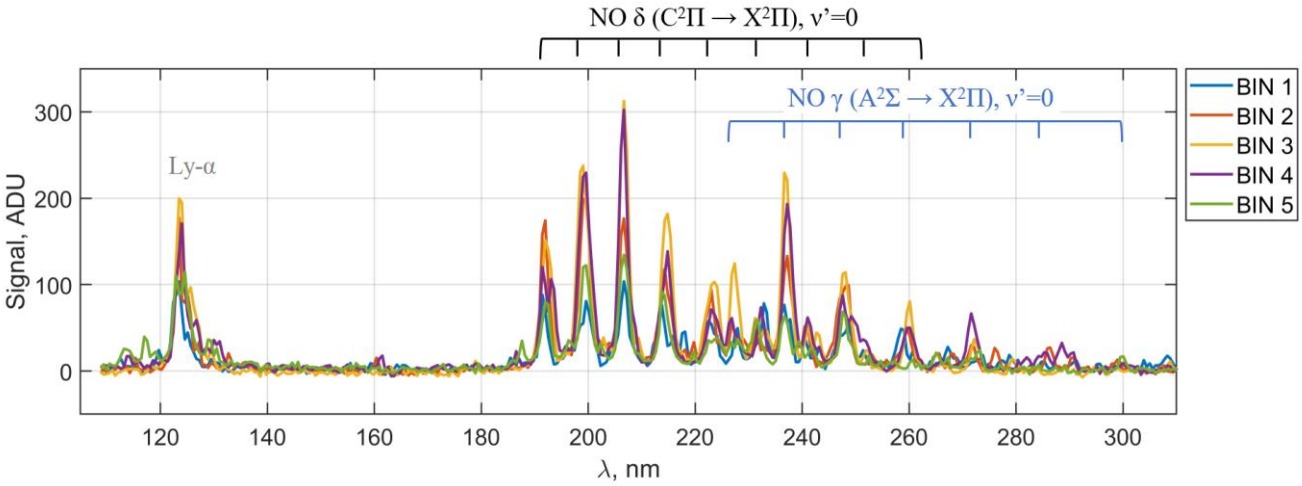

Figure 3.7. An example of the emission spectrum of nitric oxide (190-270 nm) and the Lyman-α line (121.6 nm) measured by SPICAV UV using a narrow part of the slit (orbit # 0516A11, observation of the limb).

SPICAV UV covers a range that includes the δ- and γ- emission bands of nitric oxide NO (190-240 and 225-270 nm respectively). This radiation on Venus was first detected by the Mariner-5 orbiter (Feldman et al., 1979). This is the most intense airglow recorded during stellar occultations; it dominates the stray

light component of most stars observed in the night. Its distribution in the atmosphere of Venus is horizontally non-uniform and its vertical distribution is characterized by a Chapman-like peak observed around 115 km. Without the slit, the CCD can be overwhelmed by the NO emission signal especially at the lowest accessible altitude where the stellar signal becomes fainter (Royer et al., 2010).

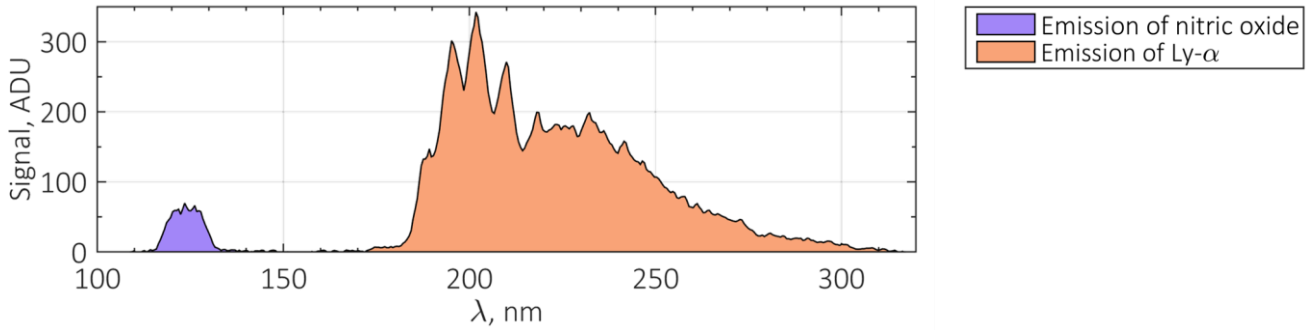

Figure 3.8. Example of emission spectra of nitric oxide and Lyman-α emission measured using the wide part of the slit (observation #2778A03, stellar occultation).

The NO night glow is the result of global atmospheric circulation. The products of dissociation of CO_2, CO, and N_2 molecules are oxygen and nitrogen atoms which are transferred from the day side where they are produced to the night side due to the solar-to-antisolar (SSAS) circulation. In the night side, atoms recombine at altitudes of ~115 km. Thus, by observing the airglow of NO, one can track the circulation processes of the atmosphere at altitudes of 100-120 km. The monitoring of NO night glow performed by SPICAV from 2006 to 2011 in a nadir observing mode revealed that the maximum brightness is shifted from the anti-solar point towards the morning terminator and the South Pole. The emission is brighter in the area from 1:00 to 3:00 hours and 10°N up to 25°S (Stiepen et al., 2013). The vertical distribution of the airglow intensity has a maximum at the altitude of ~115 km (Royer et al., 2010; Royer et al., 2016).

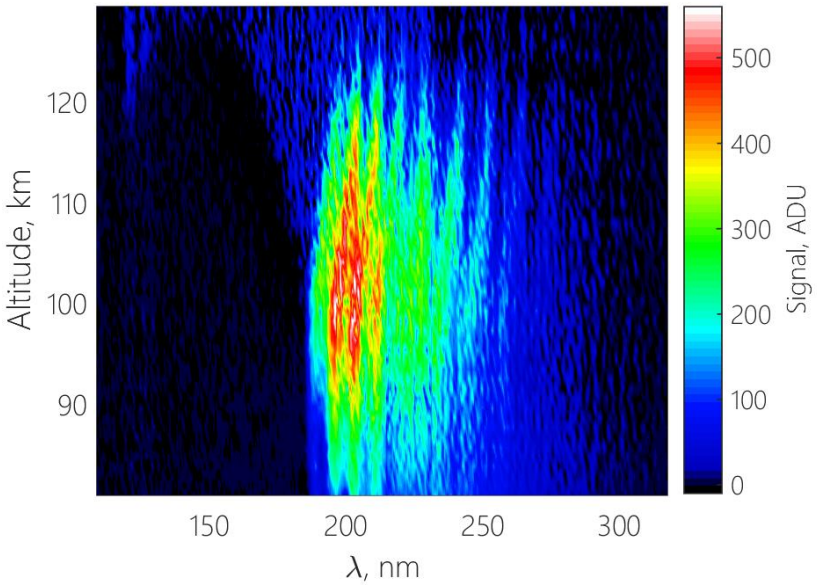

Figure 3.9. NO tracking plotted as a function of altitude and wavelength, as extracted from measurements during observation #2738A06.

3.2.4.3. Solar radiance in the stellar occultation spectra

The Sun in the UV range can be detected in a stellar occultation performed at a low phase angle, when light is reflected from a Venus crescent close to the field of view. The solar illumination was recorded even when using a slit narrowing the spectrometer field of view.

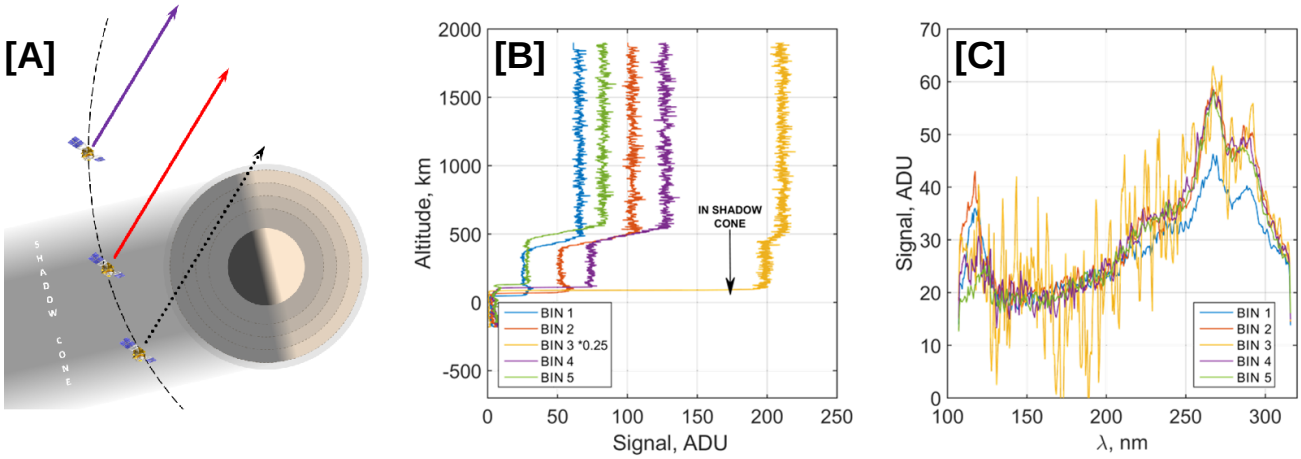

Figure 3.10. (A) The orientation of the spacecraft when crossing the shadow cone. (B) Change with height of the average signal in the wavelength range of 250-300 nm in the occultation session #2721A05. The observation session was performed using the slit (gain HT = 160, n = 8 lines/bin covering rows from 185 to 225 on the CCD, with a solar zenith angle of 136.4°). It is shown how the signal changes when the spacecraft crosses the planet's shadow. (C) View of the solar spectrum, when separated from that of the star. The intensity of the blue spectrum corresponding to the first bin is lower since a part of the narrow slit is partially captured. More detailes of the the Lyman-α and solar signal extraction can be found in Annex 5.

3.2.5. Wavelength-to-pixel registration

To extract information on gas absorption from the measured spectra, it is necessary to perform a number of calibrations. First, raw data remains in analogue to digital units (ADU) and has no spectral registration. During the SPICAV UV ground-based calibrations, a parabolic law was determined describing the dependence of the wavelength (λ) on the pixel or spectel number (N_{pix}), presented in Equation 2.10 (Villard, 2008). Under flight conditions, this dependence may shift by some value of $\Delta\lambda$, which had to be retrieved for each observation session.

$$\lambda(N_{pix}, \Delta\lambda) = \Delta\lambda + 325.48 - 0.54596 \cdot (N_{pix} + 9) - 4.9096 \cdot 10^{-6} \cdot (N_{pix} + 9)^2 \qquad (2.10)$$

To solve this problem, each spectrum of a star measured above the dense layers of the atmosphere, i.e. unaffected by absorption, was aligned with our catalogue of UV stellar spectra, that is the International UV Explorer (IUE) dataset. The IUE operated at the near-Earth orbit in 1978–1996 (Boggess et al., 1978) and its channels covered wavelengths from 115 to 320 nm, which corresponds to the SPICAV UV range. The instrument spectral resolution reached 0.02 nm. During one occultation from tens to hundreds of spectra of stars were measured without distortion by atmospheric absorption depending on the duration of the session and the geometry of the observations. For each of these spectra, calibration is

carried out individually, then for the entire session, the average value of the shift $\Delta\lambda$ is found depending on $\lambda(N_{pix}, \Delta\lambda)$.

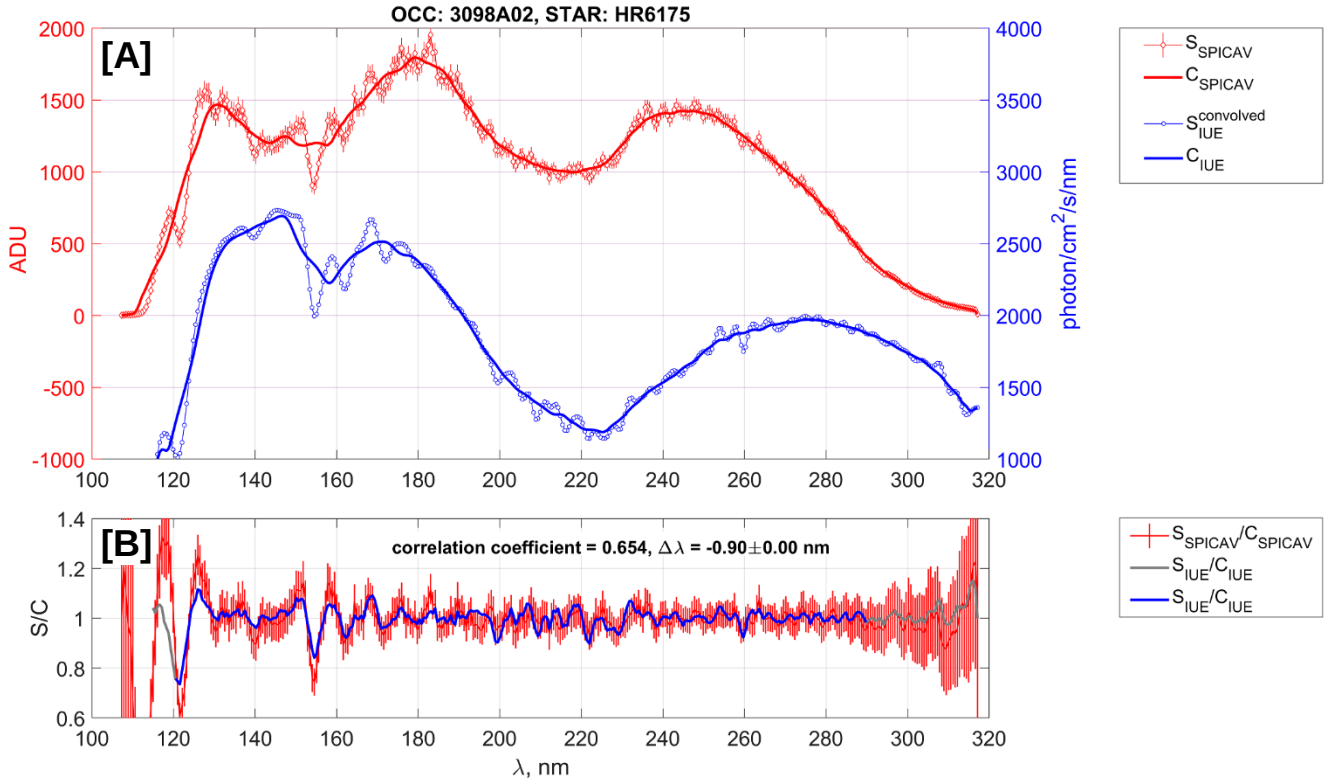

Figure 3.11. Wavelength-to-pixel numbers registration for occultation session #3098A02. The plots represent the alignment of the positions of the star lines. (A) SPICAV UV spectrum (S_{SPICAV}) and IUE spectrum converted to the SPICAV UV resolution ($S_{IUE}^{convolved}$). (B) Relative spectra obtained by SPICAV UV and IUE after co-aligning the stellar lines, which were calculated as the ratio between the original spectra and their smoothed curves. Pixels with a low signal level shown by a grey line continuing the IUE spectrum were excluded from the range where the analysis was carried out.

It was found that a robust way to determine $\Delta\lambda$ was to compare the observed SPICAV spectra with the IUE spectra, keeping only the fine spectral structure; i.e. spectral emission lines, excluding the influence of the continuum that is instrument dependent. The continuum for each experiment depends on the spectral sensitivity of the detector of each spectrometer, and an attempt to unify would increase the calibration error. Thus, the relative spectrum of the star was calculated from the ratio between the measured signal and its smoothed version using a simple moving average filter. The shapes of the SPICAV and IUE spectra and the corresponding continua are shown in Figure 3.11A, while the relative spectra are shown in Figure 3.11B. The smoothing interval was chosen empirically for the best selection of stellar lines, taking into account the current spectral resolution. It is equal to 21 spectral points of the SPICAV instrument, which corresponds to a spectral interval of ~11 nm. In the end, the function $\lambda(N_{pix})$ is determined with high precision: the resulting value of the $\Delta\lambda$-shift has an error of 1-10% of the width of one pixel. In addition, it was shown that there is no time evolution of the $\Delta\lambda$- shift.

3.2.6. Spectral inversion

The initial dataset for retrieving the slant concentrations of each gas is the atmospheric transmission spectra, which are the ratio between signals from the star partially absorbed in the atmosphere and the undistorted reference stellar spectrum obtained in the same observation session (Equation 2.1). For each atmospheric transmission spectrum an inverse problem called spectral inversion must be solved (Quemerais et al., 2006).

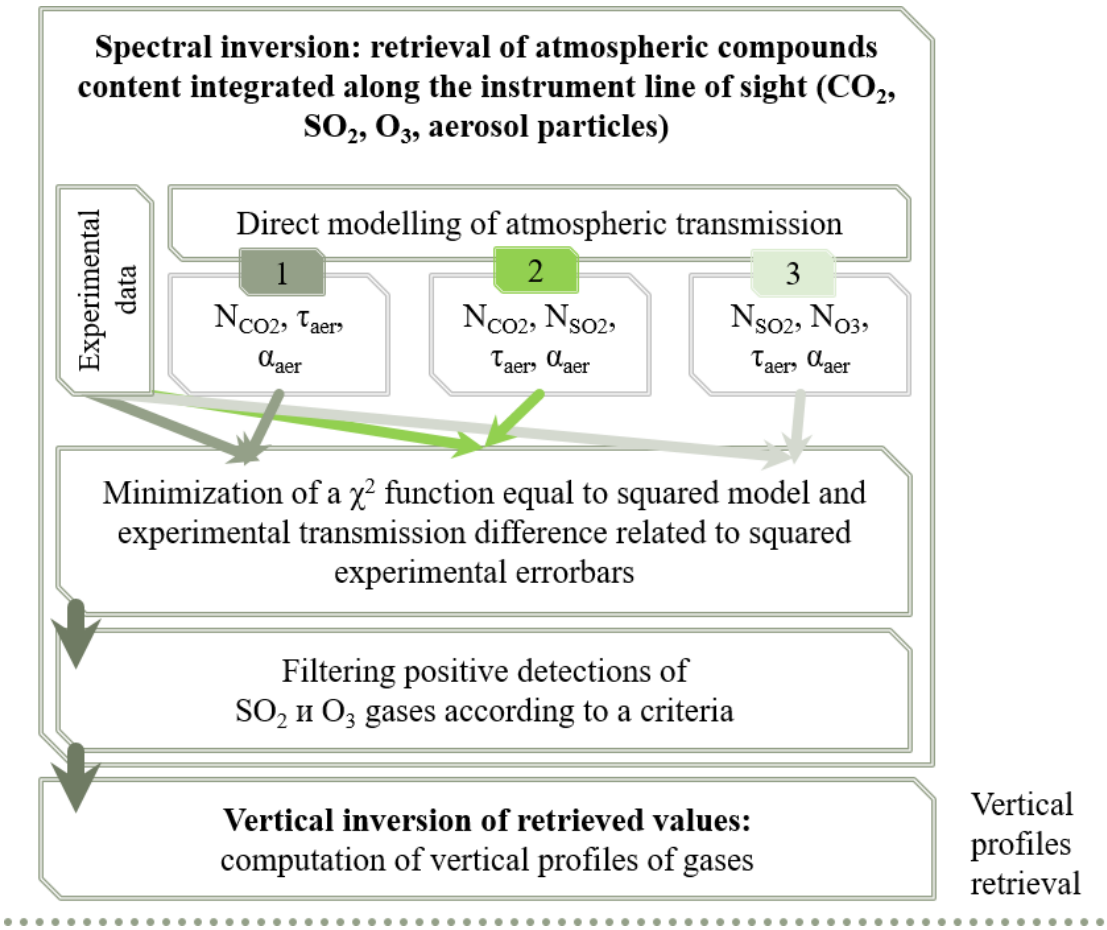

Figure 3.12. General scheme of data processing steps to retrieve the content of atmospheric components from transmission spectra.

The atmospheric gas absorption model is determined by the values of the slant density of gases absorbing along the LOS of the device: CO_2, SO_2, SO and O_3. However, the resolution of the SPICAV UV device is not enough to distinguish the SO_2 and SO absorption lines separately. Therefore, the parameters N_{CO2}, N_{SO2} and N_{O3} were set for the gas absorption model, and the density of sulphur monoxide N_{SO} was fixed equal to 1/50 of N_{SO2} according to night-time observations of the ground-based JCMT telescope (Sandor et al., 2010). Also, N_{CO2} specified the Rayleigh scattering prevailing at altitudes below 100 km.

The aerosol absorption model was determined by the τ_{ref} coefficients and the Ångström coefficient α according to Equation 2.5.

Thus, the atmospheric transmission model at height z, $T_{mod}(\lambda, z)$, is determined by five free independent parameters. By varying these parameters, the optimization problem of the model to the current experimental spectrum is solved. To this purpose, the Levenberg-Marquardt algorithm is used to find a

minimum of the reduced χ^2 function. The latter is normalized by the number of free parameters (number of independent spectral points minus the number of retrieved parameters).

$$\chi^2\left(N_{CO2}, N_{SO2}, N_{O3}, \tau_{ref}, \alpha\right) = \sum \left[\frac{\left(T_{exp}(\lambda_i) - T_{mod}\left(\lambda_i, N_{CO2}, N_{SO2}, N_{O3}, \tau_{ref}, \alpha\right)\right)}{\delta_{exp}(\lambda_i)} \right]^2 / N_{free} \quad (2.11)$$

N_{free} – number of free parameters, $\delta_{exp}(\lambda_i)$ – experimental transmission uncertainty $T_{exp}(\lambda_i)$.

SPICAV PSF effect weighted by the flat field are needed to compute the model transmittance T_{mod} that is calculated as follows ([BIN] - consideration of the summing of signal within one bin)

$$T_{mod}\left(N_{CO2}, N_{SO2}, N_{O3}, \tau_{ref}, \alpha\right) = \frac{[BIN][FF][PSF]\left(T_{theor}\left(N_{CO2}, N_{SO2}, N_{O3}, \tau_{ref}, \alpha\right) \cdot S_{ref}\right)}{S_{ref}} \quad (2.12)$$

where T_{theory} is described by Equation 2.2.

Optimization of the Equation 2.12 is performed by the Levenberg-Marquardt algorithm. It also allows to estimate a converge parameters covariance as a reverse Hessian matrix (H) equal to

$$diag(\sigma^2) = C = [H]^{-1} = (J^T J)^{-1} \quad (2.13)$$

where J is a Jacobian of the χ-function (Press et al., 2007). The standard errors of estimating parameters of the atmospheric absorption and scattering are the diagonal elements of the covariance C.

3.2.6.1. Cases of positive gas detection

It has been found that the densities of minor gases such as sulphur dioxide and ozone are subject to brutal changes, and sometimes their concentrations are below the detection limit. The detection limit is directly related to the error of experimental data which varies with observing sessions and which mostly depends on the brightness of the observed star. However, the determination of a reliable detection limit is a needed task for characterizing the atmospheric composition in the various layers probed by the instrument. The general scheme for retrieving gas abundances from the atmospheric transmission spectra is shown in Figure 3.12.

First, it is necessary to establish a criterion for detecting small gas components. The spectral inversion problem is solved in three successive steps with every step adding a new species whose influence on the fit can then be precisely monitored.

In the first step, only the slant density of CO_2 is fitted, while absorption by sulphur oxides and ozone is not taken into account. Simultaneously the aerosol opacity parameters τ_{ref} and α are also kept free.

In the second step, the slant density of SO_2 tied to that of SO is added to CO_2 and aerosols as free parameters, but ozone remains excluded from the fit.

In the last step, the O_3 absorption in the Hartley band is added to the algorithm. At the same time N_{CO2} is fixed to the value that provides the best fit for the first and second steps. This approach is justified, since there is no overlap between the absorption bands of O_3 and CO_2 at 150-300 nm, and it gives us the

opportunity to reduce the number of free parameters. The aerosol parameters at the third step were also retrieved.

For each step, a minimum value of the reduced χ^2 is obtained and stored. The resulting three values are compared with each other. Positive detection of any trace gas in the observed layer (i.e. in one spectrum) is established if χ^2 decreases significantly compared to the model in Step 1, which assumes only CO_2 and aerosol absorptions. A detection criterion was then established empirically:

$$\delta\chi^2 = \frac{\chi^2(SO_2\ or/and\ O_3, CO_2)}{\chi^2(CO_2)} < 0.95 \qquad (2.14)$$

An example of a positive identification of SO_2 absorption at an altitude of 87 km is shown in Figure 3.13A where the relative decrease in χ^2 is 0.74. Here, the best fit is reached when considering the residuals at wavelengths of SO_2 absorption bands (Figure 3.13B).

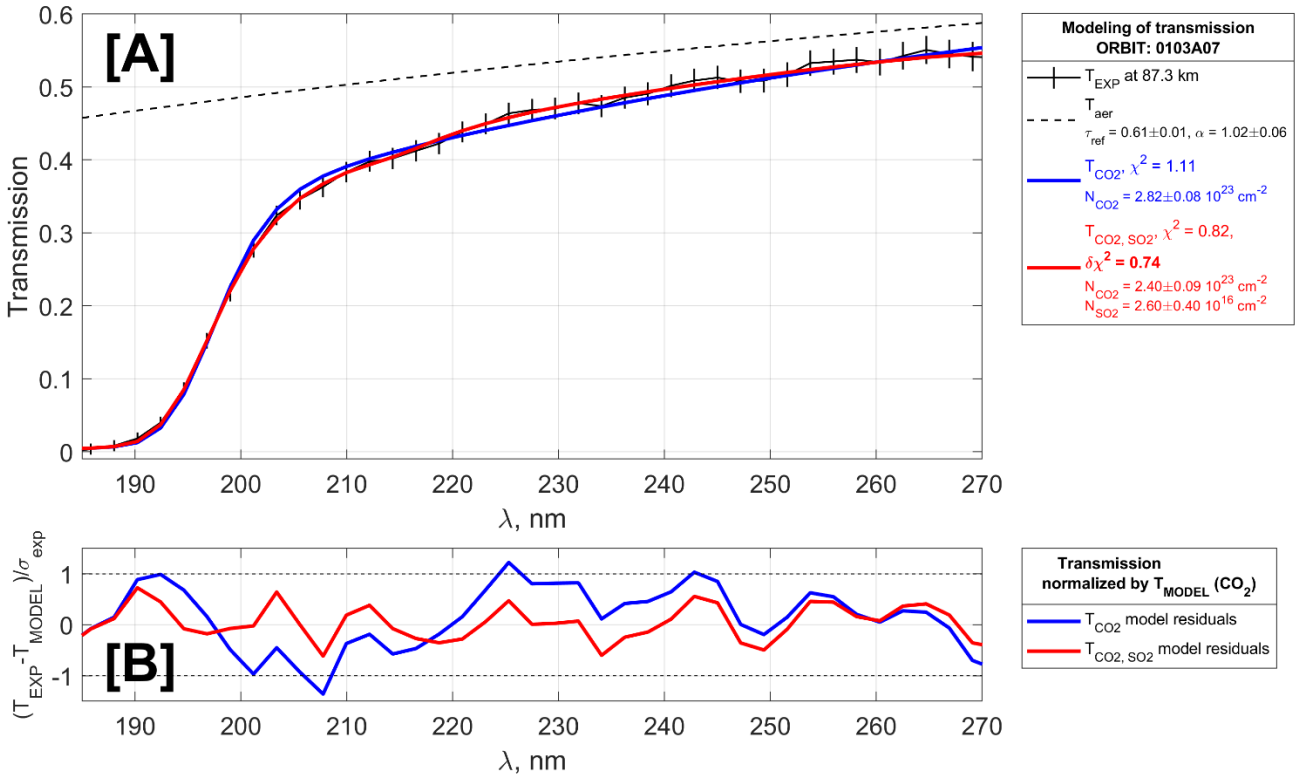

Figure 3.13. Example of positive detection of SO_2 absorption at the altitude of 87.3 km in the stellar occultation session #0103A07 (August 2, 2006; at latitude 3.9°S and longitude 241.9°; local time 23.37 hours). (A) Measured transmission spectrum T_{EXP} with corresponding error bars (black solid line); aerosol continuum T_{aer} (black dashed line), the model atmospheric transmission for carbon dioxide absorption T_{CO2} only (blue solid line) and for joint carbon dioxide and sulphur dioxide absorption $T_{CO2,SO2}$ (red solid line). The model spectra are convolved taking into account the spectrometer point spread function ([PSF]) and detector flat field ([FF]), see Equation 2.12. (B) Residuals of two different models related to experimental errors. The solid blue line corresponds to the CO_2 absorption model. The solid red line corresponds to a model that takes into account the atmospheric absorption of CO_2 and SO_2. Dotted black lines indicate the level of error bars.

Data processing algorithms used in previous and accompanying works of SPICAV UV (Montmessin et al., 2011, Marcq et al., 2019, 2020) use a similar strategy. However, criteria chosen to conclude on a

positive detection were different. In the paper of Montmessin et al. (2011) the firm detection of ozone in stellar occultations was concluded when the O_3 absorption band is very pronounced: $\delta\chi^2_{2011} \leq 0.5$ or *5-σ* significance. In the recent reanalysis of SPICAV UV nadir observations (Marcq et al., 2019, 2020) O_3 and SO_2 detections within the significance interval of *3σ* corresponded to $\delta\chi^2_{2019} \leq \frac{1}{5.5} \approx 0.18$. However, there is a difference in spectral filtration considered in those papers and in our work. In present analysis any high-pass filter is not used, in contrast to a moving-average filter with the 8-nm window in Montmessin et al. (2011) and a special selection of spectral points in Marcq et al. (2019, 2020). These techniques lead to an increase of χ^2 values meaning an underestimation of computed data errors, and to the decrease of $\delta\chi^2$. For example, $\delta\chi^2$ is 2 times lower if the moving-average filter with 8-nm window is applied to the spectrum presented in Figure 3.13A. As well, $\delta\chi^2_{2011} \leq 0.5$ is fulfilled when the current $\delta\chi^2$ is lower than 0.85. However, the SPICAV UV stellar occultation measurements are heterogeneous in terms of noise level, and it is difficult to choose one particular approach for smoothing outliers and noise fluctuations for the whole dataset. In order to unify the detection criterion, it was decided not to apply smoothing techniques to the resulting transmission spectra. In general, the resulting values of reduced χ^2 for any set of fitting parameters are in the range of 0.55-2.5. It means that an underestimation and overestimation of data errors are both possible, forcing conclusions based on $\delta\chi^2$ rather than χ^2. It was concluded that a 5% decrease of reduced χ^2 corresponds to the detection with a significance of *1σ*.

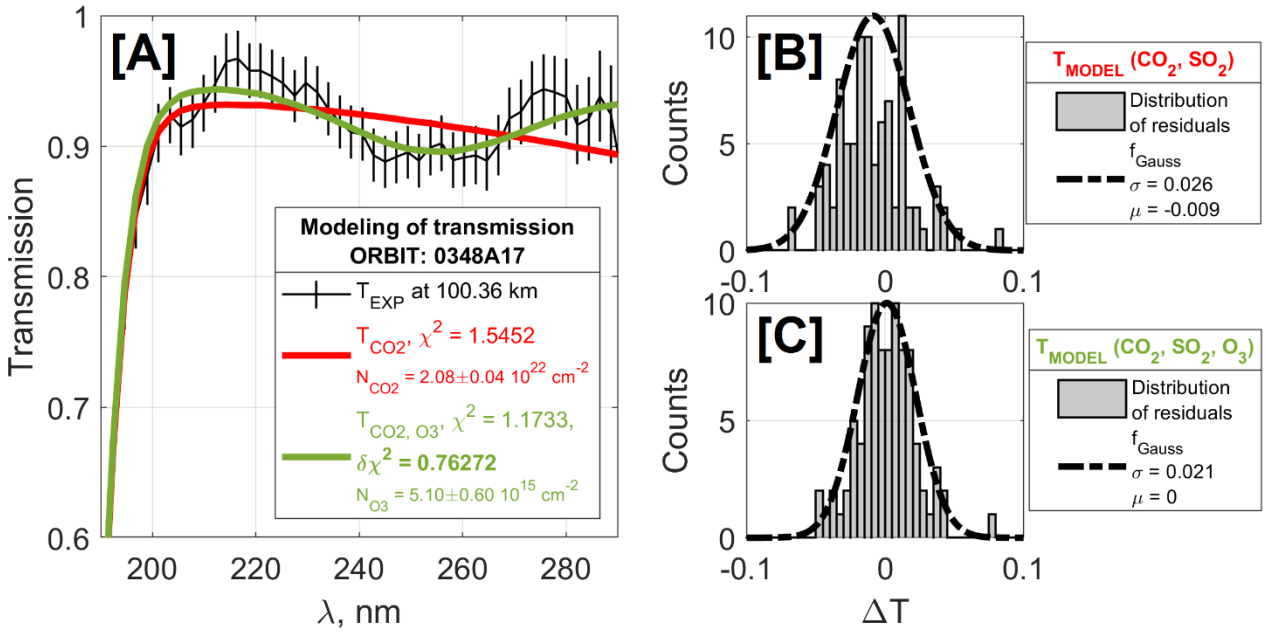

Figure 3.14. A case of positive O_3 detection at an altitude of 100.36 km in the stellar occultation session #0348A17, that is the same as reported in Montmessin et al., 2011 (April 4, 2007; at latitude 4.1°S and longitude 245.3°; local time 1.57 hours). (A) Measured transmission spectrum T_{EXP} with corresponding errors (black solid line); the model atmospheric transmission for carbon dioxide absorption T_{CO2} (red solid line) and $T_{CO2, O3}$ (green solid line). B and C: Residual distribution histograms for two models. (B) The residuals of the T_{CO2} model and the optimal normal distribution for the given histogram. (C) Residuals of the $T_{CO2,O3}$ model, and the optimal normal distribution for the given histogram.

Overall, SPICAV data have revealed that O_3 is far less abundant than SO_2 in the Venusian mesosphere. Moreover, data are more uncertain in the range of the Hartley band due to the overlapping emission band

of NO. To avoid false positive detections, the positive detection criterion for SO_2 needs to be narrowed. In addition to the χ^2 reduction, we have analysed a histogram representing the distribution of the transmission residuals within the Hartley absorption band. A proof of the goodness of fit is given when the Gaussian is symmetric about zero. If the histogram fulfils this requirement without considering O_3 absorption, we can conclude that O_3 is absent from the analysed spectrum. Conversely, an offset of the Gaussian maximum could potentially reveal an unaccounted absorption due to O_3. In that case, the final Gaussian distribution after adding O_3 to the retrieval was also checked against symmetry about zero. To filter out noisy spectra hiding a weak O_3 absorption, we considered only spectra when the standard deviation of residual histograms is lower than 0.05.

3.2.6.2. Upper detection limits for two gases.

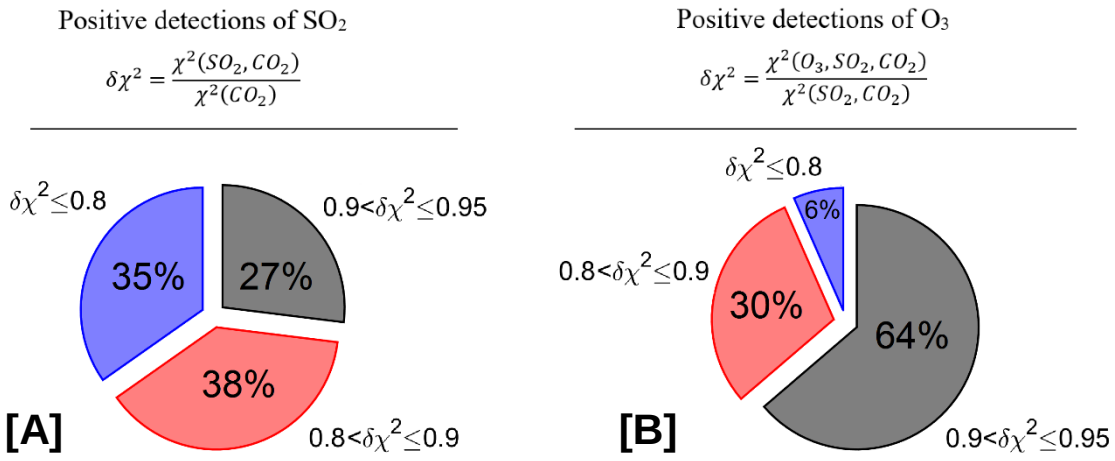

Figure 3.15. Statistics of the χ^2 value for SO_2 (A) and O_3 (B) detections.

Both SO_2 and O_3 appear highly variable in time yet some observations do not lead to a firm detection. A deeper analysis of the χ^2 function can help us to address the problem of estimating correctly a detection limit. It was mentioned above that the positive detections correspond to at least 5% reduction of χ^2 value after a certain trace gas has been added to the fit. In most cases a χ^2 reduction of >10% is observed for SO_2 (Figure 3.15A). The opposite proportion is obtained for the ozone retrievals (Figure 3.15B). It means that the experiment reaches a detection limit for ozone that needs to be quantified.

SPICAV observed stars with various brightness and in different stray light configurations that defined a noise of atmospheric transmission spectra. It leads to changing detection limits that are unique for each spectrum. A simple approach was used to determine them for each gaseous compound. The limit is considered to be linked to the 1-σ uncertainty of the spectral data, which can be associated to a value for the slant density. The σ value is determined as standard deviation computed for a ration of an experimental spectrum and a corresponding best-fit model. The spectral range for σ computation is limited to spectral bands of minor species, thus, the interval of 210-280 nm is considered. Due to this limitation the uncertainties related to lower spectral signals were not taken under consideration.

Detection limit slant density is assumed to provide a 1-σ absorption quantity in a maximum of studying trace gas band. It is estimated around a maximum of the absorption band that correspond to 245-265 nm

for O_3. The interval of 190-210 nm is used for SO_2 detection attempts since this absorption band is the strongest for SO_2 in the SPICAV UV spectral range. The algorithm solves the spectral inversion problem for one gas. If one neglects the convolution by the instrumental PSF for this problem, the transmission is computed by $\exp(-\sigma_{gas}\ N_{gas})$ where σ_{gas} are gaseous cross-sections. However, The PSF convolution should be considered in the analysis since the experimental transmission spectra are not deconvolved. Therefore, for detection limit estimation the transmission is calculated as a ratio between two synthetic spectra (Equation 2.15) when only one considers the studying gas. The atmospheric transmission model is supplemented by the SO_2 absorption when the O_3 detection limit is estimated.

$$T_{gas}(N_{CO2}, N_{SO2}, N_{O3}, \tau_{ref}, \alpha) = \frac{T_{mod}(N_{CO2}, N_{gas}, \tau_{ref}, \alpha)}{T_{mod}(N_{CO2}, \tau_{ref}, \alpha)} \quad (2.15)$$

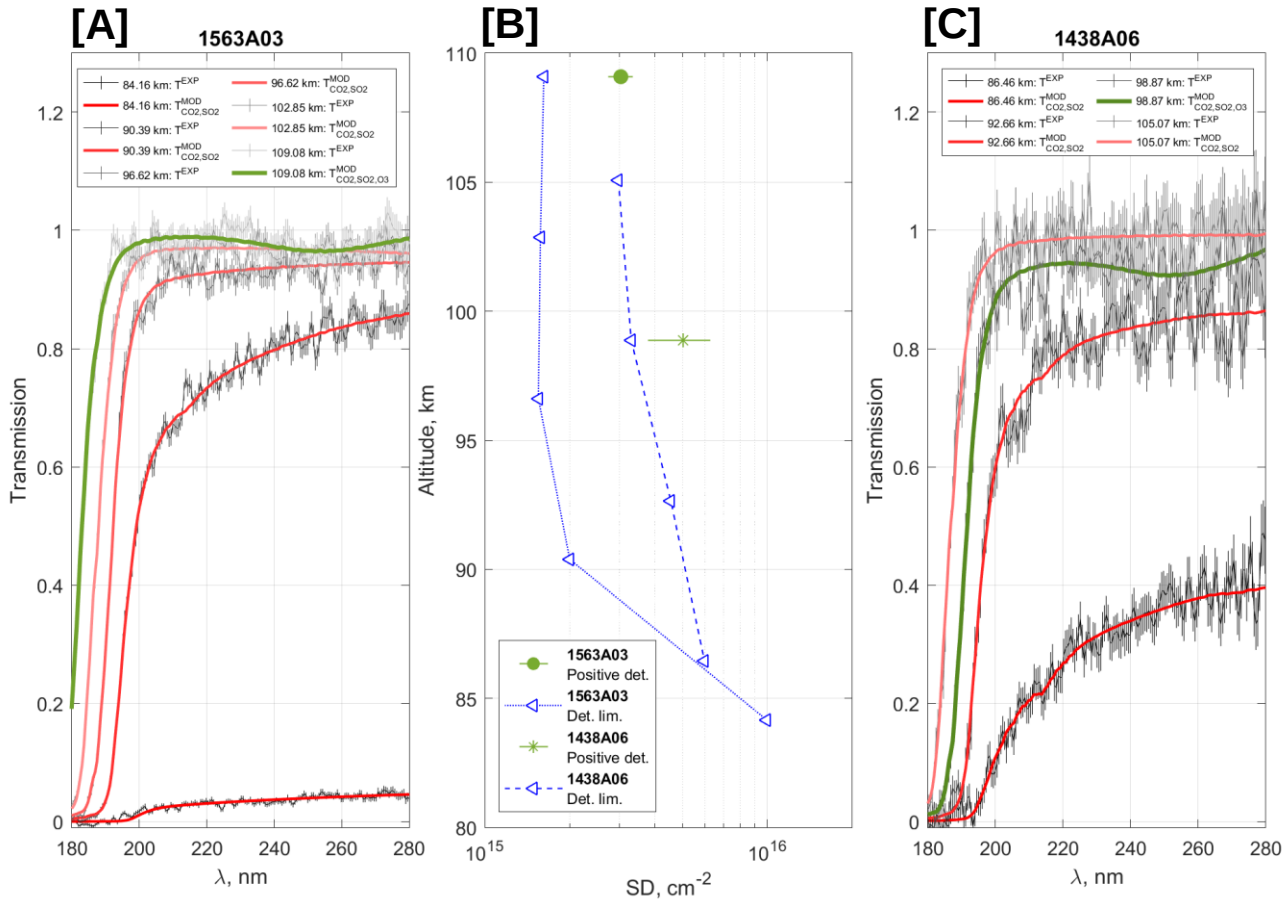

Figure 3.16. A and C: Atmospheric transmission spectra of occultations #1563A03 (August 1, 2010; at latitude 24.4°N and longitude 107°; local time 2.07 hours) and #1438A06 (March 29, 2010; at latitude 3.1°S and longitude 46.6°; local time 2.29 hours) within altitude range of 83-110 km. Grey curves with error bars are the experimental data. The red tones curves are the synthetic transmission spectra assuming the absorption by CO_2 and SO_2. The green curves are the model also including the ozone absorption. The experimental spectra are shown with best fit models. (B) The estimated detection limits presented by blue triangles, and ozone slant densities successfully retrieved (the green circle for #1563A03 and the green star for #1438A06).

An example of our analysis is presented in Figure 3.16 for two occultation sessions (#1563A03 and #1438A06) characterized by different signal fluctuation levels. There are positive detections of ozone at altitudes of 109 and 99 km respectively in #1563A03 and #1438A06, where O_3 absorption band is clearly

distinguishable in those of transmissions. Figure 3.17A represents the evaluated 1-σ uncertainty for each spectrum. The detection limits for O_3 for these two cases vary by a factor of two. However, for each observation the 1-σ value is nearly constant over most of the probed altitude range, and equivalently for the corresponding upper limit on slant density. When this detection limit on slant density quantity is divided by the CO_2 slant density obtained at the same altitude, then the 1-σ uncertainty in terms of VMR can be derived. Considering that the 1-σ uncertainty on the slant density is constant with altitude, then the corresponding 1-σ uncertainty on the VMR necessarily decreases with decreasing altitude as the CO_2 slant density increases (see Figure 3.17C).

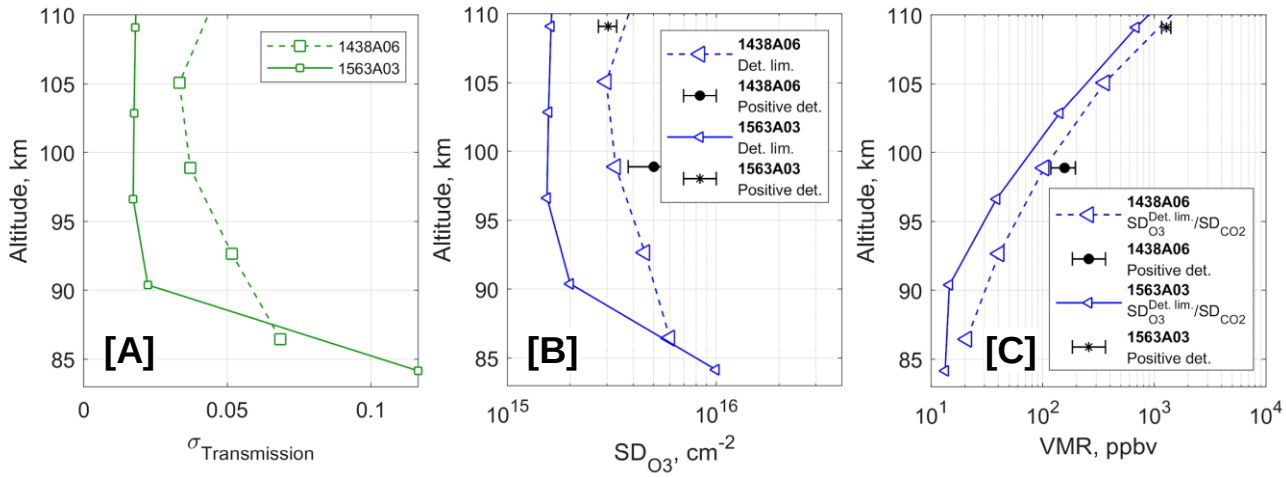

Figure 3.17. (A) 1-σ value variation with altitude found for orbits #1563A03 (August 1, 2010; at latitude 24.4°N and longitude 107°; local time 2.07 hours) and #1438A06 (March 29, 2010; at latitude 3.1°S and longitude 46.6°; local time 2.29 hours). (B) Estimated detection limits are presented by blue triangles, while filled circles and stars indicate successfully retrieved O_3 slant densities (the black circle for #1563A03 and the black star for #1438A06). (C) 1-σ uncertainty as well as detection values obtained for O_3 VMR corresponding to the slant densities presented in B.

This algorithm is applied to every available observation made by SPICAV UV in order to compute the detection limits for O_3 and SO_2. The orbits with at least one positive detection are combined to estimate the general characteristics of the stellar occultation experiment by SPICAV.

Within the altitude range of 90-110 km the mean detection limit is estimated to be equal to $3.3\pm0.1\times10^{15}$ cm^{-2} (Figure 3.18). It is shown that the detected O_3 concentrations are in general just 1-3 times larger than the estimated limit. However, the values over 103 km should be considered with caution even if some observations were performed with a low noise level permitting not false positive detections of slant densities lower than the mean detection limit. Less than 15% of the spectra led to O_3 detection.

The SO_2 detection limit is about two times higher than the one retrieved for O_3. In the 90-110 km range it is $5.8\pm0.2\times10^{15}$ cm^{-2} (Figure 3.19). This difference in detection limit can be explained by the difference in cross-sections between the two gases. The detection limit is reached at an altitude of about 100 km while below the majority of the detections are significantly higher than corresponding detection limits. These detections constitute the SO_2 layer that can be found in the 83-100 km altitude range.

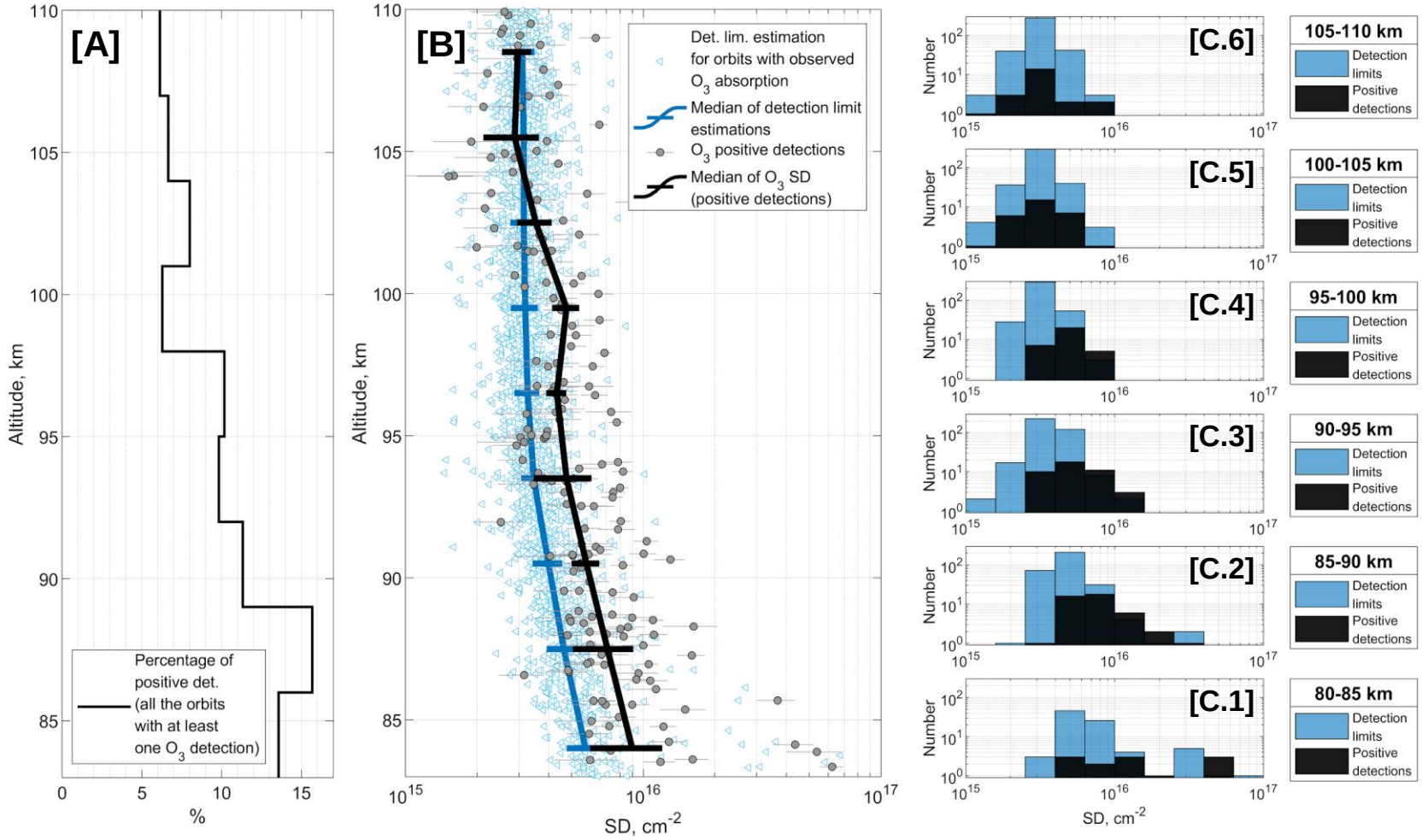

Figure 3.18. O_3 detection limit estimated for occultation sessions with at least one positive detection. (A) Percentage of positive detections of ozone absorption depending on altitude. (B) Slant density detection limits (light blue triangles) and the corresponding median values (blue curve). The median values are calculated within altitude intervals binned by 3 km from 83 to 110 km. Grey circles with error bars show positive detections of O_3, and it is accompanied by a median calculated on the same grid as one of the detection limit median (black curve). (C.1-C.6) Histograms represent the distribution of the values of detection limit slant densities and detected ozone slant densities within layers of 5 km.

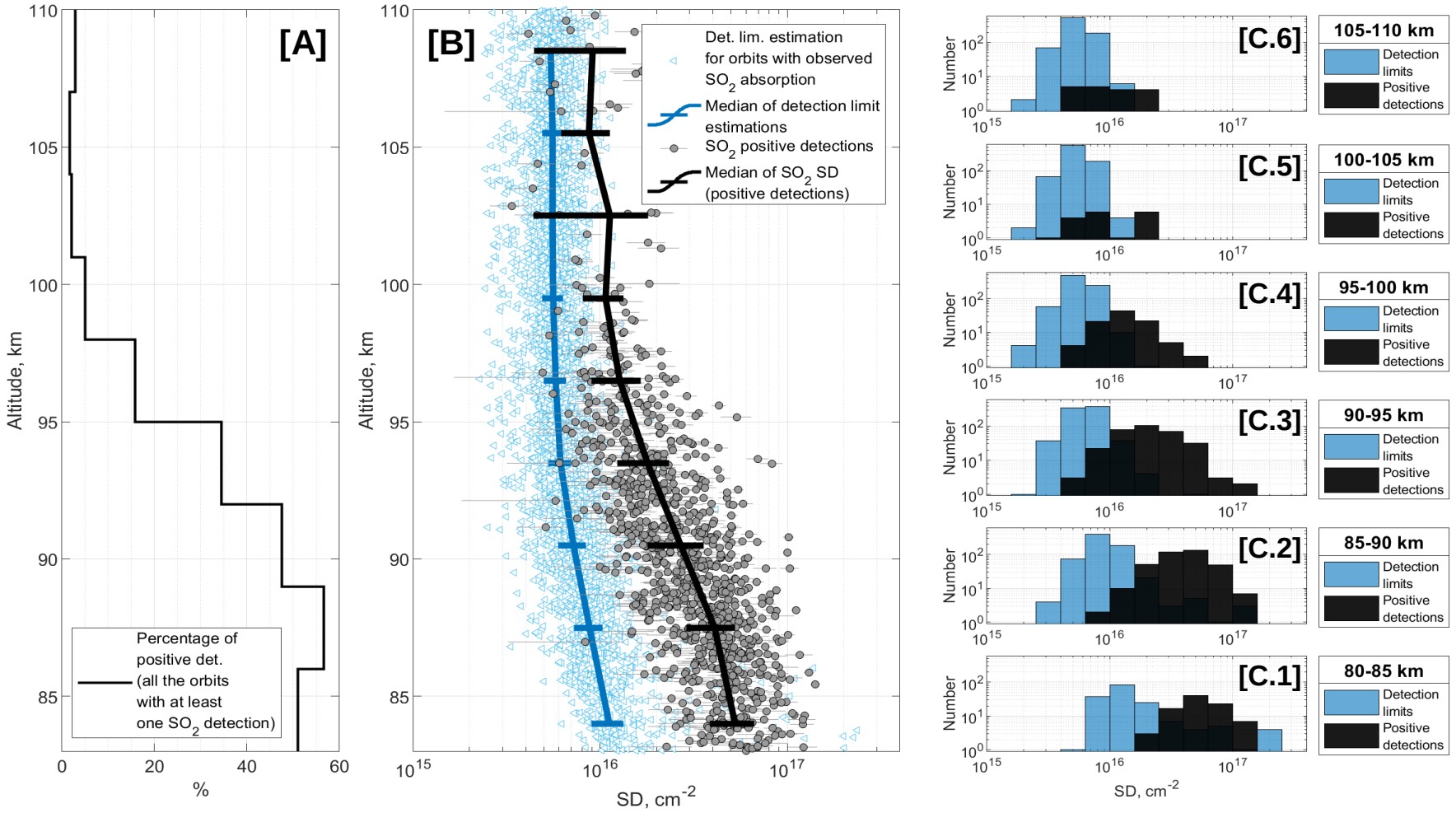

Figure 3.19. SO_2 detection limit estimated for occultation sessions with at least one positive detection. (A) Percentage of positive detections of SO_2 as a function of altitude. (B) Slant density detection limits (light blue triangles) and the corresponding median values (blue curve). The median values are calculated within altitude intervals binned by 3 km from 83 to 110 km. Gray circles with error bars show positive detections of SO_2, and it is accompanied by a median calculated on the same grid as one of the detection limit median (black curve). (C.1-C.6) Histograms represent the distribution of the values of detection limit slant densities and detected SO_2 slant densities within layers of 5 km.

3.2.6.3. Chlorine oxide absorption band

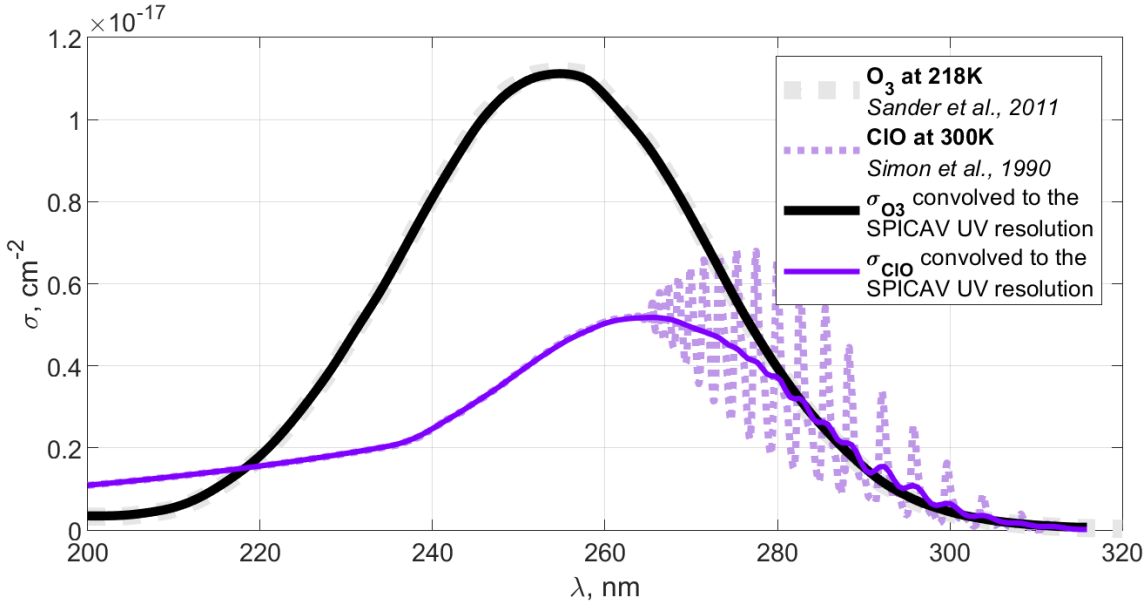

Figure 3.20. Ozone and chlorine oxide absorption cross-sections in the range 200-320 nm. Absorption cross-sections for chlorine oxide are taken from Simon et al. (1990), and they were measured at 300K.

In addition to SO_2, SO and O_3, the range of the SPICAV UV spectrometer also covered the absorption band of the chlorine oxide (ClO) molecule. This gas absorbs the UV radiation in the 240-300 nm wavelength range, which overlaps the O_3 Hartley band (Figure 3.20). However, the ClO absorbance is twice weaker than that of O_3.

Such overlapping of ClO and O_3 absorption bands results in a strong correlation (exceeding 0.7) between their slant densities if they are used simultaneously as free parameters in the numerical spectral inversion problem. At the same time chlorine compounds should destroy the ozone molecules, so their anti-correlation is expected from a chemical point of view. Thus, the retrieval of ClO slant density is always performed after fixing O_3 abundance. However, the attempts to discriminate ClO absorption using stellar occultations were not successful.

A detection limit for ClO estimated with SPICAV spectra turned out to be on average 3-4 times higher than the one for ozone. With an average detection limit for O_3 is 3.3×10^{15} cm^{-2}, the average detection limit for ClO is estimated at 10^{16} cm^{-2}. In terms of mixing ratio, it corresponds to ~30 ppbv at 85-90 km and ~300 ppbv above 105 km. These values are determined mainly by the lower ClO absorbance. In some observations a noise increase is observed at wavelengths longer than 280-300 nm, where the sensitivity of the detector is lower. This also influences the ClO detection limit.

The estimated detection limit is at least 10 times higher than the recent ClO detection at 85 km in the nightside mesosphere. The detection was made using the sub-millimetre ground based JCMT at λ~0.85 mm in 2010. The chlorine oxide abundance was measured in quantities of 3.7±0.9 and 1.5±0.5 ppbv in October and November 2010 respectively (Sandor et al., 2018). Such a ClO absorption level unfortunately would not be distinguishable in the SPICAV UV spectra. The experimental data was

examined for a presence of larger values, but the consideration of ClO in the atmospheric transmission model did not improve χ^2 more than 0.5%.

3.2.7. Vertical inversion problem

The previous formulas establish a relationship between transmission values and linear gas concentrations. To compute the volume concentration, an algorithm called the «onion-peeling» method (Figure 3.21) is implemented. The slant value is an integral of volume densities along the LOS through the atmosphere. To compute it numerically, the atmosphere is assumed as consisting of spherically symmetric homogeneous layers. Inside each layer, the value of the gas volume concentration n^g (cm^{-3}) is assumed constant. Then the slant concentration N_g is equal to the sum over all layers of the products of the volume concentration (n_j^g) by the path of the LOS of the device inside the layer (Δl_i). Taking into account the error $\varepsilon(z)$, N_g is:

$$N_g(z) = \sum_{z_i=z}^{\infty} n_i^g \Delta l_i + \varepsilon(z) \qquad (2.16)$$

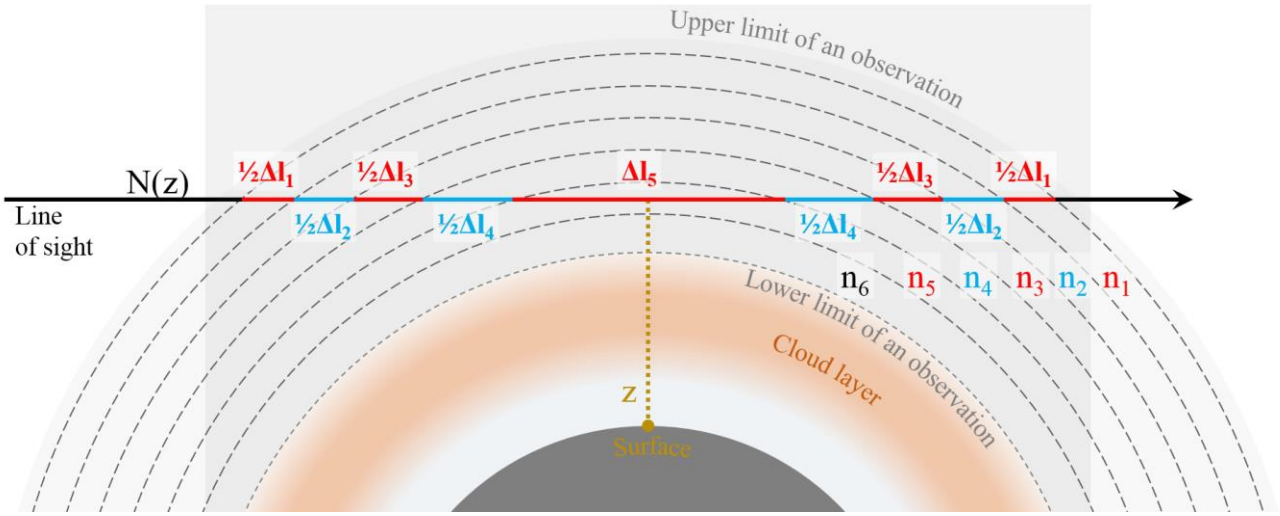

Figure 3.21. Scheme of dividing the atmosphere into spherically symmetric layers when performing vertical inversion by the «onion-peeling» method.

In matrix form, the slant concentration profile is expressed from the volume profile through the Abel matrix [A]

$$N = [A] \cdot D + \varepsilon \qquad (2.17)$$

whose elements are equal to the LOS path in the layer j, which is characterized by the height of the target point z_j, when observing the height z_i, and $z_{max\,j}$ and $z_{min\,j}$ are the maximum and minimum heights of layer j, and R_{Venus} is the radius of Venus.

$$A_{ij} = 2\left(\sqrt{\left(z_{max\,j} + R_{Venus}\right)^2 - (z_i + R_{Venus})^2} + \sqrt{\left(z_{min\,j} + R_{Venus}\right)^2 - (z_i + R_{Venus})^2}\right) \qquad (2.18)$$

Then the volume density profile is

$$D = [K] \cdot N \tag{2.19}$$

$$[K] = ([A]^T [C_N]^{-1} [A])^{-1} \cdot ([A]^T [C_N]^{-1}) \tag{2.20}$$

where $[C_N]$ is the covariance matrix for the slant density profile, i.e. a diagonal matrix. The elements of its diagonal are the squared errors of the concentration values. The covariance matrix of the volume concentration, in this case, is equal to:

$$[C_D] = [K][C_N][K]^T = ([A]^T [C_N]^{-1} [A])^{-1} \tag{2.21}$$

In practice, there is an altitude limit above which the instrument is no longer sensitive and is unable to characterize the mass of gases lying above this limit. Therefore, the presented formula is modified to include this unknown part in the Abel matrix operand where it is represented by an additional parameter A_{Ch} - the Chapman factor (Sekera, 1968).

$$A_{ij\,max} = A_{Ch} = \sqrt{2\pi(z_{max} + R_{Venus})H} \tag{2.22}$$

$$H = \frac{RT}{\mu G} \tag{2.23}$$

where R_{Venus} is the radius of Venus, H is the scale height of the outer atmosphere, R is the universal gas constant, T is the assumed temperature, μ is the molar mass of the atmosphere, G is the gravitational constant at the altitude z_{max}.

The inversion problem is ill-posed, that means the unstable solution. So the direct computation of the Equation 2.19 in most cases would increase noise or biases of the slant density profile. The smoothness of the result requires a modification of the basic inverse problem to make it pseudo-inverse. The Tikhonov regularization method is one of the instruments (Tikhonov and Arsenin, 1977; Twomey, 1977) and it is used in the analysis (Quemerais et al., 2006). Following this method, $[K]$ becomes

$$[K] = ([A]^T [C_N]^{-1} [A] + \lambda_s [L]^T [L])^{-1} \cdot ([A]^T [C_N]^{-1}) \tag{2.24}$$

$$[L] = \frac{1}{h^2} \begin{pmatrix} -1 & 1 & 0 & & 0 & \cdots & 0 \\ 1 & -2 & 1 & \cdots & 0 & \cdots & 0 \\ 0 & 1 & -2 & & 0 & \cdots & 0 \\ & \vdots & & \ddots & & \vdots & \\ 0 & \cdots & 0 & & -2 & 1 & 0 \\ 0 & \cdots & 0 & \cdots & 1 & -2 & 1 \\ 0 & \cdots & 0 & & 0 & 1 & -1 \end{pmatrix} \tag{2.25}$$

The additional parameter of $\lambda_S [L]^T [L]$ is responsible for the regularisation. The matrix $[L]$ represents an operator of the second derivative with the h as a difference of altitude of the layers. The smoothness of the method is defined by the λ_S. A large value of this coefficient leads to the vertical resolution degradation since more neighbour layers are involved to derive a local density at the particular altitude. Determination of the correct regularization parameter is puzzling. The analysis of this question was done for the stellar occultations on Mars by Quemerais et al. (2006). It is proposed to tie a value of $\lambda_S(z) \sim 1/\sigma_D(z)^2$ where $\sigma_D(z)$ is an estimated error of the local density at altitude z. This assumption allows the release of an iteration scheme for the density profile retrieval. The first iteration is an inversion of a slant

density profile by Equation 2.19 and an estimation of $\sigma_D(z)$ based on Equation 2.21. Then a corresponding value of $\lambda_S(z) = \lambda_0/\sigma_D(z)^2$ is computed to perform the next iteration by the regulazing scheme of Equation 2.19 with the operator in Equation 2.24. It was obtained that the scheme converges in less than 10 iterations. In the current analysis 5 iterations perform a good converging of the problem.

3.2.8. Calibration influence on the spectral inversion

The accuracy of the results obtained for determining the gas concentration in a stellar occultation experiment can be significantly affected by systematic errors appearing during the calibration step of the raw data. The uncertainties under consideration are mainly related to two aspects:

1. Wavelength-to-pixel registration;
2. Stray light estimation.

Transmission spectra can be modelled by the Beer-Lambert law whose parameters are wavelength-dependent. An accurate wavelength-to-pixel registration is therefore a prerequisite to the fitting process. The wavelength shift Δλ is estimated for every observation can be a source of both underestimation and overestimation of the obtained concentrations. For example, consider the error in the retrieved Δλ shift equal to the width of one pixel, 0.54 nm, and investigate the effect on the resulting values of the slant density of CO_2 for observation #1269A03. So, the error of the final slant density of carbon dioxide reaches 20% for the deeper layers of the mesosphere (Figure 3.22). As a side note, gas concentration is traditionally normalized by the CO_2 concentration to produce volume mixing ratios (VMR). Therefore, such metrics will inevitably be impacted on both parts of the ratio and amplify the adverse effect of a shift estimation error.

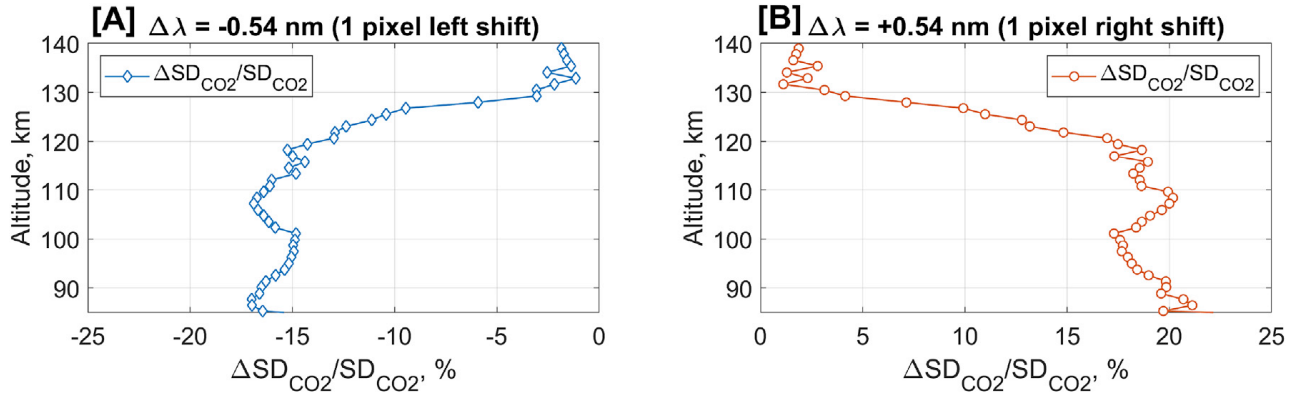

Figure 3.22. The difference in the percentage of slant CO_2 concentration values at different altitudes obtained from the same observation #1269A03 using two different wavelength-to-pixel assignments. The ratio is calculated relative to the CO_2 profile obtained from spectra calibrated using the accurate stellar line alignment. (A) Negative offset for one pixel wide (-0.54 nm) is applied to the «reference» calibration. (B) A positive offset of one-pixel width (0.54 nm) is applied.

The wavelength calibration based on aligning with the stellar catalogue was preferred over another algorithm for wavelength calibration which is based on the alignment of the CO_2 absorption band position (Figure 3.23) in the atmospheric transmission spectra. This has been described in details in Quemerais et al. (2006) for the atmosphere of Mars at altitudes where pressure is comparable to the Venus upper mesosphere. The shape of the CO_2 absorption band in the range of 120–170 nm is observed

by SPICAV UV at altitudes from 120 to 140 km. At lower altitudes, increased CO_2 density ends up in the band saturation, which makes the application of such wavelength calibration method useless.

The Venus Express spacecraft had a very elongated elliptical orbit around the planet. The difference in altitude between the exposures of each spectrum was determined by the distance of the spacecraft from the target point. This altitude step could reach 8 km and only 3-4 spectra per observation session can be used for the wavelength to pixel allignment based on the CO_2 absorption band. This statistical limitation provides an inaccuracy in determining $\Delta\lambda$ comparable to the width of one pixel, which could significantly distort the resulting vertical profiles of the studying gases, as it is shown above. On the contrary, in the other approach from tens to hundreds of measurements were used to perform the calibration, and then the obtained $\Delta\lambda$ values were averaged. It reduced the uncertainty in determining the wavelength by at least 10 times to values of 1-10% of the pixel width. As well, the possible $\Delta\lambda$ change with altitude was examined and it was found that for a particular orbit $\Delta\lambda$ remains stable with altitude.

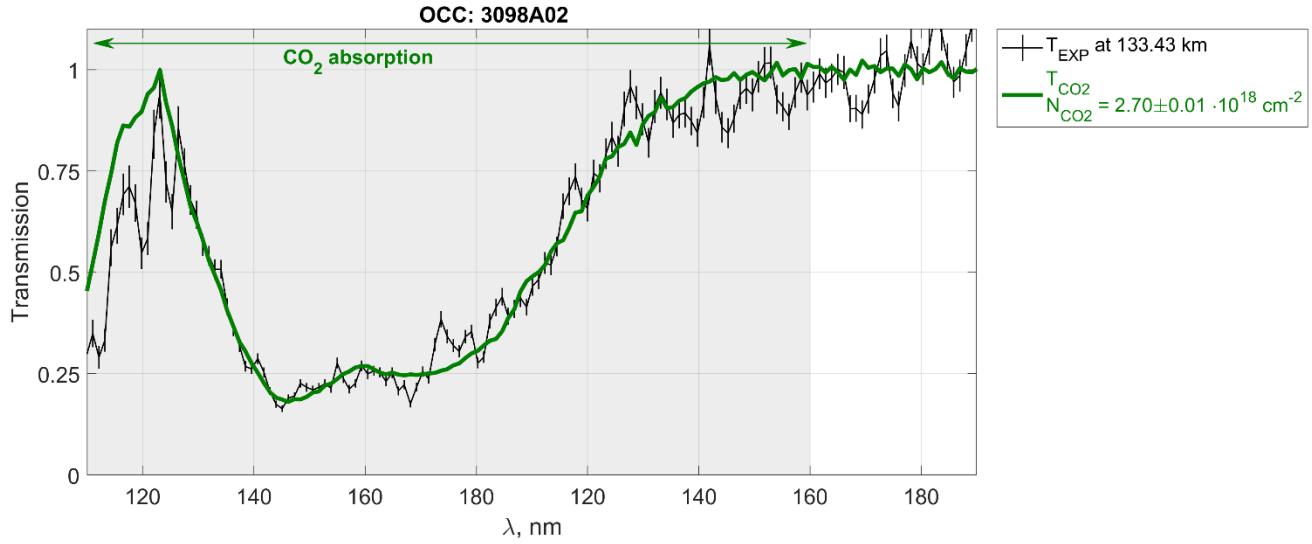

Figure 3.23. Wavelength-to-pixel assignment obtained for observation session #3098A02. (A) Transmission spectrum (black solid line) with corresponding error bars measured by SPICAV UV (T_{SPICAV}) at an altitude of 133.43 km which demonstrates the shape of the CO_2 absorption band. The synthesized spectrum (green solid line) of the CO_2 absorption (T_{CO2}) for the appropriate wavelength calibration.

The error in retrieved gas concentrations along the LOS was also affected by the accuracy of the stray light estimation. Systematic errors in the retrieved profiles of atmospheric components, caused by overestimation or underestimation of the transmission when extracting the illumination, can be significant. They are comparable to the effect of wavelength-to-pixel assignment error. One assumes that the stray light is on average overestimated by 0.5%, which corresponds to an underestimation of the atmospheric transmission. Then three different spectral ranges that define the absorption of each of the three test gases are considered:

1. CO_2 absorption band;
2. emission range of NO, which coincides with the absorption band of SO_2;
3. and the Hartley absorption band of O_3.

In Figure 3.24 the estimated deviations from a nominal value are shown. The slant density of CO_2 does not change significantly for altitudes where the absorption band of CO_2 is unsaturated (Figure 3.24A). However, the deviation from the original profile is almost 100% when the relative values of trace gases SO_2 and O_3 are considered (Figure 3.24B and 3.26C).

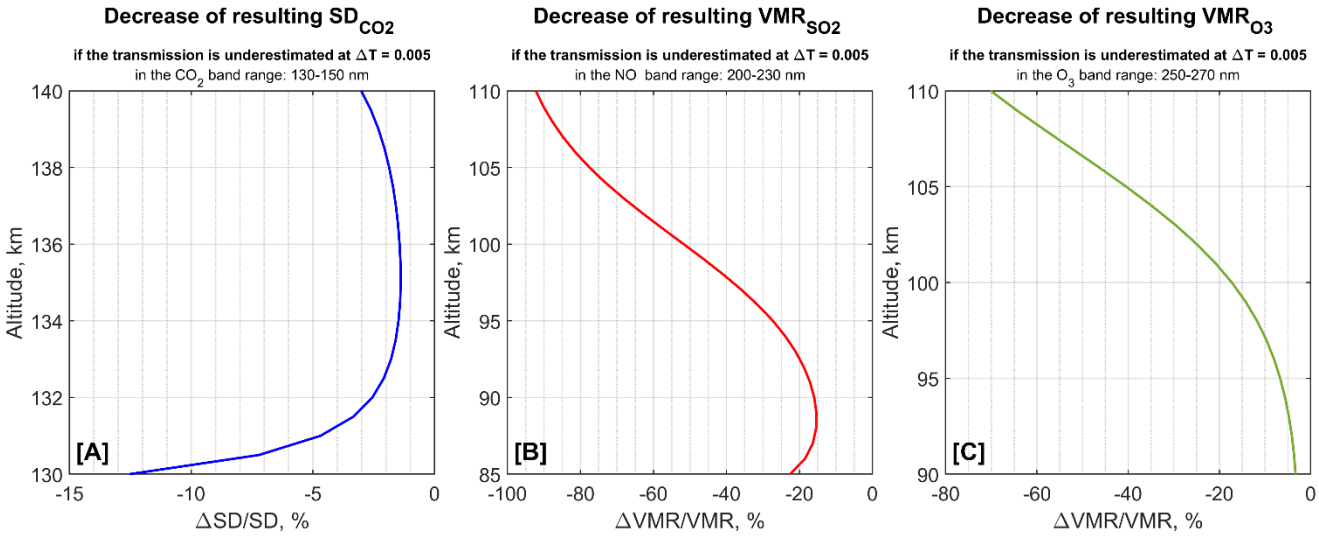

Figure 3.24. Effect of underestimating transmission level on the resulting profiles of CO_2 slant density (A) and mixing ratios (VMR) of SO_2 (B) and O_3 (C) as a function of altitude.

This study demonstrates the importance of accurate separation the atmospheric transmission and emission spectra. Various studies have suggested two different approaches for removing stray light. These two approaches are based on the imaging capabilities of the SPICAV spectrometer since the targeted stellar signal and the UV emission one are distributed differently on the detector. The methods separately described by Royer et al. (2010), Piccialli et al. (2015) and Belyaev, Evdokimova et al. (2017) was analysed in detail to determine the most efficient algorithm.

3.2.9. Stray light elimination technique

A package of five spectra corresponding to the five bins (Figure 1.16, Section 1.6.1), which are recorded during one exposure of the detector, are summed from the superposition of the star image and the additional illumination spread over the CCD. The star is a point source and its image at every wavelength on the detector is determined by the instrumental PSF function. The stray light is scattered similarly over all the detector; however, its extended nature makes its signal distribution over the detector being more homogeneous than the stellar one. The superposition of all signals for each bin (S_i^{SPICAV}) can be represented as follows:

$$S_i^{SPICAV}(\lambda) = \alpha_i S^{ref}(\lambda) T(\lambda) + S_i^{STRL}(\lambda), i = 1 \dots 5 \qquad (2.26)$$

where S_i^{STRL} is the component describing the part of the stray light that fell into the i bin, α_i is the fraction by the PSF in this bin, S^{ref} is the spectrum of the star multiplied by the atmospheric transmission (T). Nominally, the star is focused on the central or 3rd bin, and 90% of its signal is contained there. Extended sources illuminate the entire CCD and they are also characterized by a slower temporal variability in comparison with the evolution of the stellar signal. These two factors were used in two algorithms to

separate the stray light in the stellar occultation data. Both methods make it possible to subtract the emission spectrum from the spectra of stars based on the signal in non-central bins that contains the wings of the PSF distribution of the star image. However, their accuracy was examined considering the differences between these algorithms. Further on in this research these methods will conventionally reffered as «Method #1» and «Method #2», implying respectively the method described in Royer et al. (2010) and Picciali et al. (2015), and the method presented in Belyaev, Evdokimova et al. (2017).

3.2.9.1. Method #1

The first method reviewed was presented in Royer et al. (2010) and in Picciali et al. (2015) in more detail. The algorithm assumes that the stray light spectrum in the third bin (S_3^{STRL}) is a linear combination of the scattered light spectra in other, non-central bins (S_i^{STRL}, $i \neq 3$).

$$S_3^{STRL}(\lambda) = \sum_{i=1,2,4,5} k_i S_i^{STRL}(\lambda) \tag{2.27}$$

Accurate determination of the linear coefficients k_i is the key to the correct subtraction of the emission signal from the transmission spectra. They can be reliably estimated at altitudes where the atmosphere becomes completely opaque for a star radiation. Usually, altitudes below 60 km are considered. For these spectra, the resulting coefficients best describe the Equation 2.27, thus correspond to the minimum of the following function χ^2:

$$\chi^2\,(k_1, k_2, k_4, k_5) = \sum_{z=-200\ km}^{z=60\ km} \sum_{\lambda} \left(\frac{S_3^{STRL}(\lambda) - \sum k_i S_i^{STRL}(\lambda)}{\sigma^{STRL}(\lambda)} \right)^2 \tag{2.28}$$

where $\sigma^{STRL}(\lambda)$ - errors of experimental data measured below 60 km.

The resulting values are then used in the stellar occultation region (85-140 km) to determine the atmospheric transmission spectra using the following formula, taking into account that the fraction of the PSF distributed to the outer bins constitute only a few percent.

$$T(\lambda, z) = \frac{S_3^{SPICAV}(\lambda, z) - \sum k_i S_i^{SPICAV}(\lambda, z)}{S^{ref}(\lambda)} \tag{2.29}$$

3.2.9.2. Method #2

The second method also aims to determine the fraction of stray light contained in the central (3rd) spectrum. It was mentioned above that this bin usually collects about 90% of the stellar signal, and the 1st and 5th bins correspond to only 1-3% (Figure 1.16, Section 1.6.1). Therefore, it is possible to calculate the template stray light spectrum ($S_{template}^{STRL}$) by averaging the spectra of the 1st and 5th bins.

$$S_{template}^{STRL}(\lambda) = \frac{1}{2}\left(S_1^{SPICAV}(\lambda) + S_5^{SPICAV}(\lambda) \right) \tag{2.30}$$

This template can be included in the spectral inversion problem for each measurement within the studied altitude range. Then the χ^2-function describing the approximation of experimental spectra by the model

(Equation 2.31) will depend on the additional free parameter *k* which scales the intensity of the template spectrum in order to avoid an overestimation of the atmospheric transmission model:

$$\chi^2\left(k, N_g, \tau_\alpha\right) = \sum_\lambda \left(\frac{S_3^{SPCAV}(\lambda) - [T^{MODEL}\left(\lambda, N_g, \tau_\alpha\right) + k \cdot S_{template}^{STRL}(\lambda)]}{\sigma(\lambda)} \right)^2 \quad (2.31)$$

where $\sigma(\lambda)$ is the $S_3^{SPCAV}(\lambda)$ spectrum error.

T^{MODEL} is an atmospheric transmission model, which depends on the following parameters: slant gaseous concentration N_g and aerosol optical thickness (τ_α) along the LOS. In this case, the atmospheric transmission spectrum is calculated by the formula:

$$T(\lambda, z) = \frac{S_3^{SPICAV}(\lambda, z) - k \cdot S_{template}^{STRL}(\lambda, z)}{S^{ref}(\lambda)} \quad (2.32)$$

3.2.9.3. Comparison of methods

Both methods determine the stray light pattern and thus show similar results. Each orbit, when the SPICAV UV spectrometer has successfully observed stellar transmission, was processed by two ways to study their accuracy. An example of correct processing by both algorithms is shown in Figure 3.25, where in the initial data contains a strong illumination from the atmospheric NO airglow at wavelengths of 200-250 nm. This signal significantly distorts the transmission values.

Atmospheric transmission decreases from 1 to 0 as the instrument's LOS moves down into denser layers of the atmosphere. The CO_2 absorption band quickly saturates and the atmospheric transmittance goes to zero below 120 km at wavelengths shorter than 150 nm. At altitudes above 115 km and wavelengths longward of 180 nm, absorption by small gaseous components and aerosols is negligible, and the spectrum remains equal to 1.

Considering this altitude dependence, the resulting atmospheric transmission spectra were studied in three different spectral intervals of the SPICAV UV range corresponding to absorption bands of three studied molecules:

(1) the absorption band of CO_2 (130-150 nm),

(2) one of the SO_2 band (200-230 nm),

(3) one of the O_3 band (250-270 nm).

In Section 3.2.8 the impact on concentration retrievals from a transmission uncertainty was explored for the same spectral ranges. The considered absorption band of SO_2 is particularly interesting since it corresponds to the peak of the nitric oxide emission.

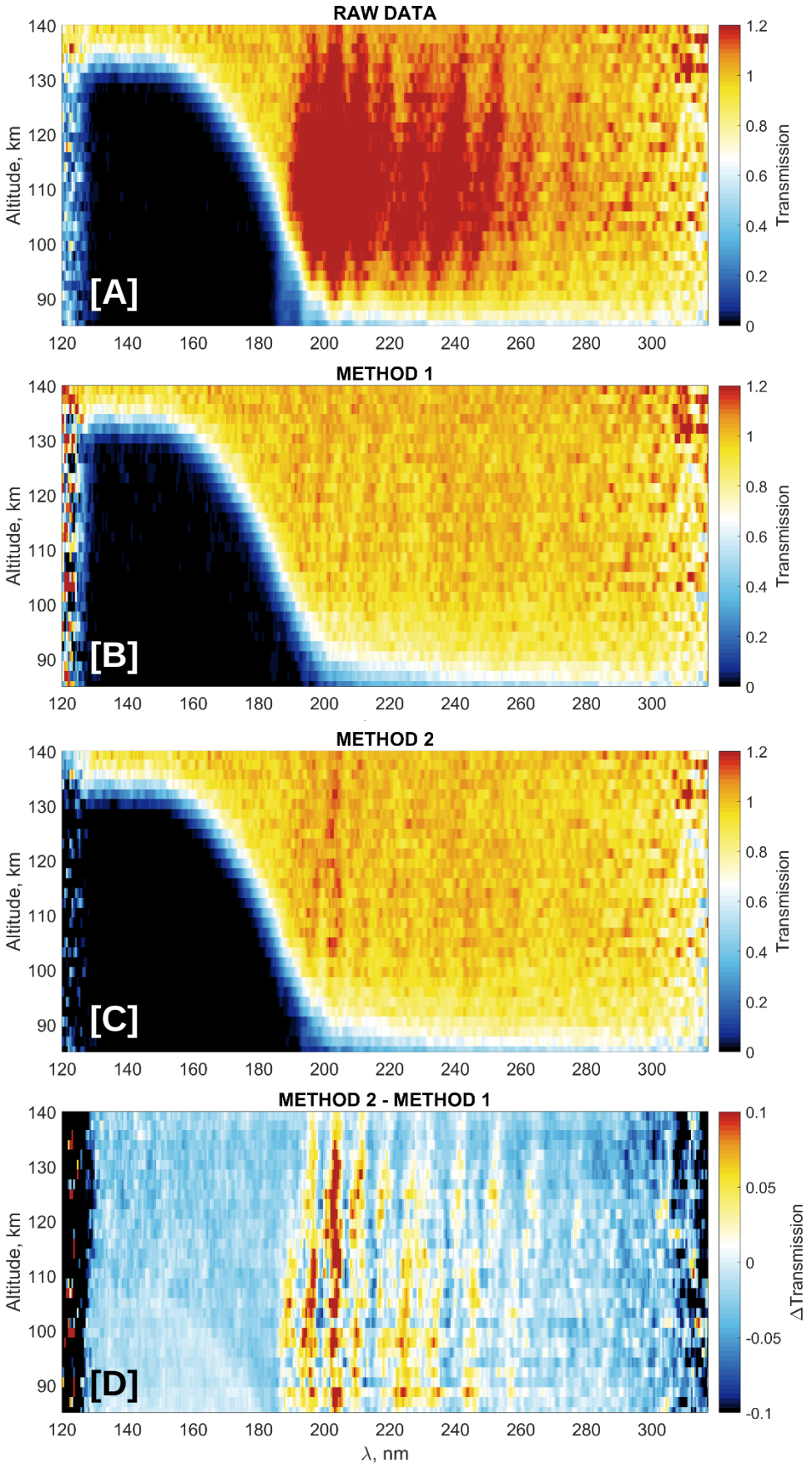

Figure 3.25. Altitude dependence of the transmission spectra for orbit #3071A02. (A) Raw data; (B) data processed by method 1; (C) data processed by Method #2, and (D) the difference between the results of applying each method. The latter demonstrates an insufficient evaluation of NO emission by Method #2.

The results of applying both methods are compared in the following way. For each resulting atmospheric transmission spectrum, three values are calculated averaging over each spectral interval. A set of mean transmission altitude profiles is obtained. The uncertainties in each of the two methods cause some statistical dispersion around the expected transmittance: 0 (Figure 3.26.1A and 3.26.2A) or 1 (Figure 3.27.1A and 3.27.2A; Figs 3.28.1A and 3.28.2A). In most cases, both methods lead to nearly the same results. After applying each of the methods, we will consider the general statistics on the average transmission values for each spectral interval and the corresponding altitude range. The transmission in the 130-150 nm range is zero below 120 km, and it is equal to one in the 200-230 nm and 250-270 nm ranges above 115 km. The uncertainties of the two methods cause some statistical dispersion around the expected values, i.e. zero or one.

As a result, for each investigated spectral range, we obtain a pair of statistical distributions of the average transmission, which can be conveniently expressed in terms of probability density functions (PDF). In the case of the most effective application of the method, the obtained distributions must strictly correspond to the PDF of the normal distribution. Therefore, for each histogram, the parameters μ (mean) and σ (standard deviation) were calculated, corresponding to the optimal Gaussian distribution curve (Table 3.2).

Table 3.2. Distribution parameters.

	Method #1	**Method #2**
CO_2 absorption band (Figure 3.26 1B and 2B)	$\mu_0 = (69.5 \pm 0.2)$ e-05 $\sigma_0 = 0.0020 \pm 3.1$e-06	$\mu_0 = (8.2 \pm 0.7)$ e-05 $\sigma_0 = 0.0021 \pm 1.1$e-05
	$\mu_1 = 0.0049 \pm 2.2$e-05 $\sigma_1 = 0.0106 \pm 1.7$e-05	$\mu_1 = 0.0054 \pm 1.4$e-05 $\sigma_1 = 0.0095 \pm 1.5$e-05
NO emission band (Figure 3.27 1B and 2B)	$\mu_0 = 0.9989 \pm 0.0003$ $\sigma_0 = 0.0087 \pm 0.0002$	$\mu_0 = 1.0009 \pm 0.0003$ $\sigma_0 = 0.0085 \pm 0.0002$
O_3 absorption band (Figure 3.28 1B and 2B)	$\mu_0 = 0.9823 \pm 0.0005$ $\sigma_0 = 0.0156 \pm 0.0003$	$\mu_0 = 0.9829 \pm 0.0006$ $\sigma_0 = 0.0180 \pm 0.0004$

The CO_2 absorption band range (Figure 3.26) is most conveniently used to evaluate the effectiveness of methods. Carbon dioxide in the mesosphere partially or completely absorbs UV light at the wavelengths of its absorption band, which ultimately leads to a transmission of zero. Thus, any deviations seen on the histograms are solely due to method errors (Figure 3.26 1A and 2A). It is seen that the usual Gaussian function does not correspond to the obtained distribution. For the best description of the data obtained, it was necessary to use a bimodal normal distribution. Bimodality is most evident in the statistical distribution of the results of Method #2 (Figure 3.26 2B). Thus, the modes of the obtained distribution are characterized by $\mu 0 \cong 0$ and $\mu 1 = 0.0054$. The results of Method #1 are also better described with the addition of the second mode to the normal distribution with respect to 0, but the bimodality is much less pronounced and is used only to describe the tail of the distribution (Figure 3.26 1B).

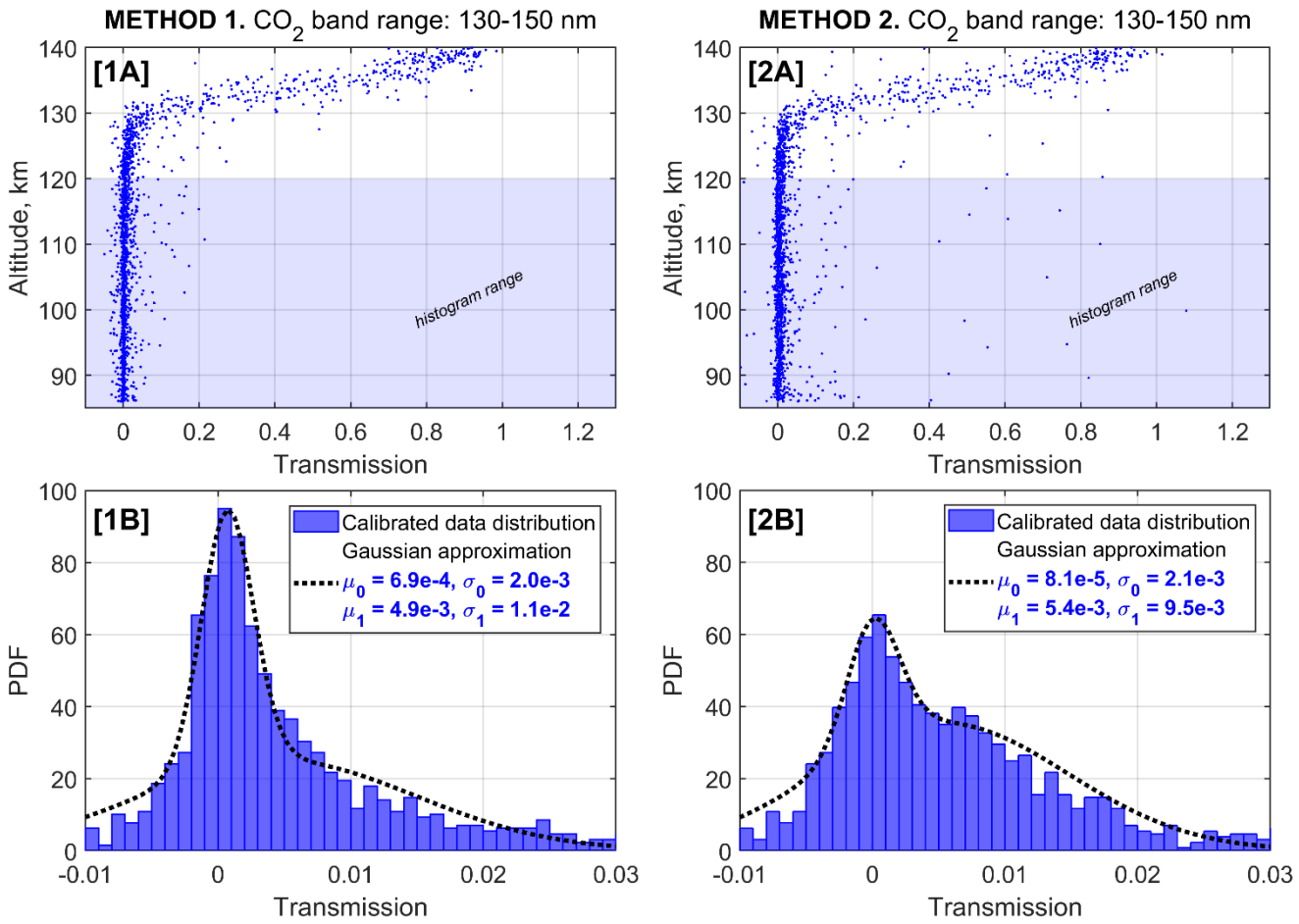

Figure 3.26. 1A and 2A. Transmission profiles obtained by Method #1 and Method #2, respectively, averaged over the CO_2 absorption band range (130-150 nm). Distributions of these values are plotted within 120–140 km. The points that are used to build histograms correspond to the selected areas of the transmission profiles. 1B and 2B. Histograms are plotted in terms of the probability density function (PDF) for each sample. The black dashed line shows the Gaussian model that describes each distribution in the best way and that is characterized by the parameters presented in Table 3.2.

In the intervals corresponding to the maximum of NO emission (Figure 3.27) and the ozone absorption band (Figure 3.28), the obtained statistical distributions are in good agreement with the Gaussian law. The range 200-230 nm is characterized by an average transmittance μ_0 close to 1, which fully corresponds to expectations (Figure 3.27 1B and 2B). The resulting bias is covered by this experimental uncertainty. Transmittance deviations from 1 can also be associated with variations in atmospheric absorbers in addition to inaccurate estimates of the illumination component.

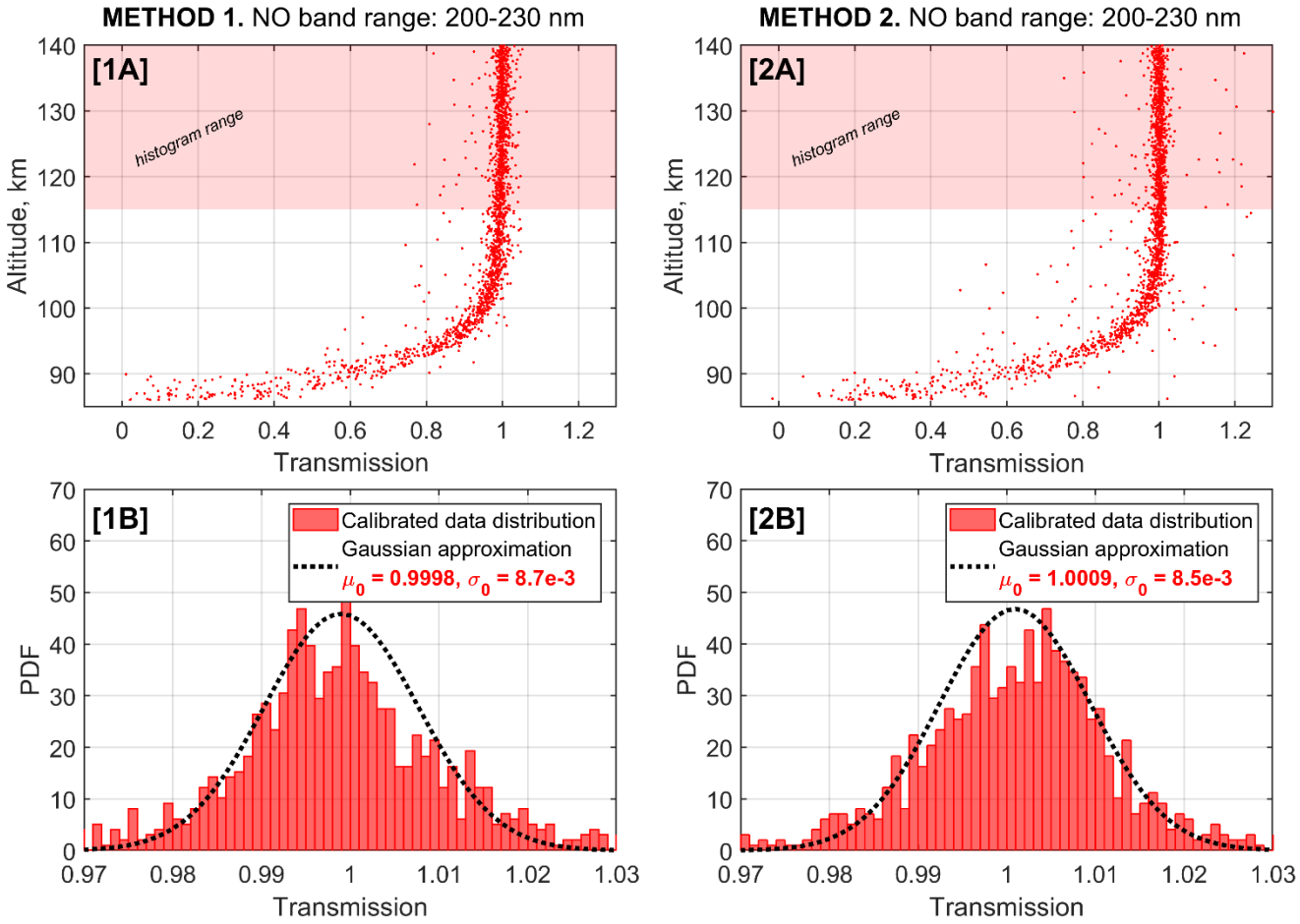

Figure 3.27. 1A and 2A. The transmission profiles obtained by Method #1 and Method #2, respectively, averaged in the range of the maximum emission of NO (200-230 nm) and the absorption band of SO_2. Distributions of these values are plotted within 85–115 km. The points that are used to build histograms correspond to the selected areas of the transmission profiles. 1B and 2B. Histograms are plotted in terms of the probability density function for each sample. The black dashed line shows the best Gaussian model that describes each distribution and is characterized by the parameters in Table 3.2.

For the Hartley absorption band, Method #2 also demonstrates the deviation of the resulting transmission distribution from normal (Figure 3.28). It should also be noted that the values of μ_0 for both methods in this spectral range are slightly less than 1. This may be due to the noisiness of the atmospheric transmission spectra, which increases in this range due to (1) a decrease in the star signal, (2) an increase in the backlight signal, or (3) the presence of ignored illumination in the reference spectrum of the star. However, these inaccuracies are the same for both methods and do not affect their results.

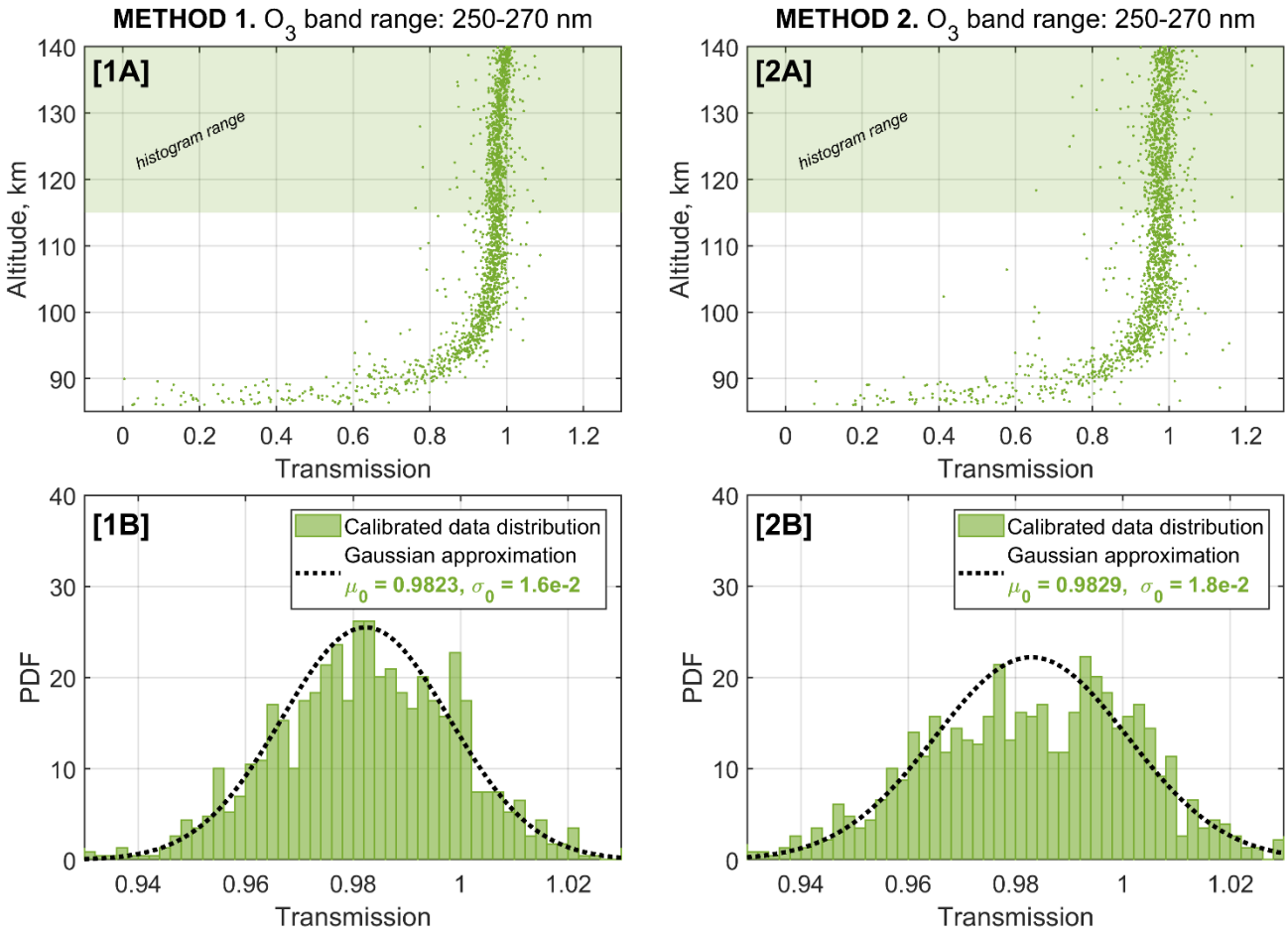

Figure 3.28. 1A and 2A. Transmission profiles obtained by Method #1 and Method #2, respectively, averaged over the O_3 absorption band range (250-270 nm). Distributions of these values are plotted within 85–115 km. The points that are used to build histograms correspond to the selected areas of the transmission profiles. 1B and 2B. Histograms are plotted in terms of the probability density function for each sample. The black dashed line shows the Gaussian model that best describes each distribution, which is characterized by the parameters presented in Table 3.2.

3.2.9.4. Atmospheric transmission and error bars estimation.

For the current task, Method #1 is the best. It is chosen in a calibration phase of the signal. However, each spectrum was evaluated for residual illumination in the region of the spectrum where full absorption of incoming star light is achieved. Thus, in this region the mean value should be 0.

Atmospheric transmission spectra are evaluated by Equation 2.29. The resulting error bars of a particular transmission are defined by uncertainties of the initial stellar spectrum, the reference stellar spectrum and a stray light composite error. The stray light error bars include the uncertainties of obtained 4 spectra in non-central bins and an error of *k*-coefficients estimated by the Levenberg-Marquardt optimisation algorithm.

3.2.10. Altitude assignment

Raw data transmitted to Earth also require calculation of geometric parameters of observation. Knowing the exact time of each measurement and the coordinates and orientation of the spacecraft in space, all necessary parameters are calculated. For observations in tangential geometry such parameters are, first

of all, the parameters of the target point: altitude, its geographical coordinates (latitude and longitude), local time, solar-zenith angle. Also parameters of the spacecraft position, as the distance from the planet, phase angle between the observer and the sun, etc. All these values have already been calculated for each spectrum package used in this work. Detailed information about them can be found on the official ESA archive.

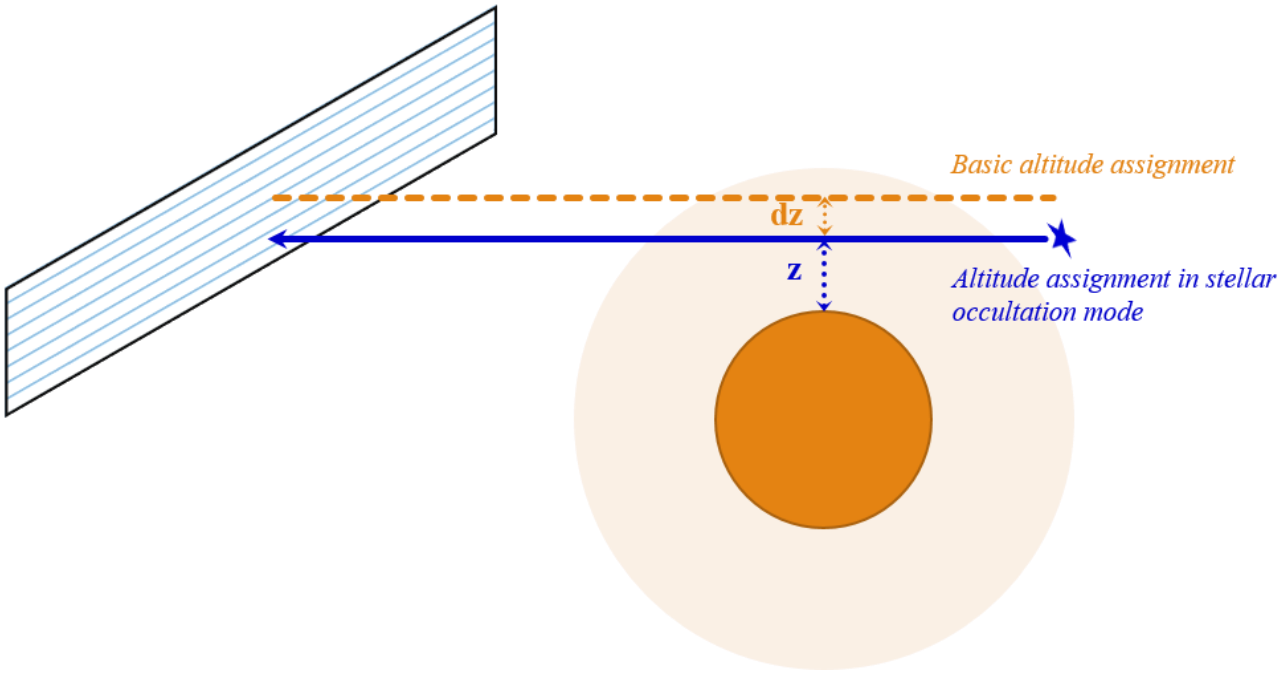

Figure 3.29. Scheme of a star focus shift in stellar occultation mode with respect to the center of the 3rd bin on the CCD. Its influence on determining altitude of the target point.

For the solar occultation mode and when observing spread emission sources on the planet's limb, all parameters for the device's LOS and target point are calculated relative to the LOS corresponding to the centre of each of the 5 bins on the matrix. The 5 respective spectra in these observations averages a signal of the entire FOV of one bin. However, the situation is different in stellar occultation mode. A point source as a star has a precise localization in the spectrometer FOV. Thus, all geometrical parameters of the target point are unambiguously linked to the LOS directed to a star. From 4 to 32 rows of pixels are summed up in each bin on the matrix in this mode. The star is focused on the third bin, but not necessarily to its centre, which is observed in the resulting spectra packets. Thus, the difference in target point altitude (*dz* in Figure 3.29) computed to the LOS from the centre of the 3rd bin and the LOS directed to the star may differ by 5 km or more. Parameters are very different depending on a position of the device in the planet's orbit. The observations in the pericenter have the smallest FOV on the planet limb, but are made with a large step between spectra. When the spacecraft is distant, its FOV increases, but it becomes possible to scan the planet's limb in more detail. However, the spacecraft is moving away from the planet, the possible difference in parameters assignment increases if the star focus is shifted from the centre of the bin. Therefore, in the stellar occultation mode, the geometric parameters are supplemented with the values calculated with respect to the LOS directed to the point source. These are the parameters used in this analysis.

3.3. Summary

The stellar occultation experiment is a powerful technique to measure the detailed vertical distributions of gases and aerosols in the night-time mesosphere of Venus. The SPICAV UV spectrometer (118-320 nm) was able to identify and quantify the absorption of CO_2, SO_2 and O_3 molecules in the range covered by SPICAV.

Stellar spectra obtained by SPICAV were processed in two steps. In a first step, the raw dataset was calibrated using an updated calibration protocol, which minimizes impacts of systematic errors. The protocol features in particular:

- An improved pixel-to-wavelength assignment based on aligning stellar spectra measured by SPICAV with a reference taken from the IUE observations, whereas it used to be aligned with CO_2 spectral features between 110 and 160 nm.
- An efficient way to eliminate «stray light» from observed spectra. This removal relies on an algorithm where the stray light pattern is estimated based on a linear combination of the spectra collected from those matrix lines where no stellar signal is observed.

This updated calibration allowed the regeneration of the full SPICAV dataset of atmospheric transmission spectra.

The second step concerns the spectral inversion problem, which has been developed to find optimal parameters needed to fit calibrated atmospheric transmissions with a forward model including detailed spectroscopy of all target gases, as well as a representative instrumental function. Slant density of the trace gases (SO_2 and O_3) integrated along the LOS is sometimes too small to produce a firm detection by SPICAV UV. For this reason, a specific approach was developed to establish detection limits for O_3 and SO_2. On average, these limits are found to be

- $N_{SO2} = 5.8 \pm 0.2\ 10^{15}$ cm^{-2};
- $N_{O3} = 3.3 \pm 0.1\ 10^{15}$ cm^{-2}.

A ClO absorption band is also present in the spectral range covered by the SPICAV UV channel. However, attempts to detect it proved unsuccessful. The detection limit of ClO is 3-4 times higher than the one for ozone, that is on the order of 10^{16} cm^{-2}.

CHAPTER 4. Sulphur dioxide

4.1. CO_2 and SO_2 retrievals: from column abundances to profile and its variability.

Vertical profiles of the linear concentrations of CO_2 and SO_2 were retrieved for 375 observation sessions that fulfilled the following criteria:

- Level 1 "clean" data did not include any NaN value;
- the session was performed at a solar zenith angle exceeding 95° to minimize possible contamination by the scattered solar light;
- stellar signal was successfully separated from "stray" light component.

The filtered observations correspond to the period from June 2006 to December 2014, covering all longitudes and latitudes from 80ºS to 80ºN. The local solar time coverage corresponds to the whole night period from 18:00 to 6:00 (Figure 4.1).

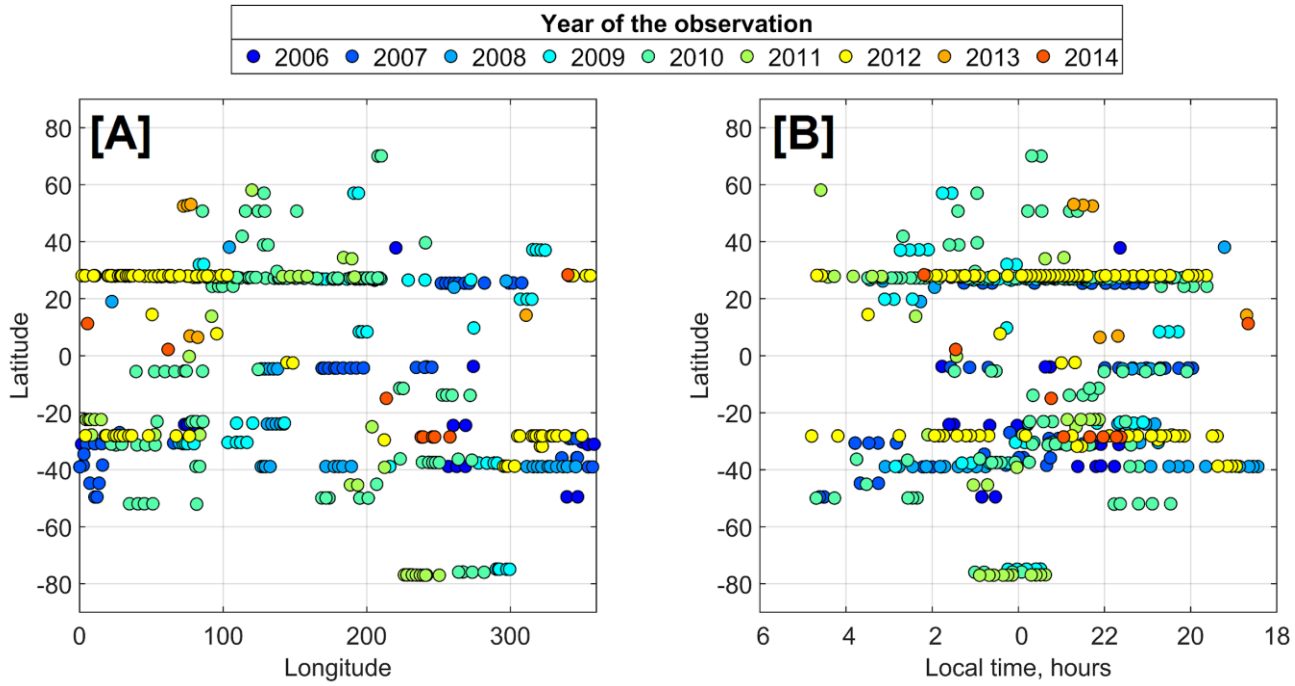

Figure 4.1. (A) Spatial distribution of observed positions of the target point. (B) Local time and latitude coverage achieved by SPICAV UV.

The instrument was capable of detecting atmospheric absorption from an altitude of 145-150 km to an altitude of 82-85 km. The maximum and minimum values are given in ranges as they depend on the noise of the transmission spectra. The minimum height also depends on the aerosol density in the path of the line of sight; the aerosol scattering determines the lower boundary of the experiment in this spectral range. In order to be consistent in analysing the results, this paper considers the range of heights from 145 km to 83 km. However, the resulting profile of the CO_2 slant density was checked for a possible bias in the lower studied layers. If any were obtained, the results were excluded from consideration and the following calculations at the particular altitude. For each occultation session, the detection limit for

sulphur dioxide was also calculated in the range up to 110 km. In Annex 1 there are the obtained profiles of the linear concentrations of CO_2 and SO_2 and the SO_2 detection limit if the gas is not detected for each individual session (Figure A1.1)

Vertical profiles of the volume concentrations of CO_2 and SO_2 were sequentially retrieved by the «onion-peeling» algorithm. In stellar occultations by SPICAV UV, the values are obtained with height steps from ~1 km to ~8 km, which are inversely proportional to the distance of the spacecraft to the target point. For sparse profiles containing just a few points the inverse problem of volume concentration computation is calculated directly. When achieving a good altitude coverage, the "onion-peeling" method is implemented with the Tikhonov's regularization. However, the SO_2 local densities are retrieved with the regularization if the gas was detected in more than 4 spectra of a particular observational session.

4.1.1. Carbon dioxide distribution in the upper mesosphere and the lower thermosphere.

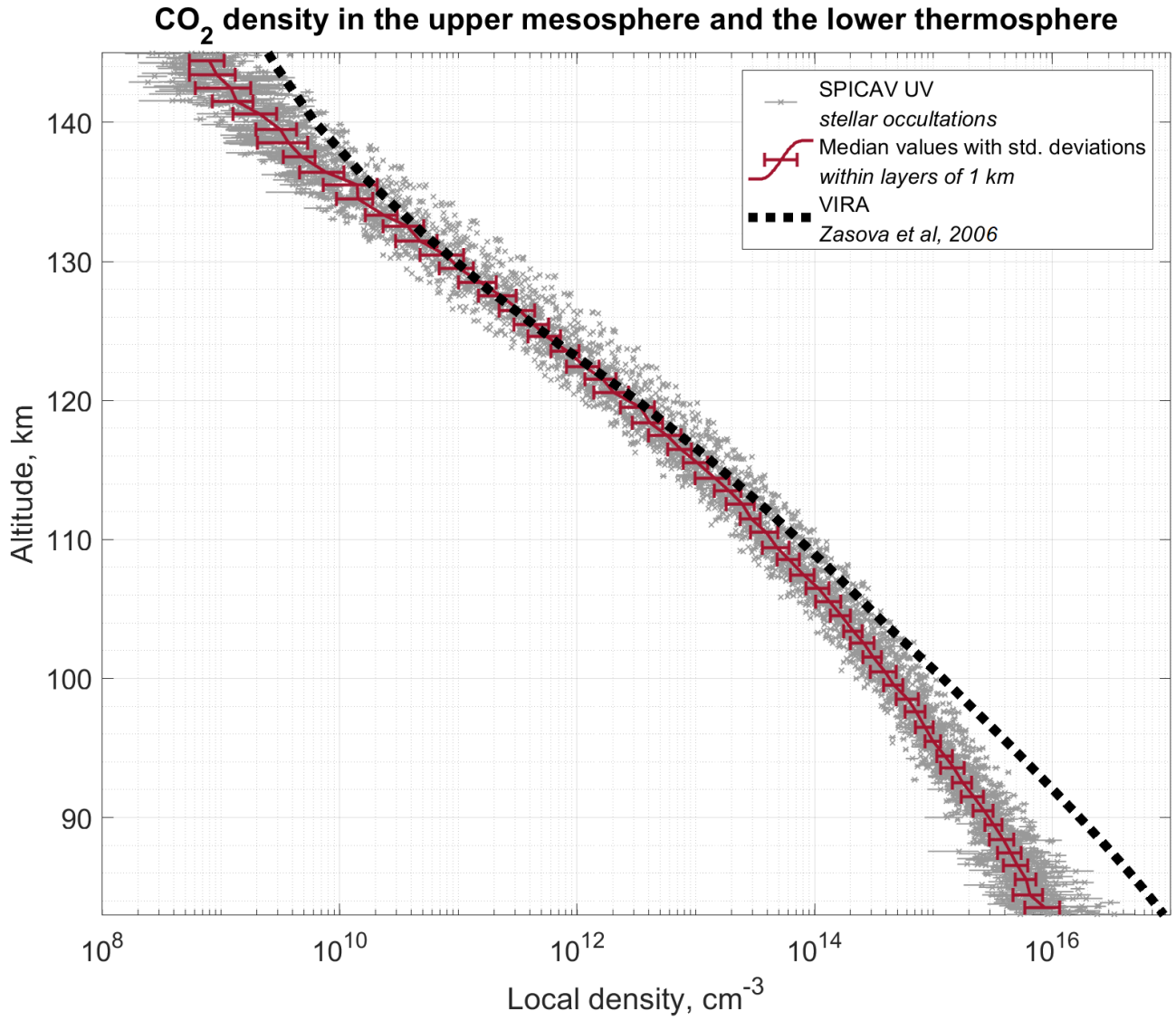

Figure 4.2. Individual profiles of the CO_2 local density accompanied by the median values estimated per 1 km. The median profile (wine red curve) is shown with the standard deviation within each layer. The dotted line corresponds to the VIRA database (Zasova et al., 2006; Seiff, 1985).

The most abundant Venusian gas is tracked in the whole altitude range of 83-145 km. Its height dependence is in agreement with the results of previous analyses of stellar occultation data. Based on the obtained altitude profiles, it is possible to supplement the study of temperature changes at these altitudes. We observe that the observation results agree with the VIRA-2 (The Venus International Reference Atmosphere) database for the main atmospheric parameters only within the thermosphere. The VIRA was recently completed with data from measurements of the vertical temperature profile by the VEGA spacecraft with high precision and high altitude resolution; measurements made with balloons of the VEGA spacecraft; radio occultation measurements of Magellan, Venera-15, and Venera-16; and temperature profiles derived from the data of infrared spectrometry obtained by Venera-15. The resulting profiles up to 100 km are local time dependent, higher altitudes remain as in Seif (1985). The comparison is made for the anti-solar point.

In the upper mesosphere, below 110 km, the profile differs significantly from the VIRA values. At these altitudes, a scale height of 4.25±0.05 km was obtained while for VIRA it is about 4 km.

4.1.2. SO_2 in the upper mesosphere

Spectral inversion was applied to each spectrum as described in Section 3.3.6 and cases of positive SO_2 detection were established (Section 3.3.6.1). Most of the $\delta\chi^2$ values for positive gas detections were lower than 0.85. These values correspond to a χ^2 reduction of more than 20% after including SO_2 abundance as a free parameter in the fitting model. Thus, the SO_2 retrieved values correspond to firm detections, enabling further statistical inspection of the SO_2 dataset.

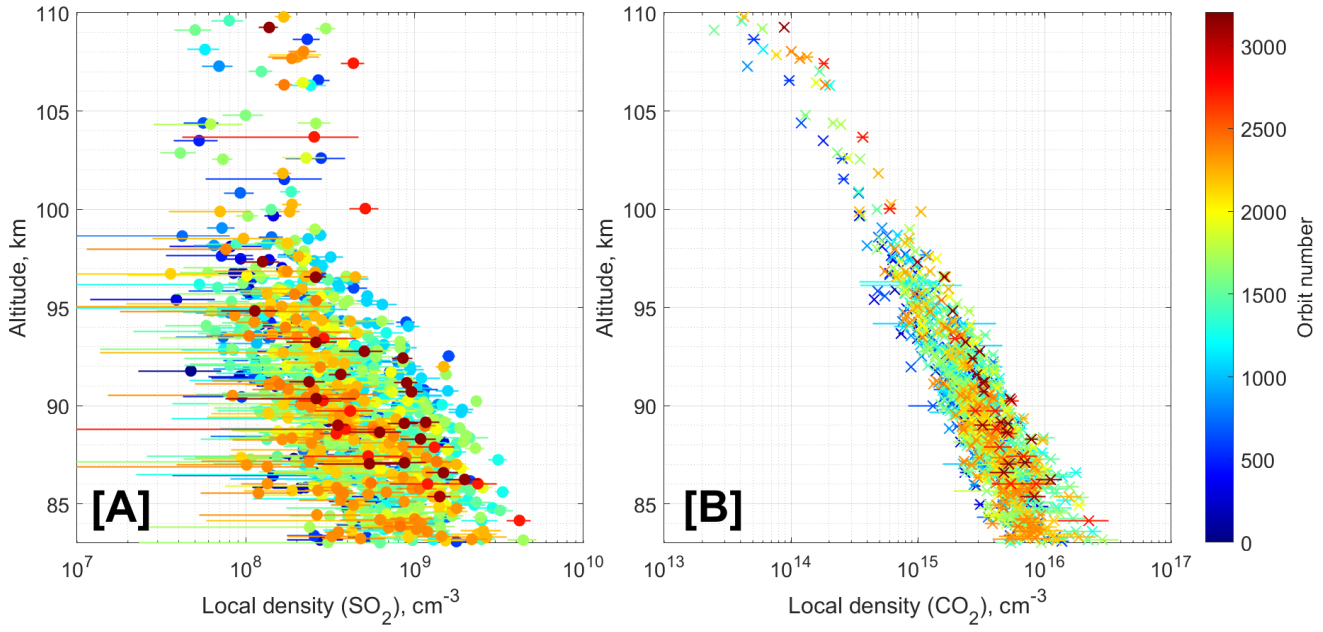

Figure 4.3. Night-time vertical distribution of SO_2 (A) and CO_2 (B) local densities retrieved from the entire SPICAV UV dataset.

Altitude profiles of the slant densities of SO_2 were vertically inverted to obtain profiles of their volume densities. All retrieved points are plotted on Figure 4.3. In general, a large variability of SO_2 concentrations are observed. The estimated mean scale height for sulphur dioxide volume concentrations

is 6.1±0.1 km corresponding to the 85-95 km altitude range where the major amount of retrieved values is concentrated.

The observed variability of SO_2 is large, with concentrations varying by one order of magnitude at a given altitude. No particular feature emerges from the consideration of the ensemble of values plotted within the 85-100 km altitude range. Over 100 km the majority of observation signifies the achievement of a detection limit (Figure 2.19) so the detected values correspond to particular occurrences of SO_2 high abundances.

4.2. SO_2 profiles: Comparison with data from previous studies.

To estimate a mean profile of SO_2 VMRs, retrieved values were grouped in 2 km altitude bins and a median was computed in each layer. Figure 4.4A presents the vertical distribution of the SO_2 volume mixing ratio (VMR). In the altitude range from 84 to 100 km, the median value is nearly constant around 120-160 ppb, while above 100 km the approaching of detection limit results in an increase of the VMR up to 300 ppbv (Figure 4.4A). Therefore, this increase has an instrumental reason but not the physical nature. The further analysis will be performed for the values obtained in the altitude range from 85 to 100 km where the majority of SO_2 detections are found (Figure 4.4 B1-B4).

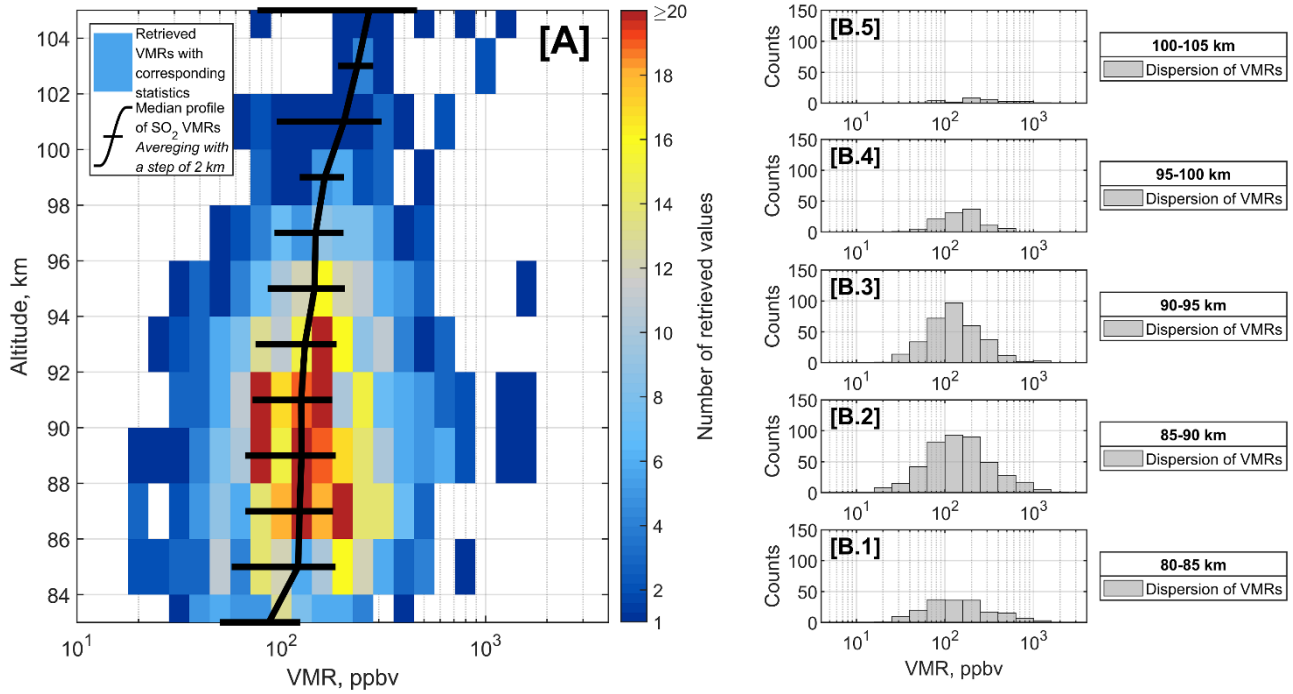

Figure 4.4. (A) Median profile of night-time SO_2 volume mixing ratio derived from SPICAV UV (black curve with standard deviation). The colours refer to the number of points included in one bin of 2 km size. (B.1-B.5) The five right panels are histograms representing the distribution of values within layers of 5 km thickness. Colour scheme displays statistics of VMRs with altitude for cells of a width of 0.1 in a logarithmic scale, i.e. $\log_{10}(10^{0.1}$ ppbv).

The first results on SO_2 from the processing of stellar occultations by SPICAV UV were first published in Belyaev, Evdokimova et al. (2017), where they were analysed in combination with the results of solar occultations. Thanks to a deeper reappraisal of calibration methods, the results were subsequently revised and augmented by retrievals from the rest of available occultations left unanalysed. The

reanalysis led to the suppression of the previously reported SO_2 VMR increase with altitude (Belyaev, Evdokimova et al., 2017), where values were found to increase from 20±10 ppbv at 85-95 km to 200±100 ppbv at 100-105 km (Figure 4.3; Individual profiles for each session are presented in Annex 2, Figure A1.2). In particular, retrieved CO_2 abundances revealed themselves to be very sensitive to wavelength calibration (Evdokimova et al., 2020), which eventually affected SO_2 VMR determination, especially below 115 km, where CO_2 absorption saturates.

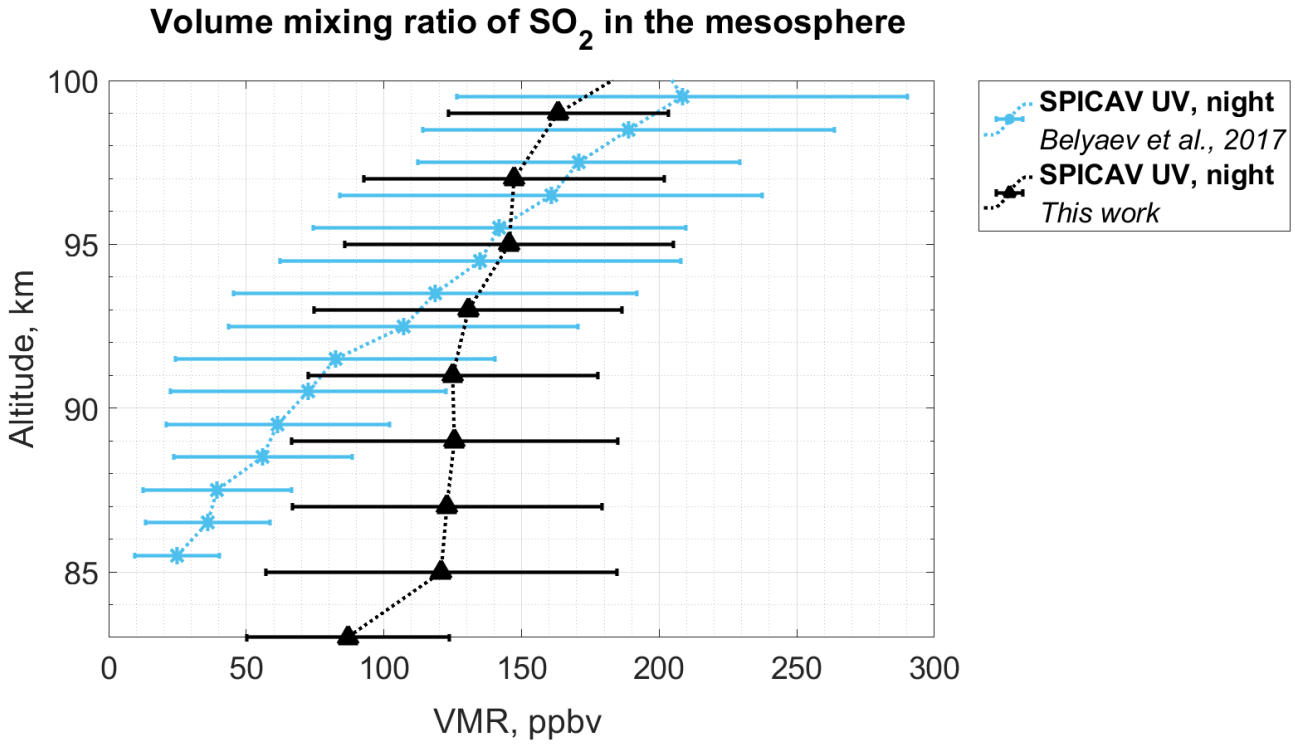

Figure 4.5. The overview of mean vertical profiles of SO_2. The black dashed curve is the current work, the blue one was obtained by Belyaev, Evdokimova et al. (2017) which did not include calibration improvements.

There are two factors that caused the differences in the obtained values (Figure 4.5). Previously, the analysis used the altitude assignment following the solar occultation scheme, i.e. the parameters were considered based on the LOS from the centre of the 3rd bin. That resulted in shifted altitudes of the slant density profiles of both species. In general, the spectral inversion problem does not depend on altitude itself. However, the altitude determination is crucial for the vertical inversion computing local densities of both species.

The second factor is a combination of two calibration methods investigated in Chapter 2. However, the study of Belyaev, Evdokimova et al. (2017) also used a wavelength to pixel assignment based on stellar lines. However, the 3 parameters of parabolic law were fitted instead of as in the current approach. The limitation of a free parameters number is a necessary measure. The stellar lines are more pronounced in the short-wavelength range that is limiting the accuracy of the second order parameter determination. Thus, the difference of the wavelengths at the edge of the CO_2 absorption band is about one-pixel width, which is significant as it was displayed before (Section 3.2.8). The stray light elimination has changed as well, however, it was concluded that it mainly impacted the statistics of good detections.

The consideration of these factors are displayed in Figure 4.6. The major and significant change of 25% was obtained for the CO_2 slant densities and it grows to 50% below 90 km. For SO_2 the difference is less pronounced considering its variations. However, if the previously reported values are considered with the precise altitude assumption the wavelength uncertainty impact is pronounced. For CO_2 absorption it decreases with altitude but remains significant (>20%) in the deep layers. For SO_2, it signifies that results of new data processing are slightly more abundant in absolute values than reported previously. It is mainly related to the intersection of the CO_2 and SO_2 absorption bands.

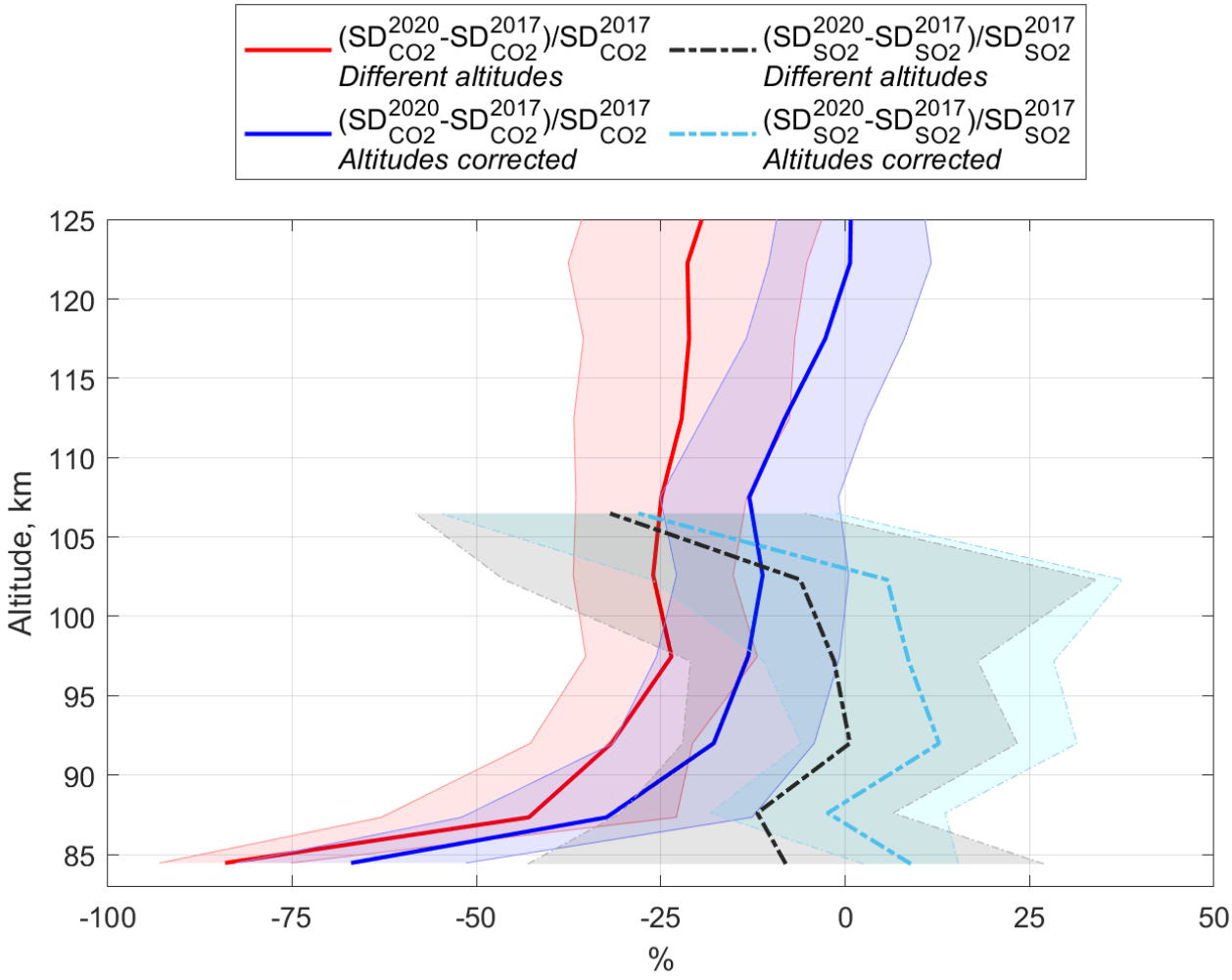

Figure 4.6. The change in slant densities values after implementation of the new wavelength to pixel assignment and reconsidered geometry definition. Solid lines correspond to a CO_2 slant density modification, dashed-dotted lines to SO_2. The red and black lines correspond to the total change in the values. The blue and cyan colours estimate new calibrations impact since the geometry is taken as in the current analysis.

Figure 4.6 explains why the main differences between the older and the updated SO_2 retrieval are located below 95 km, whereas above SO_2 VMRs are more in agreement. In contrast, at 85 km, the difference between our estimates and those of Belyaev, Evdokimova et al. (2017) reaches a factor of 10. In addition, the VMR is calculated by dividing the SO_2 density to CO_2 density with both values retrieved simultaneously.

The obtained altitude profile of the SO_2 VMR is the only such detailed scan obtained over clouds in these altitude ranges on the night side. However, two ground based facilities were also able to detect SO_2 absorption at similar altitude ranges of the night and day sides. They are the James Clerk Maxwell Telescope (JCMT) in several campaigns in 2004-2008 and the Atacama Large Millimeter/submillimeter Array (ALMA) in 2011 (Sandor et al., 2010; Encrenaz et al., 2015). Both worked in the sub-millimeter range. JCMT measured simultaneously two lines 346.652 and 346.524 GHz, and ALMA measured 346.652 GHz (~0.86 mm). These observations gave a result within 85-100 km and 88-100 km respectively and they are compared with the SPICAV UV results.

On average, VMR is found to remain around 135±21 ppbv in the 85-100 km altitude range. This value is at >2 times higher than the maximum VMR of 66±2 ppbv at 85-100 km reported by JCMT in Sandor et al. (2010). A smaller value, 12±4 ppbv in the 88-100 km range was reported by Encrenaz et al. (2015) using ALMA observations. Sandor et al. (2010) also showed that the SO_2 abundance in the 85-100 km range is much larger than in the 80-85 km range, suggesting the presence of a strong sink of SO_2 below 85 km.

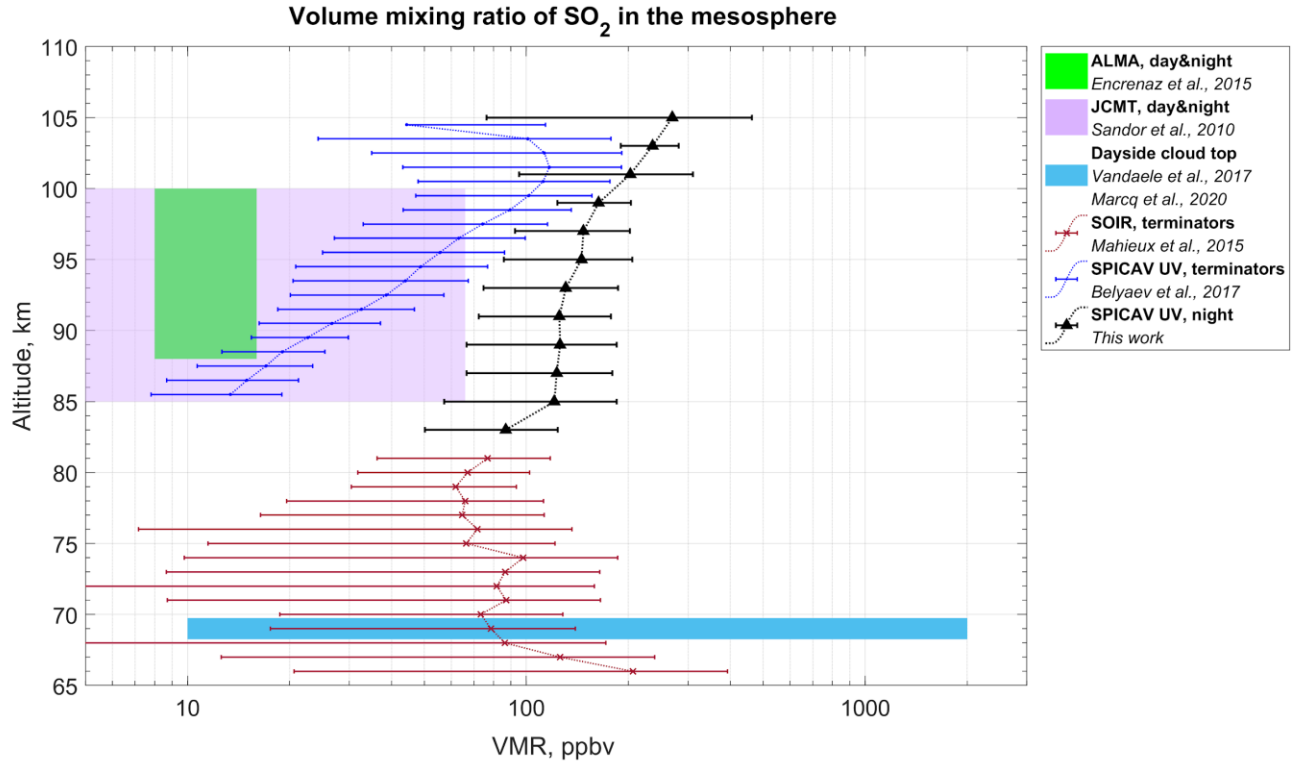

Figure 4.7. Overview of the SO_2 vertical distributions obtained by different instruments above the clouds. Curve styles and colours are given in the legend box. Vertical median profile of the SO_2 VMR obtained in this work (black triangles) is binned by 3 km. All the occultation results are presented with a dispersion of ±1 σ.

Solar occultation by SPICAV UV provided the altitude profiles of SO_2 VMR at the evening and morning terminators at 85-105 km that completed the night side data coverage by local time. SO_2 abundance obtained in the SPICAV UV solar occultation increases significantly in the altitude range of 85-100 km in comparison to the night observations. On average, measured SO_2 volume mixing ratio changes with altitude from 8-20 ppbv at 85-90 km to 50-180 ppbv at 100 km (Belyaev, Evdokimova et al., 2017).

However, in the latitude distribution, observed locations are concentrated in the north polar region while the stellar occultations mainly observed mid-latitudes. So it may be suggested that the processes on poles slightly differ from those in mid-latitudes. However, further study is needed to clarify the differences between mean profiles of terminator and night side. The consideration of overall profile revealed by ALMA observations (Encrenaz et al., 2015) are lower than the minimal values obtained at terminator.

The both considered ground based facilities report a high variability of SO_2 VMR in the observed regions. In different observations JCMT measurements reported variations of more than two orders of magnitude. Moreover, in some sessions the gas was not detected that corresponds to its abundance in particular case being lower than 2 ppb.

Sub-mm signal emanates from the superimposition of the thermal emission coming from different altitudes. UV's observations are probably less sensitive to temperature uncertainties compared to the thermal IR, however, the temperature sensitivity in the UV was not studied. However, such a strong difference between occultations and sub-millimetre (sub-mm) measurements could be partially related to the temperature uncertainties which is a critical parameter of sub-mm data retrieval.

Below 83-85 km the atmosphere becomes too opaque for UV stellar occultation. The most of measurements of occultations in UV was supported by the IR spectrometer SOIR (Mahieux et al., 2015) on board Venus Express. It explored the altitude range from 65 to 85 km. Similar to SPICAV UV occultations the vertical resolution of its observations is rather detailed. Since SOIR exclusively performed in solar occultation mode by design, it allows one to examine also the terminator regions in 65-85 km. The solar occultation data obtained by SOIR benefits from simultaneous temperatures and SO_2 abundances measurements. The IR spectra concluded the SO_2 abundance in the 65-85 km range (Mahieux et al., 2015) with a minimum of 60 ppbv detected at 70-80 km. However, the observations are followed by significant uncertainties, that are on average ~ 80%.

In theoretical description there is a lack of models particularly designed for the night atmosphere. The only one mesospheric model was developed by Krasnopolsky (2010, 2013). In this model the lower boundary is 80 km, where the SO_2 abundant is set. The estimated altitude profile remains stable and equal to 100 km. This result is in good correspondence with the average profile obtained in this study.

The diurnal averaged 1-D models by Zhang et al (2010), Zhang et al (2012) aimed to reproduce the minimum of SO_2 VMR at 70-80 km in mid-latitudinal and polar regions and Krasnopolsky (2012) are also considered. From these models the result presented in Zhang et al (2012) is in correspondence with both SPICAV UV stellar occultation and SOIR IR solar occultation results. The model represents the diurnal average of SO_2 at 75°N latitude. However, the processes in this altitude range (80-100 km) require a 3-D model which would be able to reproduce a complex dynamic of the region.

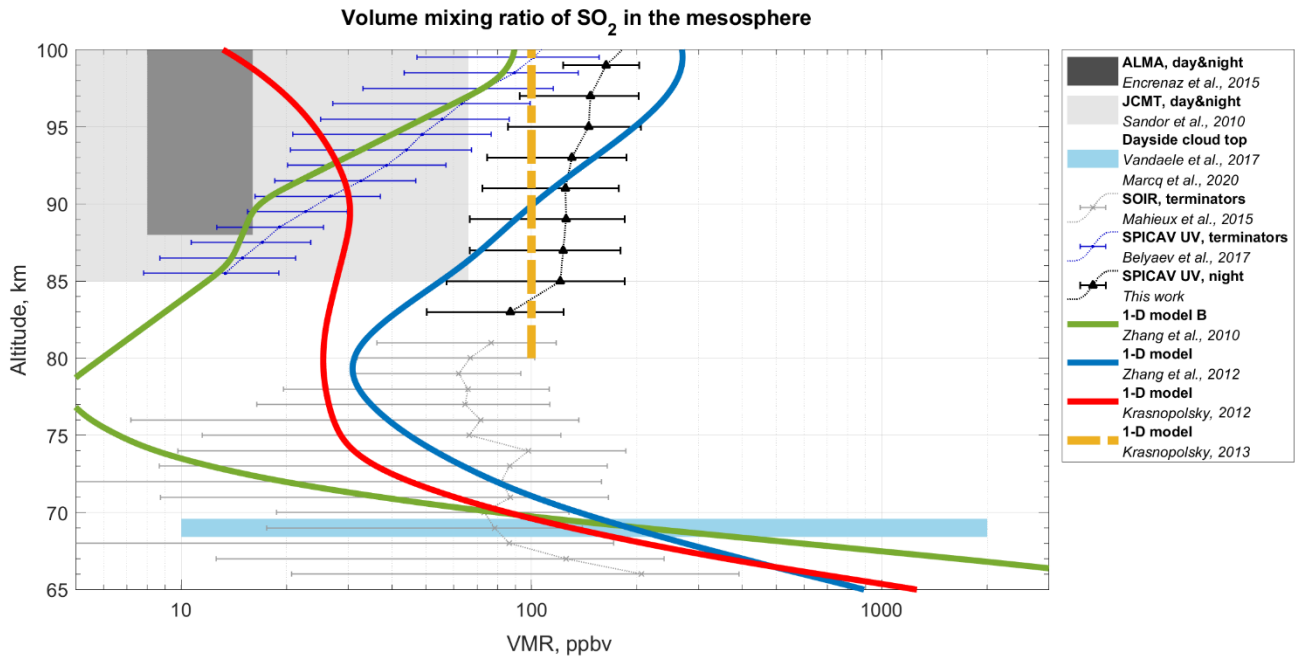

Figure 4.8. Overview of the SO_2 vertical distributions obtained by different instruments above the clouds. Curve styles and colours are given in the legend box. Vertical median profile of the SO_2 VMR obtained in this work (black triangles) is binned by 3 km. All the occultation results are presented with a dispersion of ±1 σ.

4.3. Variations of SO_2 mixing ratio

The volume mixing ratio of SO_2 displays a significant variability (Vandaele et al., 2017a; Vandaele et al., 2017b). The same result is corroborated by stellar occultations, which probe the night side.

The stellar occultation's dataset allows one to examine the dependence of SO_2 to a variety of parameters. Other observations of the Venus upper atmosphere have revealed spatial patterns that are tied to pairs of parameters: (1) local time and latitude, and (2) latitude and longitude, and time dependencies: (3) long term trends and (4) local time variations.

The dataset does not cover the night-time hemisphere in detail limiting the scope of our study of the SO_2 spatial distribution. Figure 4.1 contains an overview of all the locations where the SO_2 was obtained at any altitude. The best coverage is achieved along both long term and diurnal dimensions. To be consistent, the following analysis has been restricted to SO_2 and CO_2 concentrations with less than 50% uncertainty.

4.3.1. Short term variations

An overview of all profiles retrieved from the SPICAV UV stellar occultations point out significant changes in SO_2 content in short time scales. The changes reach an order in magnitude and highly probable that their reasons link to dynamical perturbation in the mesosphere. The same conclusion was made based on the SPICAV UV solar occultations dataset. Some individual profiles (Belyaev, Evdokimova et al., 2017) with better vertical sampling show a complicated structure. In solar occultations where the SNR remains high and stable, a series of measurements observing the same region showed perturbations akin to a gravity wave propagation.

The four sets of sequential observations made at the same latitude and at similar local time were considered. These sets also represent detected profiles of SO_2 instead of individual detections. They definitely reveal these turbulence effects. The gravity wave propagation may be expected as a plausible cause for explaining similar features in particular profiles. Moreover, the wave structure is probably detected in occultation #1683A03, while 48h before (occultation #1681A05) this pattern was not detected. Our observations are inferior to solar observations in terms of resolution in height and noise level. Therefore, for other sets of profiles, such disturbances can only be presumed.

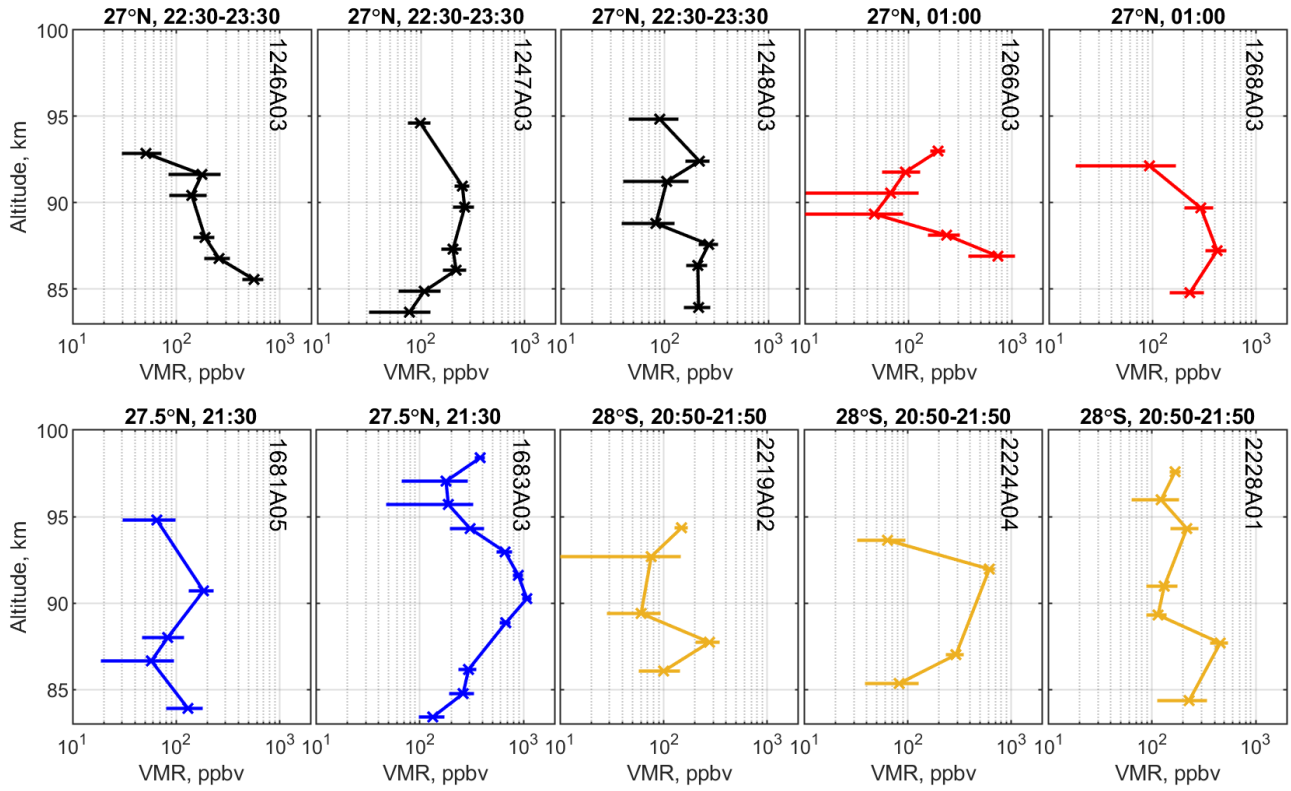

Figure 4.9. Stellar occultations that are sequential in time obtaining retrieved SO_2 volume density profiles with a small vertical step. The observations of one set were made at one latitude and at similar local times. More geographical parameters are presented in Annex 3.

4.3.2. Long term variations of SO_2 mixing ratio.

Long-term variations were considered based on the retrieved SO_2 content (Figure 4.10 A1 and A2). We analysed annual variations of SO_2 abundance grouping the values by 4 months' intervals and deriving a weighted mean (Equation A4.3 in Annex 4) for each interval. Short (<4-month) term variations are found to be larger than the long-term variations. One can however distinguish two periods of higher VMR values, before 2010 and after that, with a minimum located around 2010. A decrease to the end of the mission (2014) can be also seen (Figure 4.10 A2).

The previously reported SO_2 evolution at 90-95 km near the terminators showed several periods of VMR increases accompanied by sharp decreases. However, a steady reduction during the entire mission period was not reported (Figure 4.11).

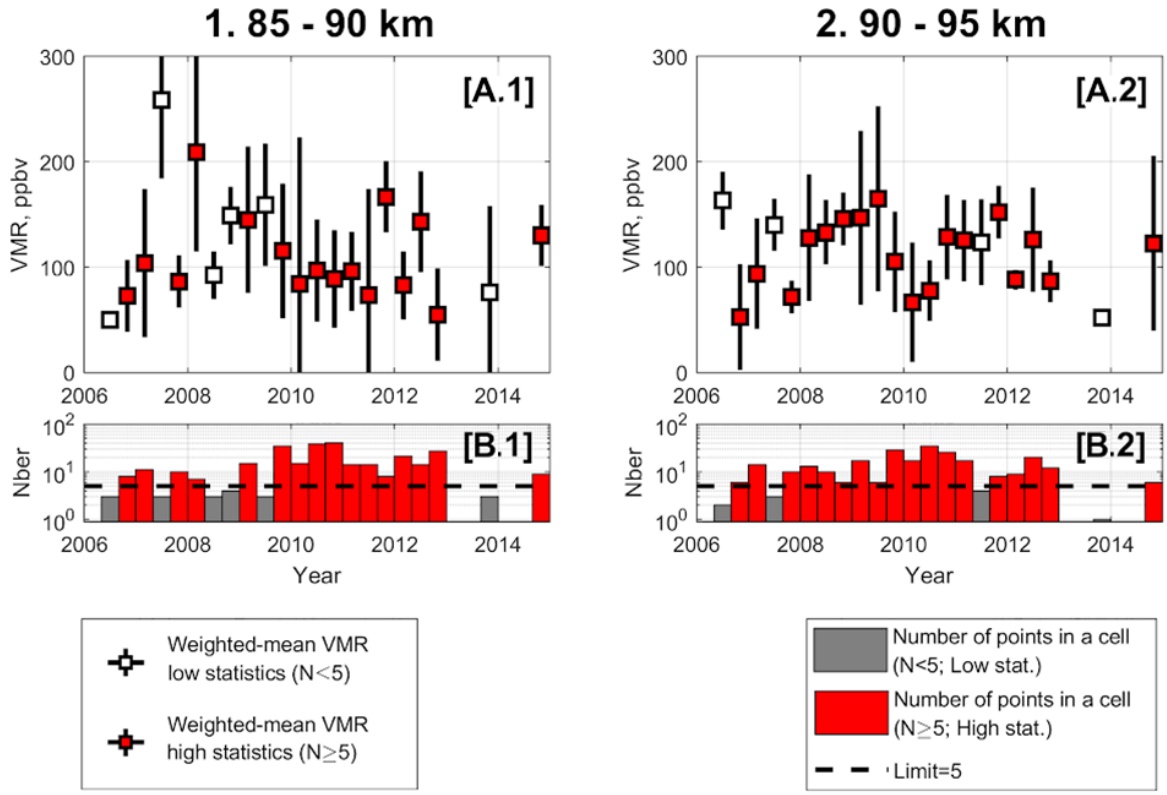

Figure 4.10. A1 and A2: Weighted-mean SO_2 VMR evolution with time for two altitude ranges: (1) 85-90 km and (2) 90-95 km. The data are binned by 4 months. Red and white squares include ≥5 and <5 individual points respectively. Standard deviation from the mean of the bin is indicated by the black vertical bar. The B panels represent the number of individual points for one bin. Black dashed lines in the histograms correspond to the level of 5 points.

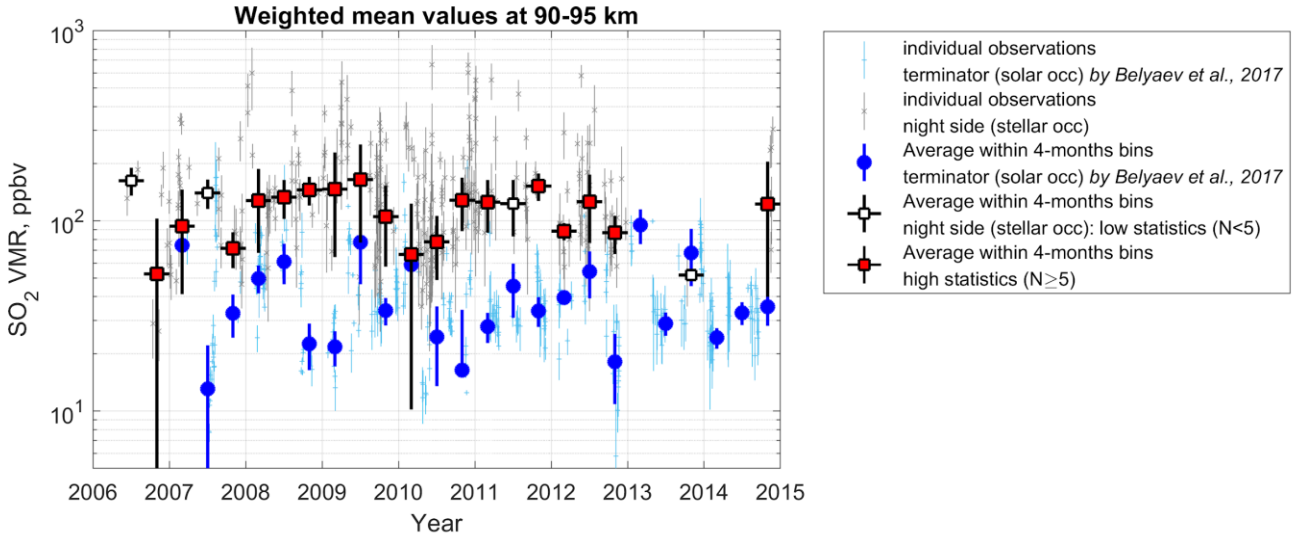

Figure 4.11. Long-term evolution of SO_2 VMR within 90-95 km corresponds to a pressure level of ~ 0.1 mbar in a comparison with the values of a same altitude range retrieved at the terminator from solar occultation spectra by SPICAV (Belyaev, Evdokimova et al., 2017).

The other long-term trend of SO_2 is based on SPICAV UV nadir observations. In this geometry, the instrument observes the vertically-integrated column density of SO_2 over the cloud tops (~ 70 km). In this set of observations, the SO_2 short-term variations were also significant (as represented by the yellow area on Figure 4.12). However, the median curve calculated on the full set of data shows a decrease of SO_2 VMR toward the end of the mission (Marcq et al., 2020) which is confirmed by UV observations by STIS/HTS (Jessup et al., 2015) and IR observations by the TEXES instrument (Encrenaz et al., 2012; Encrenaz et al., 2016). The 85-90 km range is the lower robust one provided by stellar occultations. In general, the similarities in behaviour of trends at different altitudes are not obtained. The night observations on average do not follow a specific pattern, and there are not pronounced maxima or minima as observed on the day side. Moreover, the stellar occultation data do not have enough coverage to confirm or deny the behaviour around the second local minimum observed in 2014 in nadir.

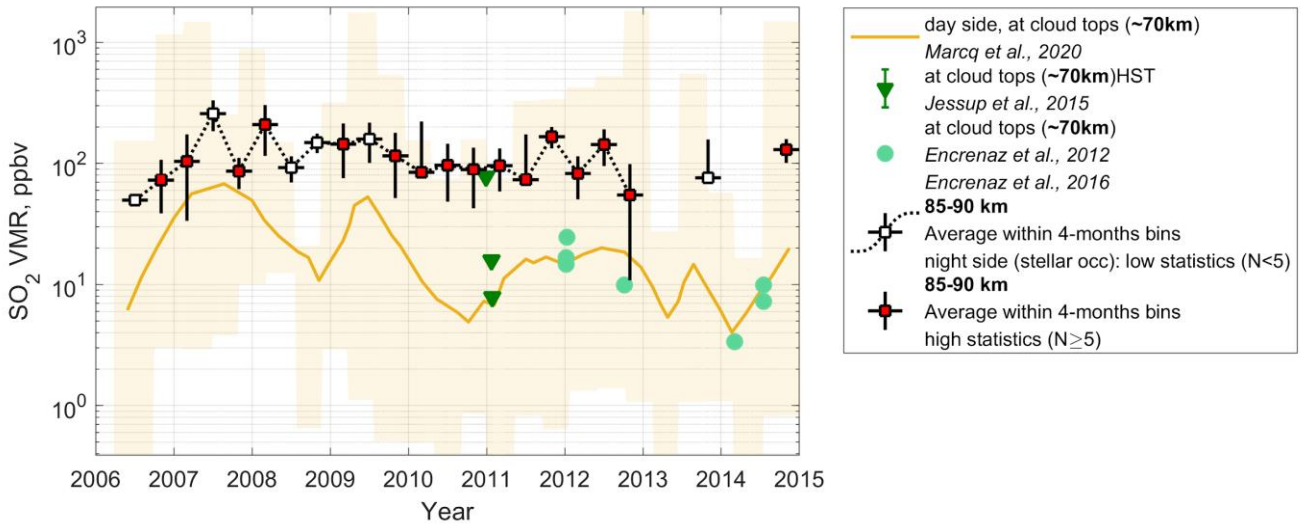

Figure 4.12. Long-term evolution of SO_2 VMR within 85-90 km compared with daytime values derived from nadir monitoring and converted into a mixing ratio at an altitude of ~70 km (cloud top) from SPICAV UV spectra (Marcq et al., 2020). Also shown are the TEXES IR observations of Encrenaz et al., 2012; Encrenaz et al. (2016) and the HST/STIS UV observations of Jessup et al. (2015).

4.3.3. Diurnal variations of SO_2

The whole dataset was explored to identify any hint of a diurnal variability in SO_2 VMR. The data was split by 30 minutes' intervals. The weighted mean (Equation A4.3 in Annex 4) was calculated within each bin. We selected two 5-km thick layers where retrieved values are more numerous (see Figure 4.4 B.2- 4.3 B.3). The analysis considers the number of points constituting the average values in each bin which are represented by histograms below the distribution (Figure 4.13 B.1-4.12 B.2). There is a slight VMR increase from 02:00 AM toward the evening terminator in the 90-95 km range: from 90±40 ppbv at 2h to 115±25 ppbv at 20h (Figure 4.13 A.2). On the other hand, we do not observe any monotonous change in the 85-90 km range (Figure 4.13 A.1) in frames of the statistical dispersion.

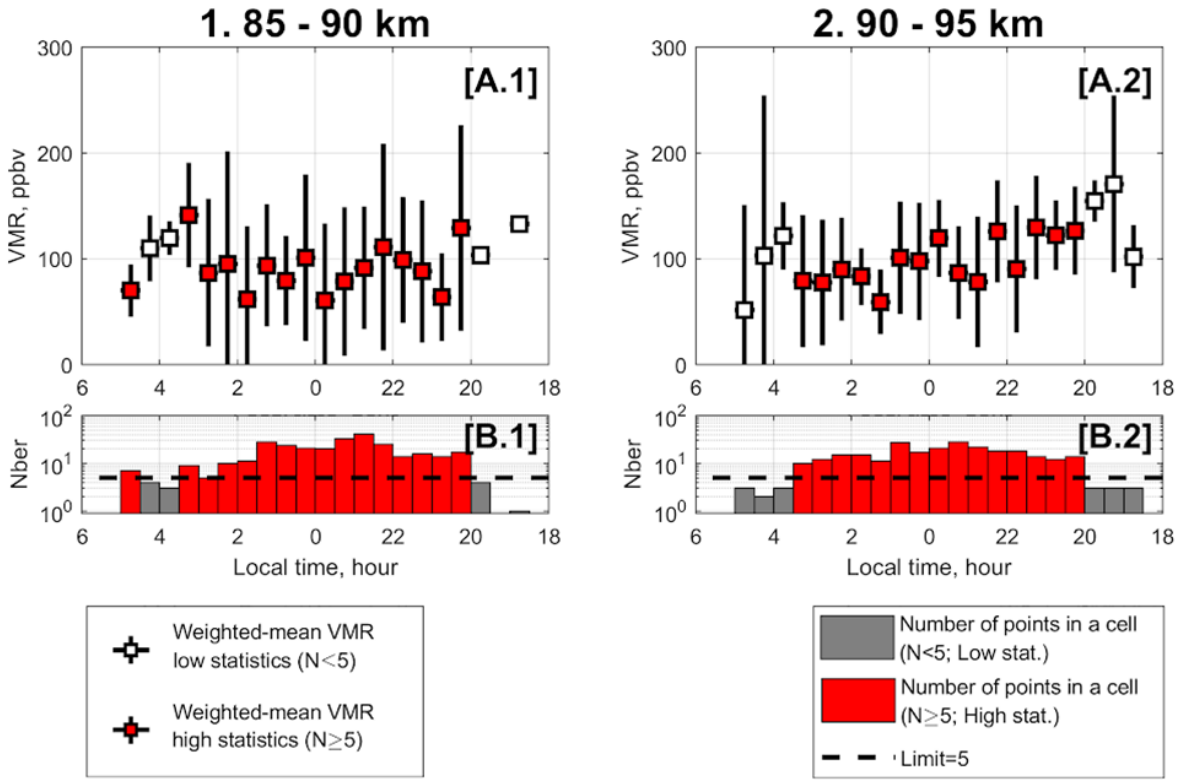

Figure 4.13. A1 and A2: Weighted-mean SO_2 VMR variations with local time for two altitude ranges of 85-90 km (1) and 90-95 km (2). The data are binned by 30 min of local time. Red and white square bins with statistical dispersions include ≥5 and <5 individual points respectively. The B panels represent the number of individual points for one bin. Black dashed lines in the histograms correspond to the level of 5 points.

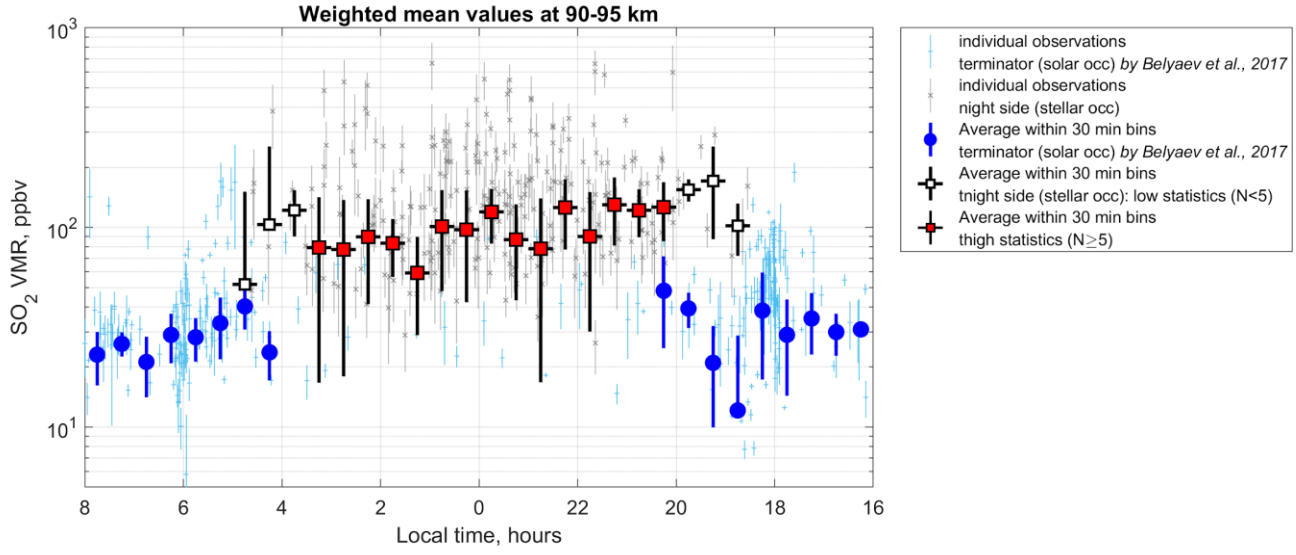

Figure 4.14. Local time evolution of SO_2 VMR at 90-95 km retrieved from stellar and solar occultations observed by SPICAV UV.

When combining the datasets obtained in stellar (night) and solar (morning/evening) occultations, an increase of values in the night side can be identified. The factor of 3 to 4 day-to-night difference is likely explained by the absence of SO_2 photolysis during the night. The comparison of local time variations of the SO_2 VMR within 90-95 km is shown on Figure 4.14. The values do not coincide between the evening

and the morning regions. Nevertheless, points at 4:30-5:00 and at 18:30-19:00 correspond to the expected decrease of SO_2 VMR. Nevertheless, the data coverage of stellar occultation is poor around 4:00-6:00 and 18:00-20:00 due to increase of solar light contamination of spectra as is presented in Figure 4.14 B.1-B.2 and it is preventing the firm conclusion about the divergence of results of stellar and solar occultations. Moreover, solar occultations were mainly restricted to the latitudes poleward 80°N.

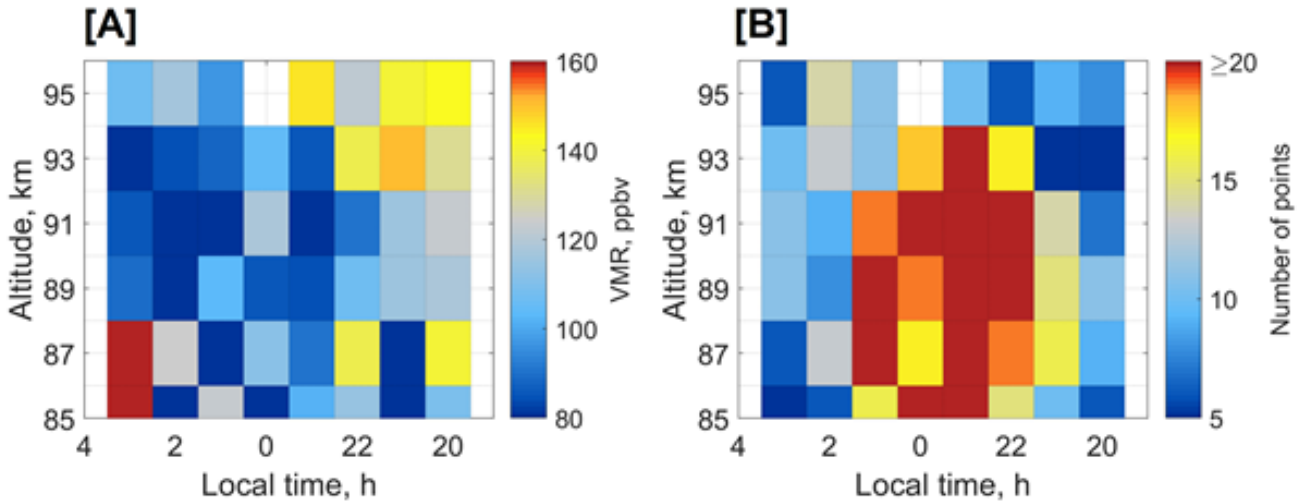

Figure 4.15. (A) Local time evolution of SO_2 VMR depending on the altitude. The values are grouped and averaged within a bin of 1h and 2 km. The bins combined with more or 5 values are considered. (B) Corresponding number of points in a bin.

The studied altitude region of the upper mesosphere corresponds to the place of transition between two global circulation regimes. The first is a fast zonal rotation below 70 km and the second is the SSAS. Our dataset is too sparse to provide a detailed distribution of SO_2 with local time, latitudes and altitudes, but it is however possible to track the altitude versus local time dependence. To this end, we mapped data over a grid of ½ h increment in time and 2 km increment in altitude. For each bin, a weighted-mean value was calculated (Figure 4.15A). Below 88 km, SO_2 is distributed rather fuzzily and any local time dependence is not concluded. The pattern is changing between 88 and 96 km. There is a constant decrease of VMR from evening terminator to 2H00 at night where a minimum is observed. The maximum values are observed between 20H00 and 22H00 at night and the minimum values are observed around 2H00 at night. Moreover, the values are growing with altitude keeping the same pattern.

Such behaviour is puzzling. It should be noted that a similar asymmetry was recently deduced from a study of the Venusian atmospheric circulation in the 90-110 km range based on tracking the oxygen emission features (Gorinov et al., 2018). Velocities of two opposite flows in zonal directions from evening and morning terminators towards midnight reach zero values around 22H30±00H30. This asymmetry in the zonal flow should affect the chemical species involved in the SO_2 photochemistry, such as chlorinated species and oxygen atoms.

4.3.4. Geographical distribution of SO_2

4.3.4.1. Local time and latitude distribution

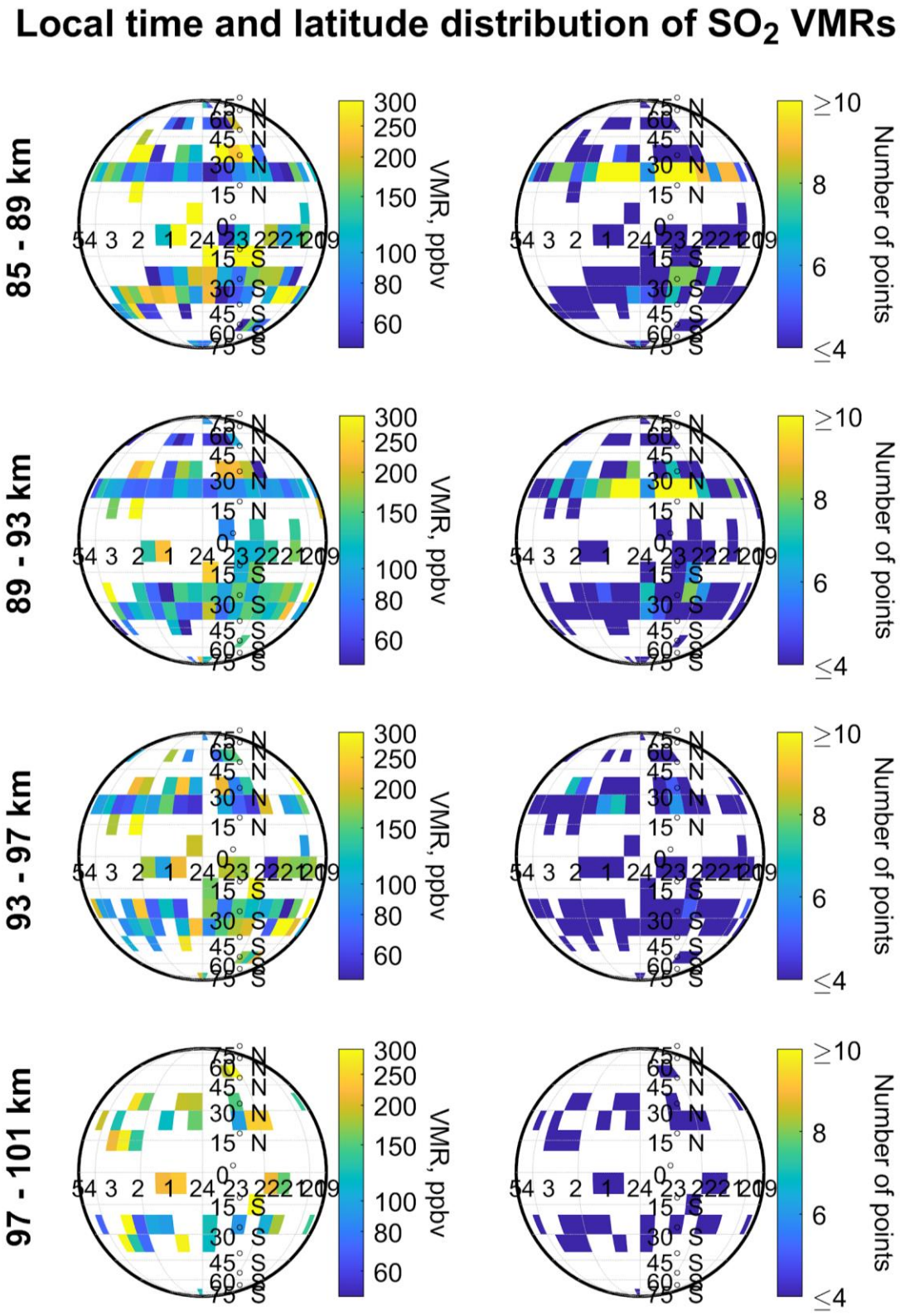

Figure 4.16. Left panels: local time and latitude map of SO_2 VMR distributions. The values are binned by 10° of latitude and 30 minutes. The right panels represent the data statistics used to calculate mean value in each bin.

A global map of SO_2 is difficult to assemble considering that observations were mostly clustered in the mid-latitudes of both hemispheres. Figure 4.16 displays maps in four different altitude ranges of 4 km wide from 85 to 101 km. The data obtained in each altitude range was grouped in 30 minute bins and 10° in latitude. A weighted mean (Equation A4.3 in Annex 4) was calculated in each bin. Each map is accompanied by the information on the number of points per bin.

Figure 4.16 shows that SO_2 peaks always correspond to low statistics. Thus, any attempt to separate the temporal and spatial distribution of SO_2 in the upper mesosphere is impossible with our dataset. Instead, characterizing the dataset in terms of SZA becomes meaningful since it merges local-time and latitude into a single parameter.

4.3.4.2. Variations with a solar zenith angle

We consider only deep night side observations with SZA>95°. Unfortunately, the SZA range of 160°-180° was too rarely observed to be statistically significant. Figure 4.16 presents the VMRs with respect to SZA values, with data divided into 4°-wide bins along the SZA dimension. The weighted-mean values and corresponding standard deviations were calculated within each bin. The minimum of VMRs was noticed in the 120-150° range while slightly higher values were measured around 110° for the both altitude intervals (Figure 4.17 A.1 and 4.17 A.2).

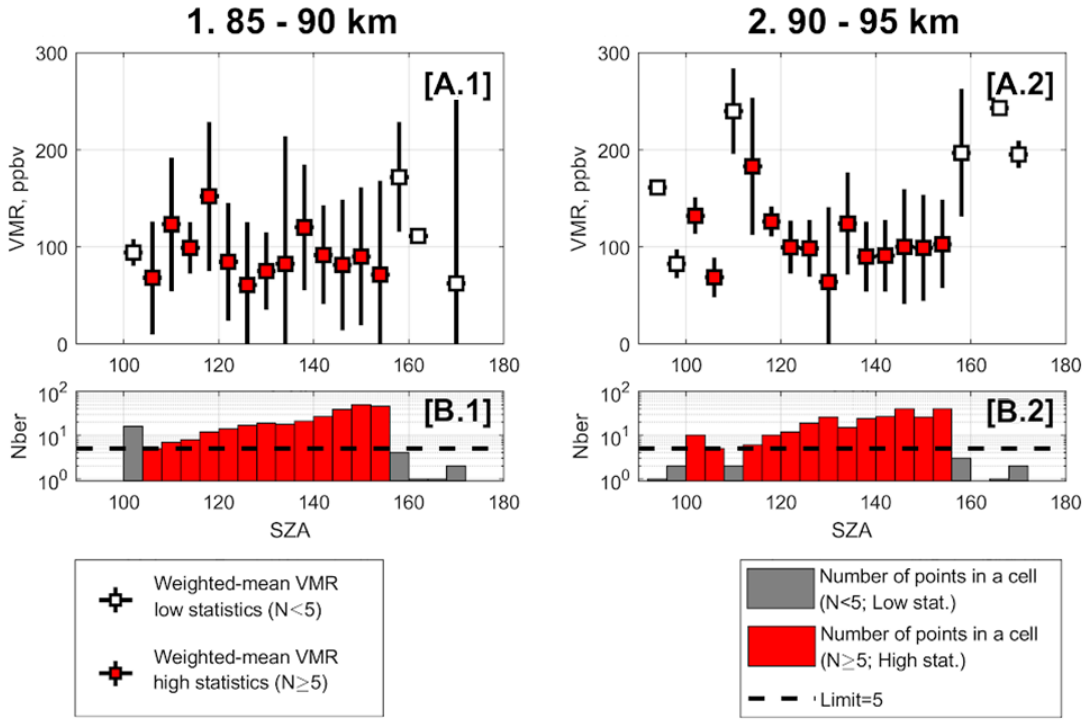

Figure 4.17. A1 and A2: Weighted-mean SO_2 VMR variations as a function of SZA for two altitude ranges of 85-90 km (1) and 90-95 km (2). The data are binned by 4°. Data are presented as in Figure 4.14.

4.3.4.3. Establishing independence from topography

Observations by the VIRTIS and the SPICAV IR instruments on board Venus Express, as well as the IR camera aboard Akatsuki showed the influence of topography on various aspects of the Venus

mesosphere (Gorinov et al., 2018). For the gaseous constituents of the upper mesosphere, topography appears correlated with the distribution of water vapour at the cloud top (Fedorova et al., 2016). It is also shown that the relief affects the dynamics of the atmosphere at an altitude of ~90 km, which was derived from observing O_2 ($\alpha^1\Delta_g$) emissions at 1.27 μm in Phoebe region (Gorinov et al., 2018). Results from the IPSL Venus GCM show a strong dependence of SO_2 to short-term dynamic processes in the mesosphere, rejecting significant connection with the surface (F. Lefèvre priv. communication).

The complete dataset accumulated over 8 years shows that the average SO_2 abundance in the layer remains nearly constant in the altitude range of 85-95 km. It was mentioned that the observations are concentrated in mid-latitudes of both hemispheres. However, at 30°S, the profile is uniform over the entire longitude range. The 20-40°N region was selected to examine the correlation in longitude between topography and SO_2. However, since a map of the surface of Venus with a resolution of 1° was used, the retrieved values of SO_2 were grouped on a similar longitude grid and averaged within each bin. Then, a linear correlation coefficient was deduced between topographic cut and the SO_2 longitude distribution.

The correlation analysis takes into account that some topography correlation may appear with a longitude shift. Such a displacement was obtained in work of Fedorova et al. (2016) considering water vapour at the cloud tops. The H_2O distribution there is shifted related to Aphrodite Terra (Fedorova et al., 2016). Here the correlation between the longitudinal distribution of VMR (SO_2) and topography is also deduced while applying a certain longitudinal shift Δl. This shift varies in the range from -30° to 50° with a step of 1°.

In general, we find no evidence for a correlation between topography and SO_2 VMR. For a specific latitude, there is an increase in correlation at Δl = 30-40°. At this latitude, the Beta Regio (max. altitude ~4 km) is located at a longitude of 280°. A significant increase in correlation is observed when considering a range of longitudes from 180° to 360° (the eastern hemisphere). In this case and for Δl = 32-36°, the correlation is more than 0.5. The error in determining the correlation coefficient is based on the data deviation in the longitudinal distribution of SO_2. However, the observations in which the SO_2 content was restored does not cover in detail the Beta Regio where its maximum heights are placed. The geographic coordinates of the observations correspond only to the slopes of the elevation.

The algorithm calculating the linear correlation coefficient took into account only those longitudes where SO_2 was retrieved. It also impacts the uncertainty of the result. Also, additional local increases in VMR (SO_2) are observed at other longitudes: 0°, 100°, 185°. These locations are not related directly to topography within the latitude range of 20-40°N. However, if one considers the shift Δl equal to 32-36° as the shift of the topography influence on the upper mesosphere then it should be noted that there are several notable elevations. Maxwell Mountains have coordinates of 0° of longitude and 65° N, Mount Aphrodite is at 80°-100° of longitude and 10°-0°S of latitude and Nokomis Mountains of Atla regio are at 180°-200° of longitude and 15°-20° N. It is impossible to test the hypothesis of the influence of topography on SO_2 in the upper mesosphere at other latitudes, due to an even smaller data coverage. Most likely, the result of a positive correlation with the Beta region is false positive, and the change in data from longitude is due more to temporal dependencies and incomplete observation statistics.

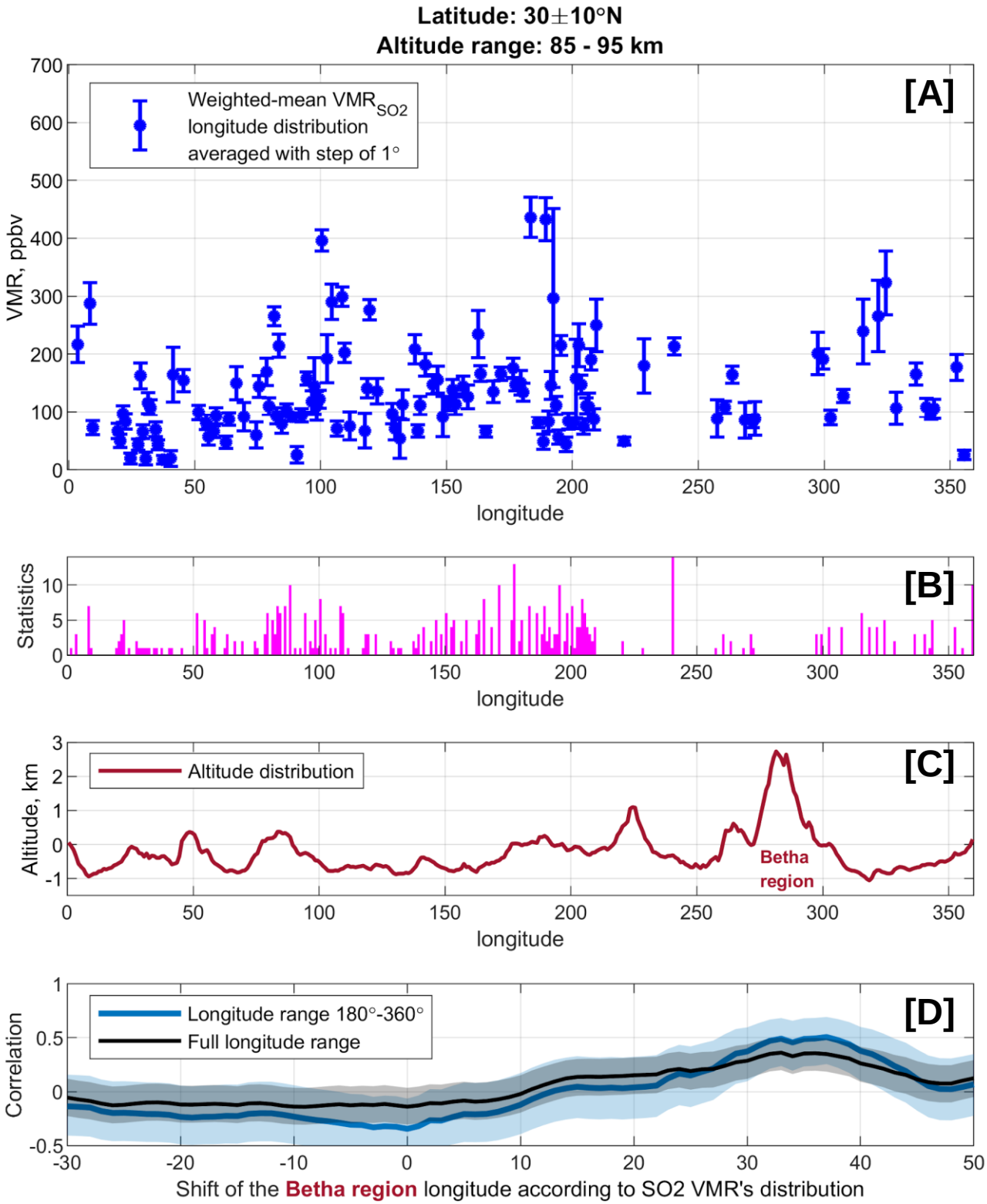

Figure 4.18. (A) Longitude distribution of the mean SO_2 VMR in the 20-40°N latitude zone. The values are binned by 1° of longitude. (B) Statistics in a bin. (C) The longitude profile of surface heights averages in the same latitude region. (D) Correlation coefficients depending on a possible shift between topography and longitude distribution of SO_2 VMR if one considers the 0-360° or 180-360° ranges of longitude.

4.4. Discussion.

4.4.1 Rapid changes in the SO_2 content

The main feature of the obtained sulphur dioxide content is its high variability. This behaviour was noted for all parameters studied in the mesosphere above the clouds. However, daytime conditions in this altitude region are rather different from the night side, which was observed in stellar occultations. Thus, for the current study it is reasonable to consider the night-time observations jointly with measurements at the terminator (Mahieux et al., 2015; Belyaev, Evdokimova et al., 2017). It allows a broad analysis since the night part of Venusian upper mesosphere is not investigated in detail by many instruments.

Sulphur dioxide oxidation and its subsequent reaction with water vapour establish the SO_2 link to the cloud formation. Several features can be noted for H_2O and aerosol. Solar occultations by SOIR show significant variations in water profile from 0.56 ppmv to 2.45 ppmv of VMR (Chamberlain et al., 2020). Such changes exceed the estimated inaccuracies of the experiment. The variation in water vapour content is minimal by 100 km and increases with decreasing altitude. SOIR measurements also show a decrease in the amount of water vapour below 100 km, which is either stabilized with altitude or forms a local minimum at about 80-85 km.

The high variability of processes in the mesosphere is also confirmed when studying the behavior of the upper haze (Luginin et al., 2018). The study of SPICAV IR solar occultation data showed rapid (1 day long) changes in the distribution of aerosol particles: formation and restructuring of detached layers of aerosol haze for northern latitudes above 58°N. On average, at the morning terminator their formation occurs at slightly lower altitudes than in the evening. Such layers were mainly observed at the altitudes of 80-88 km and 84-90 km at the morning and evening terminators of the planet respectively (Luginin et al., 2018). It means the vertical transport of the aerosol particles to the upper layers from the main «factory», i.e. the upper cloud layer where the aerosols are formed (Titov et al., 2017). The detailed mechanisms leading to the formation of observed layers of aerosol particles have not yet been fully established. It may be necessary to consider all components of the process of formation of sulphuric acid droplets together, i.e. water vapor, sulphur oxides and distribution of aerosol particles. In addition, this consideration should also take into account short periodic temperature changes, and the difference in temperature field between evening and morning terminators. On the night side, the existence of similar aerosol layers remains an open question, but it is reasonable to assume some similar processes for the night side as well.

The availability of oxygen and the efficiency of SO_2 oxidation and destruction, which forms the sulphur dioxide profile, is not yet completely solved for the Venus mesosphere. The presence of molecular oxygen airglow on the night side of Venus (Chapter 6) allowed to evaluate the profile of atomic oxygen (Soret et al., 2012). Its relative content increases sharply at altitudes higher than 95-100 km and also towards the anti-solar point, which is a direct consequence of the SSAS circulation above 100 km. These results follow from observations of O_2 ($\alpha^1\Delta_g$) airglow at 1.27 μm (Soret et al., 2012). In addition to the global average picture, which shows the maximum intensity of the O_2 ($\alpha^1\Delta_g$) airglow and, consequently, an increase in the number of oxygen atoms, in the region of the antisolar point, individual emission spots

rapidly change over time (Soret et al., 2014). The dependence of the mean profile of atomic oxygen explains the significant reduction of sulphur dioxide in photochemical models above 100 km. Moreover, the photochemical models assume an additional source of sulphur in the upper mesosphere, such as S_8 to correctly describe the increase in relative sulphur dioxide content theoretically (Zhang et al., 2012). However, one-dimensional models are significantly limited when considering a dynamically active region such as the upper mesosphere. They cannot reproduce the short-term effects of perturbations in processes of the vertical or horizontal airmass transport.

4.4.2. Global patterns in the SO_2 behaviour

First of all, it is necessary to consider the global temporal variation in sulphur dioxide content. Observations at the cloud tops level indicate a global downward trend over 40 years of observations. However, it is impossible to trace a picture of the time dependence in the period 1995-2006 (Figure 2.1, Chapter 2), when no data was obtained. Nevertheless, the time dependence during the both epochs of observations is a consecutive decrease of SO_2 content accompanied by several maxima. This behaviour was associated with possible injections of sulphur compounds into the lower atmosphere of Venus as a result of volcanic eruptions, passive degassing and pyroclastic phenomena on the surface (Esposito et al., 1984). The subsequent vertical transport of matter should distribute volcanic gases into the upper atmosphere, which forms a local increase of SO_2 content on the time scale. In the case of possible explosive eruptions, the transport of matter to the upper layers can be directly caused by this phenomenon, as shown by the simulation of possible Venusian activity (Airey et al., 2015). The observation of surface temperature showed a hot spot, i.e. a possible candidate for a volcanic eruption in June 2008 (Shalygin et al., 2015). The discussion about the Venus activity is not closed yet, and at the moment the only conclusion is that the set of observations considered in this work has not shown clear evidence of sulphur dioxide injections into the upper mesosphere above 85 km. In contrast to the observations at an altitude of 70 km on the day side, the long-term variations on the night side do not show significant long-term temporal variations. Moreover, all observations of solar and stellar occultations are consistent in such a conclusion. It should be noted, however, that nadir observations (Marcq et al., 2013; Marcq et al., 2020) provide a much more detailed statistical coverage of time and space than the occultation mode. The reason for the difference in global trends at different altitudes is not completely understood. It migt be related to the difference in the observed areas, since the terminator zone is also different from the day side. Besides it is possible that dynamic processes smooth out the effect of short-term increases in the amount of sulphur dioxide for higher altitudes.

In general, an increase of sulphur dioxide content was obtained on the night side, in comparison with terminators of the planet, at an altitude of 85-95 km. And the difference become more significant in the lower observed altitudes. However, it is difficult to determine a certain dependence on local time based on current data. Averaging over the entire period of observation shows a slight increase in content towards the evening terminator. Such behaviour is puzzling. It should be noticed that a similar asymmetry was recently deduced from a study of the Venusian atmospheric circulation in the 90-110 km range based on tracking the oxygen emission features (Gorinov et al., 2018). It was shown that velocities of two opposite zonal flows coming from evening and morning terminators towards midnight

reach zero values around 22.5±0.5 PM. This asymmetry in the zonal transport would affect chemical species involved in SO_2 photochemistry, such as chlorine species and oxygen atoms.

The dependence of sulphur dioxide on local solar time was only investigated using JCMT sub-mm observations (Sandor et al., 2010). In absolute values, the results of this work and JCMT observations are not consistent, however, they qualitatively confirm the increase in relative content on the night side. Accumulation of sulphur dioxide occurs due to the exclusion of photolysis from the chain of photochemical processes, which allows the rapid regeneration of SO_2 from sulphur monoxide.

4.5. Summary

Vertical profiles of the linear concentrations of CO_2 and SO_2 were retrieved from 375 observations in 2006-2014. The mean scale heights for these gases were computed, and they are equal to 5.25±0.05 km and 6.1±0.1 km respectively.

Based on the obtained CO_2 and SO_2 local density profiles, the volume mixing ratio of SO_2 was calculated. On average it remains around 135±21 ppbv in the range of 85-100 km. It is a correction of the previously reported result by Belyaev, Evdokimova et al. (2017). The reason for such correction was analysed. It is concluded that the used calibration methods mainly impact the CO_2 local density values. This also impacts the mixing ratios of trace gases.

Short-term variations of sulphur dioxide prevailed in the upper mesosphere. The difference in obtained values of the SO_2 VMR reaches one order in magnitude. On a long-term scale an annual trend is not observed. The local time coverage allows the study SO_2 changes in the interval from 19:00H to 5:00H of the local time. There is a possible diurnal asymmetry in relation to midnight. It is noted that the SO_2 VMR may be increasing from 2:00H to the evening terminator at an altitude range of 93-97 km. No statistically significant conclusion about the longitudinal distribution of SO_2 or possible correlation with surface topography could be drawn from the dataset available.

CHAPTER 5. Ozone

5.1. Ozone retrievals

Ozone in the night-time mesosphere of Venus is found to be sporadic. Out of the entire SPICAV UV dataset (690 observations), only 132 sessions produced positive detection of O_3. Among them, 26 spectra show a confident signature where the χ^2 improvement around the Hartley band is decreased by more than 20% with ozone. In 38 sessions, the χ^2 reduction was 10%, while the grand majority of the retrievals (93) correspond to percentages ranging from 5 to 10%. We disregard the cases where the χ^2 decrease is less than 5%. In general, only a few points can be derived from an individual occultation session, preventing a detailed characterization of the ozone vertical distribution. The retrieved number densities for all observations are grouped in Figure 5.1 (All the observational sessions with positive ozone detections are presented individually in the Annex 2). In the observed altitude range, detected local densities of ozone vary between 10^7 and 3×10^8 cm^{-3}.

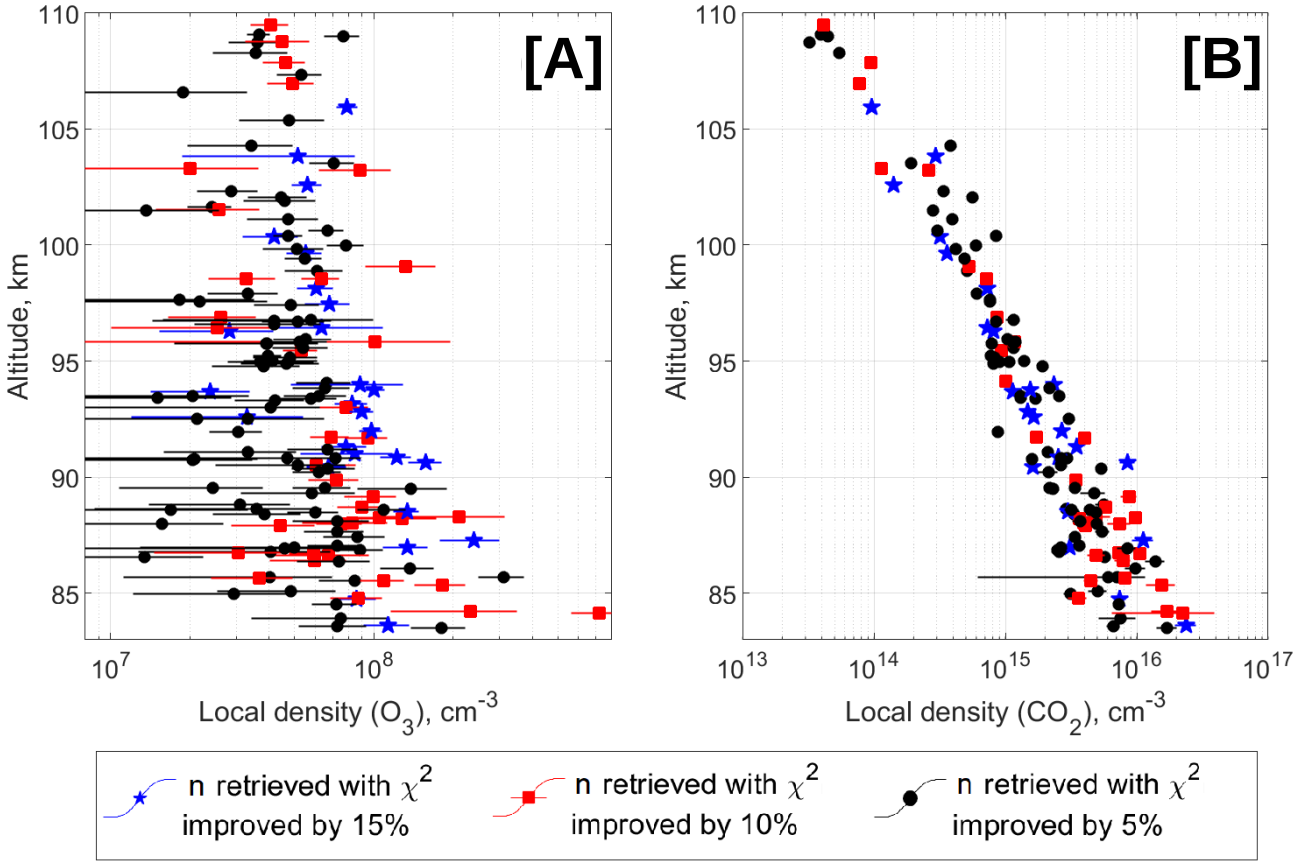

Figure 5.1. Night-time vertical distribution of ozone (A) and carbon dioxide (B) local densities retrieved from the entire SPICAV UV dataset of 2006-2015. Retrieved points are grouped by three criteria of O_3 detection: 5% of χ^2 improvement (in black); 10% of χ^2 improvement (in red); 20% of χ^2 improvement over a transmission model without ozone (in blue).

5.1.1. The main feature of the ozone positive detections

The majority of O_3 positive detections based on the chosen criteria is characterized by a single detection per profile. Assuming that the observations are done with a vertical step of 1-8 km, a single O_3 occurrence is localized within an altitude interval which should be less than 10 km.

Analysing observations with finer vertical stepping indicates that ozone detection is usually surrounded by non-detections (Figure 5.2A and 5.2B). It allows one to conclude that the experiment is only sensitive to peak ozone abundances which are close to the detection limit, while the ozone occurrences themselves are highly variable. Different observations also show an altitude shift of ozone peak within the observing range of 85-110 km. Detections do not allow deriving information on the details of the ozone distribution. Measured peaks only indicate how variable in altitude the peaks are.

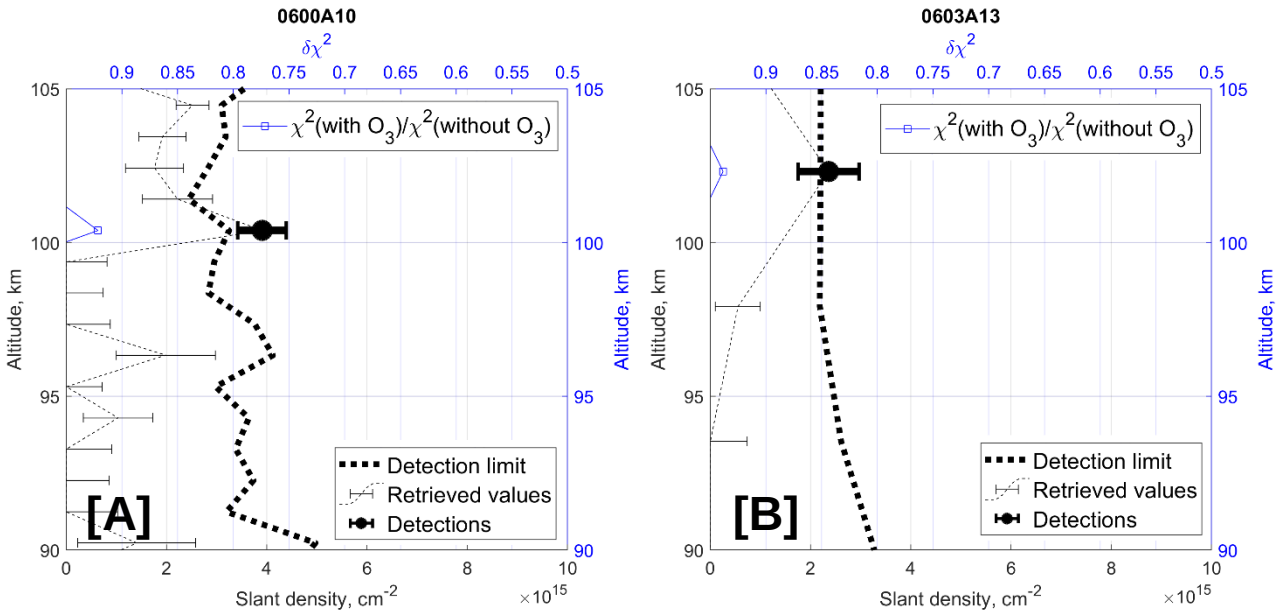

Figure 5.2. Two examples of occultation sessions made with a different vertical step of ~1 km (A) and ~5 km (B). The occultation session #0600A10: December 11, 2007; at latitude 25.5°N and longitude 307.5°; local time 1.26 hours. The occultation session #0603A13: December 15, 2007; at latitude 29.0°S and longitude 346.7°; local time 23.29 hours.

However, there are also some evident detections isolated in the profile, suggesting the ozone layer is 1 km or less thick. In Fig. 5.3 there is an example of such detection where the ozone feature is also visible in spectra, but the nearby altitudes are free from ozone absorption. This observation corresponds to no stray light conditions.

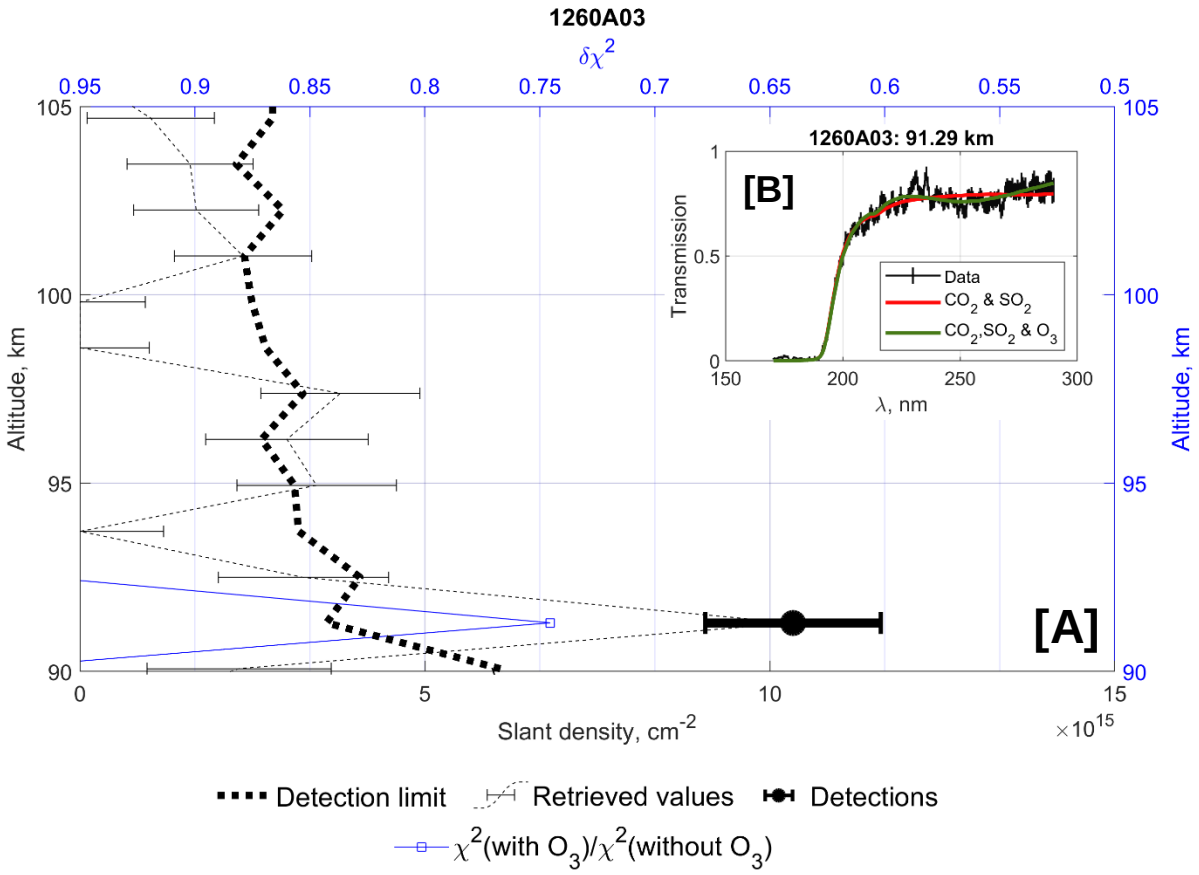

Figure 5.3. (A) An example of occultation session made with a vertical step of ~1 km and revealing strictly localized ozone detection. The occultation session #1260A03: October 2, 2009; at latitude 26.9°N and longitude 197.8°; local time 0.23 hours. (B) A transmission spectrum with error bars (black solid line) measured at 91.3 km that corresponds to ozone detection and the best atmospheric transmission models: one neglects ozone absorption (red solid line) and the other includes ozone absorption (green solid line).

The consideration of individual slant densities profiles suggests ozone exhibits very thin layers, perhaps because ozone is produced out of an oxygen layer that is already thin and that further recombination constrains ozone to be even thinner.

5.2. Ozone positive detections distribution

5.2.1. Average volume mixing ratio profile of ozone for established positive detections.

When all the positive detections observed for the whole altitude range, the mean volume mixing ratio of ozone seems to continuously increase with altitude. The mean profile goes from 10 ppbv at 85 km to 600 ppbv at 108 km. The histograms (Figure 5.4 B1-5.4 B6) represent the dispersion of retrieved values within a 5-km layer.

It should be noted that the detection limit in relative quantities also increases with altitude, but there are no reliable VMR values of ozone exceeding 100 ppbv observed below 95 km.

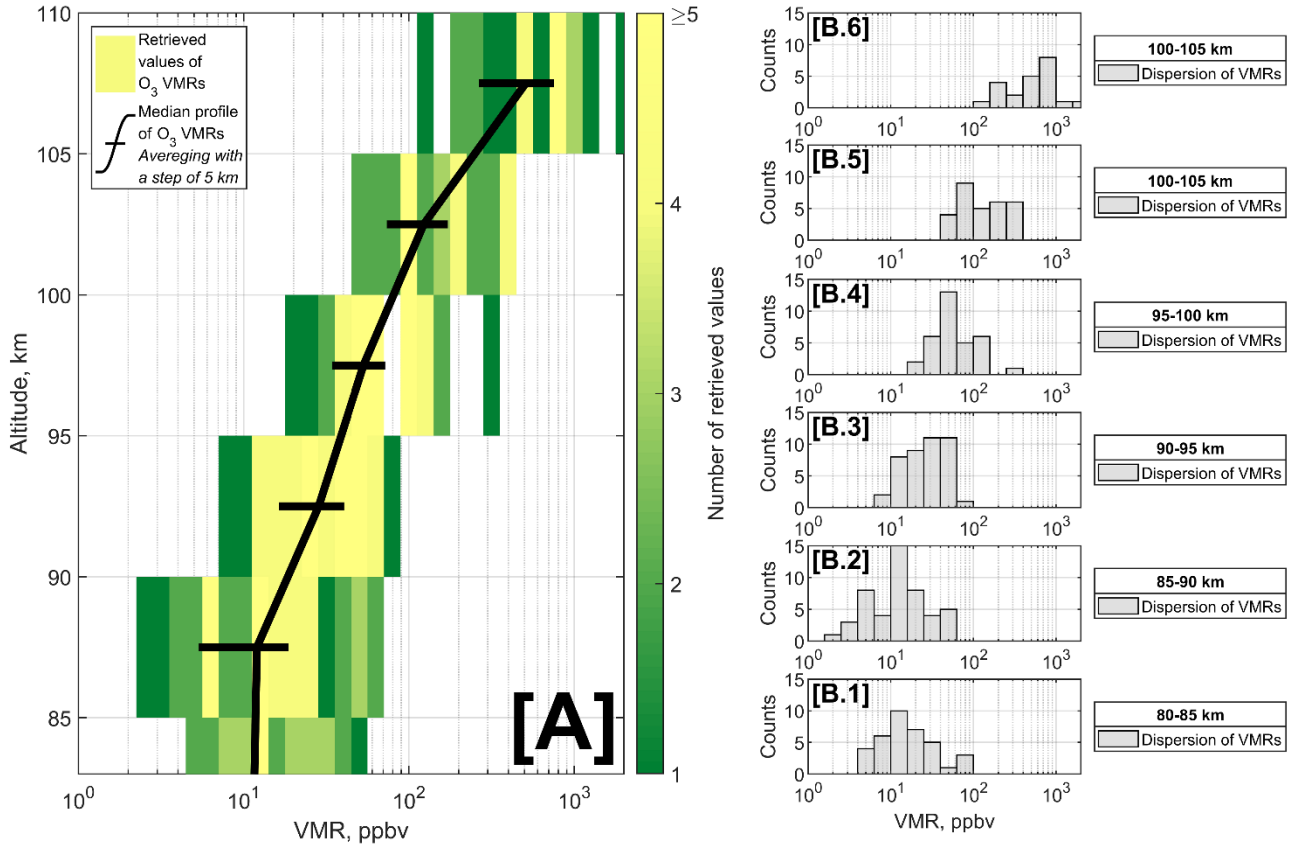

Figure 5.4. (A) Vertical median profile of the night-time ozone volume mixing ratio derived from SPICAV UV (the black curve with standard deviation). The color bar indicates the number of points within one bin of 5 km size. B.1-B.6. The right six panels are histograms of values within the layers of 5 km thickness to represent the stability of the median VMR profile. The statistics is calculated for each layer by binning the values with a step of 0.1 in a logarithmic scale, i.e. $\log_{10}(10^{0.1}$ ppbv).

5.2.2. Spatial variations of ozone positive detections

The detected values were split by 5 km from 83 to 108 km to estimate the spatial distribution of the ozone bursts. All the individual detections are presented in Figure 5.5 within four studied layers. There is no evident pattern of ozone distribution in space at night.

In general, it is expected that the behaviour of ozone is related to the SSAS circulation at altitudes around ~100 km. The SSAS transfers oxygen atoms to the night side, where they recombine, producing the molecular oxygen ($a^1\Delta_g$) emission (Gerard et al., 2009) and leading to the formation of the O_3 molecule. The O_2 airglow brightness increases towards the antisolar point and its vertical distribution demonstrates a maximum at 96±2 km. SSAS also transfers OH and Cl radicals that are likely involved in t destroying O_3 (Yung and DeMore, 1999; Krasnopolsky, 2013) and make the ozone horizontal distribution not as uniform as O_2, actually concentrating the sink region of O_3 around the antisolar region where O_2 emission is observed to be more intense. This should reduce the ozone amount towards midnight at the equator within the same layer.

Occultations concentrate in the mid-latitudes, while the polar and equatorial regions, including the antisolar point (24h), were observed rarely (Figure 4.1). However, conclusion about the space

distribution of ozone requires consideration of locations where this gas was not detected, which is discussed in Section 5.3.

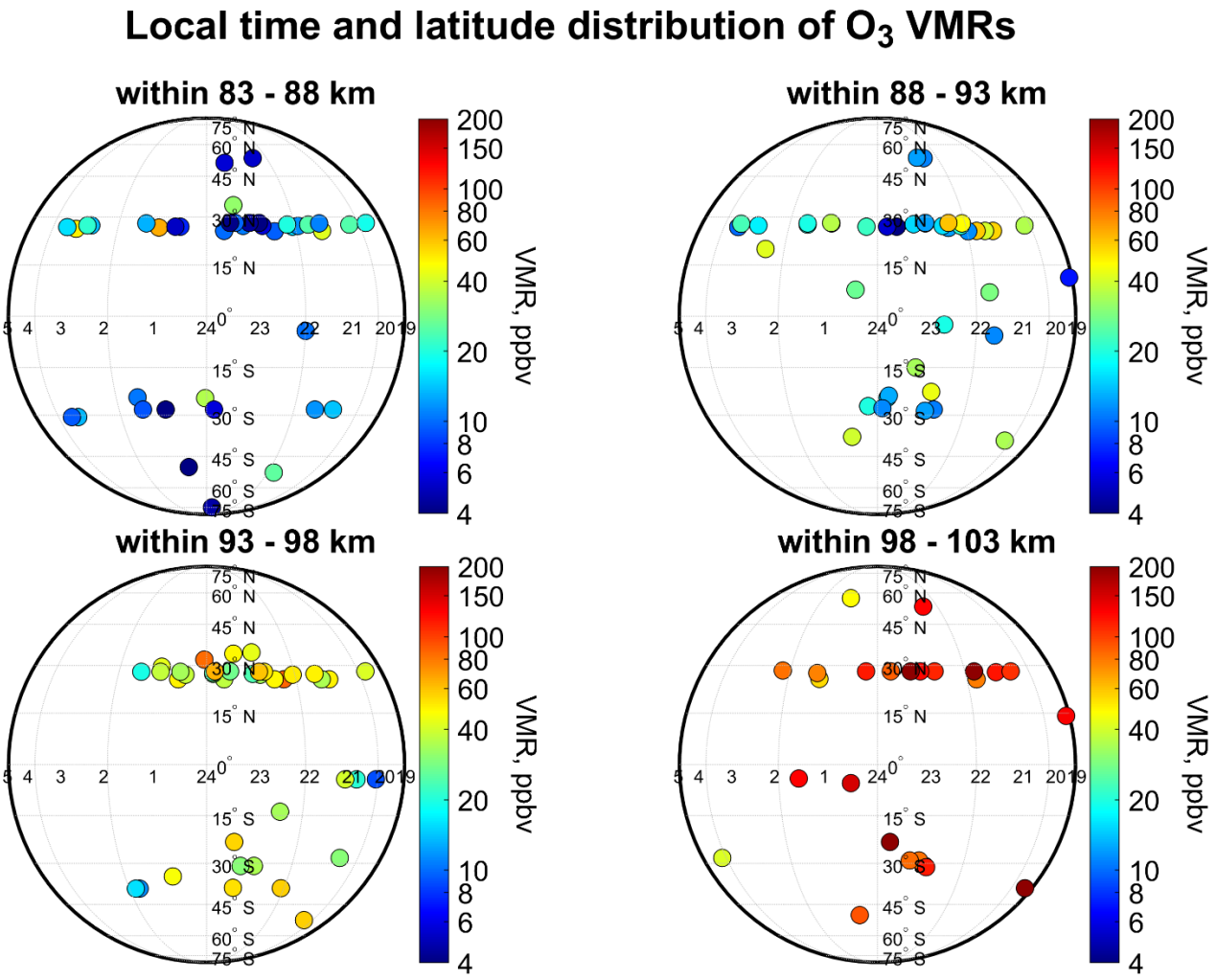

Figure 5.5. Local time and latitude distribution of observed locations where ozone was detected. Altitudes are binned into 5 km intervals between 83 and 103 km. The colour bar represents the ozone mixing ratios at a given location.

Detections found in the mid-northern latitudes (20-40°N) allow a deeper inspection of the ozone dependence to local time (Figure 5.5). Here, the increase of the gas content with altitude is more pronounced around midnight where minimal ozone VMRs below 93 km have been obtained. On the other hand, at higher altitudes there is not any pattern (Figure 5.6). Furthermore, high VMRs prevail towards the evening terminator within 83-93 km.

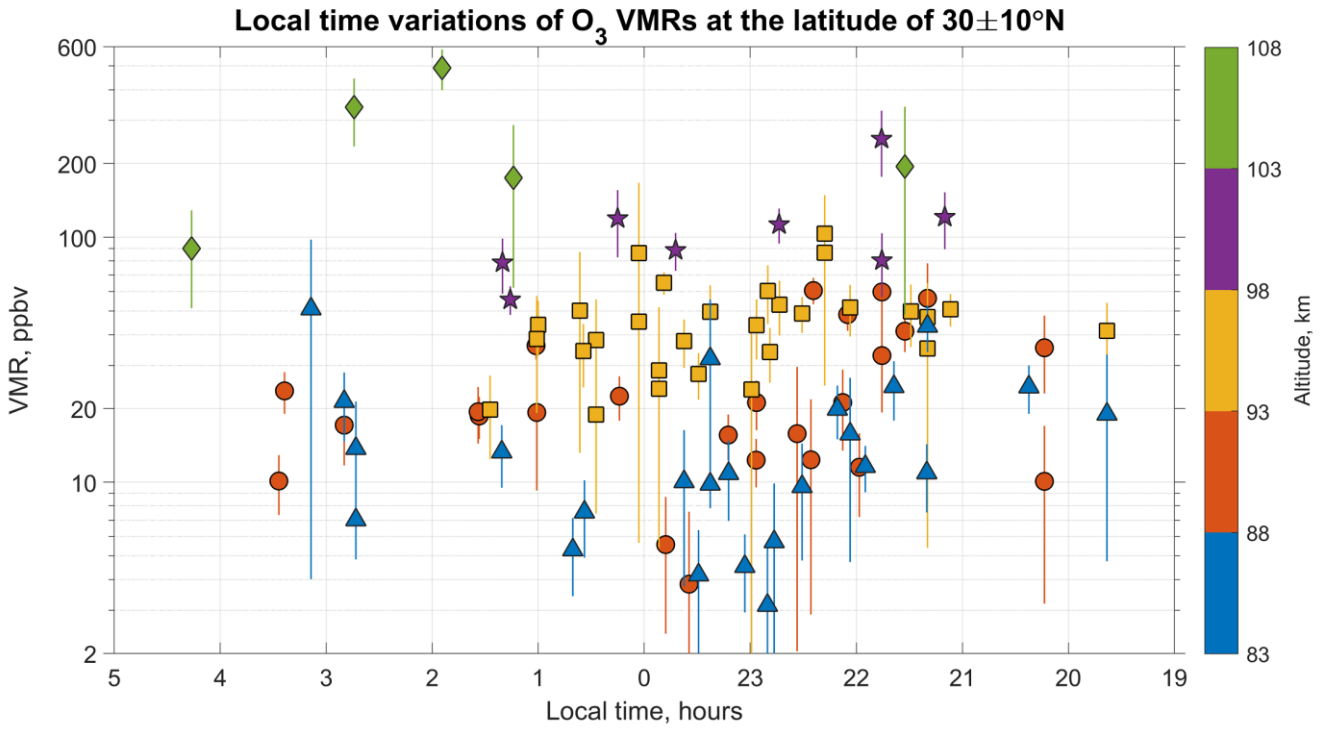

Figure 5.6. Local time variability of the ozone volume mixing ratio (ppbv) retrieved at the latitude zone of 30±10°N where the biggest number of observations was obtained. Various colors represent different altitude bins of 5 km thickness.

5.2.3. Temporal variations of ozone based on positive detections

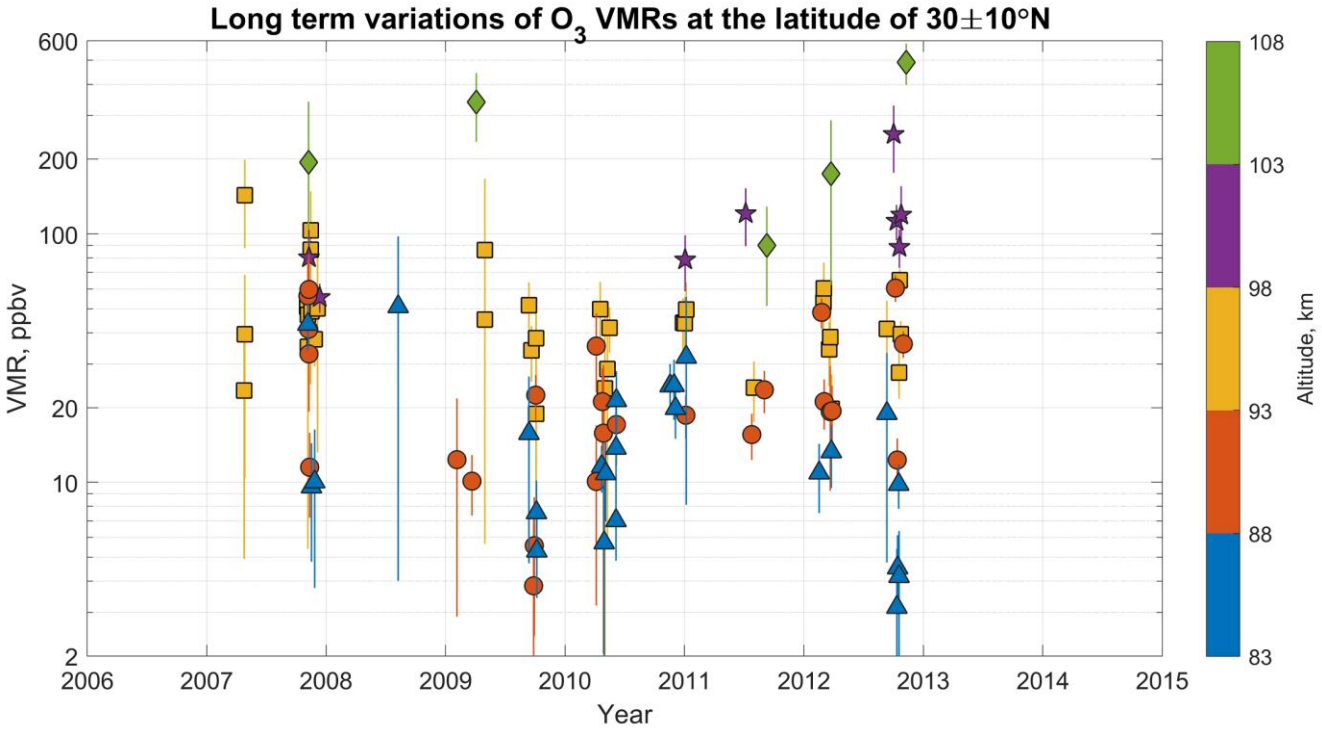

Figure 5.7. Long-term variability of the ozone volume mixing ratio (ppbv) retrieved at the latitude zone of 30±10°N. Various colors represent different altitude bins of 5 km thickness.

The evolution of ozone mixing ratio at different altitudes through eight years does not reveal any noticeable trend (Figure 5.7). However, some short-term fluctuations of the abundance can be spotted in the time series. This finding indicates the mesosphere is first and foremost dominated by rapid changes in its composition which may be tied to changes in the circulation, the latter being the most likely candidate to produce variations of that kind.

5.3. Detection limits of ozone

The entire SPICAV UV dataset ends up with only 6% of measured spectra showing a positive detection of ozone absorption. Those spectra possess a low noise level that corresponds to an average slant density detection limit less than 3.3×10^{15} cm^{-2} (Figure 3.20). Then, in order to estimate the detection limit in terms of the VMRs we calculated the mean CO_2 slant density profile as a reference. On average, it results in a limit of 10 ppbv at 90 km and of 100 ppbv at 105 km. These quantities differ from orbit to orbit but, in general, describe the pattern of obtained median O_3 VMR profile based on positive detections.

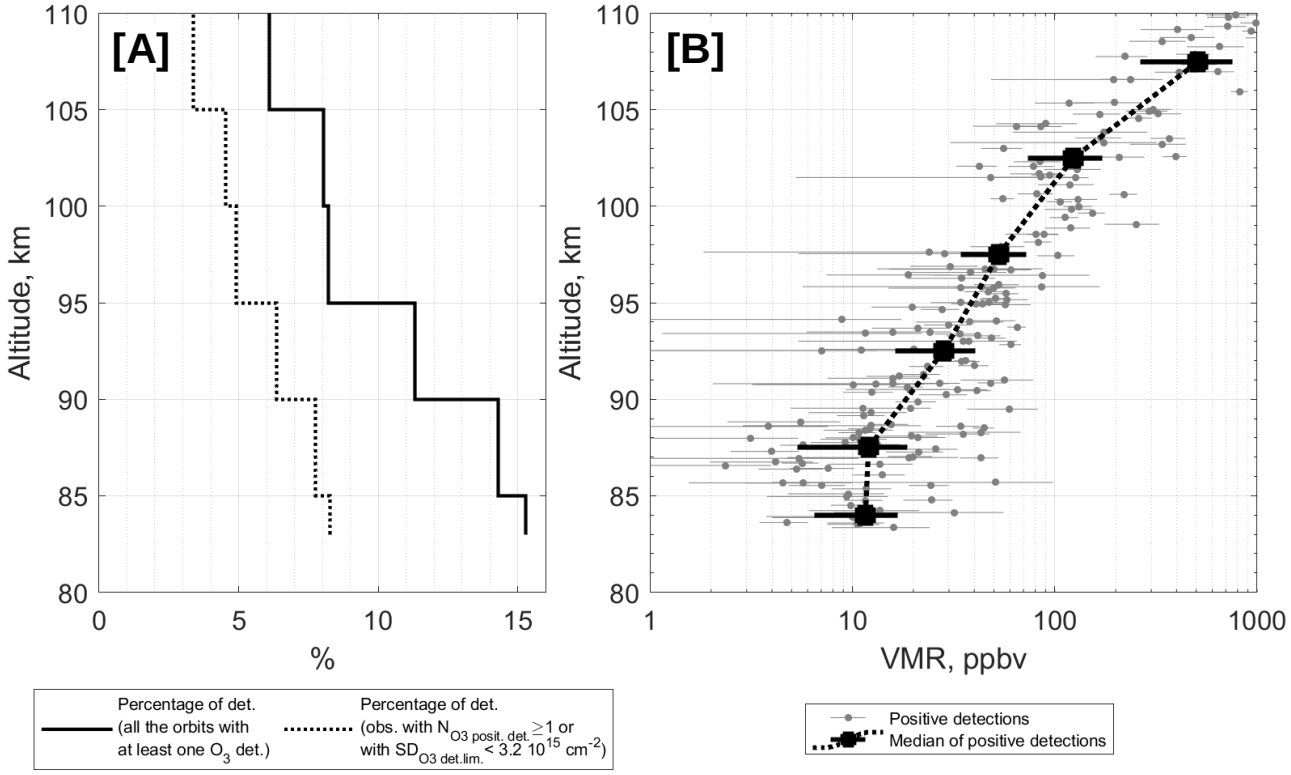

Figure 5.8. (A) Percentage of positive detections within 5 km layers. The solid black curve represents the ratio between a number of detections and all the spectra obtained in the same occultation sessions. To compute the dotted line spectra with at least 1 detection of ozone are supplemented by a number of spectra in observations characterized by a mean detection limit lower than 3.3×10^{15} cm^{-2} at altitudes over 90 km. (B) The individual retrievals of ozone and the corresponding vertical median profile of the night-time ozone VMR derived from SPICAV UV (the black curve with a standard deviation). All the VMR profiles of positive ozone detections are presented individually in the Annex 2, Figure A2.2.

The number of O_3 occurrences, i.e. percentage of detections, within each 5 km layer decrease with altitude from 8% to 3% (Figure 5.8A). In fact, the median curve of measured peaks can only represent the profile of the maximum values of O_3 occurring in the nightside mesosphere. Accounting for non-detections while averaging the values in each 5-km altitude bin, mean lower values can be deduced.

They form the lower estimation of ozone vertical profile based on the study. Values as well increase from ~1 ppbv at 85-90 km to ~6 ppbv at 100-105 km. The area between the minimum and the maximum value profiles is the first estimation to limit the mean vertical profile of O_3 in the night mesosphere (Figure 5.11).

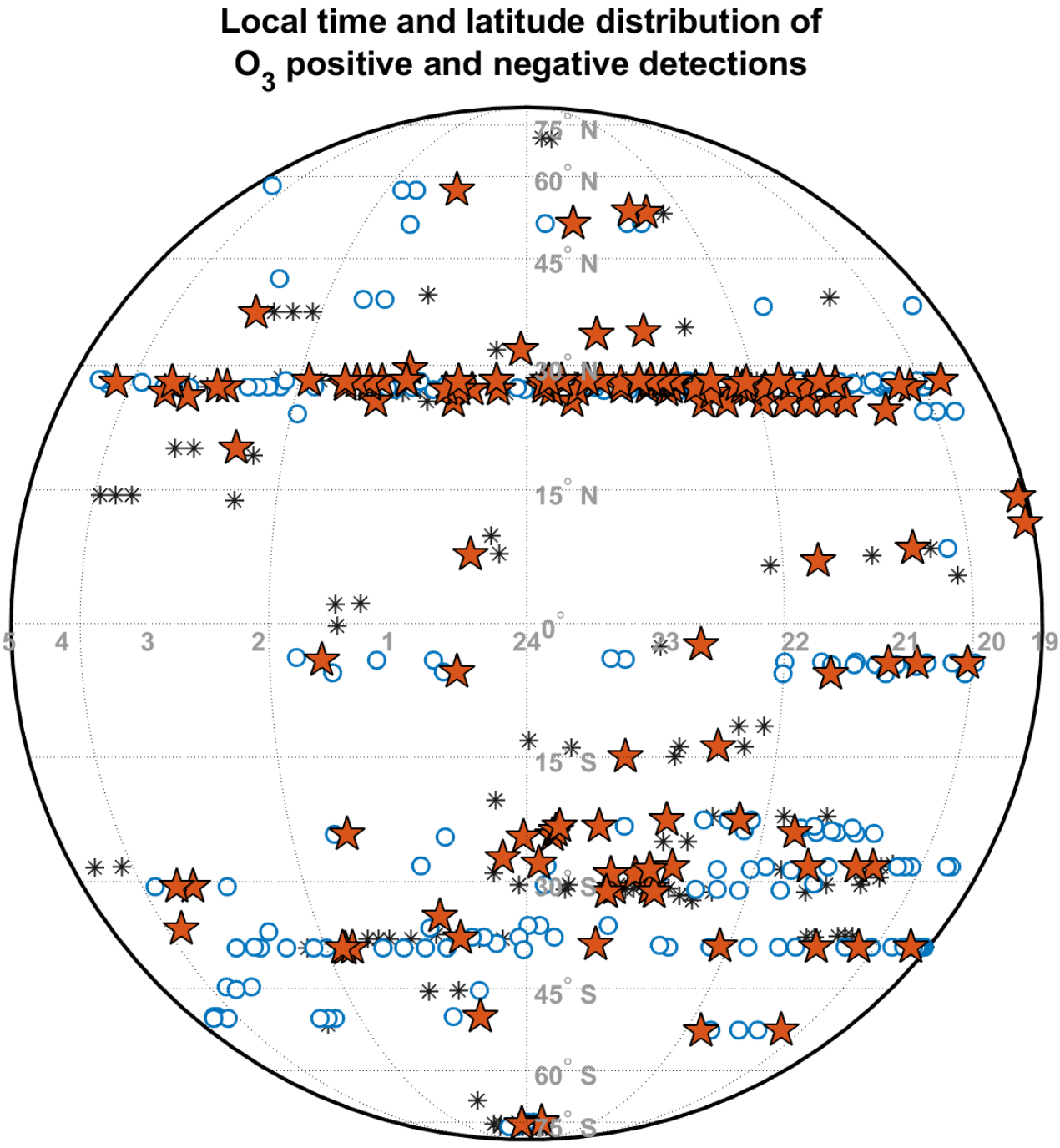

Figure 5.9. Local time and latitude distribution of observed locations where ozone was detected. Positive detections are orange stars. Blue dots correspond to observations giving the ozone detection limit lower or equal to 3.3×10^{15} cm^{-2}. Black stars represent other measurements.

The full coverage that was obtained from the SPICAV UV stellar occultation dataset is presented in Figure 5.9 where the retrieved ozone VMRs are supplemented by negative detections. Joint consideration of positive and negative detections does not prove or disprove the antisolar absence of

ozone. The coverage near the equator is anyway insufficient to allow any conclusion. Also, it is almost impossible to identify a global local time or latitude pattern of O_3 detection. However, an examination of a percentage of positive detections at 20-40°N revealed a similar value for each hour from 3:00 to 21:00 accompanied by a high number of measurements (Figure 5.10). The presence of this curious local time dependence (Figure 5.10) may be considered as a basis for future closer research, but for the existing dataset, we can only note the obtained changes. Small statistics impede the formulation of confident conclusions about any possible patterns.

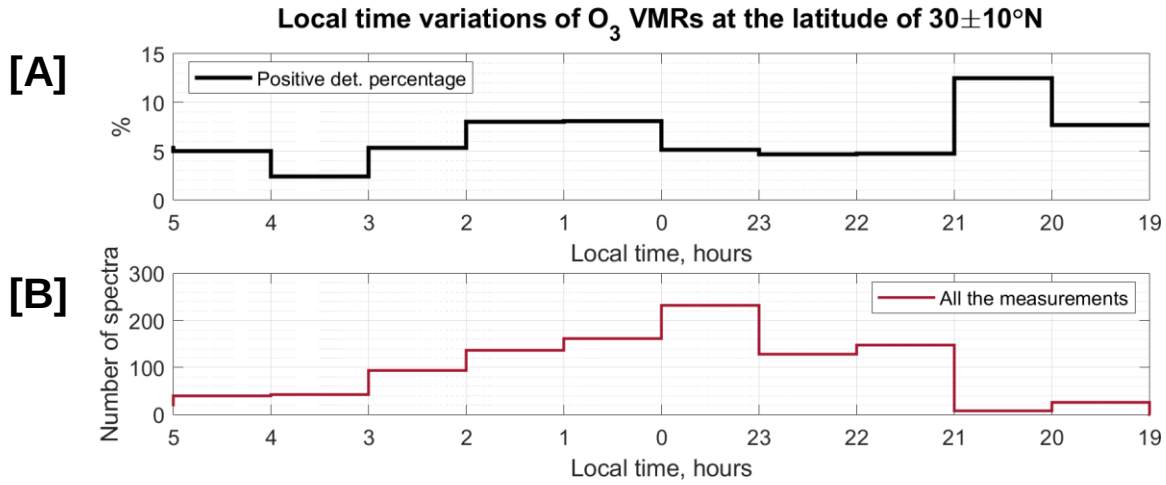

Figure 5.10. (A) Percentage of positive detections in every hour in the latitude range of 20-40°N. The ratio is computed based on spectra from observational sessions providing at least 1 detection of ozone or the mean detection limit lower than 3.3×10^{15} cm^{-2} at altitudes over 90 km. (B) The number of such spectra in every hour is shown by the dark red curve.

5.4. Review of possible correlations with other chemical compounds

The production of ozone is maintained in the upper atmosphere of Venus by the SSAS circulation at ~100 km (Yung and DeMore, 1999; Krasnopolsky, 2013). The main tracers of these dynamic processes are airglows by oxygen ($a^1\Delta_g$), nitric oxide (NO) and hydroxyl (OH). The infrared oxygen airglow first observed by Connes et al. (1979) at 1.27 μm is a result of radiative relaxation of the O_2 ($a^1\Delta_g$) metastable molecules to the ground state through the three-body process. Oxygen atoms supplying this process are produced by the CO_2 and CO photodissociation on the day side and then transferred to the night atmosphere.

The line at 1.27 μm is the strongest emission of O_2 and it has now been well documented on Venus. Its maximum brightness is observed at 96±2 km and the general spatial distribution demonstrates a significant increase in intensity towards the antisolar point (Gerard et al., 2012). It was observed with the same result by the VIRTIS (Soret et al., 2012) and SPICAV IR (Evdokimova et al., 2019b) nadir monitoring of the night side. Moreover, the O_2 emission study allowed to reconstruct the oxygen atoms distribution in the night mesosphere with a peak of O atom density (~2 10^{11} cm^{-3}) at 100 km. It is then followed by a sharp reduction deeper into the atmosphere down to negligible values at 85 km (Soret et al., 2012). The O_3 formation is regulated by the recombination of oxygen atoms and molecules that may in principle suggest that there is a strong correlation in space between ozone and molecular oxygen.

One of the possible sinks for O_3 is a reaction with hydrogen (Bertaux et al., 2007a). Partially it involves the Meinel process resulting in the OH emission (Bates and Nicolet, 1950). In comparison with oxygen IR airglow both emissions observed by the VIRTIS instrument showed similarities in the spatial distribution (Gerard et al., 2012), i.e. an increase towards the antisolar point. The hydroxyl emission intensity is weaker compared to the one from oxygen but appears at the same altitude range with the maximum at 95.3±3 km (Piccioni et al., 2008). In contradiction with the hypothesis of an ozone spatial pattern following the oxygen ($a^1\Delta_g$) airglow behaviour, the presence of hydroxyl radicals should reduce the O_3 amount around midnight at the equator in the same altitude range as the OH and O_2 nightglows.

There are also species carried by the SSAS circulation, like chlorine bearing molecules which have been observed repeatedly on Venus. Chlorine atoms are expected to play a role in the oxygen chemical cycle at these altitudes at night (Bertaux et al., 2007a). It was suggested that chlorine radicals are the main factor in the destruction of ozone (Montmessin et al., 2011) since they form a continuous SSAS flux when originated from the day-side photolysis of HCl (Yung and DeMore, 1999). A sign of such a mechanism are the molecules of ClO and HCl.

The observations of HCl by different instruments have provided rather contradictory results. SOIR measurements only at the terminator concluded an exponential increase of HCl VMR between 78 and 98 km. The VMR observed rising from ~40 ppbv to ~600 ppbv (Mahieux et al., 2015). This trend was similar in equatorial and polar regions and any significant difference between evening and morning values were obtained. The ground based observations by JCMT (Sandor et al., 2012; Sandor et al., 2017) and CSHELL (Krasnopolsky, 2010b) agree in HCl content around 400 ppbv below 80 km. JCMT was measuring subsolar and anti-solar profiles of hydrogen chloride in 70-100 km. Contrary to SOIR, the result of observations was a sharp decrease of HCl abundance above 85 km. The local time dependency was not inferred (Sandor et al., 2017), but month-scale changes were obtained. Some changes in the long term were also shown by SOIR monitoring. This instrument has accumulated a much larger dataset than ground observations. And its results demonstrate as well a large short-term variability (Mahieux et al., 2015). A big contradiction of noon and midnight and terminator data in HCl altitude behaviour is not explained. From the chemical models point of view, HCl is considered as chlorine reservoir of upper mesosphere (Yung and DeMore, 1982; Krasnopolsky 2010, 2012; Zhang et al., 2012), but none of theoretical predictions describe well neither the big increase of HCl nor its sharp decrease over 80 km.

A layer of chlorine oxide over 85 km was detected on the night side by Sandor et al. (2018). Two detections show the gas abundance of 3.7±0.9 and 1.5±0.5 ppb that is at least 4 times bigger than in the Earth polar region possessing the ozone hole. For the terrestrial stratosphere the prevailing mechanism of ozone destruction corresponds to ClOx catalysis (Brasseur and Solomon, 1986). So, in the presence of O and ClO the following net process should occur:

$$ClO + O \rightarrow Cl + O_2$$

$$O + O_2 + M \rightarrow O_3 + M$$

$$Cl + O_3 \rightarrow ClO + O_2$$

The ClO layer thickness is not certainly established. The experimental data processing has not revealed any significant difference between the layer thickness of 4 km or ≥15 km. Slight better results corresponded to a 10-km thick layer but the improvement did not outweigh the signal uncertainties. The mean value of predicted ClO layer thickness is about 10 km (20 km by Yung and DeMore (1982), 10 km by Krasnopolsky, (2012), 5 km by Zhang et al. (2012) and 4-5 km by Krasnopolsky et al. (2013)). So the suggestion was made that the obtained ClO mixing ratio should remain at least up to 90 km.

The SPICAV dataset is poorly covered by observations around the antisolar point and this prevents us any firm conclusion (Figure 5.9). The best statistics for the local time was assembled in the mid-latitudes of the Northern Hemisphere (30±10°N), far from the antisolar point. The retrieved values do not show any pronounced variation with local time above 93 km. Below this altitude, a minimum of VMR is perceptible at 23:00-24:00 (Figure 5.4). For instance, the midnight minimum for O_3 at 83-93 km (Figure 5.4) around the 30°N latitude might be also considered as an effect of the mesospheric circulation pattern. The difference in altitudes between the mentioned airglow peaks, i.e. ~95 km, and the ozone minimum may reveal a timescale involved for forming and then destroying (both with H and Cl) the bulk of O_3 as the air masses plunge deeper. The latter is clearly demonstrated by the night-time photochemical model (Krasnopolsky, 2013), it gives the column reaction rates for O_3 production and destruction processes different just in 1-4 times (Table 5.1).

Table 5.1. The night-time photochemical model (Krasnopolsky, 2013) column rate coefficient for model A and B. Model A includes the ClO and H fluxes equal to 10^{10} $cm^{-2}s^{-1}$. Model B do not consider the Cl flux.

Reaction	Column rate (Model A), $cm^{-2}s^{-1}$	Column rate (Model B), $cm^{-2}s^{-1}$
$O + O_2 + M \rightarrow O_3 + M$	5.43×10^{11}	4.48×10^{11}
$H + O_3 \rightarrow OH^* + O_2$	1.29×10^{11}	4.31×10^{11}
$Cl + O_3 \rightarrow ClO + O_2$	4.14×10^{11}	1.68×10^{10}

Joint observations of oxygen emissions and ozone would provide primary information about oxygen distribution and behaviour in the mesosphere of Venus since the latter is hardly detectable. The established high density of atomic oxygen and the low upper limits found for molecular oxygen (in general lower than 2 ppm at the 300 mbar pressure level) make it difficult to model the global CO_2 chemical cycle and to explain the stable CO_2 mixing ratio of 0.965 in the atmosphere (Mills et al., 1999). As well, the models show that the stable high abundance of CO_2 is a result of catalytic mechanism. Yung and DeMore (1982) considered three different schemes: the CO_2 recombination with HOx, NOx, and ClOx families (models A, B and C). The resulting profiles of the ozone local density for A and C are shown in Figure 5.11. The model B, based on NOx cycle, results in higher values of ozone concentration than by model A and C, and is not considered here. This 1-D model was the first preferred chlorine chemistry impacting the most. However, it was including processes relevant to daytime conditions, therefore not directly applicable to the nightside conditions.

A night-time 1-D model (Krasnopolsky, 2013) designed specifically for the night-time mesosphere, however, predicts larger values than those positively detected with SPICAV. The model concludes that the most efficient processes leading to ozone destruction are ClOx and HOx cycles. The NOx species influence much less: the column reaction rate is at least 4 times smaller. The predictions are presented in Figure 5.11 with conditions of different chlorine radicals flux and the remaining odd-hydrogen flux. A large Cl flux forms a thin layer peaking at 94 km of altitude that has never been observed, yet predicts values comparable to the obtained ozone below 100 km.

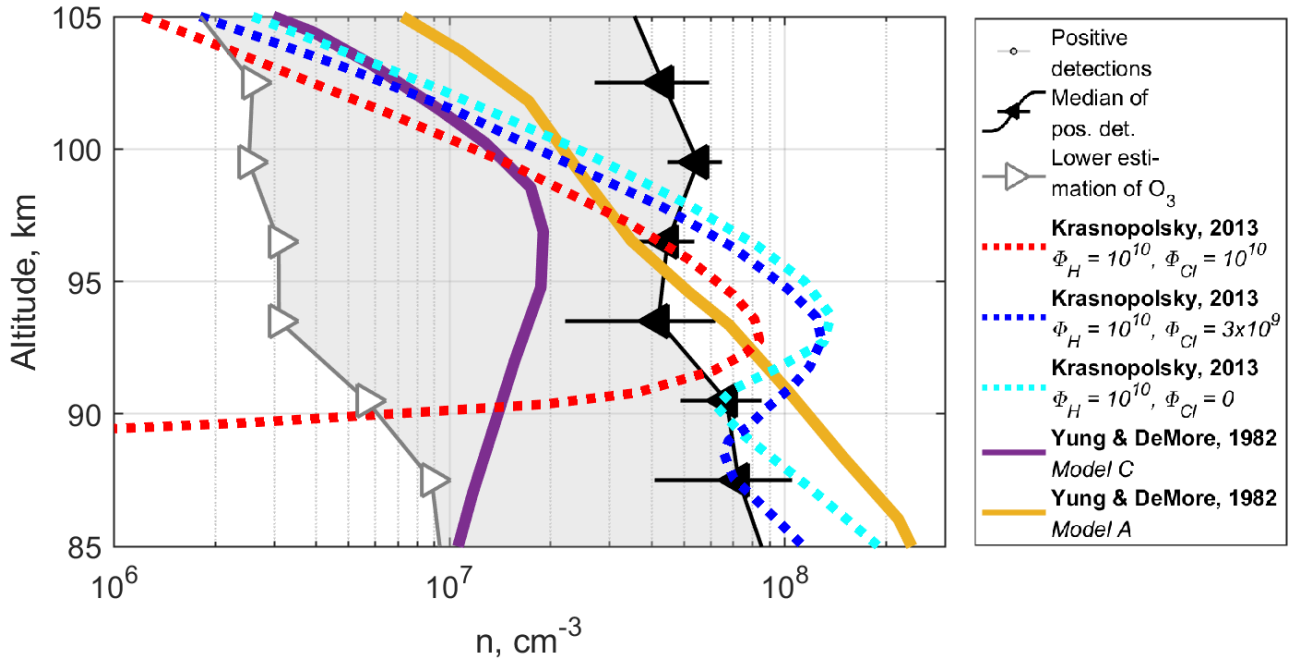

Figure 5.11. Altitude profileof O_3 local density obtained from positive detections by SPICAV UV (black triangles). The median is calculated within 3-km bin layers from 83 to 110 km. Grey triangles correspond to the lower estimation of ozone abundance estimated by multiplying the median local density and a percentage of positive detections during the entire mission. Solid violet and yellow lines correspond to 1-D photochemical models by Yung and DeMore (1982). The model A does not consider the ClOx chemistry but it is characterized by high H_2 abundance. In contrast, the model C represents the major catalytic cycle driven by the chlorine chemistry. Dashed lines represent the 1-D night-side model by Krasnopolsky (2013) characterized by the same flux of hydrogen and different by chlorine chemistry consideration.

Model C by Young and DeMore (1982) assuming chlorine cycle predicts smaller values for O_3. An O_3 decrease down to 85 km is reaching a O_3 lower estimation. However, the positive detections by SPICAV UV represent maximum values of ozone distribution at each altitude, and the mean O_3 abundance is expected to be smaller. So this hypothesis likely coincides with the profile produced by the model C. However, it is evident that the considered models predict the thinner ozone layer than the one observed by SPICAV UV while ozone absorption was detected even above 100 km in the SPICAV UV stellar occultation data.

The discovery of ozone at the cloud top (~70 km) in the polar regions (Marcq et al., 2019) indicates an influence of the global dynamics on the distribution of atmospheric species. Marcq et al. (2019) obtained O_3 VMRs around ~10 ppbv in the both southern and northern hemispheres. It should be noted, that the

IPSL Venus GCM is able to qualitatively predict the observed abundance at the cloud top (Lebonnois et al., 2010; Stolzenbach et al., 2014), and such an ozone layer is interpreted as a result of Hadley cell circulation (Marcq et al., 2019).

The studied range of altitudes (83-110 km) is mainly related to the SSAS circulation as we mentioned before, as suggested by the observed O_2 emission altitude. However, there is an evidence of influence on this transfer by the retrograde super rotation of the lower mesosphere. It is sensed by the global distribution of the nitric oxide emission (Stiepen et al., 2013) at ~115 km. Its spatial distribution surprisingly displays a significant shift towards the morning terminator (3:00-4:00) (Stiepen et al., 2013). The recent estimations of the thermospheric IPSL Venus GCM (Gilli et al., 2020) partially show the effect of zonal rotation is present up to 120 km.

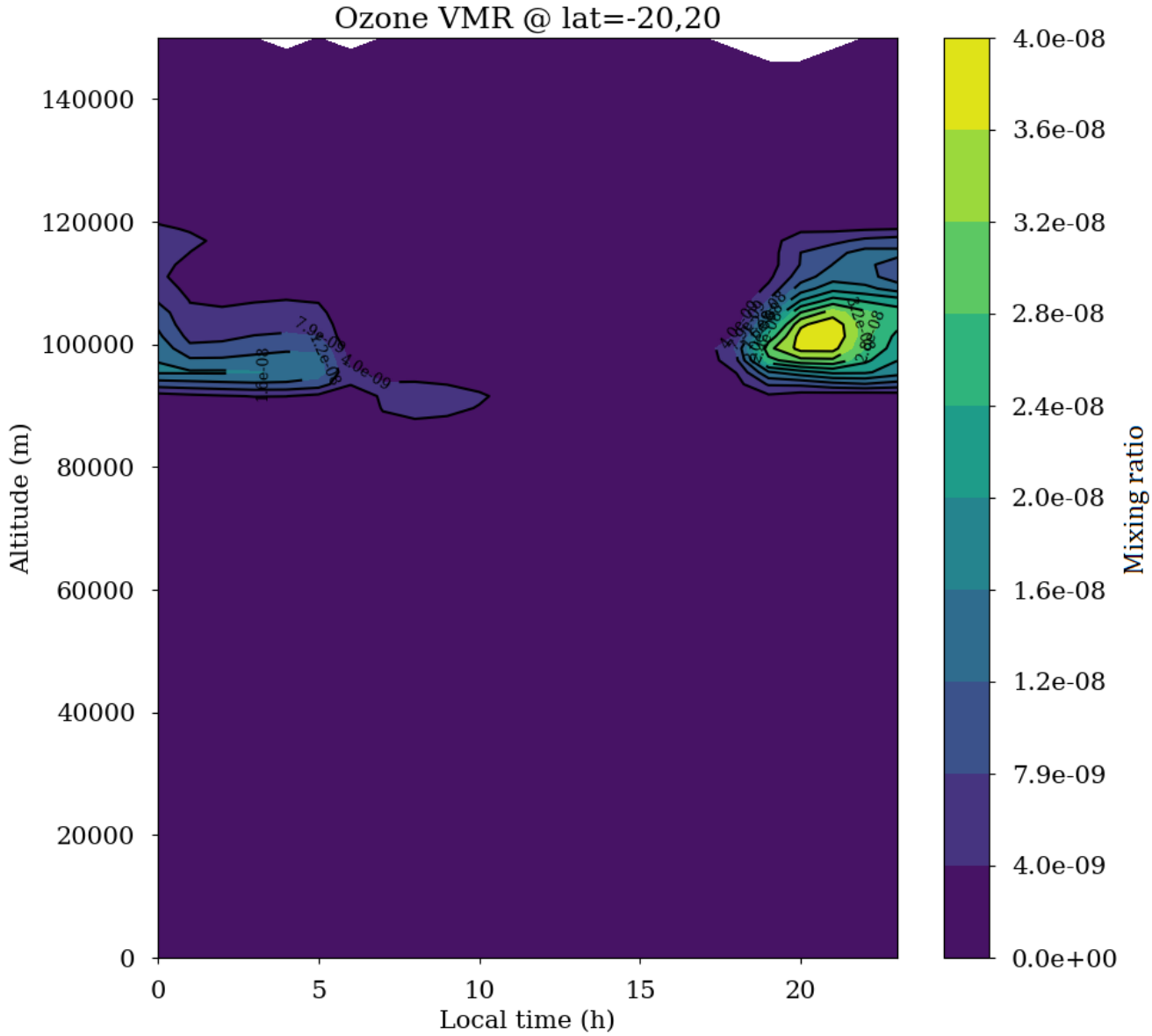

Figure 5.12. Local time ozone distribution in the equatorial zone (the latitude range of 20°S-20°N) (G. Gilli, private communication) by the thermospheric IPSL Venus GCM for 0-150 km (Gilli et al., 2017).

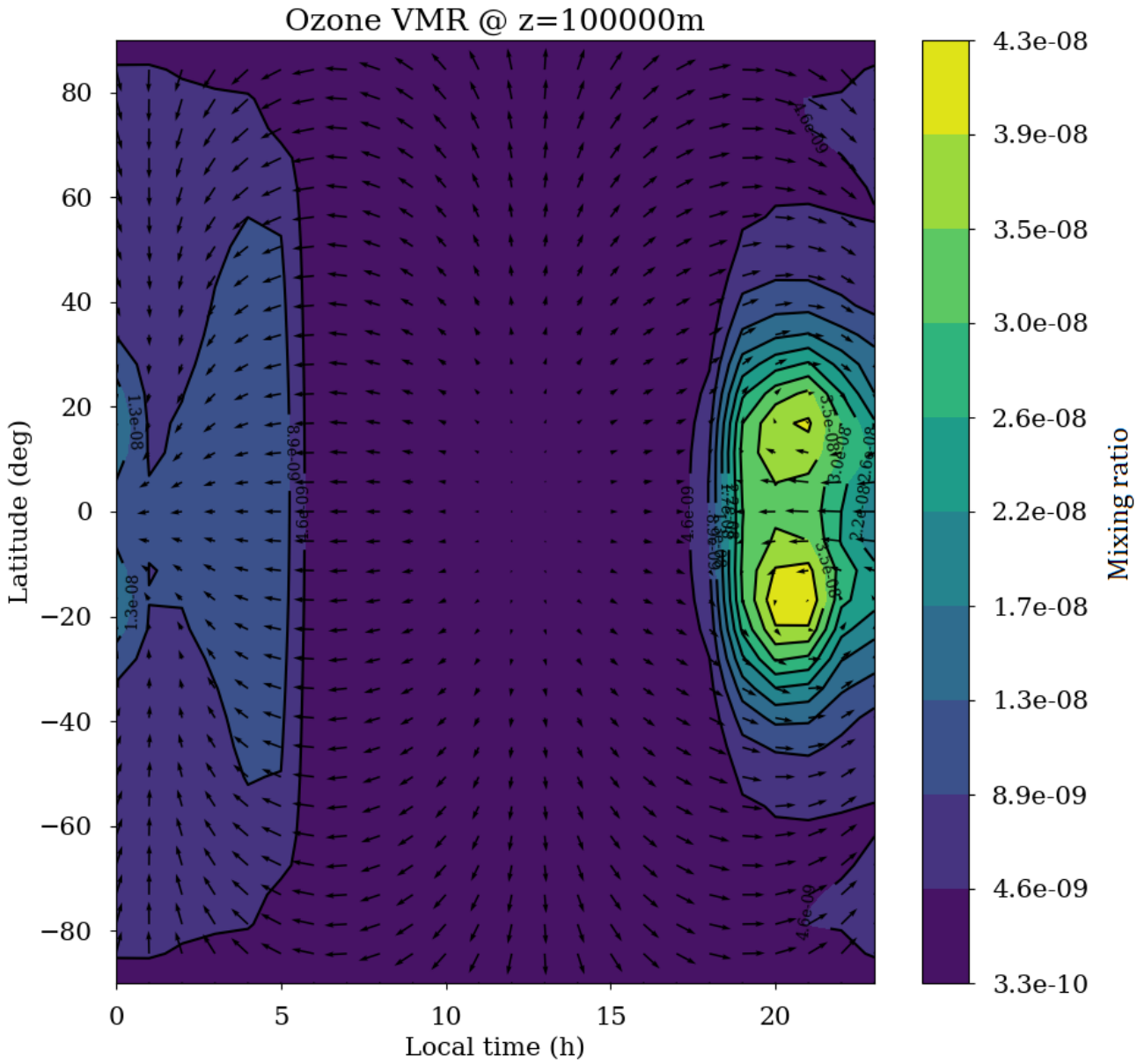

Figure 5.13. Local time and latitude distribution of O_3 at 100 km (G. Gilli, private communication) by the thermospheric IPSL Venus GCM for 0-150 km (Gilli et al., 2017).

Ozone's link to the dynamic has not been precisely described by theory considering the low number of observations of O_3. The thermospheric GCM made the first attempt to provide the ozone spatial distribution above 96 km. The results clearly show a stable ozone layer on the night side at altitudes of 90-110 km (Figure 5.12). The layer is localized in the equatorial zone. This pattern is different from the upper clouds O_3 layer found in the polar areas by both the model and observations. This reflects the theoretical link between ozone production and SSAS circulation at an altitude of 100 km. However, the theoretical maximum of ozone content is shifted towards the evening terminator, an opposite situation in comparison with other dynamical markers (O_2 and NO emissions, CO content) tending to concentrate around the antisolar point or closer to the morning terminator. About ten positive ozone detections in the 98-103 km layer at a latitude of 30°N show slight growth towards the evening, but it is not enough to establish that observations confirm what the model predicts.

The maximum VMR of 40 ppbv is predicted to be inside the local time interval of 20:00-22:00 (Figure 5.12 and 5.13). This value is generally consistent with the established upper and lower estimates of ozone content at altitudes of 85-110 km. Ozone destruction is not evidenced by data at altitudes below 90 km. Also, the increase in ozone VMR with altitude in 85-105 km is qualitatively consistent between our observations and the model. It is not possible to track the behaviour of this gas above 105-110 km from SPICAV UV, so it is not possible to confirm the gradient of ozone depletion above 110 km from our data set.

The model predicts two maxima of O_3 concentration at 20°S and 20°N (Figure 5.13). The O_3 was not detected exactly at these latitudes. There is the best achieved coverage at a latitude of 30°N, and the SPICAV values were studied depending on local time. At this parallel the model obtained a local minimum of ozone VMR in the night atmosphere at around 01:00 at 100 km. Similar behaviour, with a minimum of around 23:00-24:00, was observed by SPICAV UV at altitudes below 93 kilometres. For altitudes of 100 km, it is not possible to assess the dependence on local time

At the antisolar point, the model also predicts lower values associated with a higher concentration of chemically active compounds contributing to the attenuation of the ozone layer. This is indirectly confirmed by the experiment. In general, there is no contradiction between the simulated distribution of ozone and night observations at altitudes of 85-110 km in a qualitative comparison. A rigorous quantitative analysis based on the existing dataset is not correct.

The ozone vertical distribution is an additional instrument to investigate this complex region and to improve chemical and circulation models of the Venus atmosphere.

5.5. Comparative analysis of ozone layers in Earth, Mars and Venus atmospheres.

Among the terrestrial planets, Venus is the third one where ozone was discovered. This gas is associated with fundamental processes in the atmospheres in a way that is specific to each of terrestrial planets.

5.5.1. Ozone on the Earth

For the Earth, ozone plays an important role in atmospheric chemistry. One can distinguish two ozone layers: in the troposphere and in the stratosphere. In the troposphere O_3 is produced by polluting technogenic gases, such as nitrogen oxides and volatile organic compounds (VOCs), and tropospheric ozone may contribute to global warming (Mohnen et al., 2012).

The presence of the stratospheric ozone is a result of the evolution of life on the Earth. In the past, O_3 was filtering out the life-threatening UV radiation, allowing the biosphere formation into its current state (Holland, 1995). The atmosphere has been loaded with oxygen that led to the ozone production.

At present, the Earth possesses the most abundant ozone layer, among all the terrestrial planets. Its maximal concentration takes place at an altitude of ~20 km that corresponds to a pressure of ~30 mbar. In the stratosphere, the molecular Hartley band effectively absorbs the solar radiation at 250 nm that causes a warm layer around altitudes of 30-50 km (Figure 5.14). To compare, such a temperature inversion stratospheric ozone is not observed in the atmospheres of Venus and Mars. This radiative

heating is also the main source of energy maintaining the circulation in the upper stratosphere and mesosphere.

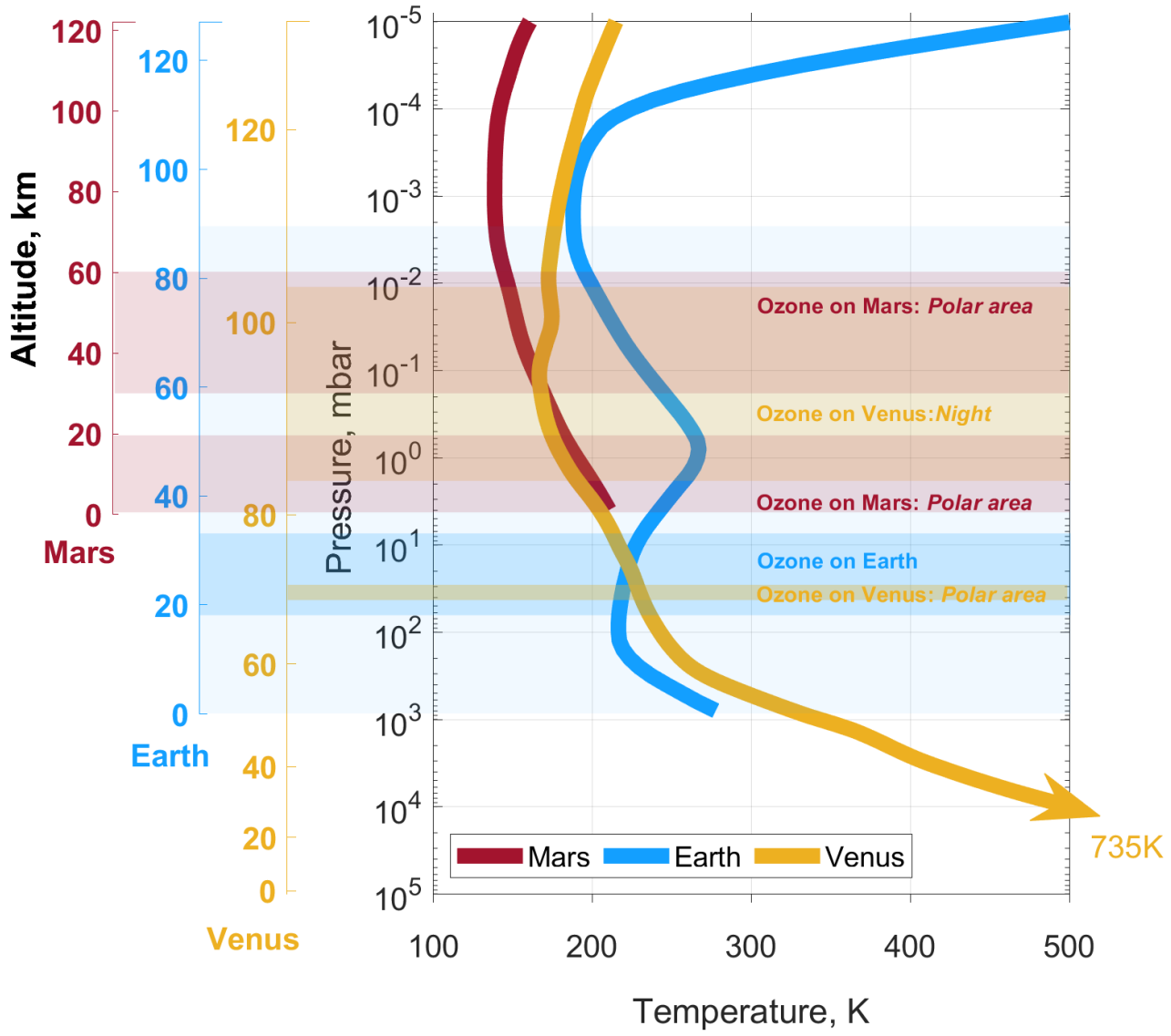

Figure 5.14. A review of ozone layer occurrences on the Earth, Mars and Venus.

In the Earth's atmosphere ozone is formed by intense UV radiation on the daytime side of the planet (Peter, 1994).

$$O_2 + h\nu\ (\lambda < 242\ \text{nm}) \rightarrow O + O$$

$$O + O_2 + M \rightarrow O + M$$

Ozone photolysis (Peter, 1994) on the dayside makes the photochemical lifetime of the molecule rather short, i.e. a few minutes. But it is not the main sink of O_3 in the stratosphere.

$$O_3 + h\nu\ (\lambda \simeq 200\text{-}320\ \text{nm}) \rightarrow O_2 + O$$

$$O + O_3 \rightarrow 2O_2$$

Ozone is also destroyed in natural catalytic cycles with hydrogen, nitrogen and chlorine compounds. In this row the chlorine compounds in the Earth atmosphere are directly linked to industrialisation. The

technogenic emissions have upset the balance between the formation and destruction of ozone molecules in the atmosphere. Emissions of chlorine- and bromine-containing volatile substances, e.g. the greatest extent the chlorofluorocarbons (freons) ejections, led to the formation of a large ozone hole over the whole of Antarctica in the 70s-80s of the last century, which had not been observed before (Farman et al., 1985). Antarctica is very distant from industrialized northern countries, and such a big impact in that region was an unexpected result for the scientists. At the same time there were observed local ozone holes at the North Pole. This phenomenon is also associated with the peculiarities of the dynamics: a polar vortex, formed around Antarctica, prevents the free mixing of air masses. A similar phenomenon contributed to the hole formation also in the Arctic (Witze, 2020; Varotsos et al., 2020). Changes in ozone in the stratosphere can both affect the quality of human life on Earth by increasing the UV index on the surface, and the processes of climate change. Inhibition of the decay of the ozone layer can also slightly reduce the rate of warming in the atmosphere. That forced humanity to take world-wide measures and the Montreal Protocol was signed in 1987. Reduction of technogenic emissions slightly improves the situation, but it is too early to conclude the restoration of the ozone layer on the Earth (WMO, 2018).

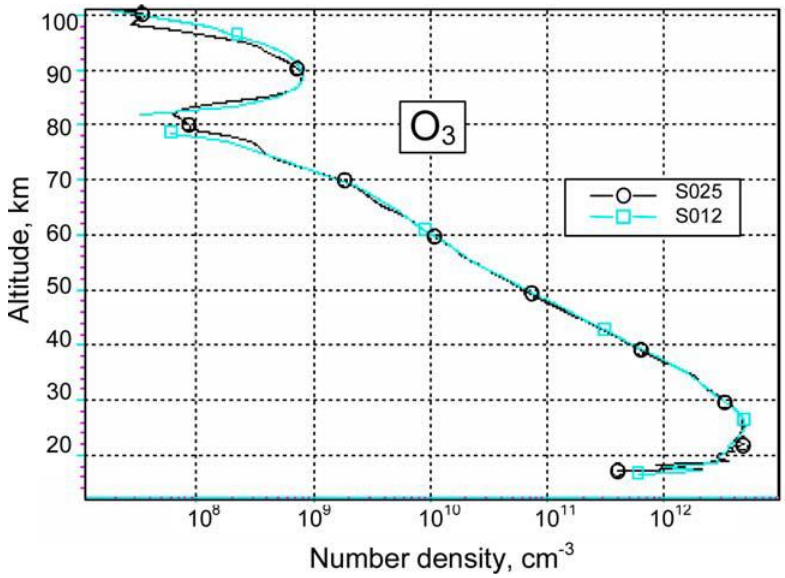

Figure 5.15. Two vertical profile of ozone obtained at night Earth's atmosphere in stellar occultations by GOMOS/ENVISAT at the same geographical location (Bertaux et al., 2004).

Local accumulations of mesospheric ozone occasionally appear upper in the mesosphere at night (>80 km). It is determined by other processes than for the stratosphere. At these altitudes oxygen molecules become a minor compound, but availability of active O atoms is increasing. Here the influence of active-hydrogen (HOx catalytic cycle) and active-oxygen chemistry is prevailing (Allen et al., 1984). Under suitable climatology conditions the three body recombination allows a formation of the ozone local layer in the mesosphere at night. On the day side, O_3 molecules are rapidly destroyed by UV. Such a structure (Figure 5.15) was measured for example by stellar occultations performed by Global Ozone Monitoring by Occultation of Stars (GOMOS) on board the European Space Agency's Envisat satellite (Bertaux et al., 2004).

5.5.2. Ozone on Mars and Venus

In the oxygen-depleted CO_2-atmospheres of Venus and Mars, there is no stable ozone layer completely covering the planet. Local ozone layers are formed in the atmospheres of both planets as a result of dynamic processes with appropriate temperature conditions. In contrast to the Earth's stratosphere, the gas is accumulated on Mars and Venus where the solar radiation is weaker or absent, but the main process for its production is the same three body recombination between oxygen atoms and molecules.

Ozone decay processes in the atmosphere of Mars are directly related to the HOx cycle. The products of water dissociation which are mainly H atoms drive the ozone depletion while the mixing ratio is high. It is the most efficient catalytic cycle on Mars where the amount of water vapour is greater than that of other compounds destructing O_3. There are three different ozone layers in water-depleted areas: in the boundary layer at the winter pole, at low and mid-latitudes at night in 30-60 km and during the southern polar night at at 40-60 km. The polar near-surface ozone layer is the result of dehydration of the atmosphere when water condenses into the polar cap. On the night side, where ozone is not destroyed by UV radiation, it is collected at water-depleted altitudes. Seasonality of O_3 distribution is traced, and ozone formation is associated with a significant decrease in water content during the cold aphelion period. When the planet is at perihelion, layers over 20 km do not form at all. The ozone layer during the southern polar night is the result of global transport. The oxygen-rich air masses are transferred from the sunlit southern latitudes and northern hemisphere to the south pole.

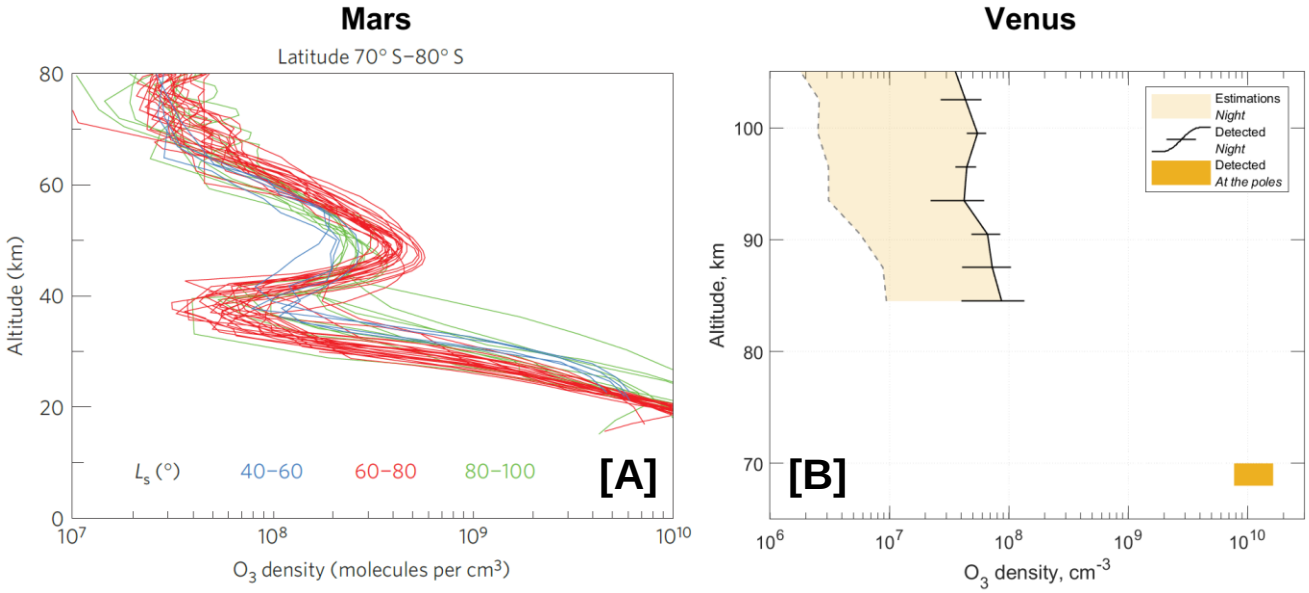

Figure 5.16. (A) Ozone layer formed over the south pole on Mars during the polar night (Montmessin and Lefèvre, 2013) and (B) the ozone detected in the atmosphere of Venus (mesospheric distribution from the current work and the polar ozone from Marcq et al. (2019).

A precise analysis of ozone variations was made possible due to joint consideration of SPICAM UV and IR instruments (Lebonnois et al., 2006) and the full 3-D general circulation model for Mars (Lefèvre et al., 2004). At the moment SPICAM dataset provides one of the widest coverage of ozone profiles on Mars (Montmessin et al., 2017). The study of ozone in the Martian atmosphere is an example of fruitful

cross-analysis between the GCM model and experimental data, that provides promising perspectives for Venus exploration (Lefèvre et al., 2004; Lebonnois et al., 2006; Montmessin and Lefèvre, 2013).

A relationship with dynamics can be found in the ozone accumulation in the atmosphere of Venus. There is a similarity between Venus and Mars in terms of ozone layer formation. On Mars, it specifically concerns Southern wintertime polar O_3 layer located at ~70 km. Its presence is due to the transfer of oxygen-rich air masses transported by the Hadley cell from the Equator. The absence of solar radiation in the south polar region allows ozone there at an altitude that corresponds to a maximum of recombination. Strangely, a symmetrical layer could be found in the north pole wintertime atmosphere. This asymmetry can be explained by the H atoms carried from the summertime equatorial hemisphere created by enhanced water vapour photolysis as the regions there are known to host a higher hygropause level and expose more water to sunlight.

The O_3 content in the upper mesosphere of Venus is mainly controlled by a chemical cycle of chlorine-containing elements (Yung and DeMore, 1982; Krasnopolsky, 2013), which makes it more comparable to the Earth's stratospheric ozone. On Venus as on Mars the O_3 chemistry is also driven by global circulation processes transferring oxygen-rich air masses. The local dynamics of atmospheric perturbations in contrast affects the other oxygen compounds (for example, O_2 ($\alpha^1\Delta_g$) emission) and probably the ozone behaviour as well.

On three planets, the study of the ozone layer is in different stages. On Earth, the chemical processes that regulate the ozone content have been sufficiently studied, they are given great importance in connection with the problem of global warming. Monitoring this gas is a daily vital task. A good result for Mars, achieved, among other things, thanks to a detailed study of the ozone content, was the creation of a 3D model of the general chemistry and circulation of the atmosphere, which made it possible to get a fairly complete picture of its state. Venus has the smallest amount of ozone among three planets. It rather obstructed the investigation of its variability and distribution in the atmosphere and the detection of ozone on the planet is very recent (Montmessin et al., 2011; Marcq et al., 2019). Moreover, one of the achievements of the Venus study is the correspondence between observations and modeling to the detection of ozone layers in polar regions at an altitude of ~ 70 km (Lebonnois, 2010; Marcq et al., 2019). However, the theoretical description of atmospheric processes above the clouds remains to be completed. The carried out and further ozone observations are one of the components to a gradual solution of this complex task.

5.6. Summary

Ozone in the night atmosphere of Venus was monitored for 8 years. The accurate analysis of SPICAV UV capabilities indicates that the obtained ozone values do not significantly exceed the detection limit. It is concluded that the positive detections of ozone correspond to peak concentrations that can be found in the upper mesosphere.

Low amounts of mesospheric ozone were obtained. The percentage of positive detections is about 6%. On average, for the positive detections, the local concentrations decrease with altitude from 10^8 cm^{-3} at 85 km to 10^7 cm^{-3} at 110 km. In general, ozone is expected to constitute VMR from 1-2 ppbv to 10-30

ppbv at altitudes of 85-95 km. At 95-105 km O_3 VMR increases, the estimation provides a value within an interval from 3-6 ppbv to 50-120 ppbv. The maximum values are the positive detection results.

Ozone positive detections are sporadic. The obtained VMR values change significantly in time and space. Majority of the detections are localized in a latitude zone of 30°N±10°due to the best coverage by observations. A decrease towards midnight from the terminators can be noted only below 93 km. The other patterns were not concluded.

CHAPTER 6. O_2 ($\alpha^1\Delta_g$) emission in the upper mesosphere

6.1. The infrared emissions in the night atmosphere

Study of the night-time composition and dynamics of Venus mesosphere derived from the UV spectra can be supplemented by infrared observations. The primary IR source is the thermal emission of the hot Venus surface and deep atmosphere in spectral transparency windows. An additional signal, which can be observed on Venus, concerns the contribution of spontaneous emissions originating from the upper layers of the atmosphere, namely airglows (Taylor et al., 1997). One of those sources is the O_2 ($\alpha^1\Delta_g$) emission at 1.27 μm produced near 95 km corresponding to the altitude range of ozone detection. O_2 ($\alpha^1\Delta_g$) and O_3 are both products of the same processes occurring in the upper mesosphere of Venus.

The origin of this bright O_2 ($\alpha^1\Delta_g$) airglow on the night side is a direct consequence of the SSAS circulation. As explained in Section 1.5, the O_2 ($\alpha^1\Delta_g$) emission originates from the recombination of oxygen atoms in a three-body chemical reaction involving CO_2 (see §1.5), such that:

$$2O + CO_2 \rightarrow O_2^* + CO_2$$

where the excited O_2^* molecule is formed. It is followed by further relaxation and an emitting light at 1.27 μm. The radiative lifetime of O_2 ($\alpha^1\Delta_g$) state is ~4300 s (Miller et al., 2001).

$$O_2^* (\alpha^1\Delta_g) \rightarrow O_2 (X^3\Sigma_g^-) + h\nu$$

Also, O_2 ($\alpha^1\Delta_g$) may be quenched by collisions with CO_2.

$$O_2^* + CO_2 \rightarrow O_2 + CO_2$$

However, it is not a dominant process above 90 km. Approximately 80% of excited O_2 ($\alpha^1\Delta_g$) molecules emits photons at altitudes where the airglow is observed to be maximum (Gérard et al., 2007).

The reaction producing the 1.27-μm emission constitutes the major mechanism removing oxygen atoms in the mesosphere. On average, the maximum of emission is located near the anti-solar point, as could be expected from the SSAS-led mechanism. In parallel, O_2 airglow spots can be observed intermittently everywhere in the night-side hemisphere (Soret et al., 2014). These spots can last more than 75 minutes that permits tracking atmospheric dynamics at an altitude of ~95 km. These features imply that the SSAS is perturbed by transient effects (Soret et al., 2014), and cannot simply be represented by a direct flow from the subsolar to the anti-solar point, but by a more hectic flow showing short-term variability. Further analysis even suggests that the influence of the topography can be identified in the airglow dataset despite the high altitude of the emission (Gorinov et al., 2018).

The O_2 ($\alpha^1\Delta_g$) airglow was initially identified using ground-based observations (Connes et al., 1979). The bright emission line is located at a wavelength of 1.27 μm which also coincides with the transparency window at 1.28 μm. For this reason, monitoring Venus' emission around the 1.28-μm spectral interval can potentially allow one to track variations in the lower cloud layer while exploring the upper mesosphere.

SPICAV IR can contribute to the O_2 ($\alpha^1\Delta_g$) airglow observations, in particular by completing the latitudinal coverage of the VIRTIS-M experiment, which barely observed the Northern Hemisphere of Venus. Nowadays, it is considered as a reference dataset to study the O_2 airglow behaviour (Gérard et al., 2007; Piccioni et al., 2009; Shakun et al., 2010; Soret et al., 2012; Soret et al., 2014; Gorinov et al., 2018; and other). The O_2 emission signal obtained by SPICAV IR must however be extracted from spectra with the IR transparency windows using a technique described thereafter.

6.2. SPICAV observations of lower atmosphere thermal emission

Venus Express had three instruments constantly monitored the thermal radiation of the night atmosphere. VMC was looking at the surface in two IR channels. Its 965-nm channel was also sensitive to deep atmospheric abundance of water vapour absorbing in the 0.94-μm band (Markiewicz et al., 2007). The data of the VIRTIS-M and -H spectrometers (Drossart et al., 2007) and SPICAV IR (Korablev et al., 2012) were better adapted to the lower atmosphere study. Their values of the resolving power were ~200 for VIRTIS-M and ~1400 for SPICAV IR. However, the VIRTIS-M instrument observations performed just in 2006-2009. Thus, over 8 years of operation, SPICAV IR has collected a global dataset with the higher spectral resolution and a consistent space-time coverage. The technical characteristics determine approaches of the O_2 airglow extraction. The oxygen emission line is well resolved in SPICAV IR spectra while in the VIRTIS data it is not resolved. Thus, the airglow signal is superimposed on the radiance of the 1.28-μm transparency window.

SPICAV IR covered the transparency windows at 1.0, 1.1, 1.18, 1.28 and 1.31 μm. The window at 1.0 μm, also used by VMC and VIRTIS, corresponds to surface radiation which contains information about the surface temperature and emissivity that can be potentially interpreted in terms of geological processes (Kappel et al., 2016; Shalygin et al., 2015). The transparency windows at 1.1 and 1.18 μm are sensitive to the first scale heights, i.e. from 0-5 to 15 km (Fedorova et al., 2015; Bézard et al., 2011; Bézard et al., 2009). Thermal emission at 1.28 and 1.31 μm is originating from altitudes ranging from 15 to 30 km, and its variations mainly reflect changes in the lower cloud density (Taylor et al., 1997).

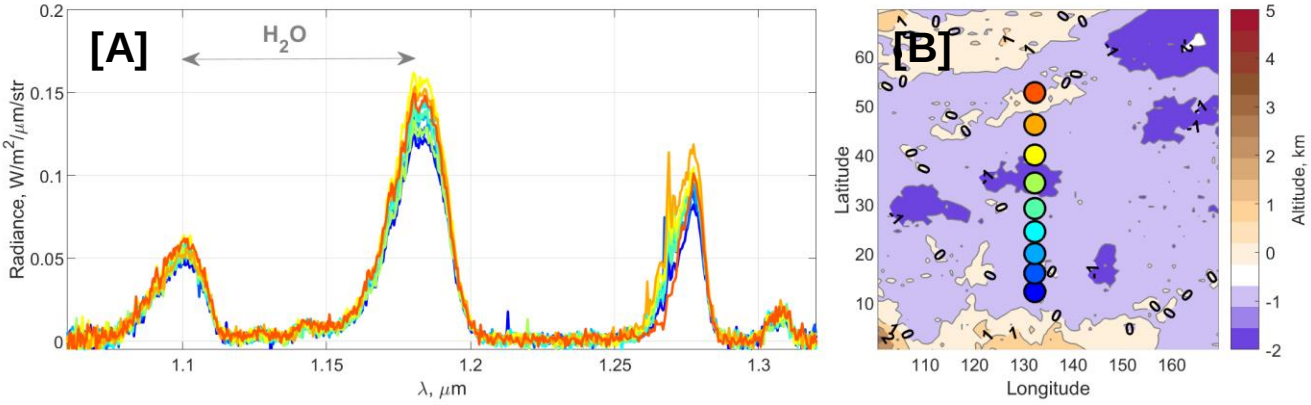

Figure 6.1. (A) The observational session #1713A02 by SPICAV IR on December 29, 2010 (local time of 02:00, SZA in 124°-149°). (B) The geographical locations corresponding to measured spectra.

Absorption bands of water vapour coincide with two transparency windows at 1.1 and 1.18 μm. According to recent ground-based observations and data from SPICAV IR, the relative water content in the lower atmosphere is 27-35 ppm (Fedorova et al., 2015; Bézard et al., 2011; Arney et al., 2014).

The intensity of the thermal radiation in transparency windows is mainly determined by the scattering by the aerosol particles of the lower and middle clouds (Taylor et al., 1997). It was used to study cloud properties and their variation in several works considering either 1.74-μm and 2.35-μm windows (Wilson et al., 2008; Satoh et al., 2009; Tsang et al., 2010; McGouldrick et al., 2012) or the entire VIRTIS-M spectral range (Haus et al., 2014; Magurno et al., 2017).

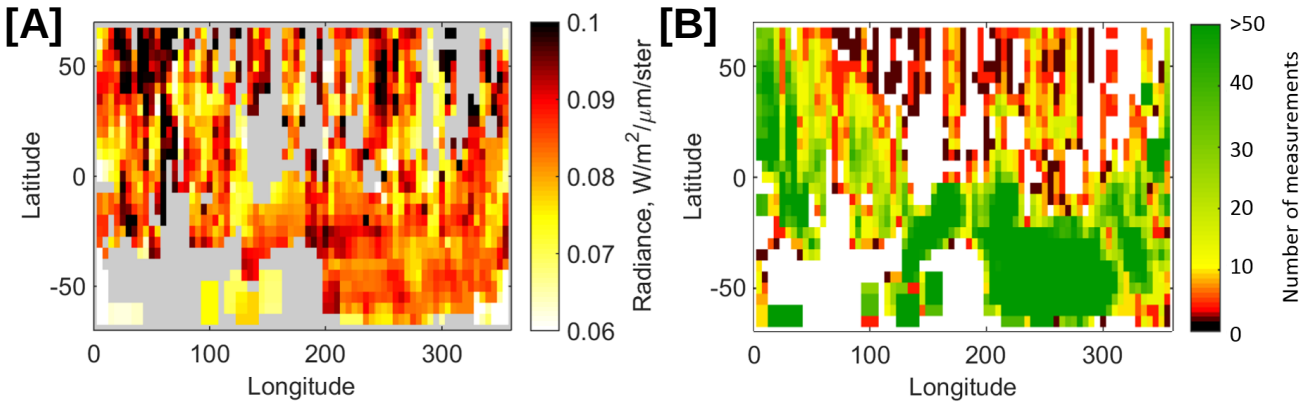

Figure 6.2. (A) Geographic distribution of radiation intensity in a transparency window of 1.28 μm obtained with emission angle ≤10°. The map is averaged within bins of 5°x5°. (B) The number of observations in each bin (Evdokimova et al., 2016).

SPICAV measurements have shown significant variability of radiation at 1.28 μm, with maximum values ranging from 0.05 to 0.1 W/m^2/μm/ster (Evdokimova et al., 2016), with a geographical distribution revealing overall a brighter Northern Hemisphere (Figure 6.2A). In case of the 1.28 μm window, the intensity is insensitive to surface properties and absorption by trace gases like water vapour and SO_2 and is modulated only by the variations of the cloud opacity.

SPICAV IR was working in 2006-2014, and for nadir night observations the accumulated dataset encompassed almost the entire Venus globe. The spatial resolution changed in range of 50-1000 km depending on the spacecraft distance to the planet due to the orbit elongation (Korablev et al., 2012). The observations in the Northern Hemisphere were performed from the orbit pericentre and here the spatial resolution is much higher than for the Southern Hemisphere. The measurements with the SZA larger than 95° are considered. It corresponds almost to the entire range from 18:00 to 6:00 of local time. It has to be noted that the spectra measured close to the terminator contained a fraction of solar radiation. The elimination of solar signal was performed by linear extrapolation of the background between the 1.18, 1.28 and 1.31 windows. In case of a strong illumination, the spectra were not considered in the analysis. As well, the observations made at nadir with emission angle ≤2° are chosen to set a zero emission angle in the radiative transfer model. In total, 605 sessions of observations were analysed, this number corresponds to ~6000 spectra. The spatial coverage and resolution by the observations is presented in Figure 6.3.

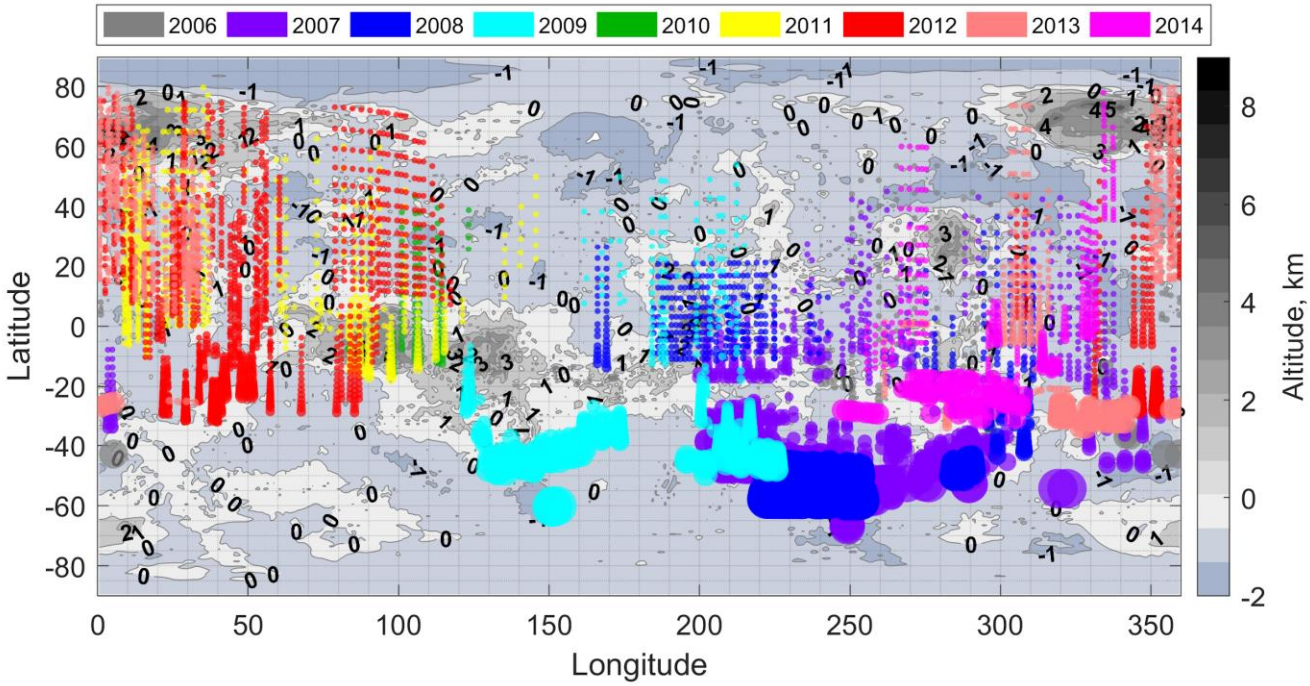

Figure 6.3. Spatial distribution of the analysed observations performed in different years. The circles represent the FOV of SPICAV IR in a particular measurement. If the diameter of the FOV is lower than 100 km, it is set equal to 100 km for the visualization.

The current analysis presents the modelling of three atmospheric windows to retrieve the water vapour abundance below clouds, the cloud opacity changes and the surface emissivity. The preliminary result of modelling is used also to eliminate the thermal emission from the O_2 ($\alpha^1\Delta_g$) airglow.

6.3. Modelling of the night thermal emission

6.3.1. Direct model

The SPICAV IR spectra were analysed by a 1-D radiative transfer model with multiple scattering. The direct model is computed by the SHDOMPP program which solves the radiative transfer equation using the method of discrete ordinates and spherical harmonics in a plane-parallel atmosphere (Evans, 2007). This routine was developed by Bruno Bézard and Anna Fedorova (Bézard et al., 2011; Fedorova et al., 2015), and it is used in this study with an updated cloud layer model. Radiative transfer is calculated on a grid of heights from -2 to 80 km with a step of 1 km independently for each wavelength. The initial level is a changing parameter to be consistent with the topography for a particular observation.

The input parameters of the model are the profiles of temperature, pressure, and CO_2 mixing ratio taken from the VIRA database (Seiff, 1985). CO_2 mixing ratio is equal to 0.965. The water vapour is initially taken as a uniformly mixed gas below the clouds, H_2O VMR is set equal to 30 ppmv.

The model takes into account the absorption of CO_2 and H_2O. CO_2 absorption is calculated according to the high-temperature spectroscopic database «High-T» proposed for these windows in work of Bézard et al., 2011 (Pollack et al., 1993; Tashkun et al., 2003; Bézard et al., 2011; Fedorova et al., 2015). The absorption of water vapour in the lower atmosphere is based on the BT2 line list (Barber et al., 2006). Rayleigh scattering by carbon dioxide molecules is also taken into account.

The gaseous, specifically CO_2, absorption in the IR is more complex to handle at the high temperature and pressure conditions of the Venusian atmosphere. The observations showed that it is necessary to consider the CO_2 continuum, i.e. the superposition of very distant wings of strong permitted CO_2 bands and the possible collision-induced transitions with this molecule. Its possible values were limited to the 1.28-μm and 1.18-μm windows in the ranges of $(0.30\text{-}0.78)\times10^{-9}$ $cm^{-1}amagat^{-2}$ and $(0.29\text{-}0.66)\times10^{-9}$ $cm^{-1}amagat^{-2}$ respectively, as described in the work of Fedorova et al. (2015). For the defined ranges, the continuum level was empirically chosen equal to 0.75×10^{-9} $cm^{-1}amagat^{-2}$ and 0.38×10^{-9} $cm^{-1}amagat^{-2}$ for transparency windows of 1.28 and 1.18 μm respectively. For 1.1-μm transparency window continuum is taken also equal to 0.38×10^{-9} $cm^{-1}amagat^{-2}$.

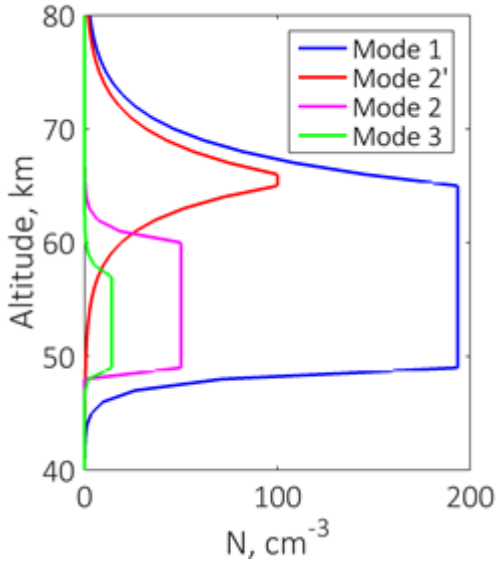

Figure 6.4. Vertical distribution of aerosol particles in the cloud layer with mode separation based on Haus et al. (2016).

The scattering in the cloud layer is computed according to the Mie theory. The chosen cloud model is an update in comparison with the previous study of Fedorova et al. (2015). Here it is considered the work of Haus et al. (2016) assumes spherical-shaped aerosol particles composed of 75%-H_2SO_4 water solution. The density profiles of aerosol (Figure 6.4) are computed by the Equation 6.1 with parameters set in Table 6.1.

$$N(z) = \begin{cases} N_0(z_b)\, exp\left(-\dfrac{(z-(z_b+z_c))}{H_{up}}\right), z > (z_b+z_c) \\ N_0(z_b), (z_b+z_c) \geq z \geq z_b \\ N_0(z_b)\, exp\left(-\dfrac{(z_b-z)}{H_{lo}}\right), z < z_b \end{cases} \quad (6.1)$$

The aerosol particles sizes of four modes are assumed to be distributed according to log-normal law. The modal radii are 0.3, 1.0, 1.4, 3.65 μm for modes 1, 2, 2’ and 3 respectively. The dispersions of modal sizes’ distributions are 1.56, 1.29, 1.23, 1.28 (Pollack et al., 1993). Refractive index of H_2SO_4-acid solution was taken from Palmer and Williams (1975). It was estimated (Evdokimova et al., 2016) that

the main impact on the 1.28-μm intensity comes from aerosol particles belonging to the Modes 2 and 3 that compose the middle and the lower cloud layers.

Table 6.1. Parameters of the aerosol distribution in the cloud layer from Haus et al. (2016).

Mode	1	2	2’	3
Lower base of peak altitude $z_{b,}$ km	49.0	65.0	49.0	49.0
Layer thickness of constant peak particle number z_c, km	16.0	1.0	11.0	8.0
Upper scale height H_{up}, km	3.5	3.5	1.0	1.0
Lower scale height H_{lo}, km	1.0	3.0	0.1	0.5
Particle number density N_0 at z_b, cm^{-3}	193.5	100	50	14

The radiative transfer model spectral step is 0.1 cm^{-1}. A convolution is carried out later to simulate the AOTF function of the spectrometer (Korablev et al., 2012) and to be consistent with the spectral resolution of SPICAV IR.

6.3.2. Inverse problem

The model set up to handle the experimental data requires a determination of three parameters:

(1) a scaling parameter applied to mode 2 and 3 particles’ distribution in the lower cloud layer (*SF* in Equation 6.2);

(2) the water vapour VMR in the lower atmosphere of Venus (VMR_{H2O} in Equation 6.2),

(3) the value of the surface emissivity for the 1.1-μm window (*EMIS* in Equation 6.2).

The inversion problem for the spectra obtained SPICAV IR were analysed using a look-up table. It represents the calculated radiation intensity for parameter values in the intervals: 70-240% for the scaling factor of aerosol concentration with a step of 5%, 2-50 ppm for the H_2O VMR with a step of 2 ppm and 70% -95% for surface emissivity with a step of 5%. Surface temperature changes due to topography are accounted for, and the radiation was modelled for various initial heights. Their values were set in the range from -2 to 9 km with a step of 1 km. Continuum values remained fixed for all calculations. The implication of Haus et all., model allowed to successfully describe the variation of 1.28-μm window intensity by varying the Mode 2 and 3 densities.

Parameters that provided the minimum value of χ^2 between the modelled radiance R_{mod} and the experimental one R_{exp} were considered as the solution. The computation of χ^2 value excludes the spectral range of 1.26-1.277 μm (blue interval in Figure 6.5A) where the IR thermal spectra is overlapped by the oxygen emission line at 1.27 μm (Figure 6.5B). The surface height in the observing location is z_0, it determines the initial level for the radiative transfer computation.

$$\chi^2\left(z_0, SF, VMR_{H_2O}, EMIS\right) = \frac{\left(R_{exp}(z_0) - R_{mod}(z_0, SF, VMR_{H_2O}, EMIS\right)^2}{\sigma_{exp}^2} \quad (6.2)$$

The error bars of the spectrum σ_{exp} are estimated using the noise-equivalent-brightness (NEB) of the instrument (Korablev et al., 2012). It has been estimated during in-flight observations of the Sun and Venus. If the exposure time is 89.6 ms and the Peltier cooler is enabled, the SNR ratio is about 50 and NEB is about 0.0025 W/m^2/μm/ster for the long-wave channel. The error of an observation made without cooling the detectors is doubled the NEB value presented above.

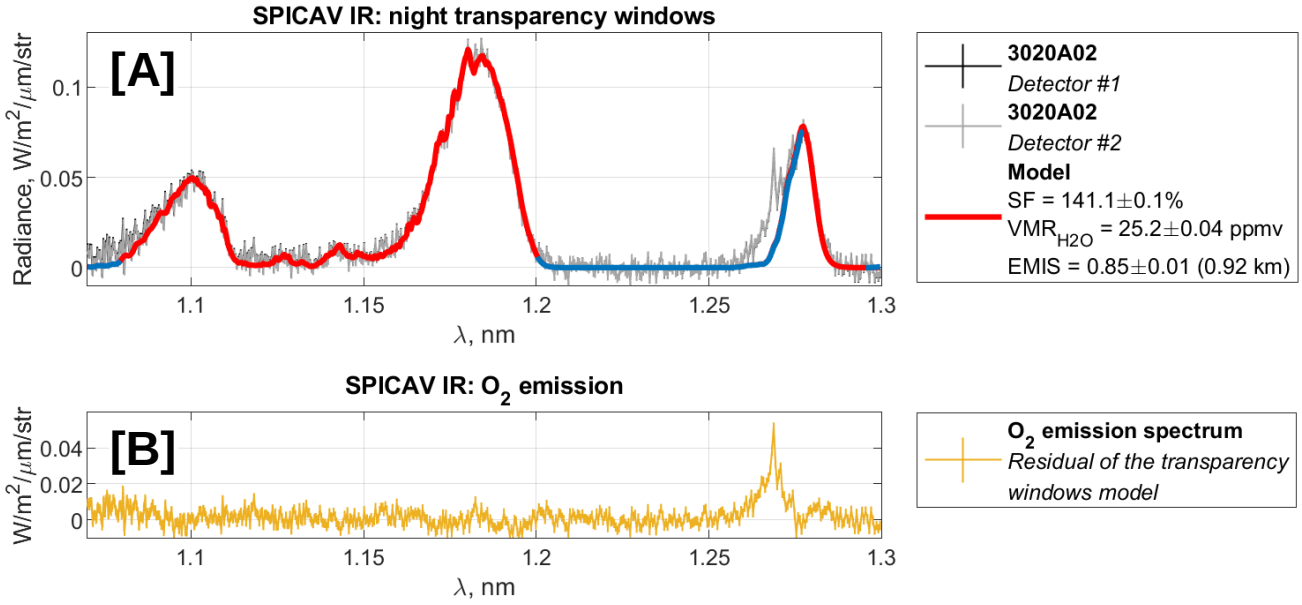

Figure 6.5. (A) Grey and black curves with error bars show the tree atmospheric transparency windows and the oxygen airglow obtained in one measurement of a nadir session collected in orbit #3020A02 (26 July 2014). The red curve is the best model of the radiation, where blue colour shows the wavelength range avoided in the best model assumption. (B) O_2 ($\alpha^1\Delta_g$) emission band at 1.27 μm, which is the residual between the model and the experiment.

6.4. Mapping water vapour and aerosols and uncertainties

Significant variations of aerosol concentrations within the cloud layer were found in the data. Such a behaviour is in correspondence with changes in the 1.28-μm transparency window intensity. The values obtained vary in the range from 80 to 180%. In column abundances these variations correspond to (1.0-2.2)×10^9 cm^{-2} for Mode 3 and (0.45-1.0)×10^{10} cm^{-2} for Mode 2'. The starting values of the fit were based on the Haus et al. (2016) model and corresponded to column densities of 1.2×10^9 and 5.7×10^9 cm^{-2} respectively.

To investigate correlations with surface topography (Figure 6.5C), a geographic distribution of the scaling factor was constructed averaging the data within bins of 10ºx10º (Figure 6.5A). The elongated orbit of Venus Express changes the size of the FOV during the orbit. Emission integrated over a larger area was observed in the Southern Hemisphere, and this was taken into account in the averaging procedure (Figure 6.5D). The geographic distribution obtained for the aerosol concentration is non-uniform, while no precise correlation with topography could be established (Evdokimova et al., 2019a).

In the lower atmosphere the water vapour content was observed by SPICAV IR to be quite stable at 25±3 ppmv, and this value is slightly lower than the obtained by previous observers (Bézard et al., 2011; Fedorova et al., 2015). The best correspondence was obtained with a value of 26±7 ppmv derived from ground based observations of the 1.18-μm window (Arney et al., 2014). In agreement with previous studies, the zonal averaging of H_2O VMR does not show any prominent latitudinal trend. A possible link with topography (Figure 6.4B) was however noted. The latter could be consolidated by minimizing the data processing uncertainties considered below.

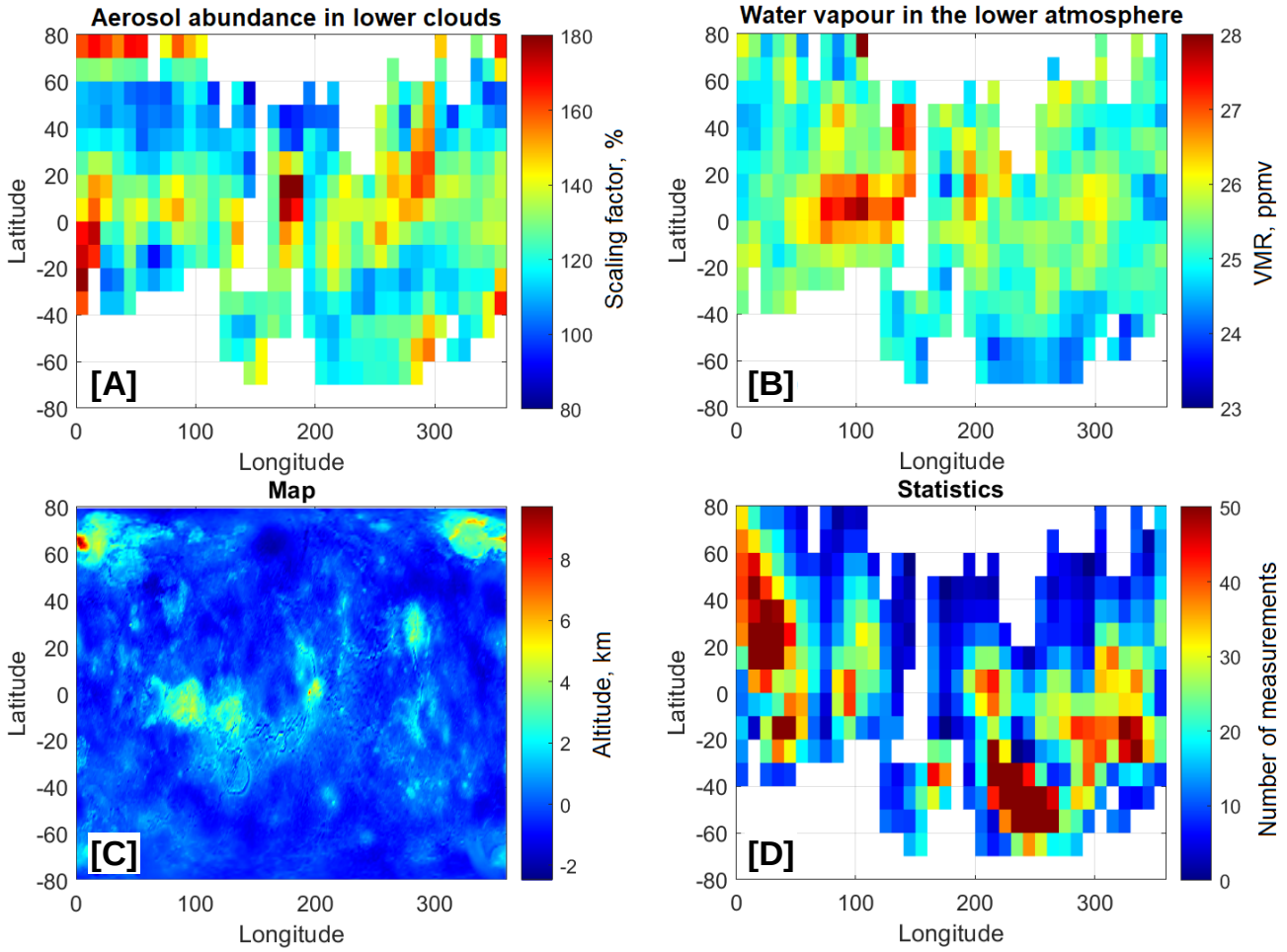

Figure 6.6. Scaling factor for concentration profiles of modes 2 and 3 aerosol particles (A) and water vapour volume mixing ratio (B) averaged by a geographical grid of 10ºx10º. (C) Planetary surface map from Magellan (Saunders et al., 1990). (D) Statistics of observations in each bin.

The parameters retrieved for the lower cloud layer and water vapour below 15 km are affected by the model uncertainties. The accuracy of the radiative transfer computations in the hot dense atmosphere of Venus depends on:

(1) the profiles of temperature, pressure and CO_2 concentration;

(2) the model of aerosol particles and their distributions within the cloud layer;

(3) the accuracy of high-temperature databases for the spectroscopic parameters associated with the vibrational-rotational transitions of the CO_2 molecule and the actual models of line wings suitable for the conditions of the hot dense lower atmosphere of Venus.

It is expected that the first source of inaccuracy is not expected to play a major role. The second and third items have similar influence. The composition of cloud particles remains subject to large uncertainty. The existing models of the cloud layers are based only on the *in situ* observations that were made by atmospheric probes which might be a good proxy for the entire cloud system. The primary constituent of the clouds is the concentrated H_2SO_4 acid water solution. However, the some *in situ* observations have argued that other chemical species might be doped in the aerosols of Mode 3 (Titov et al., 2017). Lastly, some observations as well show variations in the concentration of the acid solution (Arney et al., 2014) which may then violate our hypothesis #2. In polar regions where the cloud tops altitude is decreasing the model should also include some corrections. Therefore, while our assumptions on the scattering properties in the clouds appear in a good agreement with observed changes of IR radiance, some significant uncertainties remain.

Hypothesis #3 is related to the gaseous absorption at high temperatures. The high density and high temperatures of the lower atmosphere profoundly affect the absorption behaviour of atmospheric gases, especially CO_2. The CO_2 continuum absorption is not computed theoretically, and could only be retrieved based on actual Venus thermal spectra. Its appearance has no distinct features, yet a good scattering estimation of the IR inside the clouds greatly depends on representing it correctly. The obtained ranges are too loose to constrain the continuum and provide a good estimate necessary to conduct a qualitative analysis of the lower cloud density. This is why the continuum is fixed in our analysis since the elevation does not change significantly on Venus to alter this absorption. Areas of high mountains should however be considered more cautiously. An underestimation of the continuum probably explains the strong correlation between topography and the retrieved water vapour amount around the Aphrodita Tera area (Figure 6.6B: latitudes of 10°S-20°N and longitudes of 80-110°), but this aspect was not studied in details. Current spectroscopy should be improved by laboratory study, which would then favourably impact the analysis of the IR emission.

Further analysis of SPICAV is therefore possible. Our current analysis considers only the nadir observations really perpendicular to the surface. However, other observations performed at different angles are yet to be processed, but would require to allow the radiative transfer model handling these geometries.

6.5. Map of oxygen airglow in the night mesosphere

This preliminary modelling of the radiative transfer was sufficient to separate the O_2 ($\alpha^1\Delta_g$) emission from thermal emission spectra. The remaining uncertainties in the radiative transfer do not impede our ability to perform this separation thanks to the high resolution of the IR channel of the SPICAV spectrometer. To be more consistent the model is computed for the 1.05-1.3 μm interval instead of focusing on the 1.28-μm window. The O_2 emission may vary significantly during the monitoring while different locations are scanned. For instance, during the orbit #1713A02 the airglow is rather bright at the beginning of measurements, but at the end (Figure 6.7).

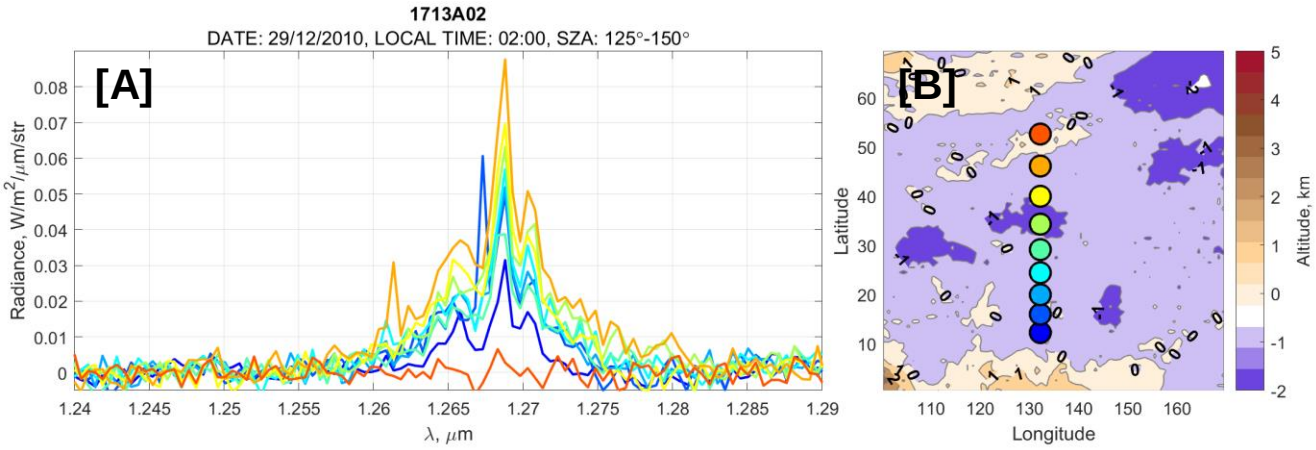

Figure 6.7. (A) The O_2 ($\alpha^1\Delta_g$) emission obtained during the observational session #1713A02 by SPICAV IR (December 29, 2010; local time of 02:00; SZA in 124°-149°). (B) The geographical locations corresponding to measured spectra.

In total, more than 600 observations were analysed based on the aforementioned procedure of O_2 emission separation. It allowed us to corroborate and complete the VIRTIS-M study of latitudinal distribution of the airglow's intensity in the nightside. The VIRTIS-M monitoring stopped in 2010 and covered mainly the night Southern Hemisphere of Venus (Gerard et al., 2009; Shakun et al., 2010; Soret et al., 2012). The SPICAV was operational until the end of 2014. SPICAV dataset finally allowed the reconstruction of the full mean distribution of airglow brightness (Figure 6.8). Each spectrum was integrated to compute the absolute intensity.

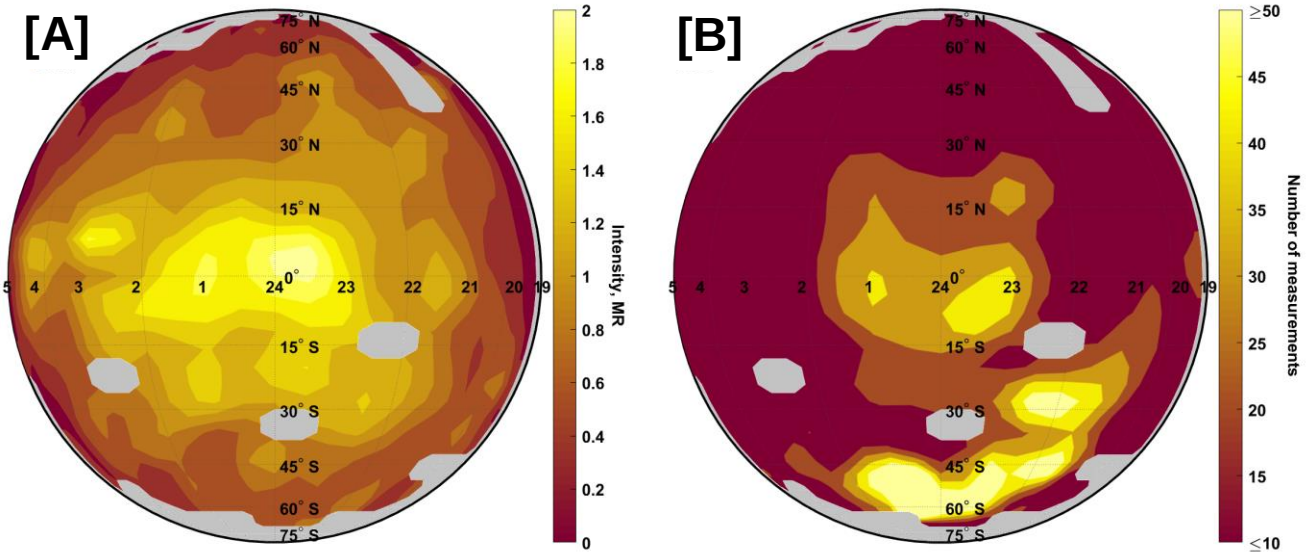

Figure 6.8. (A) Average map of oxygen airglow brightness obtained by nadir measurements of SPICAV IR (Evdokimova et al., 2019b) on the night side. The observations are grouped by a grid of 30 min in local time and 4° in latitude. (B) The corresponding statistics of observations.

An intensity maximum of 2 MR was found exactly at the antisolar point. The emission pattern is fairly symmetrical about the equator, yet shows some tendency to be slightly shifted towards the morning terminator. The brightness is decreasing significantly after 23:00 towards the evening terminator. These results are in agreement with the analysis of VIRTIS data (Shakun et al., 2010; Soret et al., 2012), yet suggest a slightly higher intensity.

The map obtained by SPICAV does not reveal any latitudinal shift of the brightest O_2 emission area. The VIRTIS-M provided in contras a slight shift (~10°) to the north. The reason for this difference with the VIRTIS-M result is unclear. It may be the result of different statistics used. Also the lower resolution of VIRTIS does not allow the robust separation of O_2 emission from IR windows as is the case for SPICAV IR. The fixed ratio between intensity of 1.18-μm and 1.28-μm windows is set for the O_2 airglow elimination (Shakun et al., 2010). However, the VIRTIS nadir pattern was confirmed by the its limb observations, whose spectra are free from IR emission. The difference between SPICAV IR and VIRTIS-M patter is a question requiring deeper analysis. But results of both experiments concur with the idea that SSAS circulation is the main mechanism explaining the O_2 ($\alpha^1\Delta_g$) airglow.

6.6. Summary

Nadir observations by SPICAV IR provided information for studying the lower atmosphere and clouds, and O_2 ($\alpha^1\Delta_g$) airglow. Our analysis of the SPICAV IR dataset allowed to separate the emission signal from thermal spectra. It represents a significant contribution to the study of the O_2 ($\alpha^1\Delta_g$) airglow, since the whole night hemisphere is covered in details. The simultaneous VIRTIS-M observations correspond mainly to the Southern Hemisphere. Statistically the maximum of the emission distribution on the night side is located near the antisolar point where the intensity reaches 2MR. This result mainly corresponds to previously reported conclusions.

CONCLUSION

This work is the first analysis of the complete dataset obtained by the SPICAV UV channel operated in the mode of stellar occultation on board the Venus Express orbiter. The goal is to study two trace gases, sulphur dioxide and ozone, in the night mesosphere of Venus. The atmospheric transmission spectra in the range of 118-320 nm, measured at different local times and geographic coordinates, have been analysed.

This goal is achieved thanks to the deep inspection of the data processing algorithms implemented for the whole statistics of stellar occultations. It includes an uncertainty estimation related to following the calibrations of the atmospheric transmission spectra: (1) a wavelength to pixel assignment, and (2) subtracting a portion of emitting atmospheric light which contaminates the analysed transmissions. The wavelength displacement along a pixel number may result in either underestimation or overestimation of retrieved concentrations. For instance, an uncertainty of one-pixel width corresponding to 0.54 nm leads to the retrieved CO_2 slant density change of 20% in the lower mesosphere (85–100 km), as it was estimated. The best accuracy is proved for a method of the pixel-to-wavelength assignment based on the spectral features of measured stars. The method compares star spectra measured by SPICAV with reference ones taken from the well-resolved IUE data. As a result, the higher accuracy was achieved versus the previous approach, based on the wavelength alignment by only CO_2 absorption bands at $\lambda <$ 200 nm. Thus, the developed algorithm reduces the uncertainty of the wavelength to pixel assignment at least by 10 times, and it was estimated to be 1–10% of the width of the pixel.

The second important uncertainty is related to different kinds of atmospheric emissions and stellar radiation in the UV registered by the spectrometer. Those emissions were considered jointly as a stray light, which overlaps a star spectrum making an atmospheric transmission overestimated. There are two different techniques developed for the elimination of such a stray light. In the present work we statistically tested and established the best of two methods to separate the UV emission signal from the incoming stellar light. To apply both methods, we used imaging capabilities of the instrument, where the stray light pattern was determined as a linear combination of spectra registered within edge bins according to the star focus position on the matrix. An algorithm, selected as the most valid, was accepted to calibrate the entire SPICAV dataset. The resulting transmission spectra were used for the spectral inversion problem to retrieve gaseous and aerosols vertical profiles for further investigations.

Thus, the preliminary data preparation finally allowed retrieving sulphur dioxide and ozone contents at altitudes of 85-100 km. The following statements can be concluded:

1. The median volume mixing ratio of SO_2 remains around 135±21 ppbv in the range of 85-100 km. In comparison to the previous study (Belyaev, Evdokimova et al., 2017) a significant correction of SO_2 VMR was obtained. It is strongly related to the calibration method that enhanced the CO_2 concentration values and, therefore, the mixing ratios of trace gases.

2. Variations of sulphur dioxide content were investigated based on 375 observational sessions. The short-term variations reach one-two orders of magnitude, i.e. from ~50 to ~500 ppbv. In detail, the local

time dependence was studied for the interval from 19:00H to 5:00H. A possible diurnal asymmetry relative to midnight is highlighted. The relative sulphur dioxide content may be increasing from 2:00H to the evening terminator at an altitude range of 93-97 km.

3. For the first time, ozone abundance was monitored for 8 years and could be detected in 132 observations. Ozone occurrences are always close to the detection limit, which implies that SPICAV could only probe the peak abundance with no information on the details of the layering. In general, ozone is only detected once when observed during an occultation sequence.

4. The detected ozone concentrations between 85 and 110 km vary from 10^7 to 10^8 cm^{-3}, and detections comprise is about 6% of the entire SPICAV observations. On average, O_3 detections correspond to the range of VMR from 1 to 30 ppbv at altitudes of 85-95 km and from 6 to 120 ppbv at 95-105 km.

5. Ozone positive detections are sporadic. Individual observations show significant changes in VMR in time and in space. Temporal variations were studied in detail in a latitude zone of 30°N±10° where the best coverage was achieved. The local time distribution of ozone content suggests a possible dependence with altitude: below 93 km a decrease towards midnight from the terminators is observed. This minimum flattens higher up in the mesosphere. The pattern is presented only for the 30°N-latitude zone where the observation statistics is dominant. The long-term variations, in turn, does not reveal any significant trends.

PERSPECTIVES

Spectroscopy is currently the most accessible tool to investigate the properties of space objects. It also concerns the study of the atmosphere of Venus, especially above the clouds. Any result of long-term monitoring of the Venusian atmosphere is always a unique set of data, the detailed analysis of which exceeds the potential of terrestrial observations, in the overwhelming majority of cases. For 8 years, the SPICAV spectrometer was accumulating a volume of atmospheric transmission and emission spectra of the lower atmosphere, of the daytime atmosphere at the cloud top level, of the evening and morning mesosphere and thermosphere and, for the first time, of the upper atmosphere in the planet's night-time. My work presents a preliminary analysis of the whole set of the IR spectra of Venus's night-time thermal radiation and the complete analysis of the UV spectra for studying the planet's night-time upper mesosphere. The results of this analysis are very promising as a basis for future investigations of Venus and the formulation of scenarios for future experiments.

Sulphur dioxide and ozone are key components of the chemical cycles in the atmosphere of the Earth's sister. Many observations of sulphur dioxide have been obtained for the entire history of the Venus exploration. This resulted in a great number of publications, but despite this, some results are still a subject of hot discussions. One such question is a reason for the annual variations in SO_2. At different heights, the trends obtained do not quite coincide between each other. Whether it results from a consequence of active dynamics in the upper mesosphere - this is a question for further more in-depth studies.

One of the tasks for researchers of the atmosphere of Venus is to build a global model of its chemistry and circulation, which will describe both transient processes at the surface and active dynamics, and changeable photochemistry above the clouds. For the upper mesosphere on the night side, detailed experimental data on the atmospheric temperature and composition will serve as a basis for validating theoretical calculations. The dataset retrieved in this work is the only detailed measurements of the vertical distributions of sulphur dioxide, carbon dioxide and ozone in the night-time mesosphere and thermosphere.

Ozone was first detected in the atmosphere of Venus using the SPICAV UV spectrometer. Analysis of data for 8 years of observations shows that we do not observe any steady O_3 layer at heights of 85-110 km. However, the registered bursts of ozone content leave the question unresolved: how the processes of formation and destruction of this gas are balanced on the night side of Venus. The processes that regulate the decay of ozone in the Earth's stratosphere and in the mesosphere of Venus are reactions with chlorine-containing components. However, on Venus, neither the global distribution of this molecule nor the substances that break it down have been finally established. This makes it difficult to obtain a model description for the observed altitude range, which is a subject to significant changes due to transient dynamic phenomena. The existing one-dimensional model of the night-time mesosphere (Krasnopolsky, 2013), for example, tends to overestimate the amount of ozone.

Of course, my work provides data for its subsequent discussion and development. It completely systematizes the methodology for processing spectral data. However, the atmosphere of Venus represents a very different environment from its terrestrial twin. Its atmosphere below the clouds is a dense incandescent gas. On the contrary, very cold temperatures are observed above the clouds. Taking these conditions into account is important for the UV spectroscopy of the cold night-time mesosphere and thermosphere, as well as for the IR spectroscopy of the night-time thermal radiation of Venus. Several studies of the atmosphere below clouds have shown that the databases on absorption lines of the carbon dioxide molecule should be supplemented by transitions that are possible only under extreme conditions. In the further analysis of new data obtained by UV spectrometers, especially of high spectral resolution, additional laboratory experiments can also be useful. Recently, it was shown how the absorption of carbon dioxide changes when the temperature drops below 200K. Venot et al. (2018) traced these changes in detail to wavelengths shorter than 180 nm at the lowest temperatures of 150 and 170 K. On the night side, lower temperatures are observed in the cryosphere. Usually, the progress of future missions implies an increase in the accuracy of the experiment, which also means a higher observation boundary, where the temperature decreases. Moreover, for the majority of minor gas components, there are no data on the temperature dependences of their UV absorption cross-sections in the literature so far. Such research, for example, can have a positive impact on the study of the cold atmosphere of Mars.

At the end of this work, I would like to express my confidence that the Venus Express and Akatsuki missions have revived the interest of the scientific community to Venus. Moreover, these studies were accompanied by a very controversial, but disturbing all of humanity, scientific report on the discovery of indirect evidence of a possible life existence in the atmosphere of Venus (Greaves et al., 2020; Encrenaz et al., 2020; Snellen et al., 2020). It convinces me that this will contribute to an active study both of the data: already received by the various instruments and of future observations. The new missions, which are slated to launch in the next decade, hold a great potential to unravel the mysteries of our space neighbour.

LIST OF PUBLICATIONS

The SO_2 night vertical profiles obtained by the author were published in the following works:

Belyaev, D.A., Evdokimova, D.G., Montmessin, F., Bertaux, J.-L., Korablev, O.I., Fedorova, A.A., Marcq, E., Soret, L., & Luginin, M.S. (2017). Night time distribution of SO_2 content in Venus' upper mesosphere. *Icarus*, 294, pp. 58-71.

Vandaele, A. C., Korablev, O., Belyaev, D., Chamberlain, S., Evdokimova, D., Encrenaz, Th., Esposito, L., Jessup, K. L., Lefèvre, F., Limaye, S., Mahieux, A., Marcq, E., Mills, F. P., Montmessin, F., Parkinson, C. D., Roberta, S., Roman, T., Sandor, B., Stolzenbach, A., Wilson, C., & Wilqueta, V. (2017). Sulfur dioxide in the Venus atmosphere: I. Vertical distribution and variability. *Icarus*, 295, pp. 16-33.

Vandaele, A. C., Korablev, O., Belyaev, D., Chamberlain, S., Evdokimova, D., Encrenaz, Th., Esposito, L., Jessup, K. L., Lefèvre, F., Limaye, S., Mahieux, A., Marcq, E., Mills, F. P., Montmessin, F., Parkinson, C. D., Roberta, S., Roman, T., Sandor, B., Stolzenbach, A., Wilson, C., & Wilqueta, V. (2017). Sulfur dioxide in the Venus Atmosphere: II. Spatial and temporal variability. *Icarus*, 295, 1-15.

Pinto, J. P., Li, J., Mills, F. P., Marcq, E., Evdokimova, D., Belyaev, D., & Yung, Y. L. (2021) Sulfur monoxide dimer chemistry as a possible source of polysulfur in the upper atmosphere of Venus. Nature Communications, 12, 175.

The study of the accuracy of the calibration methods performed by the author is published in the following work:

Evdokimova, D., Belyaev, D., Montmessin, F., Bertaux, J. L., & Korablev, O. (2020). Improved calibrations of the stellar occultation data accumulated by the SPICAV UV onboard Venus Express. *Planetary and Space Science*, 184, 104868.

The study of O_3 and SO_2 night content performed by the author were published in the following work:

Evdokimova, D., Belyaev, D., Montmessin, F., Korablev, O., Bertaux, J.-L., Verdier, L., Lefèvre, F., & Marcq, E. (2021). The spatial and temporal distribution of nighttime ozone and sulfur dioxide in the Venus mesosphere as deduced from SPICAV UV stellar occultations. *Journal of Geophysical Research: Planets*, 126, e2020JE006625.

LIST OF CONFERENCES

Evdokimova D.G., Belyaev D.A., Luginin M.S., Fedorova A.A., Korablev O.I., Montmessin F., Marcq E., Bertaux J.-L. Variations in SO_2 content in the mesosphere on the night side of Venus. The 13th All-Russian Open Conference "Modern Problems of Earth Remote Sensing from Space", Moscow, IKI RAS, November 16-20, 2015. (Abstract is in Russian)

Evdokimova D.G., Fedorova A.A., Belyaev D.A. Study of the cloud layer of Venus according to the data of night observations of SPICAV IR on board Venus Express in 2006-2014. XIII Conference of Junior Scientists "Fundamental and Applied Space Research", IKI RAS, April 13-15, 2016, Moscow. (Abstract is in Russian)

Evdokimova D., Fedorova A., Belyaev D., Korablev O., Bertaux J. L. «Studying of cloud variations using night observations data of SPICAV IR in 2006-2014» Abstracts. The Seventh Moscow Solar System Symposium, October 10-14, 2016, IKI RAS, Moscow.

Evdokimova D., Montmessin F., Belyaev D., Fedorova A. «Remote sensing of the Venus night atmosphere by SPICAV onboard the Venus Express orbiter» Abstracts. Conférence Elbereth 2016, November 21-25, 2016, IAP, Paris.

Evdokimova, D.G., Fedorova, A.A., Belyaev, D.A. Influence of Venus cloud layer parameters on the intensity of the night transparency window at 1.28 μm according to the SPICAV IR observations in 2006-2014. XIV Conference of Junior Scientists "Fundamental and Applied Space Research", IKI RAS, April 12-14, 2017, Moscow. (Abstract is in Russian)

Evdokimova, D., Baggio, L., Montmessin, F., Belyaev, D., Bertaux, J. -L. A new method to analyze UV stellar occultation data. European Planetary Science Congress 2017, 17–22 September 2017, Riga. EPSC Abstracts Vol. 11, EPSC2017-962-1, 2017.

Evdokimova, D.G., Fedorova, A.A., Belyaev, D.A., Korablev, O.I., Marcq, E. Venus cloud parameters modulating the 1.28-μm nightside window emission observed by SPICAV IR/VEX. The Eighth Moscow Solar System Symposium, 9-13 October 2017, IKI RAS, Moscow. 8MS3-PS-02. Pp 199-200.

Evdokimova D., Montmessin F., Belyaev D., Fedorova A., Baggio L., Marcq E. Studying the aerosol and gaseous composition of the night-side Venus atmosphere with SPICAV on Venus Express. Conférence Elbereth 2017, 22-24 November 2017, IAP, Paris. P. 8.

Evdokimova D., Montmessin F., Belyaev D., Fedorova A., Baggio L., Marcq E., Korablev O.I. Methods for studying gases and aerosols of the night atmosphere and clouds of Venus based on observations of the SPICAV spectrometer. XV Conference of Junior Scientists "Fundamental and Applied Space Research", IKI RAS, April 11-13, 2018, Moscow. (Abstract is in Russian) Pp. 30-31.

Evdokimova, D., Baggio, L., Montmessin, F., Belyaev, D., Bertaux, J. -L. Retrieval the gaseous composition of Venus night-side mesosphere with SPICAV UV onboard Venus Express, European Geosciences Union General Assembly 2018, 8–13 April 2018, Vienna, Austria. P. EGU2018-16084

Evdokimova, D.G., Fedorova, A.A., Belyaev, D.A., Korablev, O.I., Marcq, E., Bertaux, J.-L. Variations of the lower cloud layer and H2O in the deep atmosphere of Venus from the night windows observations by SPICAV-IR/VEX. The Ninth Moscow Solar System Symposium, October 9-12, 2018, IKI RAS, Moscow. 9MS3-VN-01. Pp 62-63.

Evdokimova, D.G., Baggio, L., Montmessin, F., Belyaev, D.A., Bertaux, J.-L. Improved retrieval of gaseous concentration profiles in Venus mesosphere using SPICAV-UV/VEX stellar occultation data. The Ninth Moscow Solar System Symposium, October 9-12, 2018, IKI RAS, Moscow. 9MS3-PS-34. Pp 287-288.

Evdokimova D. Investigation of NO emission from the data of observations of limbs and stellar occultations SPICAV-UV/VEX. School-seminar "Atmospheres of planets: From the terrestrial planets to exoplanets", March 25-27, 2019, Polar Geophysical Institute, Apatity.

Evdokimova, D.G., Belyaev D.A., Montmessin F., Venot O. Analysis of the temperature dependence of the molecular absorption cross-sections of CO_2 in the UV spectral range from 120 to 190 nm. XVI Conference of Junior Scientists "Fundamental and Applied Space Research", IKI RAS, April 15-17, 2019, Moscow. (Abstract is in Russian) Pp. 43-44.

Evdokimova D., Fedorova A., Korablev O., Marcq E., Bertaux J.-L. Variations of lower clouds and water vapor amount in deep Venus atmosphere based on night windows observations by the SPICAV-IR/Venus-Express. International Venus Conference 2019, May 31 - June 3, 2019, Niseko, Hokkaido, Japan. 09-6 IVC2019-0112. P. 123.

Evdokimova, D., Montmessin, F., Belyaev, D., Bertaux, J. -L. First global extraction of mesospheric Venusian O3 and SO2 concentrations from the entire SPICAV-UV/VEX stellar occultations dataset. EPSC-DPS Joint Meeting 2019. September 15-20, 2019, Geneva, Switzerland, EPSC-DPS2019-1469

Evdokimova, D.G., Fedorova, A.A., Korablev, O.I., Belyaev, D.A., Bertaux J.-L. (2019) Monitoring of the atmospheric oxygen airglow on the night side of Venus according to the dataset of SPICAV IR of the Venus Express spacecraft. (in Russian). The 17th All-Russian Open Conference "Modern Problems of Earth Remote Sensing from Space", Moscow, IKI RAS, 2019. DOI: 10.21046/17DZZconf-2019a

Evdokimova, D.G., Belyaev, D.A., Montmessin, F., Korablev, O.I., Bertaux, J.-L., Verdier, L., Lefevre, F., Marcq, E. (2019) Observations of ozone and sulfur dioxide in the night atmosphere of Venus at 85-105 km by SPICAV UV/Venus Express. (in Russian). The 18th All-Russian Open Conference "Modern Problems of Earth Remote Sensing from Space", Moscow, IKI RAS, 2020. XVIII.P.525

ANNEX 1. Positive detections of SO_2 presented individually

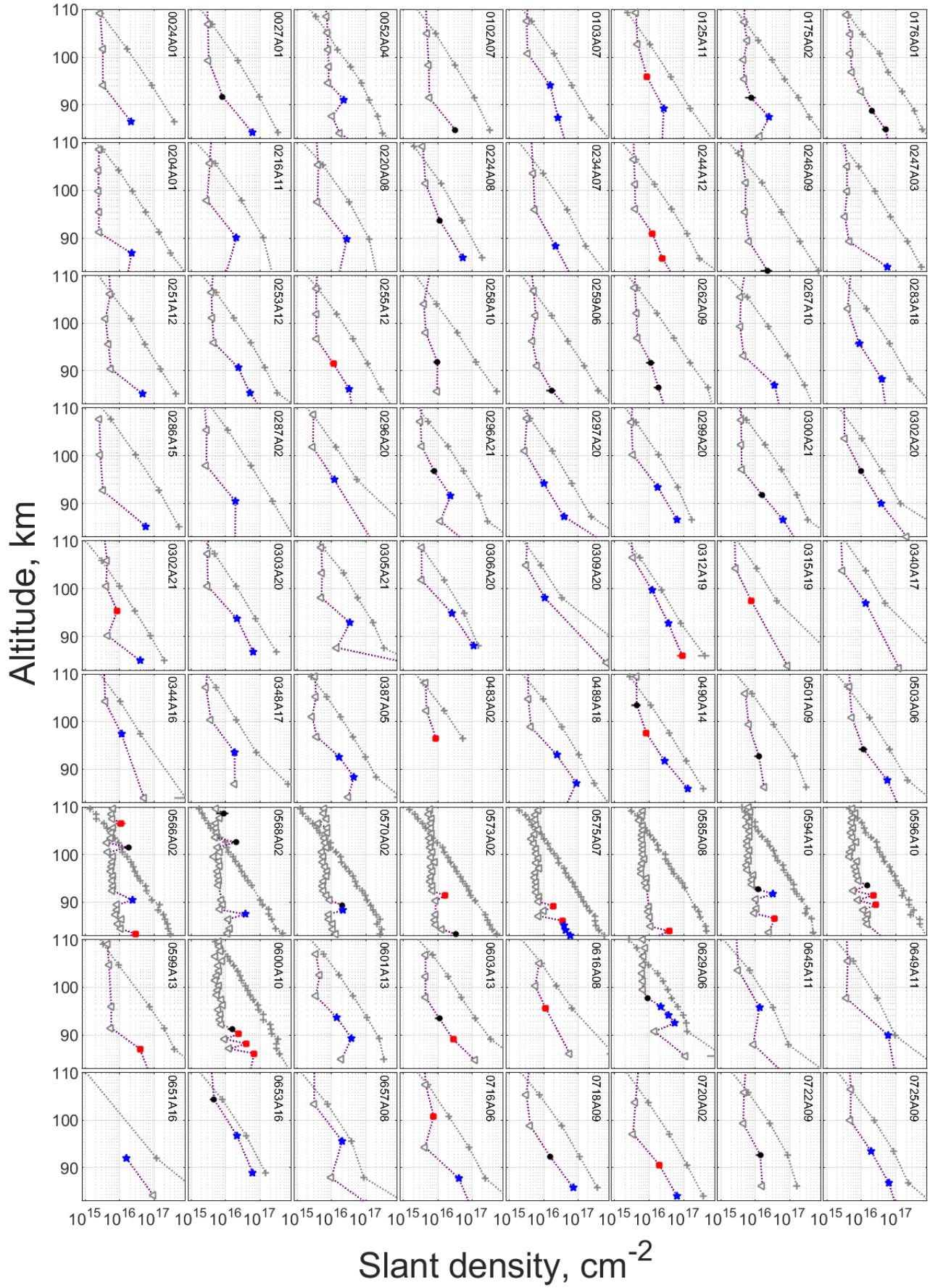

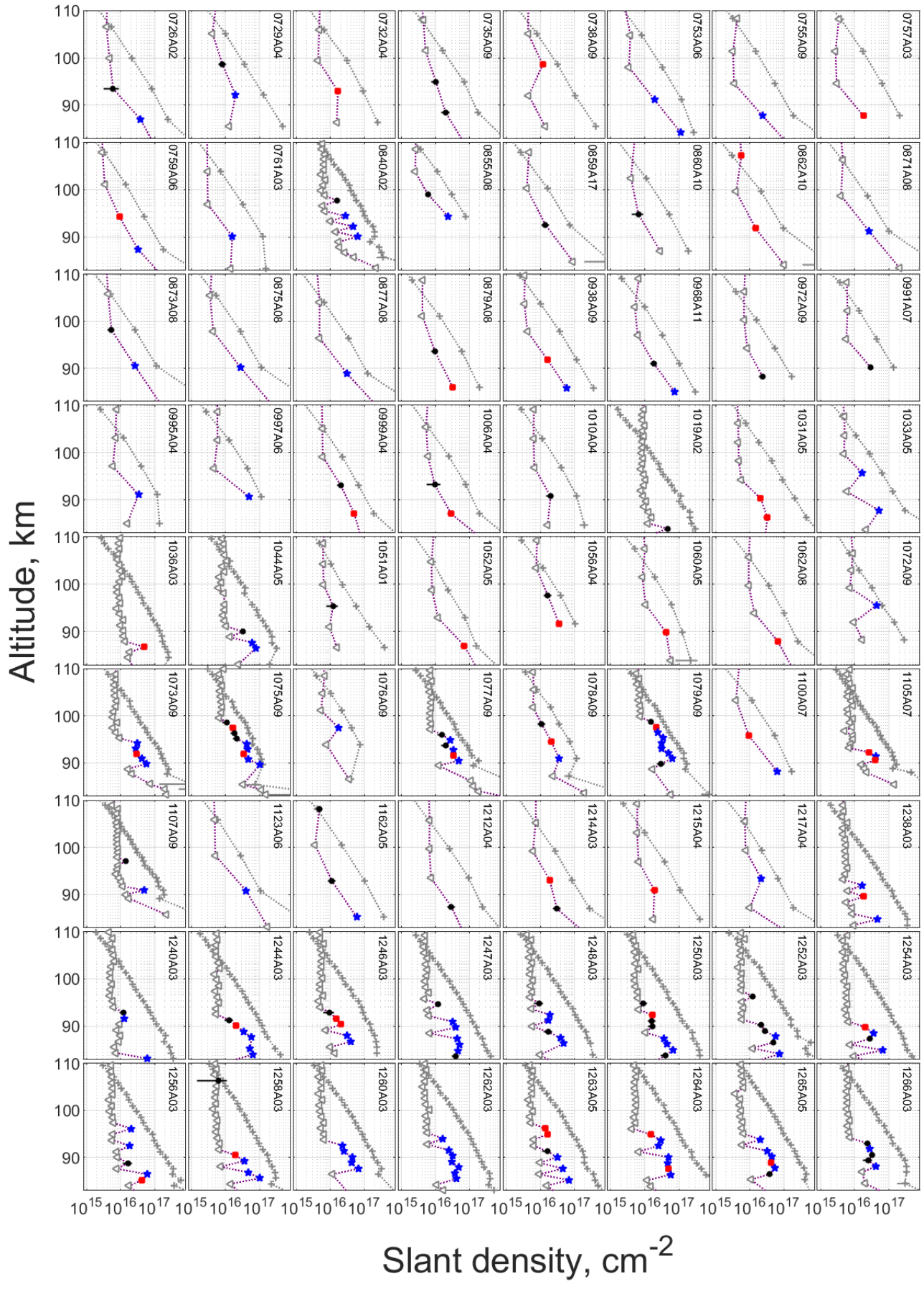
Altitude, km
Slant density, cm-2
0757A03
0871A08
0991A07
1033A05
1072A09
1105A07
1238A03
1254A03
0755A09
0862A10
0972A09
1031A05
1062A08
1100A07
1217A04
1252A03
1265A05
0753A06
0860A10
0968A11
1019A02
1060A05
1079A09
1215A04
1250A03
1264A03
0738A09
0859A17
0938A09
1010A04
1056A04
1078A09
1214A03
1248A03
1263A05
0735A09
0855A08
0879A08
1006A04
1052A05
1077A09
1212A04
1247A03
1262A03
0732A04
0840A02
0877A08
0999A04
1051A01
1076A09
1162A05
1246A03
1260A03
0729A04
0761A03
0875A08
0997A06
1044A05
1075A09
1123A06
1244A03
1258A03
0726A02
0759A06
0873A08
0995A04
1036A03
1073A09
1107A09
1240A03
1256A03

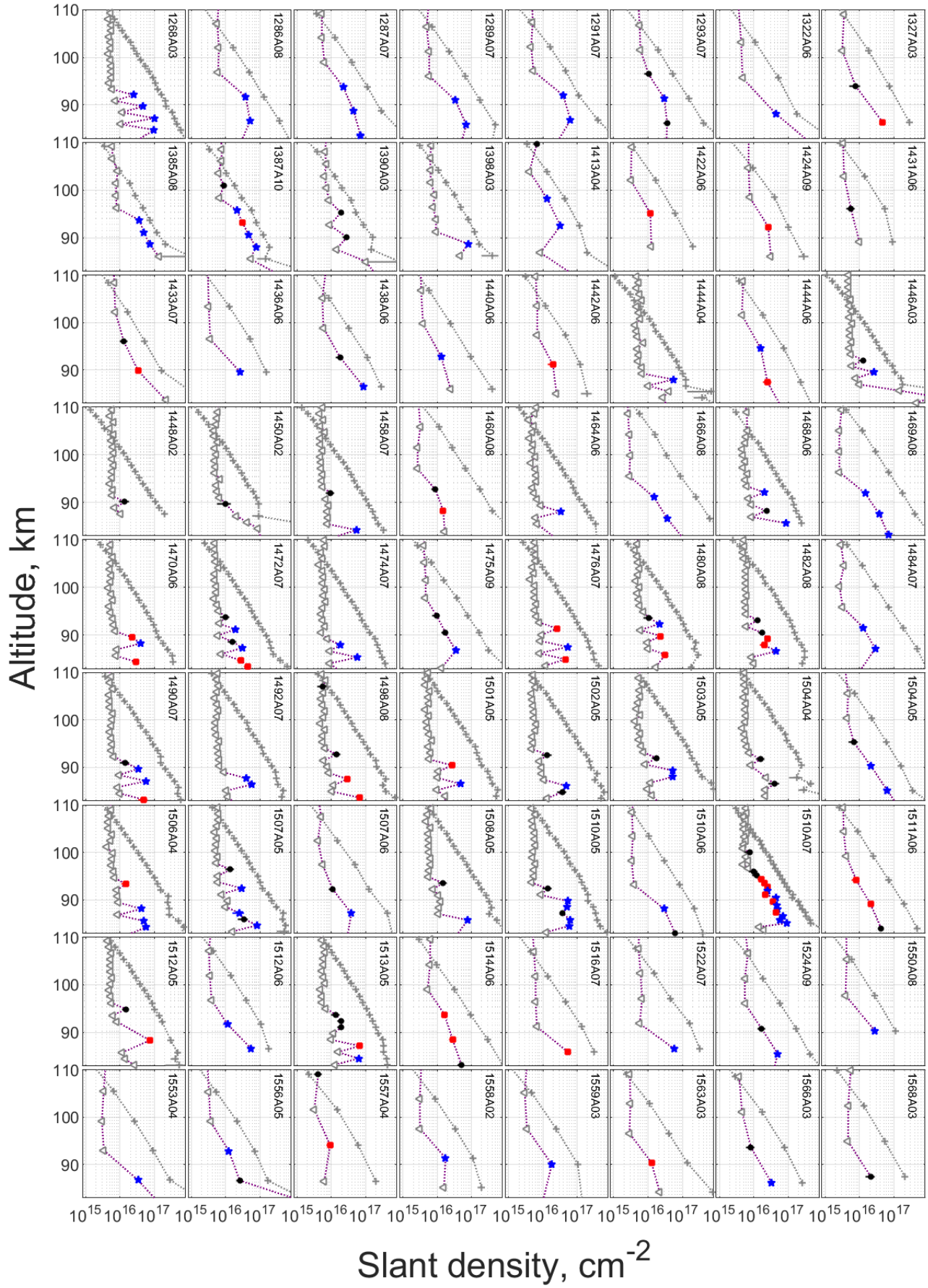
Altitude, km
Slant density, cm-2
1327A03
1431A06
1322A06
1424A09
1293A07
1422A06
1291A07
1413A04
1289A07
1398A03
1287A07
1390A03
1286A08
1387A10
1268A03
1385A08
1446A03
1444A06
1444A04
1442A06
1440A06
1438A06
1436A06
1433A07
1469A08
1468A06
1466A08
1464A06
1460A08
1458A07
1450A02
1448A02
1484A07
1482A08
1480A08
1476A07
1475A09
1474A07
1472A07
1470A06
1504A05
1504A04
1503A05
1502A05
1501A05
1498A08
1492A07
1490A07
1511A06
1510A07
1510A06
1510A05
1508A05
1507A06
1507A05
1506A04
1550A08
1524A09
1522A07
1516A07
1514A06
1513A05
1512A06
1512A05
1568A03
1566A03
1563A03
1559A03
1558A02
1557A04
1556A05
1553A04

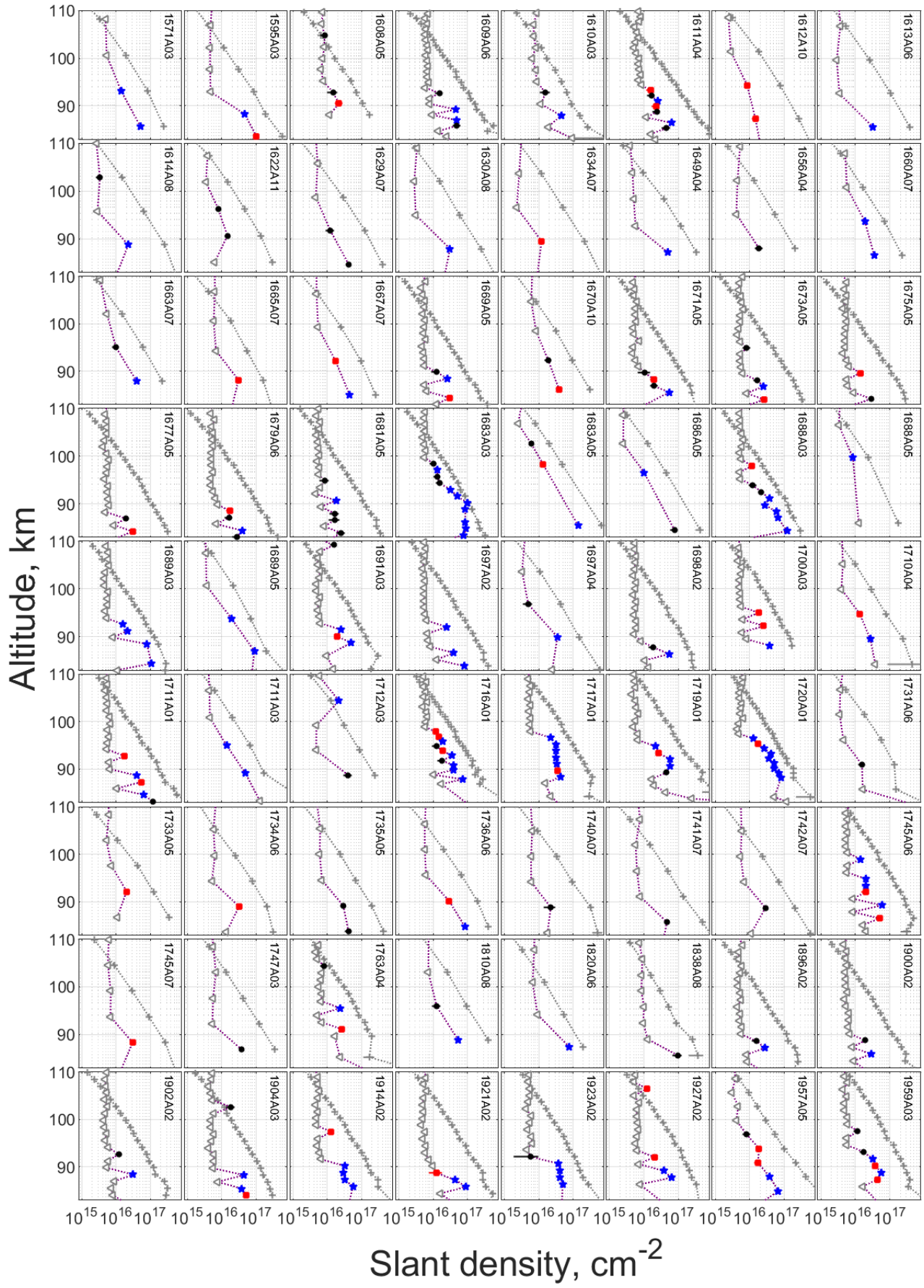
Altitude, km
Slant density, cm-2
110
100
90
1613A06
1660A07
1675A05
1688A05
1710A04
1731A06
1745A06
1900A02
1959A03
1612A10
1656A04
1673A05
1688A03
1700A03
1720A01
1742A07
1896A02
1957A05
1611A04
1649A04
1671A05
1686A05
1698A02
1719A01
1741A07
1838A08
1927A02
1610A03
1634A07
1670A10
1683A05
1697A04
1717A01
1740A07
1820A06
1923A02
1609A06
1630A08
1669A05
1683A03
1697A02
1716A01
1736A06
1810A08
1921A02
1608A05
1629A07
1667A07
1681A05
1691A03
1712A03
1735A05
1763A04
1914A02
1595A03
1622A11
1665A07
1679A06
1689A05
1711A03
1734A06
1747A03
1904A03
1571A03
1614A08
1663A07
1677A05
1689A03
1711A01
1733A05
1745A07
1902A02
10^15 10^16 10^17

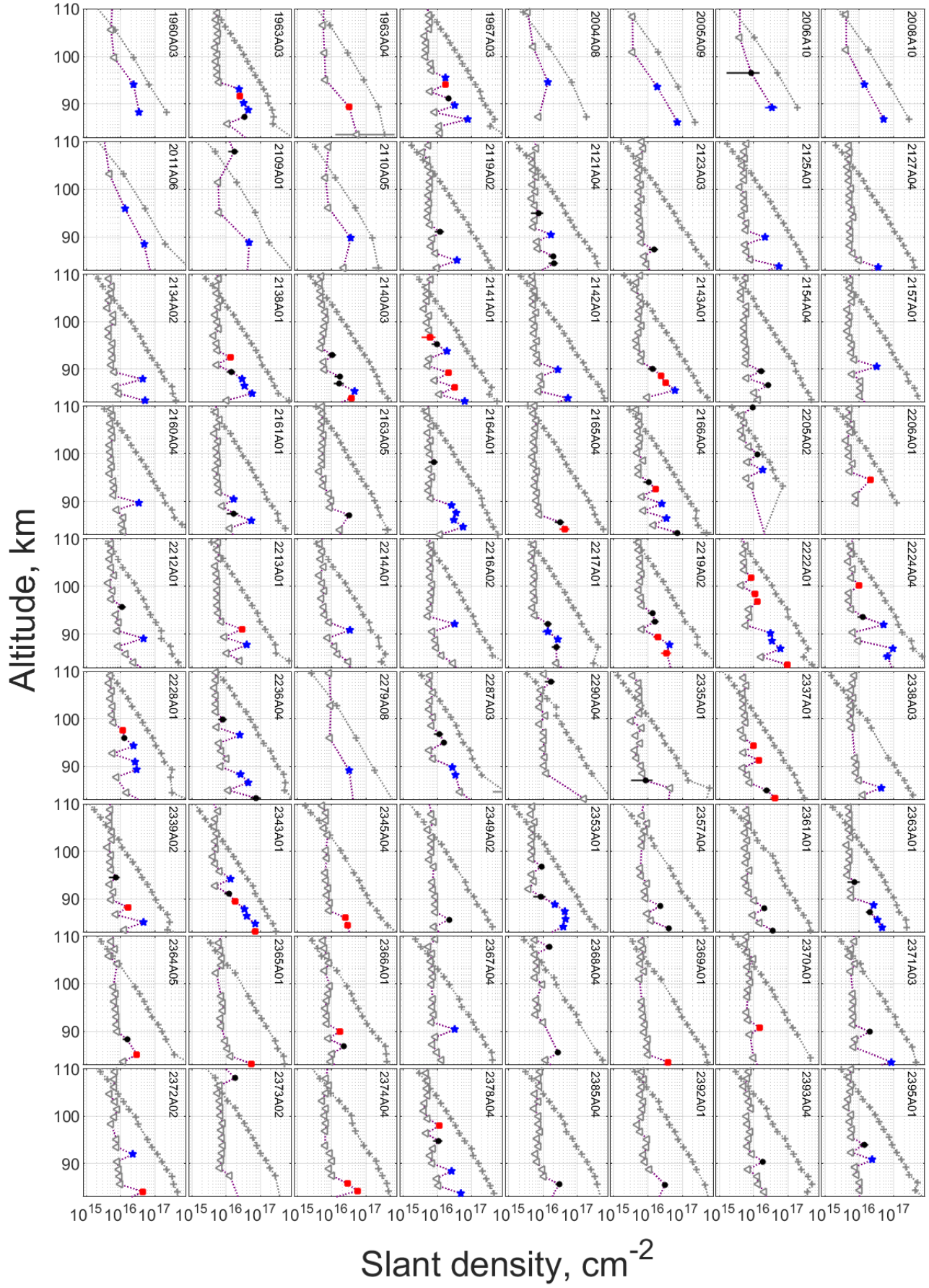
Altitude, km
Slant density, cm-2
2008A10
2127A04
2006A10
2125A01
2005A09
2123A03
2004A08
2121A04
1967A03
2119A02
1963A04
2110A05
1963A03
2109A01
1960A03
2011A06
2206A01
2157A01
2205A02
2154A04
2166A04
2143A01
2165A04
2142A01
2164A01
2141A01
2163A05
2140A03
2161A01
2138A01
2160A04
2134A02
2224A04
2338A03
2222A01
2337A01
2219A02
2335A01
2217A01
2290A04
2216A02
2287A03
2214A01
2279A08
2213A01
2236A04
2212A01
2228A01
2363A01
2371A03
2361A01
2370A01
2357A04
2369A01
2353A01
2368A04
2349A02
2367A04
2345A04
2366A01
2343A01
2365A01
2339A02
2364A05
2395A01
2393A04
2392A01
2385A04
2378A04
2374A04
2373A02
2372A02

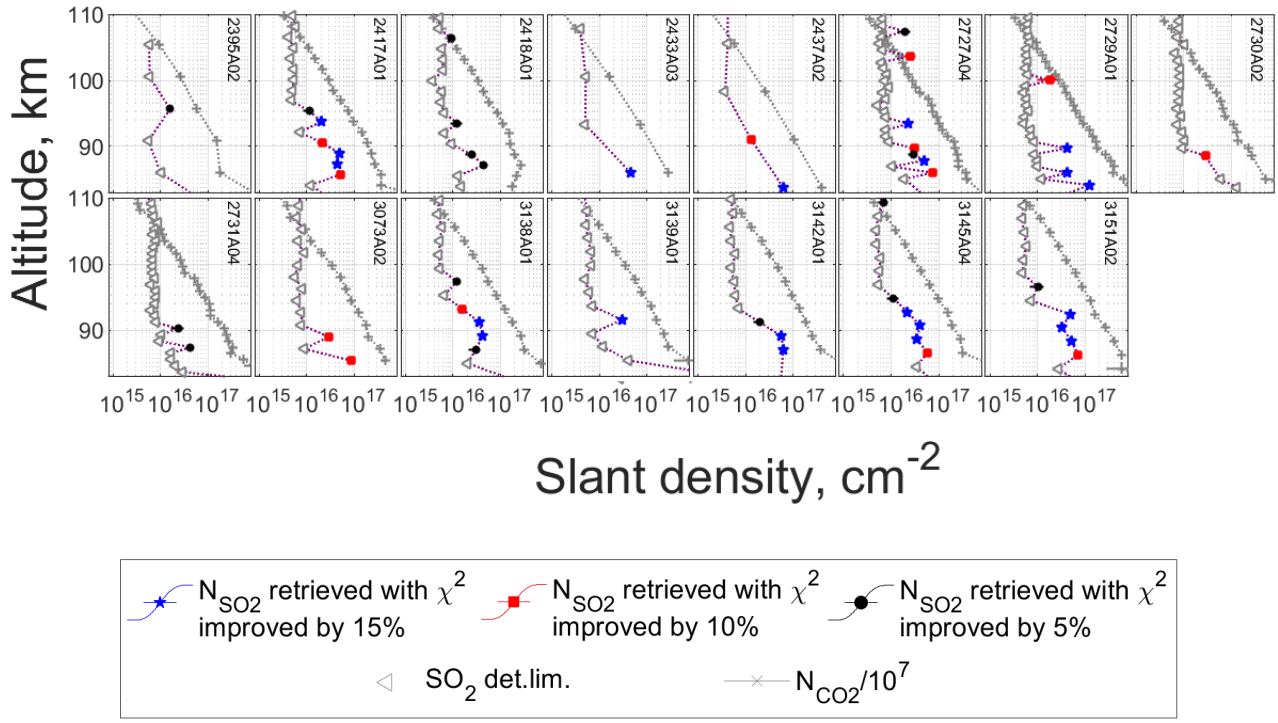

Figure A1.1. Individual slant density profiles of carbon and sulphur dioxides in 83-110 km and the SO_2 detection limit values corresponding to the SO_2 negative detections. The decrease of χ^2 in cases of the SO_2 detection is marked by different colors.

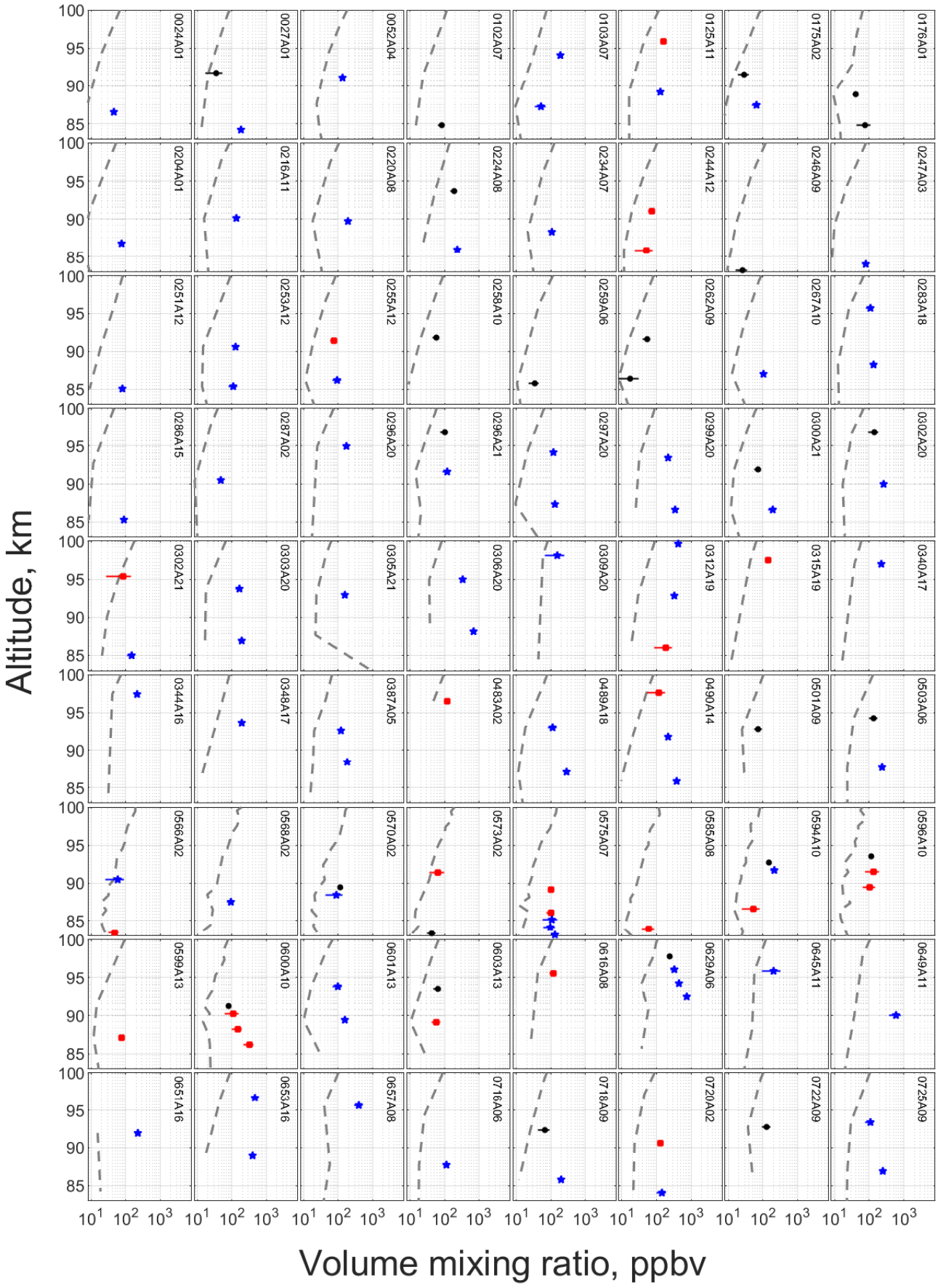
Altitude, km
Volume mixing ratio, ppbv
0176A01
0247A03
0175A02
0246A09
0125A11
0244A12
0102A07
0224A08
0103A07
0234A07
0052A04
0220A08
0027A01
0216A11
0024A01
0204A01
0283A18
0267A10
0262A09
0258A10
0259A06
0255A12
0253A12
0251A12
0302A20
0300A21
0299A20
0296A21
0297A20
0296A20
0287A02
0286A15
0340A17
0315A19
0312A19
0306A20
0309A20
0305A21
0303A20
0302A21
0503A06
0501A09
0490A14
0483A02
0489A18
0387A05
0348A17
0344A16
0596A10
0594A10
0585A08
0573A02
0575A07
0570A02
0568A02
0566A02
0649A11
0645A11
0629A06
0603A13
0616A08
0601A13
0600A10
0599A13
0725A09
0722A09
0720A02
0716A06
0718A09
0657A08
0653A16
0651A16

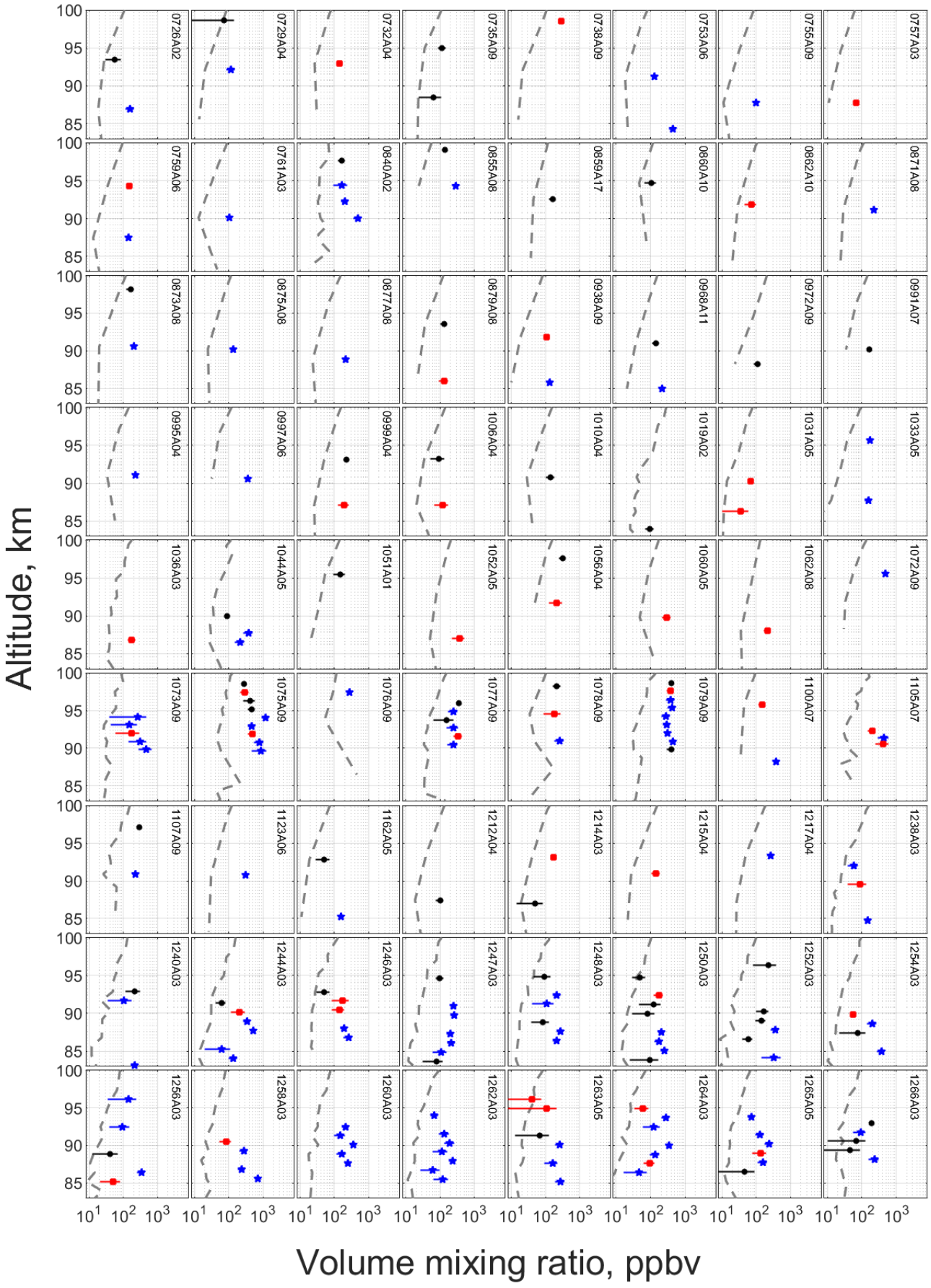
Altitude, km
Volume mixing ratio, ppbv
0757A03
0871A08
0755A09
0862A10
0753A06
0860A10
0738A09
0859A17
0735A09
0855A08
0732A04
0840A02
0729A04
0761A03
0726A02
0759A06
0991A07
0972A09
0968A11
0938A09
0879A08
0877A08
0875A08
0873A08
1033A05
1031A05
1019A02
1010A04
1006A04
999A04
997A06
995A04
1072A09
1062A08
1060A05
1056A04
1052A05
1051A01
1044A05
1036A03
1105A07
1100A07
1079A09
1078A09
1077A09
1076A09
1075A09
1073A09
1238A03
1217A04
1215A04
1214A03
1212A04
1162A05
1123A06
1107A09
1254A03
1252A03
1250A03
1248A03
1247A03
1246A03
1244A03
1240A03
1266A03
1265A05
1264A03
1263A05
1262A03
1260A03
1258A03
1256A03

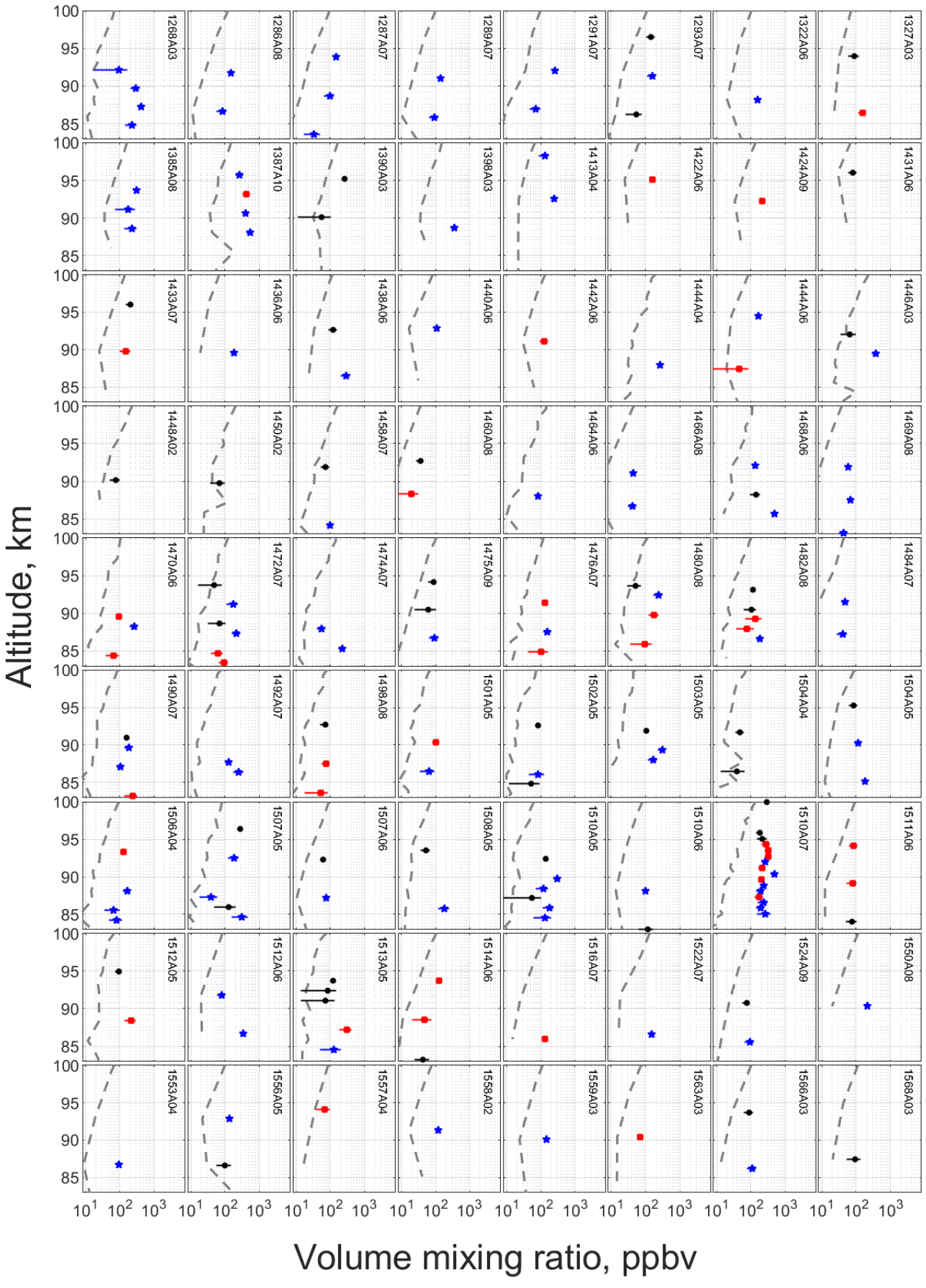
Altitude, km
Volume mixing ratio, ppbv
1327A03
1431A06
1446A03
1469A08
1484A07
1504A05
1511A06
1550A08
1568A03
1322A06
1424A09
1444A06
1468A06
1482A08
1504A04
1510A07
1524A09
1566A03
1293A07
1422A06
1444A04
1466A08
1480A08
1503A05
1510A06
1522A07
1563A03
1291A07
1413A04
1442A06
1464A06
1476A07
1502A05
1510A05
1516A07
1559A03
1289A07
1398A03
1440A06
1460A08
1475A09
1501A05
1508A05
1514A06
1558A02
1287A07
1390A03
1438A06
1458A07
1474A07
1498A08
1507A06
1513A05
1557A04
1286A08
1387A10
1436A06
1450A02
1472A07
1492A07
1507A05
1512A06
1556A05
1268A03
1385A08
1433A07
1448A02
1470A06
1490A07
1506A04
1512A05
1553A04
100
95
90
85
10^1 10^2 10^3

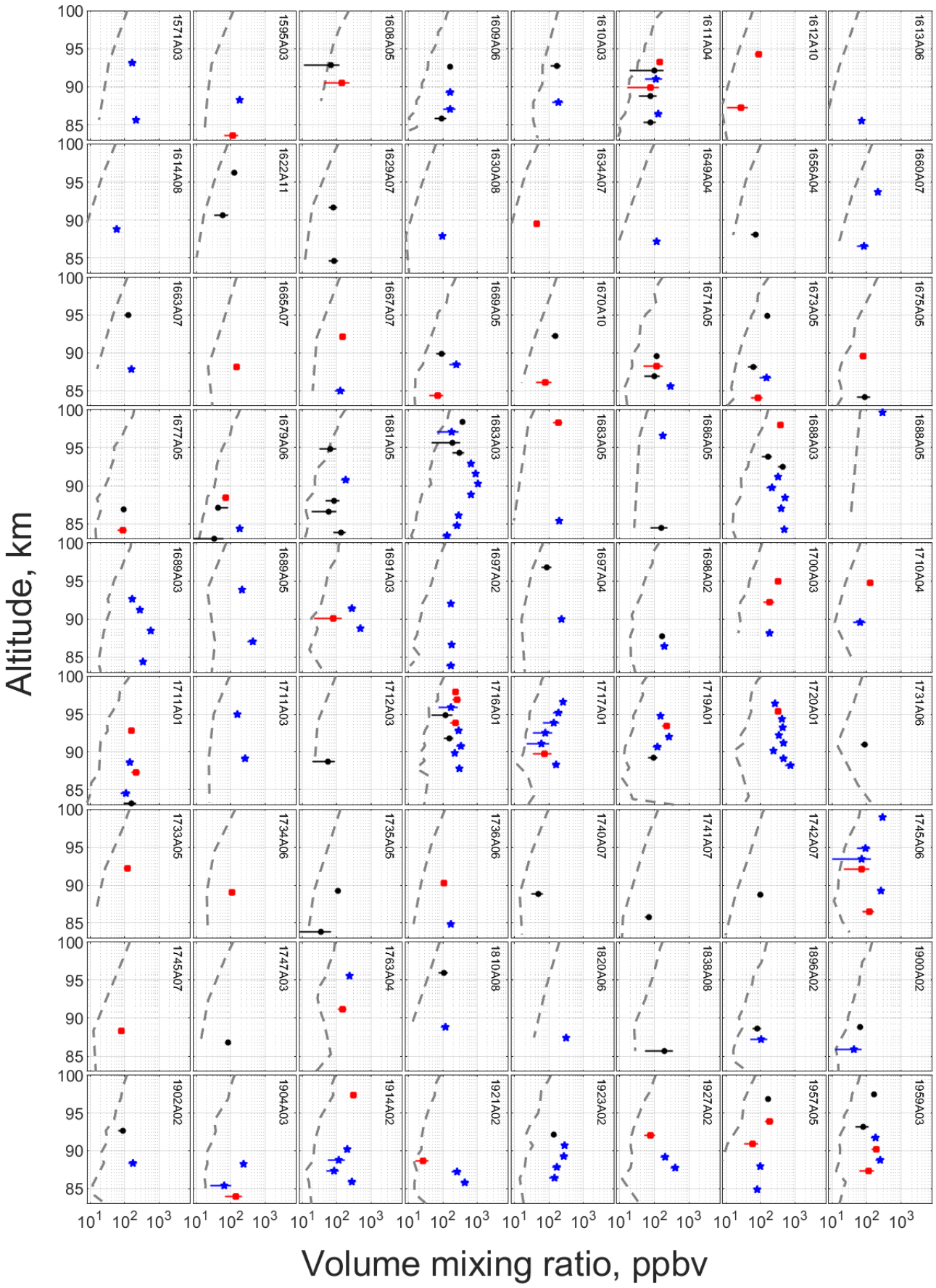
Altitude, km
Volume mixing ratio, ppbv
1613A06
1660A07
1675A05
1688A05
1710A04
1731A06
1745A06
1900A02
1959A03
1612A10
1656A04
1673A05
1688A03
1700A03
1720A01
1742A07
1896A02
1957A05
1611A04
1649A04
1671A05
1686A05
1698A02
1719A01
1741A07
1838A08
1927A02
1610A03
1634A07
1670A10
1683A05
1697A04
1717A01
1740A07
1820A06
1923A02
1609A06
1630A08
1669A05
1683A03
1697A02
1716A01
1736A06
1810A08
1921A02
1608A05
1629A07
1667A07
1681A05
1691A03
1712A03
1735A05
1763A04
1914A02
1595A03
1622A11
1665A07
1679A06
1689A05
1711A03
1734A06
1747A03
1904A03
1571A03
1614A08
1663A07
1677A05
1689A03
1711A01
1733A05
1745A07
1902A02

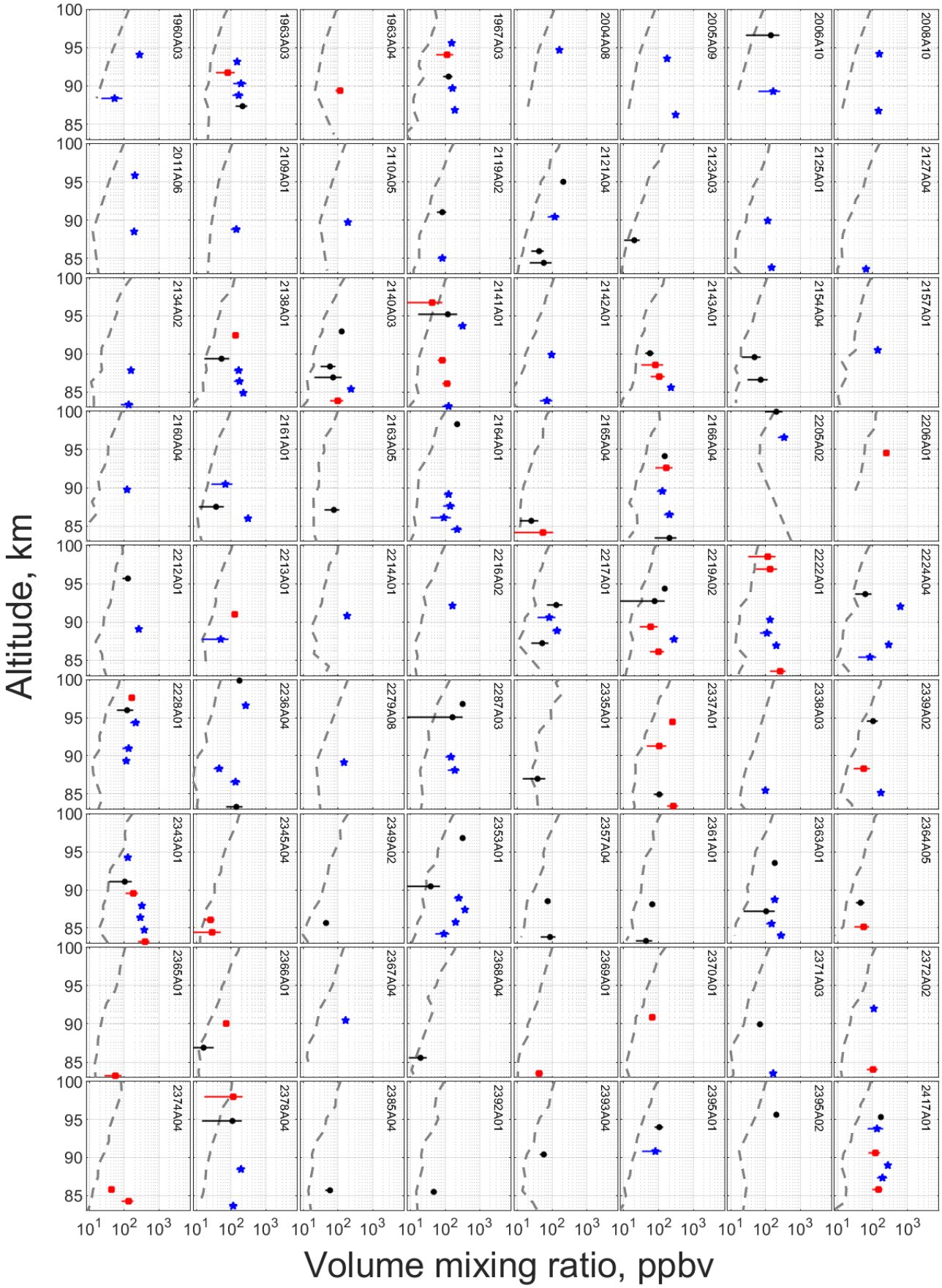
Altitude, km
Volume mixing ratio, ppbv
100
95
90
85
10^1 10^2 10^3
1960A03
1963A03
1963A04
1967A03
2004A08
2005A09
2006A10
2008A10
2011A06
2109A01
2110A05
2119A02
2121A04
2123A03
2125A01
2127A04
2134A02
2138A01
2140A03
2141A01
2142A01
2143A01
2154A04
2157A01
2160A04
2161A01
2163A05
2164A01
2165A04
2166A04
2205A02
2206A01
2212A01
2213A01
2214A01
2216A02
2217A01
2219A02
2222A01
2224A04
2228A01
2236A04
2279A08
2287A03
2335A01
2337A01
2338A03
2339A02
2343A01
2345A04
2349A02
2353A01
2357A04
2361A01
2363A01
2364A05
2365A01
2366A01
2367A04
2368A04
2369A01
2370A01
2371A03
2372A02
2374A04
2378A04
2385A04
2392A01
2393A04
2395A01
2395A02
2417A01

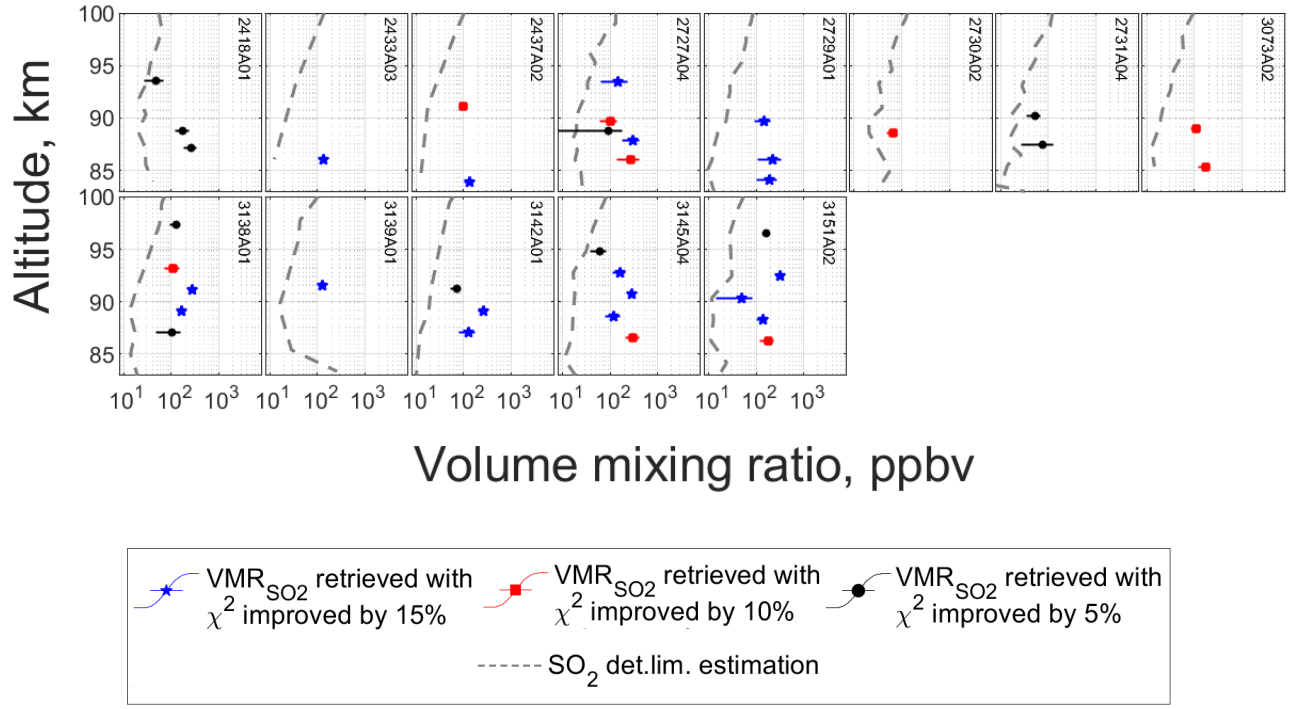

Figure A1.2 Individual volume mixing ratio profiles of sulphur dioxide in 83-100 km and the estimated SO_2 detection limit in terms of VMR (dashed curves). The decrease of χ^2 in cases of the SO_2 detection is marked by different colours.

ANNEX 2. Positive detections of O_3 presented individually

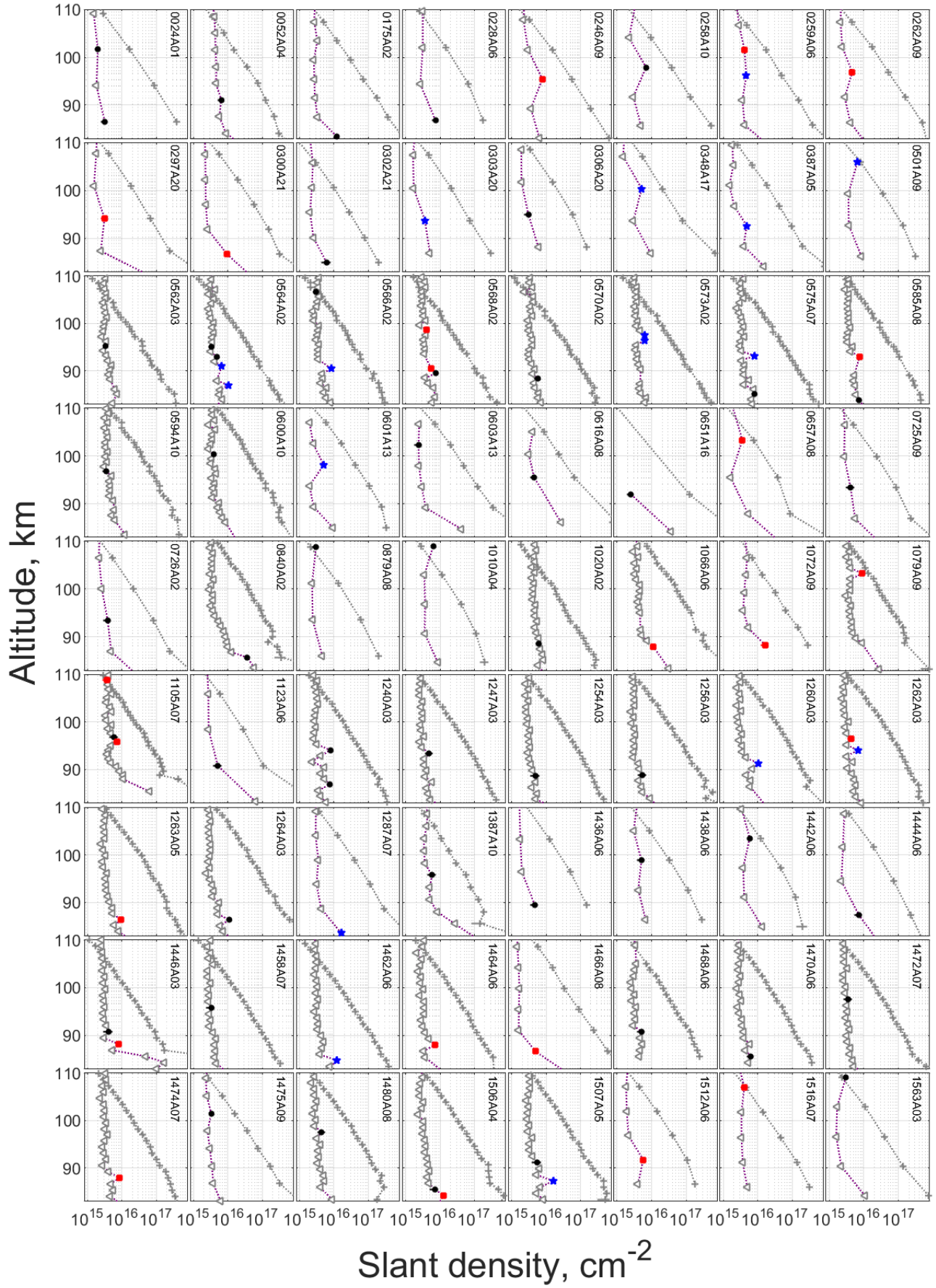

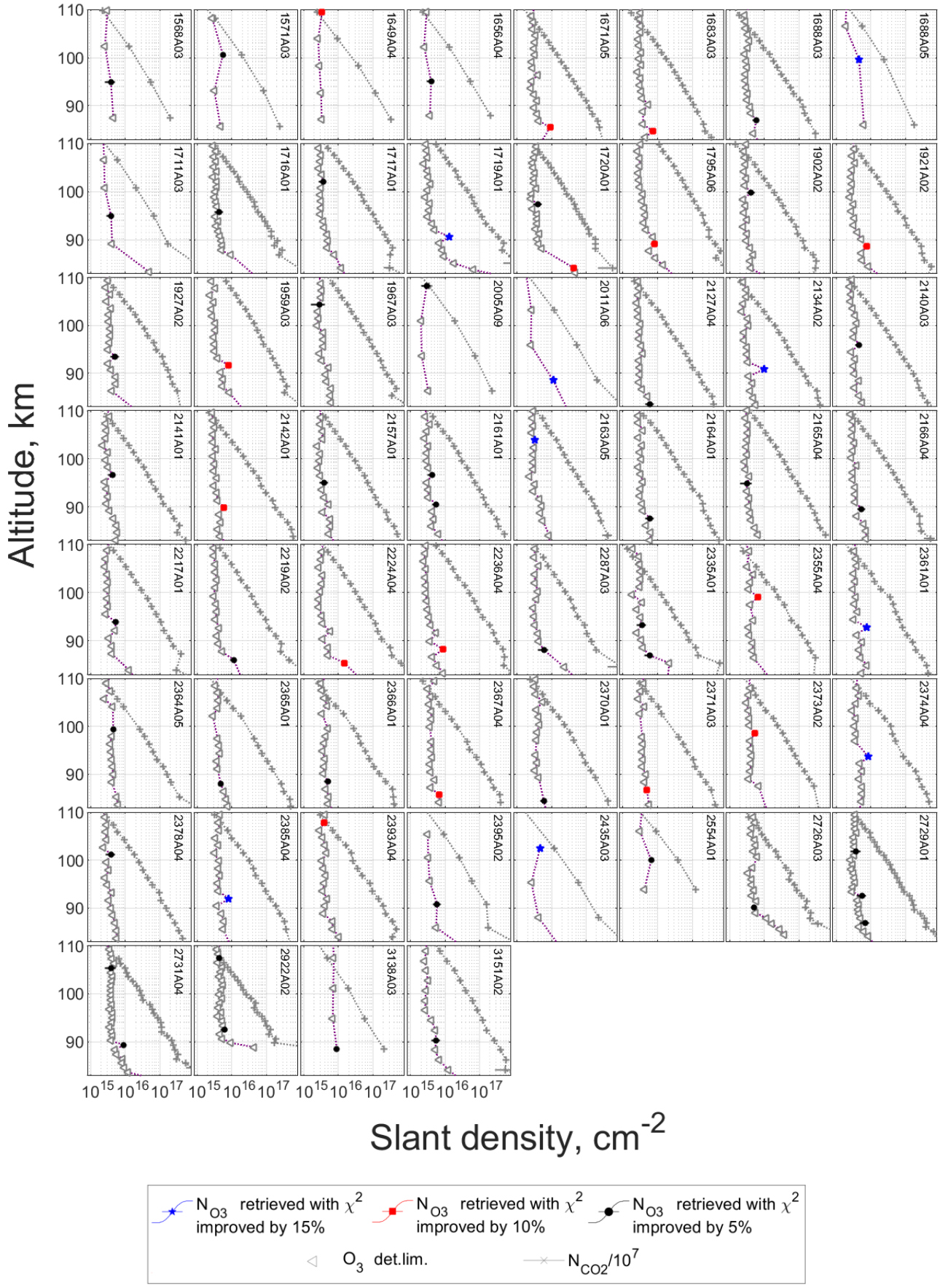

Figure A2.1. Positive detections of O_3 and slant density profiles of CO_2 in 83-110 km. The O_3 detection limits correspond to negative detections. The decrease of χ^2 in cases of the SO_2 detection is marked by different colors.

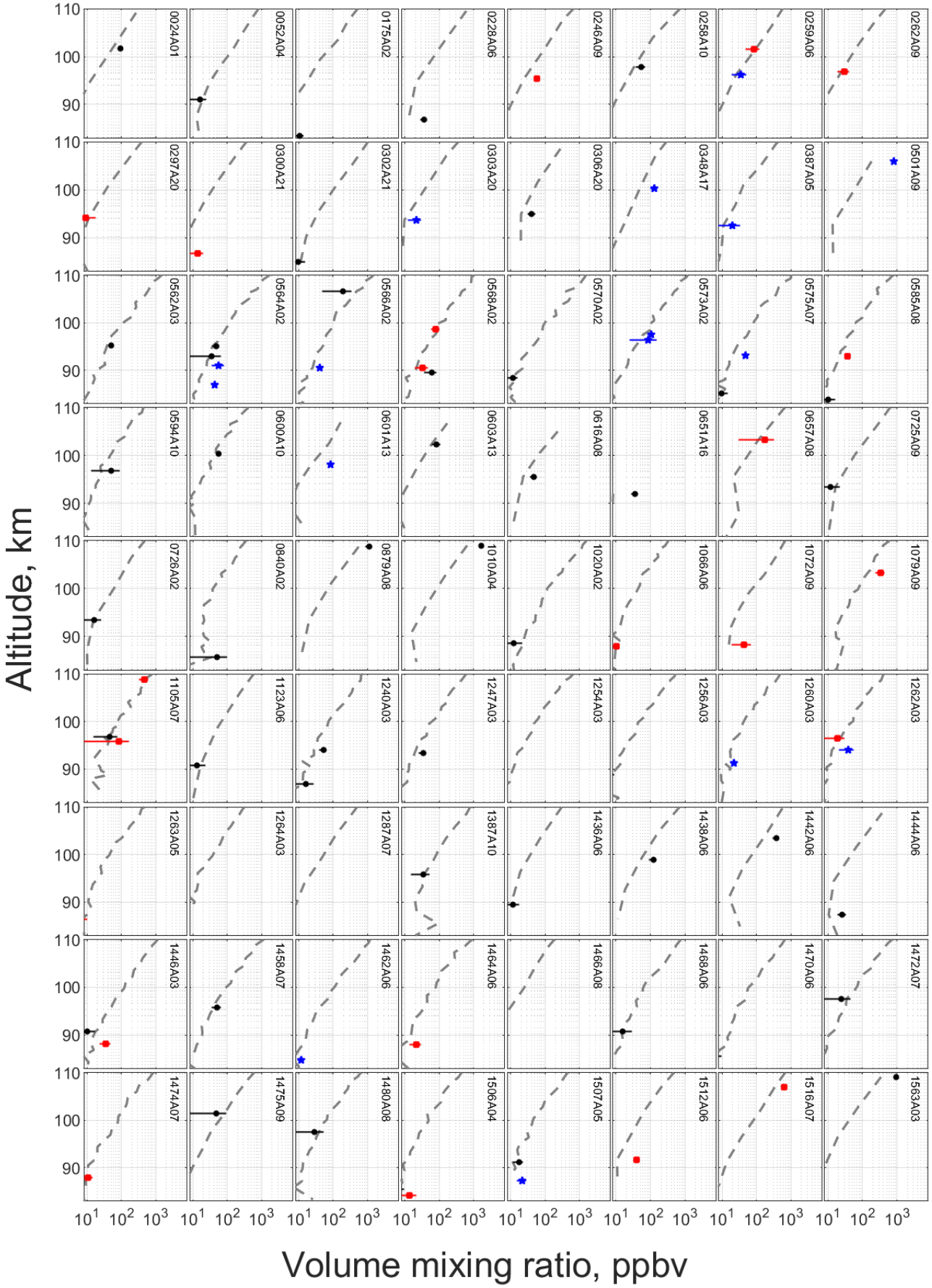
Altitude, km
Volume mixing ratio, ppbv
0024A01
0052A04
0175A02
0228A06
0246A09
0258A10
0259A06
0262A09
0297A20
0300A21
0302A21
0303A20
0306A20
0348A17
0387A05
0501A09
0562A03
0564A02
0566A02
0568A02
0570A02
0573A02
0575A07
0585A08
0594A10
0600A10
0601A13
0603A13
0616A08
0651A16
0657A08
0725A09
0726A02
0840A02
0879A08
1010A04
1020A02
1066A06
1072A09
1079A09
1105A07
1123A06
1240A03
1247A03
1254A03
1256A03
1260A03
1262A03
1263A05
1264A03
1287A07
1387A10
1436A06
1438A06
1442A06
1444A06
1446A03
1458A07
1462A06
1464A06
1466A08
1468A06
1470A06
1472A07
1474A07
1475A09
1480A08
1506A04
1507A05
1512A06
1516A07
1563A03

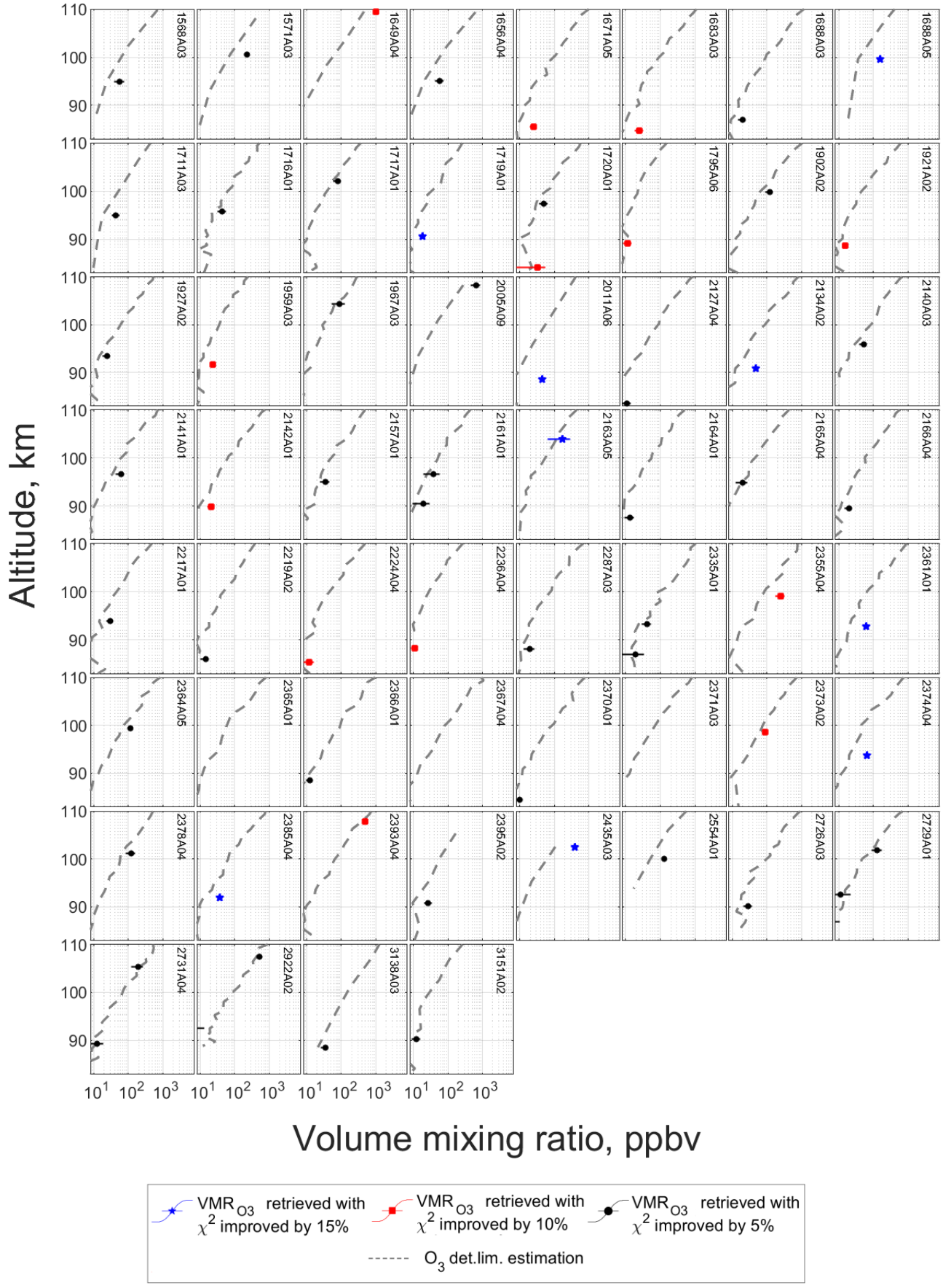

Figure A2.2. Individual positive detections of ozone in 83-110 km in terms of VMR. Dashed curves are the estimated O_3 detection limit. The decrease of χ^2 is marked by different colors.

ANNEX 3. Parameters of stellar occultation sessions

Table A1. Parameters of stellar occultation sessions where SO_2 and/or O_3 were detected.

Occultation number	Date	Local solar time	Latitude	SZA
0024A01	05/15/2006	0.53	-49.5	132.5
0027A01	05/18/2006	0.85	-49.5	131.8
0052A04	06/12/2006	23.79	-24.24	157.99
0102A07	08/01/2006	23.26	-3.93	168.08
0103A07	08/02/2006	23.37	-3.92	169.54
0125A11	08/24/2006	1.77	-3.74	152.83
0175A02	10/13/2006	1.5	-24.11	146.06
0176A01	10/14/2006	1.61	-24.11	145.05
0204A01	11/11/2006	21.64	37.83	130.11
0216A11	11/23/2006	21.77	-38.84	131.2
0220A08	11/27/2006	22.19	-38.84	134.9
0224A08	12/01/2006	22.62	-38.84	138
0228A06	12/05/2006	0.03	-24.45	157.2
0234A07	12/11/2006	0.66	-24.44	155.5
0244A12	12/21/2006	21.33	-30.26	132.9
0246A09	12/23/2006	22.09	-38.65	135.3
0247A03	12/24/2006	21.66	-31.13	136.26
0251A12	12/28/2006	22.09	-31.05	140.67
0253A12	12/30/2006	22.29	-31	142.72
0255A12	01/01/2007	22.5	-30.96	144.62
0258A10	01/04/2007	23.34	-38.48	143.05
0259A06	01/05/2007	22.92	-30.87	147.93
0262A09	01/08/2007	23.24	-30.81	149.87
0267A10	01/13/2007	0.28	-38.36	144.05
0283A18	01/29/2007	3.67	-44.72	115.7
0286A15	02/01/2007	4.51	-49.54	105.9
0287A02	02/02/2007	4.61	-49.54	104.9
0296A20	02/11/2007	19.96	-4.37	119.4
0296A21	02/11/2007	2.83	-30.6	130.43
0297A20	02/12/2007	20.06	-4.37	121
0299A20	02/14/2007	20.28	-4.37	124.17
0300A21	02/15/2007	3.26	-30.62	125.3
0302A20	02/17/2007	20.6	-4.36	128.95

Occultation number	Date	Local solar time	Latitude	SZA
1510A05	06/09/2010	3.16	27.3	128.36
1510A06	06/09/2010	0.4	-37.46	139.73
1510A07a	06/09/2010	0.95	39.61	140.36
1511A06	06/10/2010	0.51	-37.46	139.51
1512A05	06/11/2010	3.38	27.31	125.55
1512A06	06/11/2010	0.62	-37.48	139.26
1513A05	06/12/2010	3.49	27.31	124.14
1514A06	06/13/2010	23.92	-75.86	101.81
1516A07	06/15/2010	0.14	-75.88	101.88
1524A09	06/23/2010	1.01	-75.95	101.69
1550A08	07/19/2010	21.51	-23.09	136.93
1553A04	07/22/2010	19.62	24.34	112.03
1556A05	07/25/2010	19.94	24.34	116.19
1557A04	07/26/2010	21.2	-38.83	125.6
1558A02	07/27/2010	20.16	24.34	118.94
1559A03	07/28/2010	21.41	-38.83	127.7
1563A03	08/01/2010	20.68	24.35	125.67
1566A03	08/04/2010	23.21	-23.1	155.07
1568A03	08/06/2010	23.42	-23.11	156.45
1571A03	08/09/2010	23.74	-23.11	157.87
1595A03	09/02/2010	2.68	41.89	122.6
1608A05	09/15/2010	22.14	-11.43	150.96
1609A06	09/16/2010	23.47	70.01	107.33
1610A03	09/17/2010	22.35	-11.47	153.91
1611A04	09/18/2010	23.69	70.09	107.39
1612A10	09/19/2010	2.35	-49.9	124.1
1613A06	09/20/2010	2.45	-49.9	123.4
1614A08	09/21/2010	2.56	-49.9	122.6
1622A11	09/29/2010	0.9	-36.18	144.12
1629A07	10/06/2010	3.52	-45.08	117
1630A08	10/07/2010	4.27	-49.93	108.18
1634A07	10/11/2010	4.69	-49.94	104.1
1649A04	10/26/2010	3.75	-36.31	117.38

0302A21	02/17/2007	3.47	-30.63	122.65
0303A20	02/18/2007	20.7	-4.33	130.53
0305A21	02/20/2007	3.79	-30.64	118.61
0306A20	02/21/2007	21.03	-4.33	135.3
0309A20	02/24/2007	21.35	-4.32	140.1
0312A19	02/27/2007	21.67	-4.3	144.9
0315A19	03/02/2007	21.99	-4.28	149.67
0340A17	03/27/2007	0.7	-4.11	168.08
0344A16	03/31/2007	1.13	-4.09	162.03
0348A17	04/04/2007	1.57	-4.06	155.73
0387A05	05/13/2007	0.2	-26.96	150.53
0483A02	08/17/2007	23.25	-35.82	145.26
0489A18	08/23/2007	23.88	-35.74	146.87
0490A14	08/24/2007	23.99	-35.75	146.91
0501A09	09/04/2007	1.79	-39.01	136
0503A06	09/06/2007	2	-39	134.3
0562A03	11/03/2007	21.11	25.44	131.82
0564A02	11/05/2007	21.33	25.44	134.55
0566A02	11/07/2007	21.54	25.44	137.24
0568A02	11/09/2007	21.76	25.44	139.85
0570A02	11/11/2007	21.97	25.43	142.39
0573A02	11/14/2007	22.3	25.43	146.02
0575A07	11/16/2007	22.51	25.42	148.26
0585A08	11/26/2007	23.62	25.51	156.3
0594A10	12/05/2007	0.61	25.52	155.48
0596A10	12/07/2007	0.83	25.53	154.2
0599A13	12/11/2007	22.85	-29.07	144.3
0600A10	12/11/2007	1.26	25.54	150.75
0601A13	12/13/2007	23.07	-29.05	145.63
0603A13	12/15/2007	23.29	-29.03	146.74
0616A08	12/28/2007	0.79	-34.53	141.55
0629A06	01/10/2008	2.27	18.98	142.41
0645A11	01/26/2008	19.65	-38.85	108.6
0649A11	01/30/2008	20.07	-38.85	113.5
0651A16	02/01/2008	20.29	-38.85	115.9
0653A16	02/03/2008	20.5	-38.85	118.3
0657A08	02/07/2008	20.93	-38.84	122.9
0716A06	04/06/2008	0.76	-38.89	142.27
0718A09	04/08/2008	0.97	-38.9	141.36
0720A02	04/10/2008	1.19	-38.89	140.23

1656A04	11/02/2010	20.46	-51.93	112.4
1660A07	11/06/2010	20.89	-51.93	115.41
1663A07	11/09/2010	21.21	-51.93	117.53
1665A07	11/11/2010	23.14	-31	146.77
1667A07	11/13/2010	21.64	-51.93	120.1
1669A05	11/15/2010	20.16	27.51	118.47
1670A10	11/16/2010	23.67	-31.04	148.35
1671A05	11/17/2010	20.37	27.51	121.25
1673A05	11/19/2010	20.58	27.51	124.01
1675A05	11/21/2010	20.8	27.5	126.73
1677A05	11/23/2010	21.01	27.49	129.41
1679A06	11/25/2010	21.22	27.49	132.05
1681A05	11/27/2010	21.43	27.48	134.64
1683A03	11/29/2010	21.65	27.48	137.18
1683A05	11/29/2010	22.63	50.72	127.5
1686A05	12/02/2010	20.71	-4.81	130.33
1688A03	12/04/2010	22.18	27.47	143.17
1688A05	12/04/2010	0.52	-5.37	169.6
1689A03	12/05/2010	22.29	27.47	144.29
1689A05	12/05/2010	0.63	-5.37	168.31
1691A03	12/07/2010	22.5	27.47	146.42
1697A02	12/13/2010	23.15	27.46	151.77
1697A04	12/13/2010	1.48	-5.43	156.55
1698A02	12/14/2010	23.25	27.46	152.43
1700A03	12/16/2010	23.47	27.46	153.6
1710A04	12/26/2010	1.38	38.87	139
1711A01	12/27/2010	0.68	27.49	153.22
1711A03	12/27/2010	1	29.58	149.4
1712A03	12/28/2010	1.6	38.87	137.6
1716A01a	01/01/2011	22.94	34.43	144.7
1717A01	01/02/2011	1.34	27.51	148.59
1719A01	01/04/2011	1.56	27.52	146.57
1720A01a	01/05/2011	23.38	34.01	147.22
1731A06	01/16/2011	0.03	-39.16	138.33
1733A05	01/18/2011	23.37	-76.84	100.5
1734A06	01/19/2011	23.48	-76.86	100.56
1735A05	01/20/2011	23.59	-76.87	100.6
1736A06	01/21/2011	23.7	-76.89	100.67
1740A07	01/25/2011	0.14	-76.93	100.8
1741A07	01/26/2011	0.25	-76.94	100.8

0722A09	04/12/2008	1.39	-38.9	138.96
0725A09	04/15/2008	1.71	-38.88	136.7
0726A02	04/16/2008	1.82	-38.88	135.9
0729A04	04/19/2008	2.14	-38.89	133.24
0732A04	04/22/2008	2.45	-38.89	130.34
0735A09	04/25/2008	2.77	-38.88	127.23
0738A09	04/28/2008	3.09	-38.9	123.97
0753A06	05/13/2008	20.72	-4.61	130.75
0755A09	05/15/2008	20.93	-4.61	133.91
0757A03	05/17/2008	21.15	-4.61	137.13
0759A06	05/19/2008	21.36	-4.61	140.31
0761A03	05/21/2008	21.58	-4.61	143.5
0840A02	08/08/2008	3.15	26.21	128.87
0855A08	08/23/2008	19.21	38.07	105.3
0859A17	08/27/2008	18.55	-38.87	95.5
0860A10	08/28/2008	18.65	-38.87	96.8
0862A10	08/30/2008	18.87	-38.87	99.4
0871A08	09/08/2008	20.83	-23.94	127.85
0873A08	09/10/2008	21.05	-23.93	130.65
0875A08	09/12/2008	21.26	-23.93	133.42
0877A08	09/14/2008	21.47	-23.92	136.13
0879A08	09/16/2008	21.69	-23.92	138.78
0938A09	11/14/2008	1.94	24.01	141.11
0968A11	12/14/2008	20.76	-30.46	125.7
0972A09	12/18/2008	21.18	-30.45	130.57
0991A07	01/06/2009	23.21	-30.42	147.63
0995A04	01/10/2009	23.64	-30.4	148.95
0997A06	01/12/2009	23.85	-30.41	149.14
0999A04	01/14/2009	0.07	-30.39	149.06
1006A04	01/21/2009	20.29	8.41	124.12
1010A04	01/25/2009	20.72	8.4	130.56
1019A02	02/03/2009	22.32	26.48	145.45
1020A02	02/04/2009	22.43	26.49	146.56
1031A05	02/15/2009	1.54	57.02	122.31
1033A05	02/17/2009	1.76	57.01	121.5
1044A05	02/28/2009	1.04	26.55	151.79
1051A01	03/07/2009	0.27	9.76	171.75
1052A05	03/08/2009	0.23	-37.62	139.66
1056A04	03/12/2009	0.66	-37.66	138.79
1060A05	03/16/2009	1.09	-37.68	137.1

1742A07	01/27/2011	0.35	-76.95	100.8
1744A07	01/29/2011	0.57	-76.97	100.78
1745A06	01/30/2011	4.42	27.61	111.95
1745A07	01/30/2011	0.68	-76.98	100.74
1747A03	02/01/2011	0.9	-77	100.67
1763A04	02/16/2011	20.44	-27.78	121.28
1795A06	03/20/2011	23.9	-27.71	153.5
1810A08	04/05/2011	1.44	-0.27	158.38
1816A06	04/10/2011	2.1	-27.72	140.61
1820A06	04/15/2011	2.38	13.84	140.99
1838A08	05/03/2011	22.66	-24.93	150.5
1896A02	06/30/2011	20.53	27.74	123.16
1900A02	07/04/2011	20.95	27.73	128.58
1902A02	07/06/2011	21.17	27.72	131.23
1904A03	07/08/2011	21.38	27.72	133.83
1914A02	07/18/2011	22.45	27.7	145.7
1921A02	07/25/2011	23.21	27.7	151.9
1923A02	07/27/2011	23.42	27.7	153.1
1927A02	07/31/2011	23.86	27.7	154.5
1957A03	08/30/2011	3.17	27.81	128.06
1957A05	08/30/2011	4.59	58.1	103.15
1959A03	09/01/2011	3.39	27.82	125.27
1960A03	09/02/2011	0.72	-45.31	131.31
1963A03	09/05/2011	3.83	27.83	119.61
1963A04	09/05/2011	1.04	-45.36	130.32
1967A03	09/09/2011	4.27	27.84	113.85
2004A08	10/16/2011	22.13	-22.36	144.78
2005A09	10/17/2011	22.23	-22.37	146.03
2006A10	10/18/2011	22.34	-22.37	147.22
2008A10	10/20/2011	22.55	-22.38	149.53
2011A06	10/23/2011	22.86	-22.39	152.68
2109A01	01/29/2012	22.53	-31.75	142.44
2110A05	01/30/2012	22.64	-31.75	143.19
2119A02	02/08/2012	20.49	27.94	122.5
2121A04	02/10/2012	20.7	27.94	125.22
2123A03	02/12/2012	20.91	27.93	127.9
2125A01	02/14/2012	21.12	27.93	130.54
2127A04	02/16/2012	21.33	27.93	133.13
2134A02	02/23/2012	22.08	27.92	141.71
2138A01	02/27/2012	22.51	27.91	146.1

1062A08	03/18/2009	1.31	-37.68	135.99
1066A06	03/22/2009	3.45	26.65	124.85
1072A09	03/28/2009	2.46	19.85	139.85
1073A09	03/29/2009	2.09	37.19	134.34
1075A09	03/31/2009	2.31	37.15	132.37
1076A09	04/01/2009	2.89	19.82	134.06
1077A09	04/02/2009	2.52	37.07	130.31
1078A09	04/03/2009	3.1	19.82	131.12
1079A09	04/04/2009	2.74	37.02	128.17
1100A07	04/25/2009	21.32	-23.65	134.33
1105A07	04/30/2009	0.05	31.97	147.66
1107A09	05/02/2009	0.27	32.04	147.23
1108A08	05/03/2009	22.17	-23.64	144.67
1123A06	05/18/2009	23.76	-23.64	157.48
1162A05	06/26/2009	2.85	-38.85	126.8
1214A03	08/17/2009	22.97	-30.84	146.01
1215A04	08/18/2009	23.07	-30.85	146.57
1217A04	08/20/2009	23.29	-30.85	147.53
1238A03	09/09/2009	21.84	26.9	139.91
1240A03	09/12/2009	22.06	26.89	142.33
1244A03	09/16/2009	22.49	26.89	146.84
1246A03	09/18/2009	22.71	26.89	148.89
1247A03	09/19/2009	22.82	26.89	149.82
1248A03	09/20/2009	22.92	26.89	150.71
1250A03	09/22/2009	23.14	26.89	152.32
1252A03	09/24/2009	23.36	26.89	153.69
1254A03	09/26/2009	23.58	26.9	154.7
1256A03	09/28/2009	23.8	26.9	155.3
1258A03	09/30/2009	0.02	26.91	155.5
1260A03	10/02/2009	0.23	26.91	155.35
1262A03	10/04/2009	0.45	26.91	154.77
1263A05	10/05/2009	0.56	26.92	154.33
1264A03	10/06/2009	0.67	26.92	153.8
1265A05	10/07/2009	0.78	26.92	153.2
1266A03	10/08/2009	0.89	26.93	152.51
1268A03	10/10/2009	1.11	26.93	150.92
1286A08	10/28/2009	23.48	-74.84	102.6
1287A07	10/29/2009	23.59	-74.85	102.67
1289A07	10/31/2009	23.81	-74.87	102.79
1291A07	11/02/2009	0.03	-74.89	102.86

2140A03	02/29/2012	22.73	27.91	148.03
2141A01	03/01/2012	22.83	27.91	148.94
2142A01	03/02/2012	22.94	27.91	149.8
2143A01	03/03/2012	23.05	27.91	150.6
2154A04	03/14/2012	0.25	27.92	154.2
2157A01	03/17/2012	0.57	27.93	153.2
2160A04	03/20/2012	0.9	27.94	151.5
2161A01	03/21/2012	1.01	27.94	150.74
2163A05	03/23/2012	1.23	27.95	149.1
2164A01	03/24/2012	1.34	27.95	148.17
2165A04	03/25/2012	1.46	27.95	147.2
2166A04	03/26/2012	1.57	27.96	146.17
2205A02	05/04/2012	19.39	-28.16	107.51
2206A01	05/05/2012	19.5	-28.16	108.93
2212A01	05/11/2012	20.15	-28.14	117.51
2213A01	05/12/2012	20.26	-28.14	118.91
2214A01	05/13/2012	20.37	-28.13	120.3
2216A02	05/15/2012	20.58	-28.13	123.08
2217A01	05/16/2012	20.69	-28.13	124.44
2219A02	05/18/2012	20.91	-28.12	127.16
2222A01	05/21/2012	21.23	-28.12	131.14
2224A04	05/23/2012	21.45	-28.11	133.73
2228A01	05/27/2012	21.89	-28.1	138.7
2236A04	06/04/2012	22.75	-28.07	147.29
2246A01	06/13/2012	23.83	-28.04	153.2
2254A01	06/21/2012	0.69	-28.03	152
2256A04	06/23/2012	0.9	-28.03	150.89
2258A02	06/25/2012	1.11	-28.03	149.5
2259A01	06/26/2012	1.22	-28.03	148.7
2261A04	06/28/2012	1.42	-28.03	147.01
2264A04	07/01/2012	1.74	-28.04	144.2
2265A04	07/02/2012	1.84	-28.04	143.17
2274A01	07/11/2012	2.76	-28.07	132.96
2279A08	07/17/2012	3.49	14.45	125.42
2287A03	07/25/2012	22.68	-2.39	160.3
2288A01	07/25/2012	4.19	-28.14	115.08
2294A02	07/31/2012	4.8	-28.17	107.08
2335A01	09/10/2012	19.64	28.11	111.3
2337A01	09/12/2012	19.85	28.1	114.1
2338A03	09/13/2012	19.95	28.1	115.5

1293A07	11/04/2009	0.24	-74.9	102.9
1322A06	12/03/2009	21.11	-23.35	131.62
1327A03	12/08/2009	21.64	-23.35	138.42
1385A08	02/04/2010	22.29	-13.79	152.31
1387A10	02/06/2010	22.5	-13.82	155.13
1390A03	02/09/2010	22.81	-13.86	159.2
1398A03	02/17/2010	23.66	-13.9	167.55
1413A04	03/04/2010	2.57	-36.63	130.31
1422A06	03/13/2010	20.09	-5.55	121.3
1424A09	03/15/2010	21.39	-31.29	132.37
1431A06	03/22/2010	21.05	-5.55	135.53
1433A07	03/24/2010	22.35	-31.28	141.4
1436A06	03/27/2010	21.58	-5.55	143.42
1438A06	03/29/2010	22.88	-31.29	145.13
1440A06	03/31/2010	22.01	-5.55	149.69
1442A06	04/02/2010	23.31	-31.31	147.13
1444A04	04/04/2010	20.01	27.27	116.63
1444A06	04/04/2010	21.78	-52.05	120.7
1446A03	04/06/2010	20.22	27.27	119.43
1448A02	04/08/2010	20.44	27.26	122.22
1450A02	04/10/2010	20.65	27.26	124.97
1458A07	04/18/2010	21.49	27.2	135.47
1460A08	04/20/2010	22.81	50.72	128.37
1462A06	04/22/2010	21.91	27.19	140.48
1464A06	04/24/2010	22.13	27.19	142.85
1466A08	04/26/2010	23.46	50.72	130.5
1468A06	04/28/2010	22.56	27.18	147.23
1469A08	04/29/2010	23.78	50.72	131.1
1470A06	04/30/2010	22.77	27.18	149.2
1472A07	05/02/2010	22.99	27.18	150.94
1474A07	05/04/2010	23.21	27.18	152.45
1475A09	05/05/2010	0.96	57.02	123.94
1476A07	05/06/2010	23.42	27.18	153.7
1480A08	05/10/2010	23.86	27.19	155.1
1482A08	05/12/2010	0.08	27.19	155.2
1484A07	05/14/2010	1.4	50.72	128.6
1490A07	05/20/2010	0.96	27.21	151.82
1492A07	05/22/2010	1.18	27.22	150.17
1498A08	05/28/2010	1.84	27.24	143.95
1501A05	05/31/2010	2.17	27.26	140.33

2339A02	09/14/2012	20.06	28.1	116.89
2343A01	09/18/2012	20.48	28.09	122.4
2345A04	09/20/2012	20.7	28.09	125.1
2349A02	09/24/2012	21.12	28.08	130.44
2353A01	09/29/2012	21.55	28.08	135.6
2355A04	10/01/2012	21.76	28.07	138.06
2357A04	10/03/2012	21.98	28.07	140.46
2361A01	10/07/2012	22.41	28.07	144.91
2363A01	10/09/2012	22.62	28.06	146.96
2364A05	10/10/2012	22.73	28.06	147.9
2365A01	10/11/2012	22.84	28.06	148.8
2366A01	10/12/2012	22.95	28.06	149.67
2367A04	10/13/2012	23.05	28.06	150.44
2368A04	10/14/2012	23.16	28.06	151.2
2369A01	10/15/2012	23.27	28.06	151.82
2370A01	10/16/2012	23.38	28.06	152.4
2371A03	10/17/2012	23.49	28.06	152.9
2372A02	10/18/2012	23.6	28.06	153.4
2373A02	10/19/2012	23.71	28.06	153.7
2374A04	10/20/2012	23.81	28.06	154
2375A01	10/21/2012	23.92	28.06	154.1
2378A04	10/24/2012	0.25	28.07	154
2385A04	10/31/2012	1.02	28.08	150.58
2387A02	11/02/2012	1.24	28.08	148.9
2392A01	11/07/2012	1.8	28.1	143.81
2393A04	11/08/2012	1.91	28.1	142.69
2395A01	11/10/2012	2.13	28.11	140.3
2395A02	11/10/2012	0.42	7.72	171.89
2417A01	12/02/2012	4.57	28.17	109.95
2418A01	12/03/2012	4.67	28.17	108.5
2433A03	12/18/2012	18.94	-38.75	100.1
2435A03	12/20/2012	19.15	-38.75	102.7
2437A02	12/22/2012	19.37	-38.75	105.2
2554A01	04/18/2013	18.7	14.22	99.97
2726A03	10/07/2013	21.69	6.92	144.1
2727A04	10/08/2013	22.28	52.51	120.91
2729A01	10/10/2013	22.5	52.8	121.59
2730A02	10/11/2013	22.11	6.44	150.22
2731A04	10/12/2013	22.71	53.08	122.15
2922A02	04/21/2014	18.66	11.27	99.5

1502A05	06/01/2010	2.28	27.26	139.06
1503A05	06/02/2010	2.39	27.27	137.77
1504A04	06/03/2010	2.5	27.27	136.47
1504A05	06/03/2010	23.75	-37.35	139.97
1506A04	06/05/2010	2.72	27.28	133.83
1507A05	06/06/2010	2.83	27.29	132.47
1507A06	06/06/2010	0.07	-37.41	140.1
1508A05	06/07/2010	2.94	27.29	131.13

3073A02	09/13/2014	2.19	28.38	139.49
3097A03	10/05/2014	1.45	2.19	158.2
3138A01	11/13/2014	21.62	-28.51	135.7
3138A03	11/13/2014	23.24	-14.96	161.41
3139A01	11/14/2014	21.72	-28.51	136.86
3142A01	11/16/2014	22.03	-28.5	140.2
3145A04	11/19/2014	22.34	-28.49	143.39
3151A02	11/25/2014	22.95	-28.47	148.7

ANNEX 4. Weighted mean

The weighted mean as it is presented in Bevington and Robinson (2003).

We consider a sample $x_1, x_2 \ldots x_n$ where each value is from a Gaussian distribution having the same mean μ but a different standard deviation σ_i.

$$\mu^* = \frac{\sum_{i=1}^{N} w_i x_i}{\sum_{i=1}^{N} w_i} \tag{A4.1}$$

In Equation A4.1 the weighting factor is taken equal to the inversed square of the error:

$$w_i = \frac{1}{{\sigma_i}^2} \tag{A4.2}$$

Then the weighted mean is

$$\mu^* = \frac{\sum_{i=1}^{N} w_i x_i}{\sum_{i=1}^{N} w_i} = \frac{\sum_{i=1}^{N} x_i \left(1/{\sigma_i}^2\right)}{\sum_{i=1}^{N} \left(1/{\sigma_i}^2\right)} \tag{A4.3}$$

The error on the weighted mean can now be calculated by

$$\sigma^2(\mu^*) = \frac{1}{\sum_{i=1}^{N} w_i} = \frac{1}{\sum_{i=1}^{N} \left(1/{\sigma_i}^2\right)} \tag{A4.4}$$

ANNEX 5. Estimation of an impact of diffrent stray light types

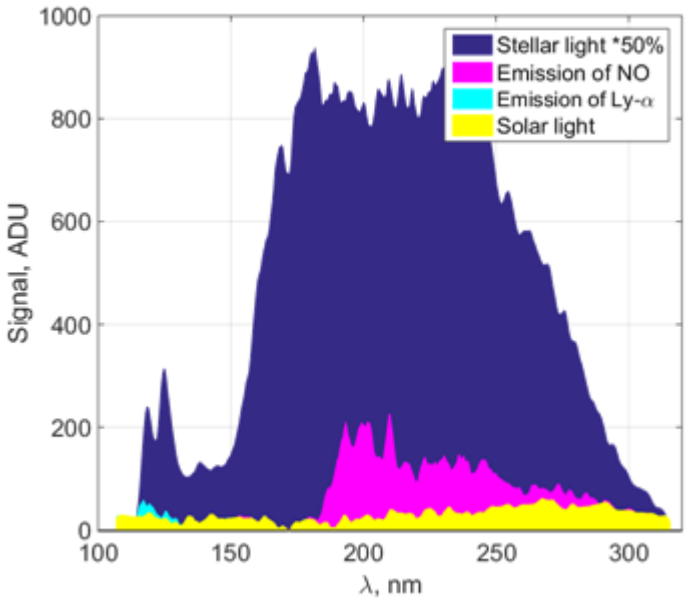

Figure A5.1 (Figure 3.4) Several components of the signal obtained in the occultation session #2721A05: (1) the spectrum of a star (purple) with atmospheric absorption lines at 98 km whose intensity is divided by two to better visualize the signal from other weaker UV radiation source, (2) the NO (pink), (3) Lyman-α (cyan), (4) the Sun scattered light (yellow). The NO emission obtained in 90-110 km, the Lyman-α and solar spectra are averaged over 200 km.

A separation of signals from different UV emission sources in the stellar occultation is a complicated task, which is possible to solve only in particular cases. As it is mentioned in Section 3.2.4, the instrument detects light coming from three types of extended sources in addition to stellar radiation: nitric oxide and Lyman-α emissions and scattered solar radiation.

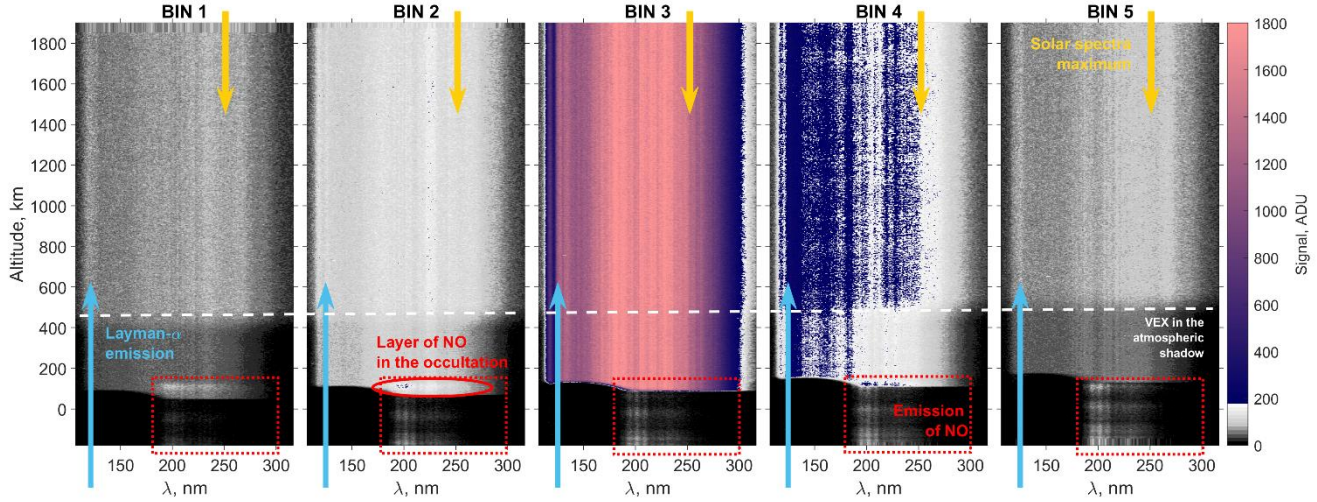

Figure A5.2. Signal registered in each bin of SPICAV UV during the whole observational session #2721A05. The white dashed line shows when the Venus Express spacecraft crossed the atmospheric shadow boarder. Blue arrows point to the Lyman-α emission range, yellow arrows indicate the range near the solar spectrum maximum. Nitric oxide emission signal is highlighted by red rectangles. The red ellipse displays the NO layer overlapped the occultation altitude range.

In this section, we consider the observational session #2721A05, which was dedicated specially for stray light sources' identification, and it was done with the applied spectrometer slit. Spectra of stray light measured without the slit are not isolated in particular spectral ranges. In such a case more complex techniques are needed, for example, a deconvolution by method Richardson-Lucy (Lucy, 1974). However, there would be no straightforward technique (as it is presented in this section) to distinguish between different sources.

Elimination of the nitric oxide emission spectra is discussed in details in Section 3.2.9. It was applied accordingly for this observation when the instrument moved into the atmospheric shadow, where the solar contamination disappears from the recording data. The difference between the stellar signal measured before and after VEX crossing of the shadow would provide the solar signal. The mean solar spectrum is estimated as

$$S^{SUN} = \sum_{i=1}^{5} \left(\sum_{z=600\ km}^{z=800\ km} S_i^{SPICAV}(z) - \sum_{z=200\ km}^{z=400\ km} S_i^{SPICAV}(z) \right) \quad \text{(A5.1)}$$

The UV Lyman-α radiation is very weak, however it is also distinguishable. The emission changes very slowly with altitude decrease until a level where the CO_2 absorption around 121.6 nm becomes significant. In the observation #2721A05 this spectral shape is clear because of a high value of the raw signal intensification (HT=160 from the 0-255 range). One can simulate how the stellar signal without atmospheric absorption is spread along the CCD rows by the instrument PSF. After this simulation, the additional signal resting around 121.6 nm will correspond to the Lyman-α spectrum (Franck Montmessin and Jean-Loup Bertaux, in priv. commun.). Equation A5.2 represents the iterative algorithm to extract the Lyman-α spectrum. As this glow evolves very slowly in space, its spectrum recorded by the 3rd bin is determined as an average one, extracted from non-central bins. Since the original spectrum contains the Lyman- α contamination, the iterative algorithm is required:

Iteration #0:
$$\begin{aligned} & S_0 = S_3^{SPICAV} \\ & S_{i=1,2,4,5} = [BIN][PSF]\, S_0 \\ & S^{Ly-\alpha} = \overline{S_i^{SPICAV} - S_i}, i = 1,2,4,5 \\ & S_3^{SPICAV} = S_3^{SPICAV} - S^{Ly-\alpha} \end{aligned} \quad \text{(A5.2)}$$

Iteration #1: $S_1 = S_3^{SPICAV}$ …

While the CO_2 absorption turns the stellar signal to zero, the shape of the Lyman-α spectrum can be extracted directly (Figure A5.3). This method is applicable only if the stellar light strongly dominates in the 3rd bin. This criterion is not satisfied in the occultation altitude range where the nitric oxide emission is present. As a possible solution there is a linear extrapolation of the signal from higher altitudes to the range where emission of NO is observed.

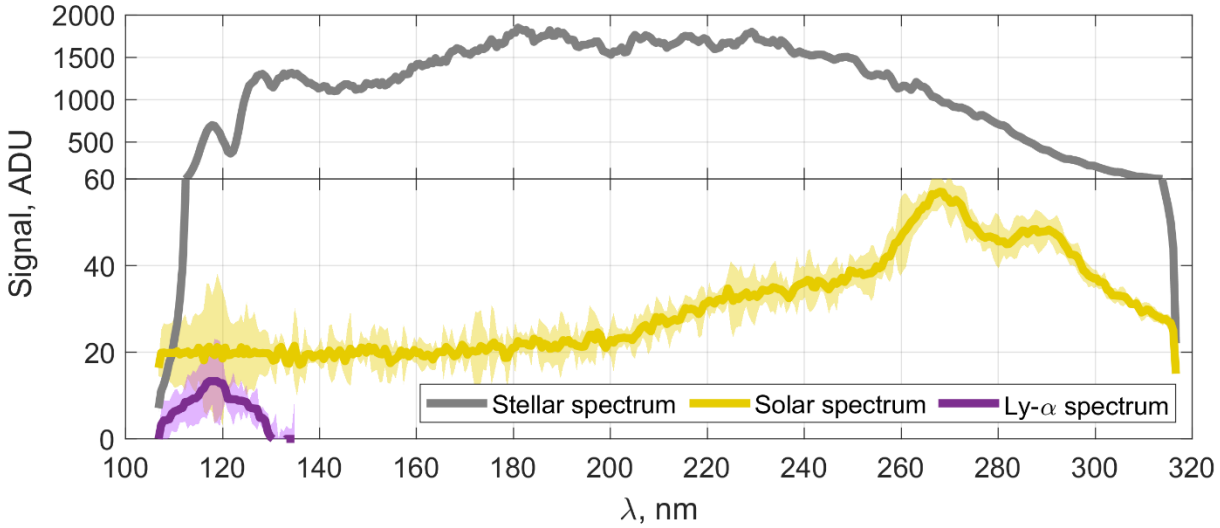

Figure A5.3. Extracted mean solar (yellow line) and Lyman-α (violet lone) spectra over 200 km and the mean stellar spectra (grey line) averaged in 200-400 km (the atmospheric shadow).

Figure A5.3 shows the extracted signals from the Sun and from the Lyman-α emissions. The observations when the spacecraft crosses the atmospheric shadow are rather rare. Thus, this algorithm of extraction of the solar contamination cannot be applied for the whole dataset of SPICAV stellar occultations. In contrast, the iterative algorithm applied to Lyman-α extraction might supplement its observations on the limb in the UV by SPICAV.

ANNEX 6. Résumé de la thèse en français

Les objectifs de la thèse

La structure de l'atmosphère de Vénus et l'étude de sa composition sont restées depuis longtemps un défi pour la communauté scientifique: quels processus de l'évolution de la planète ont conduit aux conditions atmosphériques observées, et qui sont si différentes de l'atmosphère terrestre. Divers modèles basés sur les données disponibles démontrent qu'une compréhension globale de la composition et de la dynamique de l'atmosphère n'a toujours pas été obtenue. Avant la mission Venus Express (VEX) (2006-2014), une étude détaillée de l'atmosphère et des composants gazeux trace au-dessus des nuages, où se déroulent les processus déterminants, n'avait jamais été réalisée. Pour la première fois, des occultations solaires et stellaires réalisées par VEX ont permis d'étudier en détail la structure verticale de l'atmosphère aux deux terminateurs de la planète.

Le spectromètre SPICAV a pu observer pendant 8 ans plusieurs gaz à l'état en utilisant son canal UV (118-320 nm). La méthode d'occultation stellaire a permis d'observer les altitudes allant de 85 à 110 km. Une grande quantité d'informations a été accumulée, aboutissant à une étude détaillée des variations des composants atmosphériques. Le dioxyde de soufre et l'ozone sont les deux espèces atmosphériques mineures qui font l'objet de cette étude dans la mésosphère de Vénus, avec un accent particulier sur leur distribution dans la mésosphère de nuit.

Le dioxyde de soufre possède des bandes d'absorption ultraviolette entre 190 et 300 nm. Ce gaz a été abondamment observé par les télescopes terrestres et les orbiteurs du côté jour de Vénus au niveau du sommet des nuages (~70 km) pendant plus de 40 ans. D'autre part, l'instrument SPICAV/SOIR de la mission Venus Express a exploré la distribution verticale du SO_2 à des altitudes de 65-110 km au niveau du terminateur. Les variations de la teneur en SO_2 sont extrêmement élevées dans la mésosphère du jour et du crépusculaire. Jusqu'à présent, on ne disposait d'aucune donnée sur les distributions de SO_2 dans la mésosphère de nuit où les conditions photochimiques et les températures diffèrent considérablement de celles rencontrées de jour. Le premier objectif de cette étude fut d'obtenir la distribution mésosphérique du dioxyde de soufre côté nuit. Les variations spatiales et à long terme ont été comparées aux résultats précédents.

Le deuxième objectif scientifique concerne la découverte d'une couche d'ozone dans la mésosphère de Vénus (Montmessin et al., 2011). L'absorption de l'ozone dans la bande de Hartley (~250 nm) a été observée par SPICAV-UV en occultation stellaire à des altitudes de 90-100 km. Des détections éparses d'O_3 avec un rapport de mélange de quelques dizaines de ppbv ont été relevées de 2006 à 2010 sur 29 observations. Ces résultats étaient cohérents avec un cycle de production et de destruction de l'ozone associé aux réactions entre les atomes d'oxygène et de chlore au niveau du point antisolaire où là de la très haute atmosphère (>90 km) converge et est aussi connue sous le nom de circulation SubSolaire-à-Anti-Solaire (SSAS), et faisant écho à un mécanisme bien connu dans la haute stratosphère de la Terre. En parallèle, une couche d'ozone a été récemment découverte au sommet des nuages vénusiens près des régions polaires (Marcq et al., 2019), ce qui illustre la connexion de l'ozone avec la dynamique

atmosphérique. Dans ma recherche, l'ensemble des statistiques des occultations stellaires de SPICAV-UV en 2006-2014 a été traité, soit plus de 400 séquences de mesures. J'ai ainsi pu caractériser la distribution de l'ozone à des altitudes 90-100 km, dans la région correspondant au changement de circulation des masses d'air. Cette étude du comportement de l'ozone du côté de la nuit est supposée aider à améliorer les modèles photochimiques existants pour l'atmosphère de Vénus et révéler les différences entre les atmosphères des planètes telluriques.

Le processus conduisant à la formation de l'ozone est aussi le responsable d'une émission aéronomique de l'oxygène ($\alpha^1\Delta_g$) à 1.27 μm principalement formée à 95 km où les détections d'ozone ont été faites. Pour cette raison, j'ai complété mon analyse avec les observations de l'émission de O_2 par le canal IR de SPICAV réalisées côté nuit.

Avant de pouvoir étudier la distribution verticale de SO_2 et O_3, les spectres d'occultation stellaire de SPICAV ont dû faire l'objet d'une étape de préparation approfondie pour les corriger d'effets instrumentaux et les calibrer précisément en longueur d'onde. Cette étape a été fondamentale en vue d'assurer une détection à de très faibles concentrations des gaz recherchés. L'importance de la calibration a pu être révélée au travers de l'analyse de la distribution verticale du SO_2 en s'appuyant sur deux approches de calibration différentes (Belyaev, Evdokimova et al., 2017 vs. Evdokimova et al., 2020).

Chapitre 1. Venus et son atmosphère

Dans ce chapitre est présenté un aperçu des connaissances élémentaires sur Vénus et son atmosphère.

Les premières observations spectrométriques réalisées dans les années 1930 ont permis d'établir que l'atmosphère très dense (pression de 90 atm à la surface) de Vénus est constituée à 96.5 % de dioxyde de carbone (CO_2). Le deuxième gaz le plus abondant est l'azote, les autres gaz étant des constituants mineurs: dioxyde de soufre (SO_2), vapeur d'eau (H_2O), etc. CO_2 et H_2O sont les principaux déclencheurs de l'effet de serre qui réchauffe l'atmosphère et porte la surface à plus de 477°C. Ces molécules absorbent efficacement le rayonnement infrarouge de la surface, et réémettent beaucoup moins en comparaison vers l'espace. La couche nuageuse à 47-70 km, qui est opaque sur la majeure partie du spectre, y contribue également. La formation de particules d'aérosol qui composent ces nuages est le processus chimique le plus important se produisant dans la mésosphère de Vénus, et s'appuie sur le cycle chimique des composés soufrés de l'atmosphère de la planète. Il est également probable que la source du soufre dans l'atmosphère soit liée à l'activité volcanique. Le principal composant des particules d'aérosols de la couche nuageuse de Vénus est une solution aqueuse d'acide sulfurique (à la concentration de 75-90%), dont le SO_2 est la source principale.

Comme pour l'atmosphère terrestre, on peut distinguer plusieurs couches dans l'atmosphère de Vénus. La mésosphère, qui englobe la couche nuageuse supérieure (>65 km) et s'étend jusqu'à 120 km, est probablement la région la plus active en termes de dynamique et de chimie. Ici, la nature de la circulation atmosphérique change. La couche nuageuse est dominée par un fort transport zonal de matière (super-rotation), où les vitesses de vent atteignent 100 km/s (4 jours) à 70 km. À ~100 km, les molécules et les atomes des composants atmosphériques sont soumis à la circulation SSAS.

Bien que l'existence de l'atmosphère de Vénus ait été suggérée il y a plus de deux cent cinquante ans, les principales découvertes sur sa structure, sa composition et sa dynamique ont dû attendre le les premiers véhicules spatiaux. L'exploration récente de Vénus a débuté en 2006 (15 ans après la dernière mission), avec le lancement de la sonde Venus Express par l'Agence spatiale européenne, suivie de la mission Akatsuki de la JAXA. Venus Express a fonctionné jusqu'à la fin de 2014, mais l'analyse des résultats se poursuit encore aujourd'hui. Parmi les découvertes, citons la première observation d'un double vortex au pôle sud de la planète, la détection de OH et O_3 dans l'atmosphère de Vénus, un rapport D/H anormalement élevé, par rapport à la Terre, dans la haute atmosphère. Pour la première fois, des expériences d'occultationéclipse ont été menées depuis l'orbite de la planète, ce qui a permis une étude détaillée de la structure verticale de la mésosphère.

Le spectromètre SPICAV (Spectroscopie pour l'étude des caractéristiques de l'atmosphère de Vénus) de la sonde Venus Express a été utilisé avec succès pendant huit ans d'exploitation de la sonde en orbite (Bertaux et al., 2007b). Il se composait des canaux UV (118-320 nm) et IR (0,65-1,7 μm). Les canaux UV et IR de l'instrument ont permis d'observer l'atmosphère dans différents modes incluant le nadir, la visée au limbe de la planète, et les occultations solaires et stellaires. Des spectres à haute résolution en longueur d'onde ont permis l'étude du rayonnement thermique de la basse atmosphère et de la surface, ainsi que l'émission de l'oxygène à 1.27 μm à 95 km d'altitude dans le domaine du proche infrarouge ont été mesurés par le canal du spectromètre IR au nadir du côté nuit. Les occultations solaires de la haute atmosphère de Vénus ont été observées pour la première fois dans deux bandes spectrales, ainsi que par le spectromètre SOIR (Solar Occultation in InfraRed). La première utilisation des occultations stellaires, a permis d'étudier la distribution des gaz CO_2, SO_2 et O_3 dans la mésosphère de nuit.

Chapitre 2. Le dioxyde de soufre et l'ozone dans l'atmosphère de Vénus

Ce chapitre présente en détail les résultats passés sur l'observation de SO_2 et O_3. L'interprétation de ces données observées est sommairement présentée sur la base de modèles photochimiques qui ont abouti à notre connaissance des processus chimiques affectés et leur lien avec la circulation atmosphérique. SO_2 et O_3 sont deux composants principaux des cycles chimiques de la mésosphère de Vénus: le cycle de CO_2 et des SO_x.

Les composés soufrés jouent un rôle clé dans la chimie de l'atmosphère de Vénus. SO_2 est le troisième gaz le plus abondant dans l'atmosphère de Vénus et sa présence conduit à la formation des nuages composées de gouttelettes H_2SO_4. Ainsi, des variations significatives de SO_2 au-dessus des nuages peuvent influencer les processus photochimiques et la dynamique de l'ensemble et de la couche nuageuse.

L'une des questions restées en suspens concerne la cause exacte des variations du dioxyde de soufre observées au-dessus des nuages. Des augmentations et des diminutions de SO_2 dans la couche supérieure des nuages supérieurs (~70 km) et au-dessus ont été rapportées depuis des décennies. On impute ce comportement à l'activité géologique qui est une source de soufre dans l'atmosphère, mais aucune preuve n'a encore été apportée.

Une autre question en suspens, liée cette fois à la couche nuageuse, est l'origine de la substance inconnue qui réduit considérablement l'albédo de Vénus dans le domaine de l' UV. Celle-ci pourrait également être liée aux composés soufrés (Frandsen et al., 2016; Krasnopolsky, 2018).

Avant la mission Venus Express, la distribution du SO_2 au-dessus de 70 km n'avait jamais été mesurée. Cependant, les occultations solaires ont montré qu'en moyenne, son contenu relatif diminue avec l'altitude et atteint un minimum à ~85 km pour ensuite augmenter. Cette dépendance à l'altitude est difficile à expliquer. Les modèles qui peuvent reproduire cette inversion nécessitent la présence d'autres composés de soufre au-dessus de ~85 km. Ces composés n'ont pas été observés expérimentalement. En outre, toutes les expériences présentent des variabilités significatives sur des échelles de temps courtes (quelques jours).

L'oxydation est un processus chimique important de la mésosphère de Vénus. Le pourcentage de dioxyde de carbone est élevé sur Vénus, donc le processus de sa récupération après photodissociation du côté jour est efficace. Cela indique une grande efficacité des cycles catalytiques dans la mésosphère. Il s'agit de réactions avec le chlore et les radicaux hydroxyles principalement. Un autre produit chimique fortement dépendant de ces processus est l'ozone. La teneur en oxygène moléculaire, qui n'a jamais été mesurée directement, est estimée faible, <2 ppmv. L'ozone sur Vénus a été découvert par Montmessin et al. (2011) dans les spectres UV des occultations stellaires de SPICAV. Il a été détecté côté nuit lors de 29 sessions à ~100 km d'altitude au début de la mission, avec une concentration moléculaire de 10^7-10^8 cm^{-3} ~10,000 inférieure à celle de l'atmosphère terrestre.

La production d'ozone et l'émission de l'oxygène sont le résultat de la recombinaison des atomes d'oxygène. Les atomes sont produits par photodissociation côté jour et sont ramenés côté nuit par la dynamique de la haute mésosphère et de la thermosphère où ils se recombinent. Plus récemment, l'analyse des observations UV SPICAV au nadir côté jour a permis d'établir une teneur en O_3 d'environ 10-20 ppbv dans les nuages supérieurs (~70 km) à des latitudes supérieures à 50° dans les deux hémisphères (Marcq et al., 2019). Un modèle de circulation planétaire tenant compte de la photochimie a permis d'interpréter ce résultat (Lebonnois et al., 2010).

Chapitre 3. Le traitement des données des spectres d'occultation stellaire

Dans ce chapitre, on décrit le jeu de données utilisé et la technique d'observation employée par SPICAV UV. L'algorithme de traitement des données est présenté en détail, y compris un test de la sensibilité et les améliorations qui ont été effectuées.

La méthode de l'occultation stellaire est effectuée quand le spectre d'une étoile est mesuré lorsque le satellite se déplace le long de son orbite. Le rayonnement d'une étoile est absorbé par l'atmosphère lorsque cette étoile se lève et se couche derrière la planète. Vénus ayant une atmosphère opaque en raison de ses épais nuages, cette méthode n'est applicable que pour la partie située au-dessus des nuages de l'atmosphère. La limite supérieure de la méthode est imposée par l'altitude à laquelle les bandes d'absorption du spectre sont comparable au bruit de fond. Par conséquent, la méthode d'occultation stellaire est efficace à des altitudes supérieures à 85 km et seulement côté nuit. En effet, au côté jour, le rayonnement du Soleil masque celui de l'étoile sur une grande partie du spectre. Cependant, c'est l'outil

le plus efficace pour étudier la structure verticale de l'atmosphère nocturne de la planète. Pour reconstruire les distributions verticales de gaz, des problèmes d'inversion spectrale et d'inversion verticale doivent être résolus, et la précision de la solution dépend de la qualité des étalonnages initiales des données. Dans ce travail, une analyse détaillée des méthodes d'étalonnage a été réalisée, et à la suite de cette analyse, les algorithmes les plus efficaces ont été sélectionnés.

Les incertitudes considérées sont principalement liées à deux aspects de l'étalonnage : (1) l'attribution d'une longueur d'onde à un pixel, et (2) la lumière d'émission UV contaminant les spectres de transmission analysés.

Une attribution erronée de la longueur d'onde à un pixel peut entraîner une sous-estimation ou une surestimation des concentrations récupérées. Par exemple, une incertitude d'une largeur d'un pixel correspondant à 0.54 nm entraîne un changement de densité colonne de CO_2 de 20 % à 85-100 km. On a testé une nouvelle méthode d'attribution pixel-longueur d'onde calée sur les raies spectrales stellaires. Les spectres des étoiles mesurées par SPICAV ont été comparés avec des spectres de référence tirés des données de l'International Ultraviolet Explorer. L'approche précédente était basée sur l'alignement des longueurs d'onde par la bande d'absorption du CO_2 à $\lambda<200$ nm. L'attribution de la longueur d'onde à partir de la bande d'absorption du CO_2 à 120-170 nm est limitée par une augmentation rapide de l'épaisseur optique de la mésosphère. Nominalement cela ne permet que de mesurer 3-4 spectres avec la bande de CO_2 non saturée lors d'une session d'occultation. En revanche, des centaines de spectres d'étoiles, mesurés hors atmosphère avant (ou après) chaque occultation, ont été utilisés pour les calibrations en longueur d'onde. Par conséquent, la précision est au moins 10 fois supérieure à celle de l'approche précédente, et elle a été estimée à 1-10% de la largeur du pixel.

La sous-estimation possible des abondances des gaz et des aérosols est aussi un effet des différents types d'émission de lumière dans l'UV enregistrés par SPICAV. Le signal mesuré se compose de la lumière provenant de l'étoile, de l'émission d'oxyde d'azote (NO) enregistrée avec un maximum à 115 km (160-240 nm), de l'émission d'hydrogène diffusée dans la bande Lyman-alpha (121.6 nm), et de la lumière dispersée du Soleil (200-320 nm). Ces émissions ont longtemps été considérées comme une lumière parasite, qui se superpose au spectre de l'étoile et génère une sous-estimation de la transmission atmosphérique. Deux méthodes ont été envisagées afin de séparer la composante d'émission du NO et la lumière de l'étoile. Les spectres obtenus par SPICAV UV ont été traités par les deux méthodes et les transmissions résultantes ont été comparées pour établir la manière la plus efficace d'extraire la composante d'émission totale.

Les deux méthodes sont basées sur les capacités d'imagerie de l'instrument. Simultanément, l'instrument mesure cinq spectres correspondant aux signaux provenant de différentes altitudes de l'atmosphère. En principe, le troisième spectre ou spectre central contient le signal stellaire. Dans ce spectre, le modèle de lumière parasite a été déterminé comme une combinaison linéaire d'autres spectres enregistrés. Dans le premier algorithme, les coefficients définissants la combinaison linéaire sont calculés au niveau de l'ombre atmosphérique et ils restent fixes pour toute la gamme d'altitude d'occultation. La seconde approche considère le modèle de lumière parasite inclus dans une équation d'inversion spectrale avec un paramètre libre proportionnel au modèle de NO . Ce paramètre est récupéré

pour chaque spectre séparément. L'analyse des profils de transmission à différentes longueurs d'onde montre que la première méthode est plus efficace pour soustraire la composante d'émission de la composante stellaire en raison de l'atténuation causée par les aérosols. L'analyse statistique de l'ensemble d'ensemble de données de SPICAV permet de conclure que la composante d'émission est estimée plus précisément avec la première méthode. Par conséquent, les erreurs causées par le NO sur les profils verticaux de CO_2 et d'autres composés atmosphériques ont pu être diminués. Cet algorithme est celui qui a été utilisé pour calibrer l'ensemble de données de SPICAV.

La deuxième étape concerne le problème de l'inversion spectrale, qui a été développé pour trouver les densités de gaz optimales qui permettent de reproduire les spectres sur la base de leurs sections efficaces. La densité colonne des gaz (SO_2 et O_3) intégrée le long de la ligne de visée peut être trop faible pour être détectable par SPICAV UV. Pour cette raison, des limites de détection pour O_3 et SO_2 ont été établies. En moyenne, ces limites sont $N_{SO2} = 5.8\pm0.2\ 10^{15}$ cm^{-2} pour SO_2 et $N_{O3} = 3.3\pm0.1\ 10^{15}$ cm^{-2} pour O_3.

Une bande d'absorption ClO est également présente dans le domaine spectral couvert par le canal UV de SPICAV. Cependant, les tentatives pour la détecter se sont avérées infructueuses. La limite de détection de ClO est 3-4 fois plus élevée que celle de l'ozone, qui est ~10^{16} cm^{-2}.

Chapitre 4. Le dioxyde de soufre

Ce chapitre est consacré aux résultats obtenus sur la teneur en SO_2 et à son analyse.

Les profils verticaux des densités colonne de CO_2 et de SO_2 ont été extraits de 375 observations réalisées entre 2006 et 2014. Les hauteurs d'échelle moyennes pour ces gaz ont été calculées, et elles sont égales à 5.25±0.05 km et 6.1±0.1 km respectivement.

Le rapport de mélange volumique du SO_2 a été calculé sur la base des obtenus de densité locale du CO_2 et du SO_2 obtenus après inversion verticale. En moyenne, il est autour de 135±21 ppbv dans entre 85 et 100 km, ce qui constitue une modification des résultats précédemment rapportés par Belyaev, Evdokimova et al. (2017) où une augmentation de la valeur avec l'altitude avait été obtenue. Cette évolution a été causée par l'amélioration des techniques d'étalonnage et qui a impacté l'inversion spectrale des densités colonne de gaz. .

Le profil vertical résultant a été comparé avec les résultats d'autres observations et des modèles actuels de la mésosphère de Vénus. Les observations sub-mm réalisées par des télescopes terrestres sont les seules à avoir observé la même heure locale sur Vénus que SPICAV. Cependant, les résultats SPICAV ont révélé des valeurs beaucoup plus élevées (Figure A6.1). La raison de cette différence n'a pas été précisément établie. Une cause possible est que le signal sub-mm émane de la superposition de l'émission thermique provenant de différentes altitudes. alors que les observations dans l'UV sont moins sensibles aux incertitudes sur la température que l'IR thermique. Cependant, la sensibilité exacte à la température dans l'UV reste à être.

La Figure A6.1 montre également une différence entre les résultats d'occultation mesurés au terminateur et du côté nuit. Cependant, les occultations solaires observaient principalement la région polaire nord tandis que les occultations stellaires observaient principalement les latitudes moyennes.

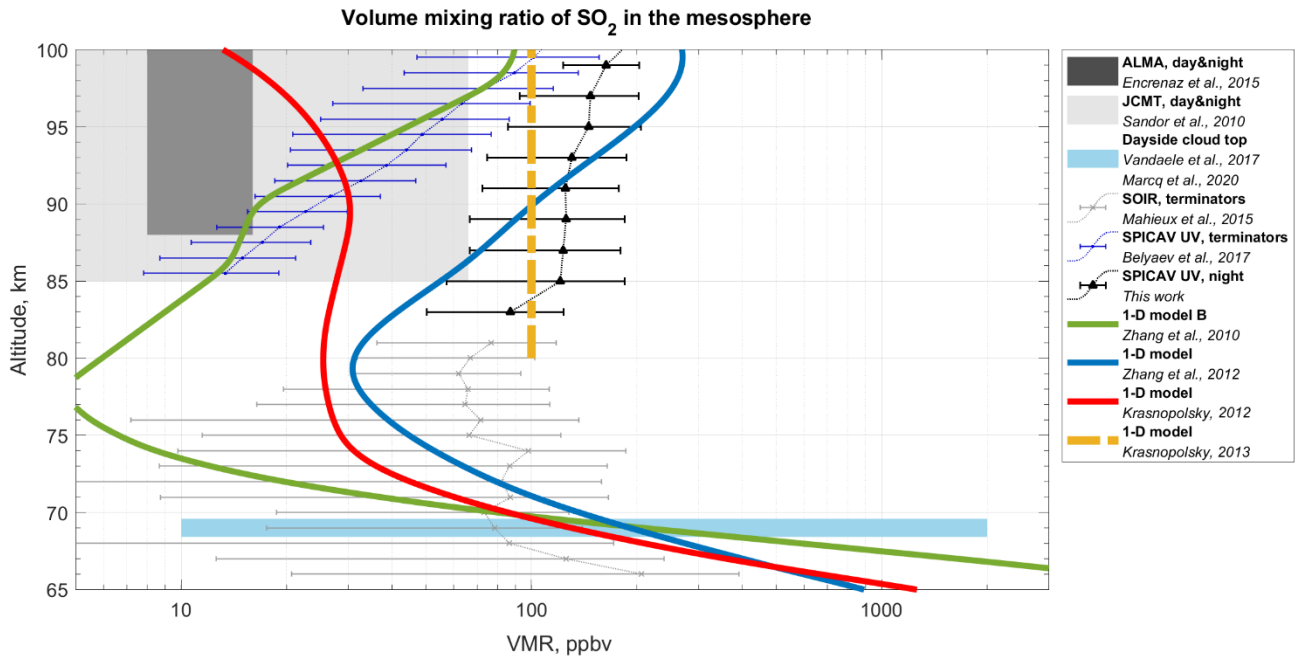

Figure A6.1. Vue d'ensemble des distributions verticales de SO_2 obtenues par différents instruments au-dessus des nuages. Les styles et les couleurs des courbes sont indiqués dans la zone de légende. Les VMR SO_2 obtenues dans cette étude sont binées avec un pas de 3 km pour obtenir le profil médian vertical (noir). Tous les résultats d'occultation sont présentés avec une dispersion de ± 1 σ.

Dans la description théorique, un seul modèle, celui de Krasnopolsky (2010, 2013) a été développé pour étudier la mésosphère de nuit. Le profil prédit est stable et égal à 100 ppbv entre 80 et 100 km. Ces résultats issus de la théorie semblent bien correspondre aux mesures déduites de cette thèse .

Zhang et al (2012) ont cherché à reproduire le minimum du rapport de mélange de SO_2 observé à 70-80 km et prédit par Krasnopolsky (2012). Les résultats de Zhang et al (2012) correspondent à la fois aux résultats en occultation stellaire de SPICAV UV mais aussi ceux obtenus en occultation solaire par SOIR. Cependant, les processus dans cette gamme d'altitude (80-100 km) nécessitent un modèle de circulation générale capable de reproduire la dynamique complexe de la mésosphère supérieure.

Les variations à court terme du SO_2 dominent dans la mésosphère supérieure. La variation de valeurs du rapport de mélange de SO_2 atteint un facteur dix entre deux versions consécutives . Sur le long terme (plus d'un an), aucune tendance n'est observée. La couverture horaire locale a permis d'étudier les changements de SO_2 entre 19:00 et 5:00 côté nuit et de révéler une asymétrie autour de minuit. On note que le rapport de mélange de SO_2 peut augmenter de 2:00 au terminateur du soir à une altitude de 93-97 km. Aucune conclusion statistiquement significative concernant la distribution longitudinale du SO_2 ou une éventuelle corrélation avec la topographie de surface n'a pu être tirée de l'ensemble des données disponibles.

Chapitre 5. L'ozone

Ce chapitre concerne les résultats de l'abondance d'O_3 et à son analyse.

L'ozone dans l'atmosphère nocturne de Vénus a été surveillé pendant 8 ans. En analysant de façon précise les capacités de SPICAV UV on observe que les valeurs d'ozone obtenues ne dépassent pas de

manière significative la limite de détection. On peut en conclure que les détections positives d'ozone correspondent à des concentrations de pointe que l'on peut trouver dans la mésosphère supérieure.

De faibles quantités d'ozone mésosphérique ont été obtenues. Le pourcentage de détections positives est d'environ 6%. En moyenne, pour les détections positives, les concentrations locales diminuent avec l'altitude, passant de 10^8 cm^{-3} à 85 km à 10^7 cm^{-3} à 110 km. En général, l'ozone devrait constituer un rapport de mélange de 1 ppbv à 30 ppbv aux altitudes de 85-95 km. À 95-105 km, le rapport de mélange de O_3 augmente, et l'estimation fournit une valeur comprise entre 3 ppbv et 120 ppbv. Les valeurs maximales correspondent aux résultats des détections.

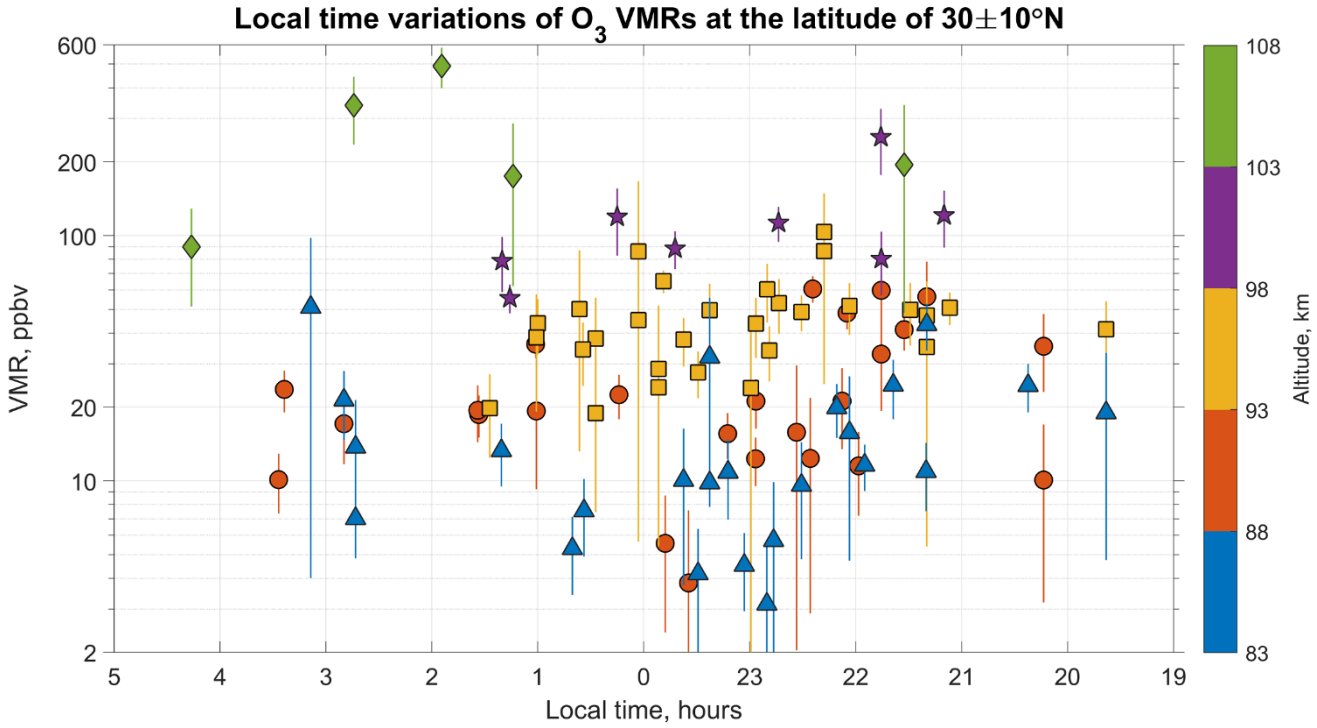

Figure A6.2. Variabilité du rapport de mélange volumique de l'O_3 (ppbv) par rapport à l'horaire local. Les valeurs valeurs proviennent des latitudes 30°N±10° où le plus grand nombre d'observations a été effectué. Les différentes couleurs représentent des gammes différentes d'altitude de 5 km d'épaisseur.

Les détections d'ozone sont sporadiques. Les valeurs du rapport de mélange obtenues varient considérablement dans le temps et l'espace. La plupart des détections sont localisées dans une zone de latitude de 30°N ± 10° en raison de la meilleure couverture par les observations. Une diminution vers minuit à partir des terminateurs peut être notée seulement en dessous de 93 km (Figure A6.2).

Ces détections clairsemées d'ozone ont également été comparées avec les schémas spatiaux d'émission d'oxygène et d'hydroxyle obtenus du côté nuit. L'émission d' O_2 indique le transfert des atomes d'oxygène à l'atmosphère nocturne. L'émission d'hydroxyle est un puits chimique d'ozone dans la mésosphère nocturne. On pourrait supposer qu'un modèle spatial d'ozone soit conforme au comportement de l'émission d'O_2 ($a^1\Delta_g$). Mais la présence de radicaux hydroxyles devrait réduire la quantité d'O_3 vers minuit à l'équateur dans la même gamme d'altitude que les lueurs nocturnes d'OH et d'O_2. Il n'y a pas de détections dans le point antisolaire, cependant, le nombre total d'observations est exigu dans cette région. Ce qui pourrait indiquer que la destruction de l'ozone est très efficace. On

s'attend également à ce que les atomes de chlore jouent un rôle important dans le cycle chimique de l'oxygène à ces altitudes la nuit (Bertaux et al., 2007a; Montmessin et al., 2011). Le signe d'un tel mécanisme sont les molécules de ClO (Sandor et al., 2018) observées dans la mésosphère nocturne et de HCl observées au terminateur (Mahieux et al., 2015; Sandor et al., 2012; Sandor et al., 2017; Krasnopolsky, 2010).

Le GCM thermosphérique a fait la première tentative de reproduire la distribution spatiale de l'ozone au-dessus de 96 km. Les résultats montrent clairement une couche d'ozone stable du côté nuit à des altitudes de 90-110 km, localisée dans la zone équatoriale. L'abondance de l'ozone est conforme à notre estimation à 85-110 km. Le maximum théorique de la distribution spatiale de l'ozone s'est décalé vers 20:00-22:00, ce qui est difficile à confirmer par nos données. Cependant, à une latitude de 30°N, le modèle a obtenu un minimum local de l'ozone VMR dans l'atmosphère nocturne vers 01:00 à 100 km. Un comportement similaire, avec un minimum vers 23:00-24:00, a été observé par SPICAV UV à des altitudes inférieures à 93 kilomètres. Au point antisolaire, le modèle prévoit également des valeurs plus faibles associées à une concentration plus élevée de composés chimiquement actifs contribuant à l'atténuation de la couche d'ozone. Ceci est indirectement confirmé par l'expérience. En général, il n'y a pas de contradiction entre la distribution simulée de l'ozone et les observations nocturnes à des altitudes de 85-110 km dans une comparaison qualitative.

Chapitre 6. L'émission d'O_2 ($\alpha^1\Delta_g$) dans la mésosphère supérieure

Ce chapitre considère la lueur atmosphérique nocturne (*airglow*) de O_2 ($\alpha^1\Delta_g$) à 1.27 μm comme une source supplémentaire d'informations sur la physique de la mésosphère nocturne de Vénus. Les observations au nadir par SPICAV IR sont utilisées pour récupérer une distribution de l'intensité de l'émission du côté de la nuit.

En plus de l'étude de l'ozone, il est possible d'observer un autre produit de recombinaison des atomes d'oxygène, qui est l'*airglow* O_2 ($\alpha^1\Delta_g$) à 1,27 mm. Cette émission apparaît en relaxation des molécules O_2^* excitées formées. La luminosité maximale est observée à ~95 km; par conséquent cet *airglow* met en évidence des processus dynamiques qui se produisent dans la mésosphère supérieure.

Les observations au nadir par SPICAV IR ont fourni des spectres qui correspondent à l'émission thermique de la basse atmosphère et des nuages, et à l'*airglow* O_2 ($\alpha^1\Delta_g$). Ces spectres ont été réalisés à haute résolution : le pouvoir de résolution de SPICAV IR est de ~1400. Notre analyse du jeu de données IR SPICAV a permis de séparer le signal d'émission des spectres thermiques. Cette séparation est obtenue par une modélisation minutieuse de l'émission thermique de Vénus. Les spectres IR de SPICAV ont été analysés par un modèle de transfert radiatif 1D avec diffusion multiple. Le modèle direct est calculé par le programme SHDOMPP qui résout l'équation de transfert radiatif en utilisant la méthode des ordonnées discrètes et des harmoniques sphériques dans une atmosphère plane-parallèle (Evans, 2007). Cette routine a été développée par Bruno Bézard et Anna Fedorova (Bézard et al., 2011 ; Fedorova et al., 2015), et elle a été utilisée dans cette étude avec un modèle de couche nuageuse actualisé par Haus et al. (2016). Les résidus du modèle correspondent alors au spectre d'émission de l'oxygène.

Au total, plus de 600 observations en 2006-2014 ont été analysées sur la base de la procédure de séparation des émissions d'O_2. Cette analyse est significative pour l'étude de l'*airglow* O_2 ($\alpha^1\Delta_g$), puisque tout l'hémisphère nocturne est couvert en détail On a permis de corroborer et d'étendre l'étude VIRTIS-M de la distribution latitudinale de l'intensité de cette émission dans l'hémisphère nocturne. Le fonctionnement de VIRTIS-M s'est arrêté en 2010 et ces observations couvraient principalement l'hémisphère sud nocturne de Vénus (Gerard et al., 2009; Shakun et al., 2010; Soret et al., 2012).

Dans cette étude, un maximum d'intensité de 2 MR a été trouvé précisément au point antisolaire. Le modèle d'émission est assez symétrique autour de l'équateur, mais montre une certaine tendance à être légèrement décalé vers le terminateur du matin. La luminosité diminue de manière significative après 23:00 vers le terminateur du soir. Ces résultats concordent avec l'analyse des données de VIRTIS (Shakun et al., 2010; Soret et al., 2012), mais suggèrent une intensité légèrement supérieure.

REFERENCES

Adams, W. S., & Dunham Jr, T. (1932). Absorption bands in the infra-red spectrum of Venus. *Publications of the Astronomical Society of the Pacific*, *44*, 243-245.

Airey, M. W., Mather, T. A., Pyle, D. M., Glaze, L. S., Ghail, R. C., & Wilson, C. F. (2015). Explosive volcanic activity on Venus: The roles of volatile contribution, degassing, and external environment. *Planetary and Space Science*, *113-114*, 33–48. DOI: 10.1016/j.pss.2015.01.009

Allen, D. A., & Crawford, J. W. (1984). Cloud structure on the dark side of Venus. *Nature*, *307*(5948), 222-224.

Allen, M., Lunine, J. I., & Yung, Y. L. (1984). The vertical distribution of ozone in the mesosphere and lower thermosphere. *Journal of Geophysical Research: Atmospheres*, *89*(D3), 4841-4872.

Andreichikov, B. M. (1987). Chemical composition and structure of Venus clouds from results of X-ray radiometric experiments made with the Vega 1 and Vega 2 automatic interplanetary stations. *Kosmicheskie Issledovaniia*, *25*, 737-743.

Arney, G., Meadows, V., Crisp, D., Schmidt, S. J., Bailey, J., & Robinson, T. (2014). Spatially resolved measurements of H2O, HCl, CO, OCS, SO2, cloud opacity, and acid concentration in the Venus near-infrared spectral windows. *Journal of Geophysical Research: Planets*, *119*(8), 1860-1891.

Atreya, S. K., Donahue, T. M., Sharp, W. E., Wasser, B., Drake, J. F., & Riegler, G. R. (1976). Ultraviolet stellar occultation measurement of the H 2 and O 2 densities near 100 km in the earth's atmosphere. *Geophysical Research Letters*, *3*(10), 607-610.

Avduevsky, V. S., Marov, M. Y., & Rozhdestvensky, M. K. (1968). *Model of the Atmosphere of the Planet Venus Based on Results of Measurements made by the Soviet Automatic Interplanetary Station Venera 4. Journal of the Atmospheric Sciences, 25(4), 537–545.*

Barabash, S., Sauvaud, J. A., Gunell, H., Andersson, H., Grigoriev, A., Brinkfeldt, K., ... & Baumjohann, W. (2007). The analyser of space plasmas and energetic atoms (ASPERA-4) for the Venus Express mission. *Planetary and Space Science*, *55*(12), 1772-1792.

Barber, R. J., Tennyson, J., Harris, G. J., & Tolchenov, R. N. (2006). A high-accuracy computed water line list. *Monthly Notices of the Royal Astronomical Society*, *368*(3), 1087-1094.

Barker, E. S. (1979). Detection of SO2 in the UV spectrum of Venus. *Geophysical Research Letters*, *6*(2), 117-120.

Barker, E. S., Stern, S. A., & Na, C. Y. (1992). Venus SO2 Abundance: 1991 Groundbased and IUE Measurements. In *Bulletin of the American Astronomical Society*, *24*, p. 996.

Barth, C. A., Pearce, J. B., Kelly, K. K., Wallace, L., & Fastie, W. G. (1967). Ultraviolet emissions observed near Venus from Mariner V. *Science*, *158*(3809), 1675-1678.

Basilevsky, A. T., & Head, J. W. (2003). The surface of Venus. *Reports on Progress in Physics*, *66*(10), 1699.

Bates, D. R., & Nicolet, M. (1950). The photochemistry of atmospheric water vapor. *Journal of Geophysical Research*, *55*(3), 301-327.

Belyaev, D. A., Montmessin, F., Bertaux, J. L., Mahieux, A., Fedorova, A. A., Korablev, O. I., ... & Zhang, X. (2012). Vertical profiling of SO2 and SO above Venus' clouds by SPICAV/SOIR solar occultations. *Icarus*, *217*(2), 740-751.

Belyaev, D. A., Evdokimova, D. G., Montmessin, F., Bertaux, J. L., Korablev, O. I., Fedorova, A. A., ... & Luginin, M. S. (2017). Night side distribution of SO2 content in Venus' upper mesosphere. *Icarus*, *294*, 58-71.

Bertaux, J. L., Widemann, T., Hauchecorne, A., Moroz, V. I., & Ekonomov, A. P. (1996). VEGA 1 and VEGA 2 entry probes: An investigation of local UV absorption (220–400 nm) in the atmosphere of Venus (SO2 aerosols, cloud structure). *Journal of Geophysical Research: Planets*, *101*(E5), 12709-12745.

Bertaux, J. L., Hauchecorne, A., Dalaudier, F., Cot, C., Kyrölä, E., Fussen, D., ... & d'Andon, O. F. (2004). First results on GOMOS/Envisat. *Advances in Space Research*, *33*(7), 1029-1035.

Bertaux, J. L., Vandaele, A. C., Korablev, O., Villard, E., Fedorova, A., Fussen, D., ... & Muller, C. (2007a). A warm layer in Venus' cryosphere and high-altitude measurements of HF, HCl, H 2 O and HDO. *Nature*, *450*(7170), 646-649.

Bertaux, J. L., Nevejans, D., Korablev, O., Villard, E., Quémerais, E., Neefs, E., ... & Hauchecorne, A. (2007b). SPICAV on Venus Express: Three spectrometers to study the global structure and composition of the Venus atmosphere. *Planetary and Space Science*, *55*(12), 1673-1700.

Bertaux, J. L., Khatuntsev, I. V., Hauchecorne, A., Markiewicz, W. J., Marcq, E., Lebonnois, S., ... & Fedorova, A. (2016). Influence of Venus topography on the zonal wind and UV albedo at cloud top level: The role of stationary gravity waves. *Journal of Geophysical Research: Planets*, *121*(6), 1087-1101.

Bevington, P. R., & Robinson, K. D. (2003). Data reduction and error analysis for the physical sciences, 3rd ed., by Bevington, P. R., & Robinson, K. D. Boston, MA: McGraw-Hill, ISBN 0-07-247227-8.

Bézard, B., De Bergh, C., Fegley, B., Maillard, J. P., Crisp, D., Owen, T., ... & Grinspoon, D. (1993). The abundance of sulfur dioxide below the clouds of Venus. *Geophysical research letters*, *20*(15), 1587-1590.

Bézard, B., Fedorova, A., Bertaux, J. L., Rodin, A., & Korablev, O. (2011). The 1.10-and 1.18-μm nightside windows of Venus observed by SPICAV-IR aboard Venus Express. *Icarus*, *216*(1), 173-183. DOI: 10.1016/j.icarus.2011.08.025

Bindschadler, D. L. (1995). Magellan: A new view of Venus' geology and geophysics. *Reviews of Geophysics*, *33*(S1), 459-467.

Blackie, D., Blackwell-Whitehead, R., Stark, G., Pickering, J. C., Smith, P. L., Rufus, J., & Thorne, A. P. (2011). High-resolution photoabsorption cross-section measurements of SO2 at 198 K from 213 to 325 nm. *Journal of Geophysical Research: Planets*, *116*(E3).

Blamont, J., Boloh, L., Kerzhanovich, V., Kogan, L., Kurgansky, M., Linkin, V., ... & Hildebrand, C. (1993). Balloons on planet Venus: final results. *Advances in Space Research*, *13*(2), 145-152.

Boggess, A., Carr, F. A., Evans, D. C., Fischel, D., Freeman, H. R., Fuechsel, C. F., ... & Pyle, E. J. (1978). The IUE spacecraft and instrumentation. *Nature*, *275*(5679), 372-377.

Bougher, S. W., Alexander, M. J., & Mayr, H. G. (1997). Upper atmosphere dynamics: Global circulation and gravity waves, in *Venus II: Geology, Geophysics, Atmosphere, and Solar Wind Environment*, (Ed.) Bougher, S. W., Hunten, D. M., & Phillips, R. J., pp 259-292, The University of Arizona Press, Tucson.

Brasseur, G. P., & Solomon, S. (2006). *Aeronomy of the middle atmosphere: Chemistry and physics of the stratosphere and mesosphere* (Vol. 32). Springer Science & Business Media.

Broadfoot, A. L., Sandel, B. R., Shemansky, D. E., Atreya, S. K., Donahue, T. M., Moos, H. W., ... & McConnell, J. C. (1977). Ultraviolet spectrometer experiment for the Voyager mission. *Space Science Reviews*, *21*(2), 183-205.

Bullock, M. A., Grinspoon, D. H., & Head III, J. W. (1993). Venus resurfacing rates: Constraints provided by 3-D Monte Carlo simulations. *Geophysical research letters*, *20*(19), 2147-2150.

Carlson, R.W., Piccioni, G., Filacchione, G., Yung, Y.L., & Gao, P. (2016). Venus's ultraviolet absorber: cyclo-octal (S_8) and polymeric sulfur (S_x) and their latitudinal behavior. International Venus Conference, Oxford, UK, p.27 (abstract).

Chamberlain, S., Mahieux, A., Robert, S., Piccialli, A., Trompet, L., Vandaele, A. C., & Wilquet, V. (2020). SOIR/VEx observations of water vapor at the terminator in the Venus mesosphere. *Icarus*, 113819.

Chapman, S. (1930). A theory of upper-atmospheric ozone. *Mem. Roy. Meteor.*, *3*, 103-125.

Chaufray, J. Y., Bertaux, J. L., Quémerais, E., Leblanc, F., & Sulis, S. (2015). Observations of the nightside venusian hydrogen corona with SPICAV/VEX. *Icarus*, *262*, 1-8.

Chaufray, J. Y., Bertaux, J. L., Quémerais, E., Villard, E., & Leblanc, F. (2012). Hydrogen density in the dayside venusian exosphere derived from Lyman-α observations by SPICAV on Venus Express. *Icarus*, *217*(2), 767-778.

Chicarro, A., Martin, P., & Trautner, R. (2004). The Mars Express mission: an overview. In *Mars Express: The Scientific Payload*, 1240, 3-13.

Colin, L. (1979). Encounter with Venus. *Science*, 203(4382), 743-745.

Colin, L. (1983). Basic facts about Venus. In *Venus*, (Ed.) Hunten, D. M., Colin, L., Donahue, T. M., & Moroz, V. I., pp. 10-26, The University of Arizona Press, Tucson.

Connes, P., Noxon, J. F., Traub, W. A., & Carleton, N. P. (1979). O2 (1Δ) emission in the day and night airglow of Venus. *The Astrophysical Journal*, *233*, L29-L32.

Conway, R. R., McCoy, R. P., Barth, C. A., & Lane, A. L. (1979). IUE detection of sulfur dioxide in the atmosphere of Venus. *Geophysical Research Letters*, *6*(7), 629-631.

Cottini, V., Ignatiev, N. I., Piccioni, G., & Drossart, P. (2015). Water vapor near Venus cloud tops from VIRTIS-H/Venus express observations 2006–2011. *Planetary and Space Science*, *113*, 219-225.

Counselman, C. C., Gourevitch, S. A., King, R. W., Loriot, G. B., & Ginsberg, E. S. (1980). Zonal and meridional circulation of the lower atmosphere of Venus determined by radio interferometry. *Journal of Geophysical Research: Space Physics*, *85*(A13), 8026-8030.

Crisp, D., McMuldroch, S., Stephens, S. K., Sinton, W. M., Ragent, B., Hodapp, K. W., Probst, R.G., Doyle, L.R. Allen, D.A., & Elias, J. (1991). Ground-based near-infrared imaging observations of Venus during the Galileo encounter. *Science*, *253*(5027), 1538-1541.

Crisp, D., Meadows, V. S., Bézard, B., De Bergh, C., Maillard, J. P., & Mills, F. P. (1996). Ground-based near-infrared observations of the Venus nightside: 1.27-μm O2 (a 1Δ g) airglow from the upper atmosphere. *Journal of Geophysical Research: Planets*, *101*(E2), 4577-4593.

Crisp, D., & Titov, D. (1997) The thermal balance of the Venus atmosphere, in *Venus II: Geology, Geophysics, Atmosphere, and Solar Wind Environment*, (Ed.) Bougher, S. W., Hunten, D. M., & Phillips, R. J., pp 353-384, The University of Arizona Press, Tucson.

Cruikshank, D. P., (1983). The development of studies of Venus. In *Venus*, (Ed.) Hunten, D. M., Colin, L., Donahue, T. M., & Moroz, V. I., pp. 1–9, The University of Arizona Press, Tucson.

de Bergh, C., Moroz, V. I., Taylor, F. W., Crisp, D., Bézard, B., & Zasova, L. V. (2006). Composition of the atmosphere of Venus below the clouds. *Planetary and Space Science*, *54*, 1389– 1397.

Donahue, T. M., D. H. Grinspoon, R. E. Hartle, and R. R. Hodges Jr. (1997), Ion/neutral escape of hydrogen and deuterium: Evolution of water, in *Venus II: Geology, Geophysics, Atmosphere, and Solar Wind Environment*, (Ed.) Bougher, S. W., Hunten, D. M., & Phillips, R. J., pp 385–415, The University of Arizona Press, Tucson.

Donahue, T.M., & Russell, C.T., 1997. The Venus atmosphere and ionosphere and their interaction with the solar wind: An overview, in *Venus II: Geology, Geophysics, Atmosphere, and Solar Wind Environment*, (Ed.) Bougher, S. W., Hunten, D. M., & Phillips, R. J., pp 3–32, University of Arizona Press, Tucson.

Drossart, P., Piccioni, G., Adriani, A., Angrilli, F., Arnold, G., Baines, K. H., ... & Blanco, A. (2007). Scientific goals for the observation of Venus by VIRTIS on ESA/Venus Express mission. *Planetary and Space Science*, *55*(12), 1653-1672.

Drossart, P., & Montmessin, F. (2015). The legacy of Venus Express: highlights from the first European planetary mission to Venus. *The Astronomy and Astrophysics Review*, *23*(1), 5.

Encrenaz, T., Greathouse, T. K., Roe, H., Richter, M., Lacy, J., Bézard, B., ... & Widemann, T. (2012). HDO and SO2 thermal mapping on Venus: evidence for strong SO2 variability. *Astronomy & Astrophysics*, *543*, A153.

Encrenaz, T., Moreno, R., Moullet, A., Lellouch, E., & Fouchet, T. (2015). Submillimeter mapping of mesospheric minor species on Venus with ALMA. *Planetary and Space Science*, *113*, 275-291.

Encrenaz, T., Greathouse, T. K., Richter, M. J., DeWitt, C., Widemann, T., Bézard, B., ... & Sagawa, H. (2016). HDO and SO2 thermal mapping on Venus-III. Short-term and long-term variations between 2012 and 2016. *Astronomy & Astrophysics*, *595*, A74.

Encrenaz, T., Greathouse, T. K., Marcq, E., Sagawa, H., Widemann, T., Bézard, B., ... & Lee, Y. J. (2019). HDO and SO2 thermal mapping on Venus-IV. Statistical analysis of the SO2 plumes. *Astronomy & Astrophysics*, *623*, A70.

Encrenaz, T., Greathouse, T. K., Marcq, E., Widemann, T., Bézard, B., Fouchet, T., ... & Sousa-Silva, C. (2020). A stringent upper limit of the PH3 abundance at the cloud top of Venus. *Astronomy & Astrophysics*, *643*, L5.

Esposito, L. W., Knollenberg, R. G., Marov, M. Y. A., Toon, O. B., & Turco, R. (1983). The clouds and hazes of Venus, in *Venus*, (Ed.) Hunten, D. M., Colin, L., Donahue, T. M., & Moroz, V. I., pp. 484-564, The University of Arizona Press, Tucson.

Esposito, L. W. (1984). Sulfur dioxide: Episodic injection shows evidence for active Venus volcanism. *Science*, *223*(4640), 1072-1074.

Esposito, L. W., Bertaux, J. L., Krasnopolsky, V., Moroz, V. I., & Zasova, L. V. (1997). Chemistry of lower atmosphere and clouds, in *Venus II: Geology, Geophysics, Atmosphere, and Solar Wind Environment*, (Ed.) Bougher, S. W., Hunten, D. M., & Phillips, R. J., pp 415-458, University of Arizona Press, Tucson.

Esposito, L.W. (2011). SAGE New Frontiers mission to Venus, in *42nd Lunar and Planetary Science Conference*, Abstract #1519

Evans, K. F. (2007). SHDOMPPDA: A radiative transfer model for cloudy sky data assimilation. *Journal of the atmospheric sciences*, *64*(11), 3854-3864.

Evdokimova, D., Fedorova, A., Belyaev, D., Korablev O., Bertaux J. L. (2016). Studying of cloud variations using night observations data of SPICAV IR in 2006-2014. Abstracts. *The Seventh Moscow Solar System Symposium, October 10-14, 2016*, IKI, Moscow

Evdokimova, D., Fedorova, A., Korable, O., Marcq, E., & Bertaux, J.-L. (2019a). Variations of lower clouds and water vapor amount in deep Venus atmosphere based on night windows observations by the SPICAV-IR/Venus-Express. *International Venus Conference 2019*, *May 31-June 3, 2019*, Niseko, Hokkaido, Japan. 09-6 IVC2019-0112. P. 123.

Evdokimova, D.G., Fedorova, A.A., Korablev, O.I., Belyaev, D.A., Bertaux J.-L. (2019b) Monitoring of the atmospheric oxygen airglow on the night side of Venus according to the dataset of SPICAV IR of the Venus Express spacecraft. (in Russian). Materials of the 17th All-Russian Open Conference «Modern Problems of Earth Remote Sensing from Space», Moscow, IKI RAS, 2019. DOI: 10.21046/17DZZconf-2019a

Evdokimova, D., Belyaev, D., Montmessin, F., Bertaux, J. L., & Korablev, O. (2020). Improved calibrations of the stellar occultation data accumulated by the SPICAV UV onboard Venus Express. *Planetary and Space Science*, *184*, 104868.

Farman, J. C., Gardiner, B. G., & Shanklin, J. D. (1985). Large losses of total ozone in Antarctica reveal seasonal ClOx/NOx interaction. *Nature*, *315*(6016), 207-210.

Fedorova, A., Bézard, B., Bertaux, J. L., Korablev, O., & Wilson, C. (2015). The CO2 continuum absorption in the 1.10-and 1.18-μm windows on Venus from Maxwell Montes transits by SPICAV IR onboard Venus express. *Planetary and Space Science*, *113*, 66-77. DOI: 10.1016/j.pss.2014.08.010

Fedorova, A., Marcq, E., Luginin, M., Korablev, O., Bertaux, J. L., & Montmessin, F. (2016). Variations of water vapor and cloud top altitude in the Venus' mesosphere from SPICAV/VEx observations. *Icarus*, *275*, 143-162.

Feldman, P. D., Moos, H. W., Clarke, J. T., & Lane, A. L. (1979). Identification of the UV nightglow from Venus. *Nature*, *279*(5710), 221-222.

Forget, F., Hourdin, F., Fournier, R., Hourdin, C., Talagrand, O., Collins, M., ... & Huot, J. P. (1999). Improved general circulation models of the Martian atmosphere from the surface to above 80 km. *Journal of Geophysical Research: Planets*, *104*(E10), 24155-24175.

Formisano, V., Angrilli, F., Arnold, G., Atreya, S., Baines, K. H., Bellucci, G., ... & Colangeli, L. (2006). The planetary fourier spectrometer (PFS) onboard the European Venus Express mission. *Planetary and Space Science*, *54*(13-14), 1298-1314.

Frandsen, B. N., Wennberg, P. O., & Kjaergaard, H. G. (2016). Identification of OSSO as a near-UV absorber in the Venusian atmosphere. *Geophysical Research Letters*, *43*(21), 11-146.

Fukuhara, T., Futaguchi, M., Hashimoto, G. L., Horinouchi, T., Imamura, T., Iwagaimi, N., ... & Sato, M. (2017). Large stationary gravity wave in the atmosphere of Venus. *Nature Geoscience*, *10*(2), 85-88.

Garate-Lopez, I., & Lebonnois, S. (2018). Latitudinal variation of clouds' structure responsible for Venus' cold collar. *Icarus*, 314, 1-11.

Gérard, J. C., Saglam, A., Piccioni, G., Drossart, P., Cox, C., Erard, S., ... & Sánchez-Lavega, A. (2008). Distribution of the O2 infrared nightglow observed with VIRTIS on board Venus Express. *Geophysical research letters*, *35*(2).

Gérard, J. C., Saglam, A., Piccioni, G., Drossart, P., Montmessin, F., & Bertaux, J. L. (2009). Atomic oxygen distribution in the Venus mesosphere from observations of O2 infrared airglow by VIRTIS-Venus Express. *Icarus*, *199*(2), 264-272.

Gérard, J. C., Soret, L., Piccioni, G., & Drossart, P. (2012). Spatial correlation of OH Meinel and O2 infrared atmospheric nightglow emissions observed with VIRTIS-M on board Venus Express. *Icarus*, *217*(2), 813-817.

Gérard, J. C., Bougher, S. W., López-Valverde, M. A., Pätzold, M., Drossart, P., & Piccioni, G. (2017). Aeronomy of the Venus upper atmosphere. *Space Science Reviews*, *212*(3-4), 1617-1683.

Gierasch, P. (1975). Meridional circulation and the maintenance of the Venus atmospheric rotation. *Journal of the Atmospheric Sciences*, 32, 1038-1044.

Gilli, G., Lebonnois, S., González-Galindo, F., López-Valverde, M. A., Stolzenbach, A., Lefèvre, F., ... & Lott, F. (2017). Thermal structure of the upper atmosphere of Venus simulated by a ground-to-thermosphere GCM. *Icarus*, *281*, 55-72. Hourdin, F., Musat, I., Bony, S., Braconnot, P., Codron, F., Dufresne, J. L., ... & Krinner, G. (2006). The LMDZ4 general circulation model: climate performance and sensitivity to parametrized physics with emphasis on tropical convection. *Climate Dynamics*, *27*(7-8), 787-813.

Gilli G., Navarro T., Lebonnois S, Quirino D, Silva V, Lefèvre F, and Schubert G. (2020). Venus upper atmosphere revealed by a GCM: Temperature, CO, O2 and O distribution in the puzzling transition region. *EPSC Abstracts* (14), EPSC2020-353, 2020, updated on 05 Oct 2020. Europlanet Science Congress 2020.

Gilmore, M.S., Glaze, L.S., Baker, C.L., Tahu, G.J. Adams, M., Karpati, G., & Amato, M.J. (2010). Venus Intrepid Tessera Lander: Mission Concept Study Report to the NRC Decadal Survey Inner Planets Panel. http://www.lpi.usra.edu/vexag/reports/VITaL_FINAL_040809.pdf

Glassmeier, K. H., Boehnhardt, H., Koschny, D., Kührt, E., & Richter, I. (2007). The Rosetta mission: flying towards the origin of the solar system. *Space Science Reviews*, *128*(1-4), 1-21.

Glaze, L.S. et al. (DAVINCI the DAVINCI Science Team) (2016). Deep atmosphere investigation of noble gases, chemistry, and imaging, in 47th Lunar and Plan. Sci. Conf., Abstract #1560

Gorinov, D. A., Khatuntsev, I. V., Zasova, L. V., Turin, A. V., & Piccioni, G. (2018). Circulation of Venusian Atmosphere at 90–110 km Based on Apparent Motions of the O2 1.27 μm Nightglow From VIRTIS-M (Venus Express) Data. *Geophysical Research Letters*, *45*(5), 2554-2562.

Greaves, J. S., Richards, A. M., Bains, W., Rimmer, P. B., Sagawa, H., Clements, D. L., ... & Drabek-Maunder, E. (2020). Phosphine gas in the cloud decks of Venus. *Nature Astronomy*, 1-10.

Grinspoon, D., Pavlov, A., Adams, M. (2010). Venus Climate Mission (VCM). http://www.lpi.usra.edu/vexag/reports/VCM_report_FINAL.pdf

Hagemann, R., Nief, G., & Roth, E. (1970). Absolute isotopic scale for deuterium analysis in natural waters: Absolute D/H ratio of SMOW. *Tellus*, *22*, 712– 715.

Hansen, J. E., & Hovenier, J. (1974). Interpretation of the polarization of Venus. *Journal of the Atmospheric Sciences*, *31*(4), 1137-1160.

Hansen, J. E., Wang, W. C., & Lacis, A. A. (1978). Mount Agung eruption provides test of a global climatic perturbation. *Science*, *199*(4333), 1065-1068.

Hays, P. B., Roble, R. G., & Shah, A. N. (1972). Terrestrial atmospheric composition from stellar occultations. *Science*, *176*(4036), 793-794.

Haus, R., Kappel, D., & Arnold, G. (2014). Atmospheric thermal structure and cloud features in the southern hemisphere of Venus as retrieved from VIRTIS/VEX radiation measurements. *Icarus, 232,* 232–248. DOI: 10.1016/j.icarus.2014.01.020

Haus, R., Kappel, D., Tellmann, S., Arnold, G., Piccioni, G., Drossart, P., & Häusler, B. (2016). Radiative energy balance of Venus based on improved models of the middle and lower atmosphere. *Icarus*, *272*, 178-205.

Häusler, B., Pätzold, M., Tyler, G. L., Simpson, R. A., Bird, M. K., Dehant, V., ... & Selle, J. (2006). Radio science investigations by VeRa onboard the Venus Express spacecraft. *Planetary and Space Science*, *54*(13-14), 1315-1335.

Holland, H. D. (1995). Atmospheric oxygen and the biosphere. In *Linking Species & Ecosystems* (pp. 127-136). Springer, Boston, MA.

Horinouchi, T., Murakami, S. Y., Satoh, T., Peralta, J., Ogohara, K., Kouyama, T., ... & Nakamura, M. (2017). Equatorial jet in the lower to middle cloud layer of Venus revealed by Akatsuki. *Nature geoscience*, *10*(9), 646-651.

Horinouchi, T., Kouyama, T., Lee, Y. J., Murakami, S. Y., Ogohara, K., Takagi, M., ... & Yamada, M. (2018). Mean winds at the cloud top of Venus obtained from two-wavelength UV imaging by Akatsuki. *Earth, Planets and Space*, *70*(1), 1-19.

Ignatiev, N. I., Titov, D. V., Piccioni, G., Drossart, P., Markiewicz, W. J., Cottini, V., ... & Manoel, N. (2009). Altimetry of the Venus cloud tops from the Venus Express observations. *Journal of Geophysical Research: Planets*, *114*(E9).

Imamura, T., Mitchell, J., Lebonnois, S. Kaspi, Y., Showman, A. P., & Korablev, O. (2020). Superrotation in Planetary Atmospheres. *Space Science Reviews*, 216, 87. DOI: 10.1007/s11214-020-00703-9

Ityaksov, D., Linnartz, H., & Ubachs, W. (2008). Deep-UV absorption and Rayleigh scattering of carbon dioxide. *Chemical Physics Letters*, *462*(1-3), 31-34.

Jessup, K. L., Marcq, E., Mills, F., Mahieux, A., Limaye, S., Wilson, C., ... & Vandaele, A. C. (2015). Coordinated hubble space telescope and Venus express observations of Venus' upper cloud deck. *Icarus*, *258*, 309-336.

Kasprzak, W. T., Keating, G. M., Hsu, N. C., Stewart, A. I. F., Colwell, W. B., & Bougher, S. W. (1997). Solar activity behavior of the thermosphere, in *Venus II: Geology, Geophysics, Atmosphere, and*

Solar Wind Environment, (Ed.) Bougher, S. W., Hunten, D. M., & Phillips, R. J., pp 225-257, The University of Arizona Press, Tucson.

Khatuntsev, I. V., Patsaeva, M. V., Titov, D. V., Ignatiev, N. I., Turin, A. V., Limaye, S. S., ... & Moissl, R. (2013). Cloud level winds from the Venus Express Monitoring Camera imaging. *Icarus*, *226*(1), 140-158.

Khatuntsev, I. V., Patsaeva, M. V., Titov, D. V., Ignatiev, N. I., Turin, A. V., Fedorova, A. A., & Markiewicz, W. J. (2017). Winds in the middle cloud deck from the near-IR imaging by the Venus Monitoring Camera onboard Venus Express. *Journal of Geophysical Research: Planets*, *122*(11), 2312-2327.

Knollenberg, R. G., & Hunten, D. M. (1980). The microphysics of the clouds of Venus: Results of the Pioneer Venus particle size spectrometer experiment. *Journal of Geophysical Research: Space Physics*, *85*(A13), 8039-8058.

Kopparapu, R. K., Ramirez, R., Kasting, J. F., Eymet, V., Robinson, T. D., Mahadevan, S., ... & Deshpande, R. (2013). Habitable zones around main-sequence stars: new estimates. *The Astrophysical Journal*, *765*(2), 131.

Korablev, O., Fedorova, A., Bertaux, J. L., Stepanov, A. V., Kiselev, A., Kalinnikov, Y. K., ... & Sarago, V. (2012). SPICAV IR acousto-optic spectrometer experiment on Venus Express. *Planetary and Space Science*, *65*(1), 38-57.

Krasnopolsky, V. A. (2010a). Venus night airglow: Ground-based detection of OH, observations of O2 emissions, and photochemical model. *Icarus*, *207*(1), 17-27.

Krasnopolsky, V. A. (2010b). Spatially-resolved high-resolution spectroscopy of Venus 1. Variations of CO2, CO, HF, and HCl at the cloud tops. *Icarus*, *208*(2), 539-547.

Krasnopolsky, V. A. (2011). Atmospheric chemistry on Venus, Earth, and Mars: Main features and comparison. *Planetary and Space Science*, *59*(10), 952-964.

Krasnopolsky, V. A. (2012). A photochemical model for the Venus atmosphere at 47–112 km. *Icarus*, *218*(1), 230-246.

Krasnopolsky, V. A. (2013). Nighttime photochemical model and night airglow on Venus. *Planetary and Space Science*, *85*, 78-88.

Krasnopolsky, V. A., Belyaev, D. A., Gordon, I. E., Li, G., & Rothman, L. S. (2013). Observations of D/H ratios in H_2O, HCl, and HF on Venus and new DCl and DF line strengths. *Icarus*, *224*(1), 57-65.

Krasnopolsky, V. A. (2017). On the iron chloride aerosol in the clouds of Venus. *Icarus*, *286*, 134-137.

Krasnopolsky, V. A. (2018). Disulfur dioxide and its near-UV absorption in the photochemical model of Venus atmosphere. *Icarus*, *299*, 294-299.

Kremnev, R. S., Linkin, V. M., Lipatov, A. N., Pichkadze, K. M., Shurupov, A. A., Terterashvili, A. V., ... & Preston, R. A. (1986). VEGA balloon system and instrumentation. *Science*, *231*(4744), 1408-1411.

Ksanfomaliti, L. V., Vasilchikov, N. M., Ganpantserova, O. F., Petrova, E. V., Suvorov, A. P., Filippov, G. F., ... & Iabrova, L. V. (1979). Electrical discharges in the atmosphere of Venus. *Soviet Astronomy Letters*, *5*, 122-126.

Kurt, V. G., Dostovalow, S. B., & Sheffer, E. K. (1968). The Venus far ultraviolet observations with Venera 4. *Journal of the Atmospheric Sciences*, *25*(4), 668-671.

Lebonnois, S., Quémerais, E., Montmessin, F., Lefèvre, F., Perrier, S., Bertaux, J. L., & Forget, F. (2006). Vertical distribution of ozone on Mars as measured by SPICAM/Mars Express using stellar occultations. *Journal of Geophysical Research: Planets*, *111*(E9).

Lebonnois, S., Hourdin, F., Eymet, V., Crespin, A., Fournier, R., & Forget, F. (2010). Superrotation of Venus' atmosphere analyzed with a full general circulation model. *Journal of Geophysical Research: Planets*, *115*(E6).

Lebonnois, S., & Schubert, G. (2017). The deep atmosphere of Venus and the possible role of density-driven separation of CO 2 and N 2. *Nature Geoscience*, *10*(7), 473-477.

Lefèvre, F., Lebonnois, S., Montmessin, F., & Forget, F. (2004). Three-dimensional modeling of ozone on Mars. *Journal of Geophysical Research: Planets*, *109*(E7).

Lellouch, E., Clancy, T., Crisp, D., Kliore, A. J., Titov, D., & Bougher, S. W. (1997). Monitoring of mesospheric structure and dynamics, in *Venus II: Geology, Geophysics, Atmosphere, and Solar Wind Environment*, (Ed.) Bougher, S. W., Hunten, D. M., & Phillips, R. J., pp 295-324, The University of Arizona Press, Tucson.

Leovy, C. B. (1973). Rotation of the upper atmosphere of Venus. *Journal of the Atmospheric Sciences*, *30*(6), 1218-1220.

Limaye, S. S., & Suomi, V. E. (1981). Cloud motions on Venus: Global structure and organization. *Journal of the Atmospheric Sciences*, *38*(6), 1220-1235.

Limaye, S. S. (1985). Venus atmospheric circulation: Observations and implications of the thermal structure. *Advances in Space Research*, *5*(9), 51-62.

Limaye, S. S. (2007). Venus atmospheric circulation: Known and unknown. *Journal of Geophysical Research: Planets*, *112*(E4).

Limaye, S. S., Kossin, J. P., Rozoff, C., Piccioni, G., Titov, D. V., & Markiewicz, W. J. (2009). Vortex circulation on Venus: Dynamical similarities with terrestrial hurricanes. *Geophysical Research Letters*, *36*(4).

Limaye S.S. (2015) Mercury and Venus: Significant Results from MESSENGER and Venus Express Missions, in *Inner Solar System.* (Eds.) Badescu V., Zacny K. Springer, Cham. DOI: 10.1007/978-3-319-19569-8_2

Limaye, S. S., Lebonnois, S., Mahieux, A., Pätzold, M., Bougher, S., Bruinsma, S., Chamberlaind, S., Clancy T.R., Gérard, J.-C., Gilli, G., … & Zasova, L. (2017). The thermal structure of the Venus atmosphere: Intercomparison of Venus Express and ground based observations of vertical temperature and density profiles. *Icarus*, *294*, 124-155.

Limaye, S. S., Mogul, R., Smith, D. J., Ansari, A. H., Słowik, G. P., & Vaishampayan, P. (2018). Venus' spectral signatures and the potential for life in the clouds. *Astrobiology*, *18*(9), 1181-1198.

Linkin, V. M., Blamont, J., Lipatov, A. N., Deviatkin, S. I., D'yachkov, A. V., Ignatova, S. P., ... & Terterashvili, A. V. (1986). Vertical thermal structure in the Venus atmosphere from provisional Vega 2 temperature and pressure data. *Sov. Astron. Lett.*, 12, 40-42.

Linkin, V. M., Blamont, J., Deviatkin, S. I., Ignatova, S. P. & Kerzhanovich, V. V. (1987). Thermal structure of the Venus atmosphere according to measurements with the Vega-2 lander. *Kosmicheskie Issledovaniia*, 25, 659-672.

Lomonosov, M.V. (1761). The Appearance of Venus On The Sun, Observed At The St. Petersburg Imperial Academy Of Sciences On May 26, 1761. St. Petersburg, St. Petersburg Imperial Academy of Sciences (in Russian).

Luginin, M., Fedorova, A., Belyaev, D., Montmessin, F., Wilquet, V., Korablev, O., ... & Vandaele, A. C. (2016). Aerosol properties in the upper haze of Venus from SPICAV IR data. *Icarus*, *277*, 154-170.

Luginin, M., Fedorova, A., Belyaev, D., Montmessin, F., Korablev, O., & Bertaux, J. L. (2018). Scale heights and detached haze layers in the mesosphere of Venus from SPICAV IR data. *Icarus*, *311*, 87-104.

Määttänen, A., Listowski, C., Montmessin, F., Maltagliati, L., Reberac, A., Joly, L., & Bertaux, J. L. (2013). A complete climatology of the aerosol vertical distribution on Mars from MEx/SPICAM UV solar occultations. *Icarus*, *223*(2), 892-941.

Magurno, D., Maestri, T., Grassi, D., Piccioni, G., & Sindoni, G. (2017). Retrieval of Venus' cloud parameters from VIRTIS nightside spectra in the latitude band 25°-55° N. *Planetary and Space Science*, *144*, 16-31.

Mahieux, A., Vandaele, A. C., Robert, S., Wilquet, V., Drummond, R., Chamberlain, S., ... & Bertaux, J. L. (2015). Venus mesospheric sulfur dioxide measurement retrieved from SOIR on board Venus Express. *Planetary and Space Science*, *113*, 193-204.

Markiewicz, W. J., Titov, D. V., Ignatiev, N., Keller, H. U., Crisp, D., Limaye, S. S., ... & Watanabe, S. (2007). Venus monitoring camera for Venus Express. *Planetary and Space Science*, *55*(12), 1701-1711.

Marcq, E., Bézard, B., Drossart, P., Piccioni, G., Reess, J. M., & Henry, F. (2008). A latitudinal survey of CO, OCS, H2O, and SO2 in the lower atmosphere of Venus: Spectroscopic studies using VIRTIS-H. *Journal of Geophysical Research: Planets*, *113*(E5), E00B07. DOI:10.1029/2008JE003074

Marcq, E., Bertaux, J. L., Montmessin, F., & Belyaev, D. (2013). Variations of sulphur dioxide at the cloud top of Venus's dynamic atmosphere. *Nature geoscience*, *6*(1), 25-28.

Marcq, E., Mills, F. P., Parkinson, C. D., & Vandaele, A. C. (2018). Composition and chemistry of the neutral atmosphere of Venus. *Space Science Reviews*, *214*(1), 10.

Marcq, E., Baggio, L., Lefèvre, F., Stolzenbach, A., Montmessin, F., Belyaev, D., ... & Bertaux, J. L. (2019). Discovery of cloud top ozone on Venus. *Icarus*, *319*, 491-498.

Marcq, E., Jessup, K. L., Baggio, L., Encrenaz, T., Lee, Y. J., Montmessin, F., ... & Bertaux, J. L. (2020). Climatology of SO2 and UV absorber at Venus' cloud top from SPICAV-UV nadir dataset. *Icarus*, *335*, 113368.

Mayer, C. H., McCullough, T. P., Sloanaker, R. M. (1958). Observations of Venus at 3.15-cm wave length. *The Astrophysical Journal*, *127*, 1.

McClintock, W. E., Barth, C. A., & Kohnert, R. A. (1994). Sulfur dioxide in the atmosphere of Venus: I. Sounding rocket observations. *Icarus*, *112*(2), 382-388.

McElroy, M. B., Dak Sze, N., & Ling Yung, Y. (1973). Photochemistry of the Venus atmosphere. *Journal of the Atmospheric Sciences*, *30*(7), 1437-1447.

McGouldrick, K., Momary, T. W., Baines, K. H., & Grinspoon, D. H. (2012). Quantification of middle and lower cloud variability and mesoscale dynamics from Venus Express/VIRTIS observations at 1.74 μm. *Icarus*, *217*(2), 615-628.

Miller, H. C., McCord, J. E., Choy, J., & Hager, G. D. (2001). *Measurement of the radiative lifetime of O2(a1Δg) using cavity ring down spectroscopy. Journal of Quantitative Spectroscopy and Radiative Transfer, 69(3), 305–325.* DOI: 10.1016/s0022-4073(00)00086-8

Mills, F. P. (1998). *I. Observations and photochemical modeling of the Venus middle atmosphere. II. Thermal infrared spectroscopy of Europa and Callisto* (Doctoral dissertation, California Institute of Technology).

Mills, F. P. (1999). A spectroscopic search for molecular oxygen in the Venus middle atmosphere. *Journal of Geophysical Research: Planets*, *104*(E12), 30757-30763.

Mills, F. P., & Allen, M. (2007). A review of selected issues concerning the chemistry in Venus' middle atmosphere. *Planetary and Space Science*, *55*(12), 1729-1740.

Mohnen, V. A., Goldstein, W., & Wang, W. C. (1993). Tropospheric ozone and climate change. *Air & Waste*, *43*(10), 1332-1334.

Molina, M. J., & Rowland, F. S. (1974). Stratospheric sink for chlorofluoromethanes: chlorine atom-catalysed destruction of ozone. *Nature*, *249*(5460), 810-812.

Montmessin, F., Quémerais, E., Bertaux, J. L., Korablev, O., Rannou, P., & Lebonnois, S. (2006). Stellar occultations at UV wavelengths by the SPICAM instrument: Retrieval and analysis of Martian haze profiles. *Journal of Geophysical Research: Planets*, *111*(E9).

Montmessin, F., Bertaux, J. L., Lefèvre, F., Marcq, E., Belyaev, D., Gérard, J. C., ... & Vandaele, A. C. (2011). A layer of ozone detected in the nightside upper atmosphere of Venus. *Icarus*, *216*(1), 82-85.

Montmessin, F., & Lefèvre, F. (2013). Transport-driven formation of a polar ozone layer on Mars. *Nature geoscience*, *6*(11), 930-933.

Montmessin, F., Korablev, O., Lefèvre, F., Bertaux, J. L., Fedorova, A., Trokhimovskiy, A., ... & Willame, Y. (2017). SPICAM on Mars Express: a 10 year in-depth survey of the Martian atmosphere. *Icarus*, *297*, 195-216.

Moroz, V. I., Spaenkuch, D., Titov, D. V., Schaefer, K., Dyachkov, A. V., Dohler, W., ... & Nopirakowski, J. (1990). Water vapor and sulfur dioxide abundances at the Venus cloud tops from the Venera-15 infrared spectrometry data. *Advances in space research*, *10*(5), 77-81.

Moroz, V. I., Huntress, W. T., & Shevalev, I. L. (2002). Planetary missions of the 20th century. *Cosmic Research*, *40*(5), 419-445.

Mueller, R. F. (1968). Sources of HCl and HF in the atmosphere of Venus. *Nature*, *220*(5162), 55-57.

Na, C. Y., Esposito, L. W., & Skinner, T. E. (1990). International ultraviolet explorer observation of Venus SO2 and SO. *Journal of Geophysical Research: Atmospheres*, *95*(D6), 7485-7491.

Na, C. & Barker, Edwin & Stern, S. (1993). Observations of Venus SO2 in 1993. 25. 1096.

Na, C. Y., & Esposito, L. W. (1995). UV observation of Venus with HST. In *DPS*, *27*, pp. 07-01).

Nair, H., Allen, M., Anbar, A. D., Yung, Y. L., & Clancy, R. T. (1994). A photochemical model of the Martian atmosphere. *Icarus*, *111*(1), 124-150.

Nakamura, M., Imamura, T., Ishii, N., Abe, T., Satoh, T., Suzuki, M., ... & Taguchi, M. (2011). Overview of venus orbiter, Akatsuki. *Earth, planets and space*, *63*(5), 443-457.

Nakamura, M., Kawakatsu, Y., Hirose, C., Imamura, T., Ishii, N., Abe, T., ... & Fukuhara, T. (2014). Return to Venus of the Japanese Venus climate orbiter AKATSUKI. *Acta Astronautica*, *93*, 384-389.

Niemann, H. B., Kasprzak, W. T., Hedin, A. E., Hunten, D. M., & Spencer, N. W. (1980). Mass spectrometric measurements of the neutral gas composition of the thermosphere and exosphere of Venus. *Journal of Geophysical Research: Space Physics*, *85*(A13), 7817-7827.

Palmer, K. F., & Williams, D. (1975). Optical constants of sulfuric acid; application to the clouds of Venus? *Applied Optics*, *14*(1), 208-219.

Parkinson, W. H., Rufus, J., & Yoshino, K. (2003). Absolute absorption cross section measurements of CO2 in the wavelength region 163–200 nm and the temperature dependence. *Chemical Physics*, *290*(2-3), 251-256.

Patsaeva, M. V., Khatuntsev, I. V., Patsaev, D. V., Titov, D. V., Ignatiev, N. I., Markiewicz, W. J., & Rodin, A. V. (2015). The relationship between mesoscale circulation and cloud morphology at the upper cloud level of Venus from VMC/Venus Express. *Planetary and Space Science*, *113*, 100-108.

Peter, T. (1994). The stratospheric ozone layer — an overview. *Environmental pollution*, *83*(1-2), 69-79.

Peralta, J., Hueso, R., & Sánchez-Lavega, A. (2007). A reanalysis of Venus winds at two cloud levels from Galileo SSI images. *Icarus*, *190*(2), 469-477.

Petryanov, I.V., Andreychikov, B.M., Korchuganov, B.N., Ovsyankin, E.I., Ogorodnikov, B.I., Skitovich, V.I., & Khristianov, V.K. (1981). Iron in the Venus clouds. *Dokl. AN SSSR 260*, 834.

Piccialli, A., Tellmann, S., Titov, D. V., Limaye, S. S., Khatuntsev, I. V., Pätzold, M., & Häusler, B. (2012). Dynamical properties of the Venus mesosphere from the radio-occultation experiment VeRa onboard Venus Express. *Icarus*, *217*(2), 669-681.

Piccialli, A., Montmessin, F., Belyaev, D., Mahieux, A., Fedorova, A., Marcq, E., ... & Korablev, O. (2015). Thermal structure of Venus nightside upper atmosphere measured by stellar occultations with SPICAV/Venus Express. *Planetary and Space Science*, *113*, 321-335.

Piccioni, G., Drossart, P., Sanchez-Lavega, A., Hueso, R., Taylor, F. W., Wilson, C. F., ... & Lebonnois, S. (2007). South-polar features on Venus similar to those near the north pole. *Nature*, *450*(7170), 637-640.

Piccioni, G., Drossart, P., Zasova, L., Migliorini, A., Gérard, J. C., Mills, F. P., ... & Cottini, V. (2008). First detection of hydroxyl in the atmosphere of Venus. *Astronomy & Astrophysics*, *483*(3), L29-L33.

Phillips, L. F. (1981). Absolute absorption cross sections for SO between 190 and 235 nm. *The Journal of Physical Chemistry*, *85*(26), 3994-4000.

Pollack, J. B., Erickson, E. F., Witteborn, F. C., Chackerian Jr, C., Summers, A. L., Van Camp, W., ... & Caroff, L. J. (1974). Aircraft observations of Venus' near-infrared reflection spectrum: Implications for cloud composition. *Icarus*, *23*(1), 8-26.

Pollack, J. B., Dalton, J. B., Grinspoon, D., Wattson, R. B., Freedman, R., Crisp, D., ... & Ma, Q. (1993). Near-infrared light from Venus' nightside: A spectroscopic analysis. *Icarus*, *103*(1), 1-42.

Press, W. H., Teukolsky, S. A., Vetterling, W. T., & Flannery, B. P. (2007). *Numerical recipes 3rd edition: The art of scientific computing*. Cambridge University Press.

Prinn, R. G. (1971). Photochemistry of HCl and other minor constituents in the atmosphere of Venus. *Journal of the Atmospheric Sciences*, *28*(6), 1058-1068.

Prinn, R. G. (1982). Origin and evolution of planetary atmospheres: an introduction to the problem. *Planetary and Space Science*, *30*(8), 741-753.

Quémerais, E., Bertaux, J. L., Korablev, O., Dimarellis, E., Cot, C., Sandel, B. R., & Fussen, D. (2006). Stellar occultations observed by SPICAM on Mars Express. *Journal of Geophysical Research: Planets*, *111*(E9).

Rasool, S. I., & de Bergh, C. (1970). The runaway greenhouse and the accumulation of CO2 in the Venus atmosphere. *Nature*, *226*(5250), 1037-1039.

Rossi, L., Marcq, E., Montmessin, F., Fedorova, A., Stam, D., Bertaux, J. L., & Korablev, O. (2015). Preliminary study of Venus cloud layers with polarimetric data from SPICAV/VEx. *Planetary and Space Science*, *113*, 159-168.

Rossow, W. B., Del Genio, A. D., Limaye, S. S., Travis, L. D., & Stone, P. H. (1980). Cloud morphology and motions from Pioneer Venus images. *Journal of Geophysical Research: Space Physics*, *85*(A13), 8107-8128.

Royer, E., Montmessin, F., & Bertaux, J. L. (2010). NO emissions as observed by SPICAV during stellar occultations. *Planetary and Space Science*, *58*(10), 1314-1326.

Royer, E. M., Montmessin, F., & Marcq, E. (2016). Variability of the nitric oxide nightglow at Venus during solar minimum. *Journal of Geophysical Research: Planets*, *121*(5), 846-853.

Sagan, C. (1960). The Surface Temperature of Venus. *The Astronomical Journal*, *65*, 352-353.

Sánchez-Lavega, A., Lebonnois, S., Imamura, T., Read, P., & Luz, D. (2017). The atmospheric dynamics of Venus. *Space Science Reviews*, *212*(3-4), 1541-1616.

Sandor, B. J., Clancy, R. T., Moriarty-Schieven, G., & Mills, F. P. (2010). Sulfur chemistry in the Venus mesosphere from SO2 and SO microwave spectra. *Icarus*, *208*(1), 49-60.

Sander, S.P., Abbatt, J., Barker, J.R., Burkholder, J.B., Friedl, R.R., Golden, D.M., Huie, R.E., Kolb, C.E., Kurylo, M.J., Moortgat, G.K., Orkin, V.L., Wine, P.H. (2011). Chemical Kinetics and Photochemical Data for Use in Atmospheric Studies, Evaluation number 17. *Technical Report*. Jet Propulsion Laboratory.

Sandor, B. J., & Clancy, R. T. (2012). Observations of HCl altitude dependence and temporal variation in the 70–100 km mesosphere of Venus. *Icarus*, *220*(2), 618-626.

Sandor, B. J., & Clancy, R. T. (2017). Diurnal observations of HCl altitude variation in the 70–100 km mesosphere of Venus. *Icarus*, *290*, 156-161.

Sandor, B. J., & Clancy, R. T. (2018). First measurements of ClO in the Venus atmosphere–altitude dependence and temporal variation. *Icarus*, *313*, 15-24.

Satoh, T., Imamura, T., Hashimoto, G. L., Iwagami, N., Mitsuyama, K., Sorahana, S., ... & Piccioni, G. (2009). Cloud structure in Venus middle-to-lower atmosphere as inferred from VEX/VIRTIS 1.74 μm data. *Journal of Geophysical Research: Planets*, *114*(E9).

Saunders, R. S., Spear, A. J., Allin, P. C., Austin, R. S., Berman, A. L., Chandlee, R. C., ... & Gunn, J. M. (1992). Magellan mission summary. *Journal of Geophysical Research: Planets*, *97*(E8), 13067-13090.

Schofield, J., Diner, D. (1983). Rotation of Venus's polar dipole. *Nature*, 305, 116-119. DOI: 10.1038/305116a0

Seiff, A., & Kirk, D. B. (1982). Structure of the Venus mesosphere and lower thermosphere from measurements during entry of the Pioneer Venus probes. *Icarus*, *49*(1), 49-70.

Seiff, A., Schofield, J. T., Kliore, A. J., Taylor, F. W., Limaye, S. S., Revercomb, H. E., ... & Marov, M. Y. (1985). Models of the structure of the atmosphere of Venus from the surface to 100 kilometers altitude. *Advances in Space Research*, *5*(11), 3-58.

Sekera, Z. (1968). Chapman Function for an Atmosphere with a Constant Temperature Gradient. *Geophysical Journal International*, *15*(1-2), 137-145.

Shaji, N. ISRO Venus Orbiter Mission (2019). https://www.lpi.usra.edu/vexag/meetings/archive/vexag-17/presentations/Nigar.pdf

Shakun, A. V., Zasova, L. V., Piccioni, G., Drossart, P., & Migliorini, A. (2010). Investigation of oxygen O2 (a1Δg) emission on the nightside of Venus: Nadir data of the VIRTIS-M experiment of the Venus Express mission. *Cosmic Research*, *48*(3), 232-239.

Shalygin, E. V., Markiewicz, W. J., Basilevsky, A. T., Titov, D. V., Ignatiev, N. I., & Head, J. W. (2015). Active volcanism on Venus in the Ganiki Chasma rift zone. *Geophysical Research Letters*, *42*(12), 4762-4769.

Sill, G. T. (1972). Sulfuric acid in the Venus clouds. Communications of the Lunar and Planetary Laboratory 9, 191-198.

Simon, F. G., Schneider, W., Moortgat, G. K., & Burrows, J. P. (1990). A study of the ClO absorption cross-section between 240 and 310 nm and the kinetics of the self-reaction at 300 K. *Journal of Photochemistry and Photobiology A: Chemistry*, *55*(1), 1-23.

Smrekar, S. E., Stofan, E. R., Mueller, N., Treiman, A., Elkins-Tanton, L., Helbert, J., ... & Drossart, P. (2010). Recent hotspot volcanism on Venus from VIRTIS emissivity data. *Science*, *328*(5978), 605-608.

Smrekar, S.E., Hensley, S., Dyar, M.D., Helbert, J. (the VERITAS Science Team), (2016). VERITAS (Venus Emissivity, Radio science, InSAR, Topography And Spectroscopy): a proposed Discovery mission, in 47th Lunar and Plan. Sci. Conf., Abstract #2439.

Snellen, I. A. G., Guzman-Ramirez, L., Hogerheijde, M. R., Hygate, A. P. S., & van der Tak, F. F. S. (2020). Re-analysis of the 267-GHz ALMA observations of Venus: No statistically significant detection of phosphine. *Astronomy & Astrophysics*. *ArXiv preprint arXiv:2010.09761*.

Solomon, S. C., Smrekar, S. E., Bindschadler, D. L., Grimm, R. E., Kaula, W. M., McGill, G. E., ... & Stofan, E. R. (1992). Venus tectonics: An overview of Magellan observations. *Journal of Geophysical Research: Planets*, *97*(E8), 13199-13255.

Soret, L., Gérard, J. C., Montmessin, F., Piccioni, G., Drossart, P., & Bertaux, J. L. (2012). Atomic oxygen on the Venus nightside: Global distribution deduced from airglow mapping. *Icarus*, *217*(2), 849-855.

Soret, L., Gérard, J. C., Piccioni, G., & Drossart, P. (2014). Time variations of O2 (a1Δ) nightglow spots on the Venus nightside and dynamics of the upper mesosphere. *Icarus*, *237*, 306-314.

Squyres, S. (2011). Vision and Voyages for Planetary Science in the Decade 2013–2022 (National Academy of Sciences, Washington, DC, 2011). https://www.nap.edu/catalog/13117/vision-and-voyages-for-planetaryscience-in-the-decade-2013-2022

Stark, G., Yoshino, K., Smith, P. L., & Ito, K. (2007). Photoabsorption cross section measurements of CO2 between 106.1 and 118.7 nm at 295 and 195 K. *Journal of Quantitative Spectroscopy and Radiative Transfer*, *103*(1), 67-73.

Stiepen, A., Gérard, J. C., Dumont, M., Cox, C., & Bertaux, J. L. (2013). Venus nitric oxide nightglow mapping from SPICAV nadir observations. *Icarus*, *226*(1), 428-436.

Stolarski, R. S., & Cicerone, R. J. (1974). Stratospheric chlorine: a possible sink for ozone. *Canadian journal of Chemistry*, *52*(8), 1610-1615.

Stolzenbach, A., Lefèvre, F., Lebonnois, S., Määttänen, A., & Bekki, S. (2014). Three-dimensional modelling of Venus photochemistry. In: *Proceedings of the EGU General Assembly*. Vienna, Austria.

Surkov, Y. A. (1983). Studies of Venus rocks by Veneras 8, 9, and 10, in *Venus*, (Ed.) Hunten, D. M., Colin, L., Donahue, T. M., & Moroz, V. I., pp. 154-158, The University of Arizona Press, Tucson.

Surkov, Y. A., Moskalyova, L. P., Kharyukova, V. P., Dudin, A. D., Smirnov, G. G., & Zaitseva, S. Y. (1986). Venus rock composition at the Vega 2 landing site. *Journal of Geophysical Research: Solid Earth*, *91*(B13), E215-E218.

Svedhem, H., Titov, D. V., McCoy, D., Lebreton, J. P., Barabash, S., Bertaux, J. L., ... & Markiewicz, W. J. (2007). Venus Express—the first European mission to Venus. *Planetary and Space Science*, *55*(12), 1636-1652.

Tsang, C. C., Wilson, C. F., Barstow, J. K., Irwin, P. G., Taylor, F. W., McGouldrick, K., ... & Svedhem, H. (2010). Correlations between cloud thickness and sub-cloud water abundance on Venus. *Geophysical research letters*, *37*(2).

Tashkun, S. A., Perevalov, V. I., Teffo, J. L., Bykov, A. D., & Lavrentieva, N. N. (2003). CDSD-1000, the high-temperature carbon dioxide spectroscopic databank. *Journal of Quantitative Spectroscopy and Radiative Transfer*, *82*(1-4), 165-196.

Taylor, F. W., Hunten, D. M., & Ksanfomaliti, L. V. (1983). The thermal balance of the middle and upper atmosphere of Venus. In *Venus*, (Ed.) Hunten, D. M., Colin, L., Donahue, T. M., & Moroz, V. I., pp. 650-680, The University of Arizona Press, Tucson.

Taylor, F. W., Crisp, D., & Bézard, B. (1997). Near-infrared sounding of the lower atmosphere of Venus, in *Venus II: Geology, Geophysics, Atmosphere, and Solar Wind Environment*, (Ed.) Bougher, S. W., Hunten, D. M., & Phillips, R. J., pp 325-351, The University of Arizona Press, Tucson.

Tellmann, S., Pätzold, M., Häusler, B., Bird, M. K., & Tyler, G. L. (2009). Structure of the Venus neutral atmosphere as observed by the Radio Science experiment VeRa on Venus Express. *Journal of Geophysical Research: Planets*, *114*(E9).

Tikhonov, A. N., and V. Y. Arsenin (1977), Solutions of Ill-Posed Problems, V. H. Winston, Washington, D. C.

Titov, D. V., Svedhem, H., Koschny, D., Hoofs, R., Barabash, S., Bertaux, J. L., ... & Markiewicz, W. J. (2006). Venus Express science planning. *Planetary and Space Science*, *54*(13-14), 1279-1297.

Titov, D. V., Ignatiev, N. I., McGouldrick, K., Wilquet, V., & Wilson, C. F. (2018). Clouds and hazes of Venus. *Space Science Reviews*, *214*(8), 126.

Twomey, S. (1977), Some aspects of the inversion problem in remote sensing, in Inversion Methods in Atmospheric Remote Sounding, pp. 41– 65, NASA Langley Res. Cent., Hampton, Va.

Vandaele, A. C., De Mazière, M., Drummond, R., Mahieux, A., Neefs, E., Wilquet, V., ... & Bertaux, J. L. (2008). Composition of the Venus mesosphere measured by Solar Occultation at Infrared on board Venus Express. *Journal of Geophysical Research: Planets*, *113*(E5).

Vandaele, A. C., Korablev, O., Belyaev, D., Chamberlain, S., Evdokimova, D., Encrenaz, T., ... & Mahieux, A. (2017a). Sulfur dioxide in the Venus atmosphere: I. Vertical distribution and variability. *Icarus*, *295*, 16-33.

Vandaele, A. C., Korablev, O., Belyaev, D., Chamberlain, S., Evdokimova, D., Encrenaz, T., ... & Mahieux, A. (2017b). Sulfur dioxide in the Venus Atmosphere: II. Spatial and temporal variability. *Icarus*, *295*, 1-15.

Varotsos, C. A., Efstathiou, M. N., & Christodoulakis, J. (2020). The lesson learned from the unprecedented ozone hole in the Arctic in 2020; A novel nowcasting tool for such extreme events. *Journal of Atmospheric and Solar-Terrestrial Physics*, 105330.

Villard, E., 2008. L'instrument SPICAV d'etude de l'atmosphère de Venus sur la mission Venus Express: caractérisation instrumentale et observations en vol. PhD Thesis. Université Versailles Saint-Quentin-En-Yvelines.

Von Zahn, U., Kumar, S., Niemann, H., & Prinn, R. (1983). Composition of the Venus atmosphere, in *Venus*, (Ed.) Hunten, D. M., Colin, L., Donahue, T. M., & Moroz, V. I., pp. 299-430, The University of Arizona Press, Tucson.

Way, M. J., & Del Genio, A. D. (2020). Venusian Habitable Climate Scenarios: Modeling Venus Through Time and Applications to Slowly Rotating Venus-Like Exoplanets. *Journal of Geophysical Research: Planets*, *125*(5), e2019JE006276.

Widemann, T., Ghail, R. C., Wilson, C. F., & Titov, D. V. (2020). EnVision: Europe's Proposed Mission to Venus. *LPICo*, *2195*, 3024.

Wilson, C. F., Guerlet, S., Irwin, P. G. J., Tsang, C. C. C., Taylor, F. W., Carlson, R. W., ... & Piccioni, G. (2008). Evidence for anomalous cloud particles at the poles of Venus. *Journal of Geophysical Research: Planets*, *113*(E9).

Wilson, C. F., Tsang, C. C. C., Irwin, P. G. J., Taylor, F. W., Bézard, B., Erard, S., ... & Holmes, R. C. (2009). Analysis of thermal emission from the nightside of Venus at 1.51 and 1.55 μm. *Icarus*, *201*(2), 814-817.

Witze A. (2020). Rare ozone hole opens over Arctic - and it's big. *Nature 580*, 18-19 DOI: 10.1038/d41586-020-00904-w

Wofsy, S. C., & McElroy, M. B. (1974). HO x, NO x, and ClO x: Their role in atmospheric photochemistry. *Canadian Journal of Chemistry*, *52*(8), 1582-1591.

Wu, C. R., Yang, B. W., Chen, F. Z., Judge, D. L., Caldwell, J., & Trafton, L. M. (2000). Measurements of high-, room-, and low-temperature photoabsorption cross sections of SO2 in the 2080-to 2950-Å region, with application to Io. *Icarus*, *145*(1), 289-296.

Yoshino, K., Esmond, J. R., Sun, Y., Parkinson, W. H., Ito, K., & Matsui, T. (1996). Absorption cross section measurements of carbon dioxide in the wavelength region 118.7–175.5 nm and the temperature dependence. *Journal of Quantitative Spectroscopy and Radiative Transfer*, *55*(1), 53-60.

Young, A. T. (1973). Are the clouds of Venus sulfuric acid? *Icarus*, *18*(4), 564-582.

Yung, Y. L., & DeMore, W. B. (1982). Photochemistry of the stratosphere of Venus: Implications for atmospheric evolution. *Icarus*, *51*(2), 199-247.

Yung, Y.L., & DeMore, W.B. (1999). Photochemistry of Planetary Atmospheres. p. 306. Oxford University Press.

Zasova, L. V., Moroz, V. I., Esposito, L. W., & Na, C. Y. (1993). SO2 in the middle atmosphere of Venus: IR measurements from Venera-15 and comparison to UV data. *Icarus*, *105*(1), 92-109.

Zasova, L. V., Moroz, V. I., Linkin, V. M., Khatuntsev, I. V., & Maiorov, B. S. (2006). Structure of the Venusian atmosphere from surface up to 100 km. *Cosmic Research*, *44*(4), 364-383.

Zasova, L. V., Ignatiev, N., Khatuntsev, I., & Linkin, V. (2007). Structure of the Venus atmosphere. *Planetary and Space Science*, *55*(12), 1712-1728.

Zasova, L., Ignatiev, N.I., Gerasimov, M.V. (2014). Future Venus exploration: mission Venera-D, in *45th Lunar and Planetary Science Conference*, Abstract #6037.

Zhang, T. L., Baumjohann, W., Delva, M., Auster, H. U., Balogh, A., Russell, C. T., ... & Lammer, H. (2006). Magnetic field investigation of the Venus plasma environment: Expected new results from Venus Express. *Planetary and Space Science*, *54*(13-14), 1336-1343.

Zhang, X., Liang, M. C., Montmessin, F., Bertaux, J. L., Parkinson, C., & Yung, Y. L. (2010). Photolysis of sulphuric acid as the source of sulphur oxides in the mesosphere of Venus. *Nature Geoscience*, *3*(12), 834-837.

Zhang, X., Liang, M. C., Mills, F. P., Belyaev, D. A., & Yung, Y. L. (2012). Sulfur chemistry in the middle atmosphere of Venus. *Icarus*, *217*(2), 714-739.

ÉCOLE DOCTORALE
Astronomie
et Astrophysique
d'Île-de-France (AAIF)

Titre : Étude des espèces mineures dans la mésosphère nocturne de Vénus

Mots clés : COMPOSITION, SPECTROSCOPIE, ATMOSPHERE

Résumé : Les processus chimiques de l'atmosphère dense de CO_2 de Vénus sont contrôlés par des gaz à traces tels que SO_2, O_3, H_2O, CO, etc. Parmi ces composants atmosphériques, un groupe de composés soufrés et oxygènés occupe une place centrale.
L'objectif de cette thèse concerne l'étude du dioxyde de soufre et de l'ozone présents du côté nuit de la haute mésosphère de Vénus entre 85 et 110 km d'altitude. La chimie et la dynamique sont très actives dans cette région et le cycle chimique du soufre dans cette région conduit à la formation de l'épaisse couche nuageuse entre 47 et 70 km d'altitude tout autour de la planète. En outre, on n'a pas encore déterminé exactement quelles interactions chimiques étaient responsables de l'équilibre sur le long terme du CO_2. Une réelle difficulté subsiste en effet quant à notre capacité à évaluer la capacité d'oxydation de l'atmosphère vénusienne, du fait de l'absence de mesures directes de la quantité d'oxygène moléculaire. Cependant, des estimations indirectes de l'O_2 peuvent être faites sur la base des dérivés de cette molécule, dont l'un en particulier est l'ozone. On s'attend à ce que l'ozone soit impliqué dans des réactions avec des espèces principalement chlorées très présentes sur Vénus.
Mon travail de recherche est basé sur les données obtenues par le canal UV du spectromètre SPICAV (SPectroscopy for the Investigation of the Characteristics of the Atmosphere of Venus) à bord de l'orbiteur Venus Express qui a opéré entre 2006 et 2014. SPICAV est un instrument particulièrement bien adapté à la mesure de CO_2, SO_2 et O_3 du côté nuit de l'atmosphère de Vénus au-dessus de la couche nuageuse. Mon étude comprend également une ré-évaluation détaillée de la précision des méthodes de traitement des données spectrales employées jusqu'alors pour déterminer les distributions verticales de la concentrations de gaz dans l'atmosphère. Il s'agit principalement d'une séparation entre la lumière d'une étoile utilisée pour la mesure et celle d'émissions UV provenant de différentes sources, que l'on considère comme parasitant l'interprétation des données obtenues lors des occultations stellaires. Une influence très forte de la calibration en longueur d'onde a pu être mise en évidence, et a abouti à une modification de la technique de calibration se basant sur la comparaison de la position des raies stellaires avec une base de données de référence. Ainsi, cela a permis d'établir des profils de SO_2 de 85 km à 100 km principalement localisés dans les latitudes moyennes. Ces profils suggèrent que SO_2 est uniformément mélangé dans cette gamme d'altitude et qu'il est soumis à une variabilité forte sur de faibles échelles de temps. Cependant, une faible augmentation a été constatée entre le matin et le soir dans les zones du terminateur vénusien et à une altitude de 90-95 km. Enfin, après la découverte de la couche d'ozone sur Vénus faite par Montmessin et al. (2011), la présence de l'ozone a pu être confirmée dans plus de 100 séances d'occultation. L'étude actuelle montre également que les valeurs d'ozone détecté correspondent à ses valeurs maximales plutôt qu'à l'épaisse couche stable que l'on trouve près du sommet des nuages. Ces résultats représentent la première base de données sur la distribution verticale détaillée de la teneur en SO_2 et O_3 dans la mésosphère supérieure du côté nuit, ce qui ouvre de nouvelles perspective pour la compréhension théorique des processus se produisant dans l'atmosphère de Vénus.

Title : Study of minor species in the Venus night mesosphere

Keywords : COMPOSITION, SPECTROSCOPY, ATMOSPHERE

Abstract : Chemical processes of the dense CO_2-atmosphere of Venus are determined by trace gases such as SO_2, O_3, H_2O, CO, etc. Among these atmospheric components, a group of sulphur and oxygen compounds occupies a central position. The objective of this thesis is a study of sulphur dioxide and ozone at the night side of Venus' upper mesosphere that is related to altitudes from 85 to 110 km. Chemistry and dynamics of this altitude range is very active. The sulphuric chemical cycle in the mesosphere leads to a formation of the thick cloud deck at 47-70 km globally enshrouding the planet. Furthermore, it has not yet been determined exactly which chemical interactions are responsible for stabilizing the equilibrium in the chemical cycles of the atmosphere, and maintaining a high mixing ratio of CO_2. The difficulty of evaluating the oxidizing capacity of the atmosphere, due to the lack of direct measurements of the amount of molecular oxygen, is one reason for this. However, indirect O_2 estimations can be made based on derivatives of this molecule, and one of them is ozone. This gas is involved in reactions with species, probably mainly chlorinated compounds, leading to the general chemical cycles.
The research is based on the data obtained from the first stellar occultation experiment released for Venus. It was performed by the UV channel of the SPICAV (SPectroscopy for the Investigation of the Characteristics of the Atmosphere of Venus) spectrometer on board Venus Express orbiter working in 2006-2014. This is a powerful instrument to measure absorption of CO_2, SO_2 and O_3 at the night side of Venus' atmosphere above the cloud layer. This study also includes a detailed assessment of the accuracy of the spectral data processing methods used to retrieve vertical atmospheric gas concentration distributions. Mainly it concerns a separation of a stellar light from UV emission signal originated from different spread sources, which is a parasitic light for the stellar occultation data investigation. A significant influence of a calibration assignment of wavelength to a digital pixel number was obtained. The required accuracy was achieved by a determination of stellar lines position for a large set of stars' spectra measuring in each observational session. Thus, it allowed to establish a profile of the SO_2 content from 85 km to 100 km mainly devoted to mid-latitudinal range. On average, it shows a stable mixing ratio with altitude. For this gas, a prevailed short-period variability has been confirmed. However, a weak possible increase of SO_2 abundance with local time from the morning to the evening terminator at 90-95 km is noticed. After the discovery of the ozone layer on Venus made by Montmessin et al. (2011), the ozone content was confirmed in more than 100 occultation sessions. The current study also shows that the detected ozone values correspond to its maximum values rather than to the thick stable layer. These results are the first detailed vertical distribution of the SO_2 and O_3 content in the upper mesosphere on the night side, which opens up new possibilities for the theoretical description of processes occurring in the atmosphere of Venus.

Maison du doctorat de l'Université Paris-Saclay
2ème étage aile ouest, Ecole normale supérieure Paris-Saclay
4 avenue des Sciences,
91190 Gif sur Yvette, France